MECHANISMS OF ATRIAL FIBRILLATION AND ANTIARRHYTHMIC DRUG THERAPY EVALUATED BY MATHEMATICAL MODELING

by

James Ralph William Kneller

Department of Pharmacology and Therapeutics

Faculty of Medicine

McGill University

McIntyre Medical Building

3655 Sir William Osler Promenade

Montreal, Quebec, Canada H3G 1Y6

Your file Votre référence
ISBN: 0-612-88499-6
Our file Notre référence
ISBN: 0-612-88499-6

MECHANISMS OF ATRIAL FIBRILLATION AND ANTIARRHYTHMIC DRUG THERAPY EVALUATED BY MATHEMATICAL MODELING

by

James Ralph William Kneller

Department of Pharmacology and Therapeutics

Faculty of Medicine

McGill University, Montreal

A thesis submitted to the Faculty of Graduate Studies and Research

McGill University, Montreal, Canada

In partial fulfillment of the requirement of the degree of

Doctor of Philosophy

This thesis is dedicated to:

Anyone who dares to believe that there is something inside them that is superior to circumstance. Excellence is the result of caring more than others think is wise, risking more than others think is safe, dreaming more than others think is practical, and expecting more than others think is possible. God forbid that we should give out a dream of our own imagination for a pattern of the world. Go confidently in the direction of your dreams. Live the life you have imagined. The sure thing is treason to the soul.

– composed by the author, based in part on statements by
H.D. Thoreau, B. Barton, F. Bacon, and an anonymous author

ABSTRACT

Atrial fibrillation (AF) is the most common sustained arrhythmia encountered in clinical practice. Although AF has been recognized and studied extensively since the early twentieth century, AF management is far from ideal. A better understanding of AF mechanisms is essential in order to improve treatment of AF. The objectives of this study were to determine the mechanisms and significance of ionic transients in mathematical action potential models, determine the relative contributions of tachycardia-related myocyte remodeling processes to the pathologic features of the remodeled action potential, and to investigate mechanisms of AF maintenance and antiarrhythmic drugs in atrial tissue. To achieve our goals, we further developed a previously published mathematical model of the canine atrial action potential, formulated a cellular model of tachycardia-related AF, and developed a model of canine atrial tissue and cholinergic AF.

We began by formulating expressions for myocyte Cl^- transport processes which allowed us to evaluate model stability and the influence of model equation singularity, and to characterize pacing-induced ionic transients. We found that tissue and model transients are comparable, indicating that any distortion arising from dynamic equation instabilities is not likely to be significant. In addition, we found that dynamic models may reach absolute stability during sustained pacing, and that assignment of the stimulus current contributes importantly to model stability. Our results indicate that K^+ is the most appropriate stimulus current assignment, that slow rate-related changes in action potential duration are likely related to intracellular Na^+ accumulation and outward Na^+,Ca^{2+} exchanger augmentation, and that model equations formulated to reproduce short-term

electrophysiological behavior may also reproduce longer-term changes in myocyte electrophysiology.

We then measured Ca^{2+}-transients in isolated atrial myocytes in control and following tachycardia-induced remodeling and formulated the first atrial action potential model with realistic Ca^{2+}-handling properties. Our results demonstrate that both remodeling of sarcolemmal ionic currents and subcellular Ca^{2+}-handling processes contribute significantly to action potential shortening and loss of rate adaptation as occurs in chronic AF. These results given insights into underlying mechanisms and have potential clinical relevance.

Next we developed a two-dimensional model of canine atrial tissue and the first model of AF with realistic ionic and propagation properties. The model provides the first theoretical confirmation of the recent experimentally-determined conception of the mechanisms of AF maintenance, indicating that discrete "driver regions" underlie AF, and that wavelets generated by emanating wavefronts give rise to fibrillation but play a relatively passive role in maintaining AF. This ends nearly 40 years of dominance by the Moe model of AF arguing that the multiple wavelet mechanism is the fundamental process underlying AF.

Finally we used our model of AF to determine the mechanisms of AF termination by sodium channel blocking agents (class I antiarrhythmic drugs). In agreement with recent experimental findings, our results demonstrate how sodium channel inhibition first slows and organizes AF, and how the effects of decreased excitability cause AF termination in a way that is independent of wavelength changes, previously thought to be necessary for antiarrhythmic efficacy.

RESUME

En médecine clinique, la fibrillation auriculaire (FA) est l'arythmie soutenue la plus commune. Bien qu'elle ait été décrite et étudiée depuis le début du vingtième siècle, nos méthodes de traitement de la FA ne sont pas optimales. Une meilleure compréhension de la FA est donc nécessaire afin d'améliorer le traitement. Les objectifs de cette étude sont les suivants : 1. déterminer le mécanisme et l'importance des changements ioniques à l'intérieur de modèles mathématiques des potentiels d'action; déterminer la contribution relative des changements causés par la fibrillation cardiaque aux caractéristiques des potentiels d'action pathologiques; étudier les mécanismes de maintenance de la FA; étudier le mécanisme des médicaments anti-arythmiques sur la FA. À ces fins, nous avons modifié un modèle mathématique du potentiel d'action de l'oreillette canine précédemment publié, formulé un modèle cellulaire de la FA lié à la tachycardie, et développé des modèles canins de tissus de l'oreillette et de la FA cholinergique.

Nous avons tout d'abord formulé des expressions visant à répresenter le transport du chlore à l'intérieur des myomères. Ceci nous a permis d'évaluer la stabilité de notre modèle, l'influence d'équations spécifiques et de charactériser les changements ioniques causés par l'activité repetitive. Nous avons noté que les changements ioniques observés chez les tissus étaient comparable à ceux générés par notre modèle. La distorsion due aux instabilités mathématiques potentielles est donc d'une importance négligeable. De plus, nos modèles dynamiques furent en mesure d'atteindre une stabilité absolue durant le pacing – le choix du courant stimulateur contribue de manière importante à la stabilité du modèle. Nos résultats indiquent que le potassium est le choix de courant le plus approprié, que les changements de courant lents liés à la variation de la cadence sont

probablement liés à l'accumulation intracellulaire de sodium et à l'échange externe augmentée de sodium et de calcium.

Nous avons par la suite mesuré les changements de courant du calcium à l'intérieur des cellules cardiaque en condition contrôle et après altération par la tachycardie. Ceci nous a permis de formuler le premier modèle du auriculaire qui représente adéquatement le transport du calcium. Nos résultats démontrent que les transformations au niveau des courants du sarcolèmme et les mécanismes cellulaires de transport du calcium contribuent de façon significative à racourcir la durée du courant et à réduire l'adaptabilité, tels qu'observés lors de la FA chronique. Ces résultant nous instruisent donc des mécanismes de la FA et ont potentiellement des implications cliniques.

Nous avons dévelopé un modèle réalistique du tissue de l'oreillette canine ainsi que le premier modèle de la FA représentant de manière réalistique les propriétés ioniques et de propagation de courant à l'intérieur des myomères. Ce modèle représente la première confirmation théorique des mécanismes de maintenance de FA ayant été dérivés de manière expérimentale. Notre modèle indique que la FA dépend des vagues de réentrée spirales stables et que les "vaguellettes" jouent un role négligeable dans la maintenance de la FA. Ces résultats contredisent donc le modèle de Moe prévalant déjà depuis 40 ans selon lequel une multitude de vaguellettes sont à la base du processus de l'entretien de la FA.

Finallement, nous avons tenté, à l'aide de notre modèle, de déterminer le mécanisme d'interruption de la FA par les bloqueurs de cannaux de sodium (classe I anti-arythmiques). Nos résultats démontrent comment le bloquage des cannaux de sodium ralentis d'abord puis organise la FA, et comment une diminution de l'excitabilité termine la FA indépendamment des changements de courant – ceux-ci étaient précédemment considérés nécessaires à l'action anti-arythmique.

ACKNOWLEDGMENTS

My deepest appreciation is given to my principal thesis supervisor, Dr. Stanley Nattel. His laboratory has given me a unique view of cardiac electrophysiology, and the potential for laboratory science to address questions with clinical relevance. His vision for the combined application of theoretical and experimental methodologies in basic science have enabled this work. Without his extraordinary supervision, persistent encouragement, invaluable support, enthusiastic inspiration, pertinent guidance, constructive criticism, creative discussion, careful proofreading, and correcting of all the manuscripts and this thesis, and close attention to all aspects, my graduate studies and thesis would not have been completed.

I am also extremely grateful to my co-supervisor and friend, Dr. L. Joshua Leon. His expertise, profound knowledge, teaching, and association have shown me how engineering principles, both theoretical and practical, may be applied to physiological systems. His continued patience and hospitality have always been very much appreciated.

Also deserving of my gratitude is Dr. Marc Courtemanche. His mathematical expertise, many insights, and suggestions were instrumental in the initial phases of my doctoral work.

A special thanks to Dr. Jacquetta Trasler and Dr. Alan Tenenhouse, Directors of the MD, PhD Program at McGill University. Of significant importance was their continual encouragement in enabling me to achieve my goals.

This work could not have been accomplished without the help of my colleagues. In particular, I am grateful to Dr. Renqiang Zou, Dr. Edward J. Vigmond, Rafael J.

Ramirez, and Benjamin Smith for their outstanding engineering contributions. Also a heartfelt thanks to Dr. Hui Sun, Dr. Hong Shi, Dr. Lixia Yue, Denis Chartier, Dr. Katayoun Derakhchan, Dr. Danshi Li, Isaac Moss, Dr. Kaori Shinagawa, and Dr. Agnes Benardeau for their expert experimental collaboration.

I would like to extend my sincere appreciation to Dr. Yves Léger and the "Réseau Québécois de Calcul de Haute Performance (RQCHP)", and to MACI, Multimedia Advanced Computational Infrastructure for Alberta for providing essential computing resources.

I also thank Valérie Brousseau, my friend and colleague in medicine, for translation of the abstract into French.

Many thanks are also in store for all my friends and colleagues with whom I have worked during these years, including Dr. Jerome Kalifa, Dr. Gernot Schram, Dr. Manjula Weerapura, Dr. Joachim Ehrlich, Marc Pourrier, Daniel Herrera, Hani Sino, Anis Aziz, Nessrine Hanna, Dr. Akiko Takeshita, Li Pang, Ling Xiao, Sophie Cardin, Peter Melnyk, and Baofeng Yang.

Finally, I would like to thank my parents, Ralph and Marie Kneller, and my sister, Julie (Dr. Kneller), for being an ever-present source of motivation and inspiration throughout my life.

I was supported by a Canadian Institutes of Health Research (CIHR) MD, PhD Bursary and a Merck Pharmacology Fellowship during my doctoral studies.

PREFACE

Note on the format of this thesis:

In accordance with the Faculty of Graduate Studies and Research the candidate has the option of including as part of the thesis the text of original papers already published by learned journals, and original papers submitted or suitable for submission to learned journals. The exact wording related to this option is as follows:

Candidates have the option of including, as part of the thesis, the text of one or more papers submitted or to be submitted for publication, or the clearly duplicated text of one or more published papers. These texts must be bound as an integral part of the thesis.

If this option is chosen, connecting texts that provide logical bridges between the different papers are mandatory. The thesis must be written in such a way that it is more than a mere collection of manuscripts; in other words, results of a series of papers must be integrated.

The thesis must still conform to all other requirements of the "Guideline for Thesis Preparation". The thesis must include: a table of contents, an abstract in English and French, an introduction which clearly states the rationale and objectives of the study, a review of the literature, a final conclusion and summary, and a thorough bibliography or reference list.

Additional material must be provided where appropriate (e.g. appendices) and in sufficient detail to allow a clear and precise judgement to be made of the importance and originality of the research reported in the thesis.

In case of manuscripts co-authored by the candidate and others, the candidate is required to make an explicit statement in the thesis as to who contributed to such work and to what extent. Supervisors must attest to the accuracy of such statements at the doctoral oral defense. Since the task of the examiners is made more difficult in these cases, it is in the candidate's interest to make perfectly clear the responsibilities of all the authors of co-authored papers.

This thesis is composed of the following published and submitted papers co-authored by myself and others.

1. James Kneller, Rafael J. Ramirez, Denis Chartier, Marc Courtemanche, and Stanley Nattel. Time-dependent transients in an ionically-based mathematical model of the canine atrial action potential. *Am J Physiol*. 2002;282:H1437-H1451.

2. James Kneller, Hui Sun, Normand Leblanc, and Stanley Nattel. Remodeling of Ca(2+)-handling by atrial tachycardia: evidence for a role in loss of rate-adaptation. *Cardiovasc Res*. 2002;54:416-26.

3. James Kneller, Renqiang Zou, Edward J. Vigmond, Zhiguo Wang, L. Joshua Leon, and Stanley Nattel. Cholinergic atrial fibrillation in a computer model of a 2-dimensional sheet of canine atrial cells with realistic ionic properties. *Circ Res*. 2002;90:e73-e87.

4. James Kneller, Renqiang Zou, L. Joshua Leon, and Stanley Nattel. Mechanisms of AF termination by pure sodium blockade in an ionically-realistic mathematical model. *Circ Res*. [submitted].

TABLE OF CONTENTS

LIST OF FIGURES AND TABLES

Chapter 1.

Introduction

Chapter 2.

Paper 1

Chapter 3.

Paper 2

LIST OF ABBREVIATIONS

AF	Atrial fibrillation
AP	Action potential
APD	Action potential duration
APD_{50}	Action potential duration to 50% repolarization
APD_{90}	Action potential duration to 90% repolarization
APD_{-60}	Action potential duration to –60 mV repolarization
RNC	Ramirez-Nattel-Courtemanche
mRNC	modified Ramirez-Nattel-Courtemanche
r-Ctl	Revised RNC control model
BCL	Basic cycle length
SR	Sarcoplasmic reticulum
NSR	Network sarcoplasmic reticulum
JSR	Junctional sarcoplasmic reticulum
NCX	Na^+, Ca^{2+} exchange function
CPA	Cyclopiazonic acid
SERCA	Sarcoplasmic reticulum Ca^{2+}-ATPase
CHF	Congestive heart failure
ACh	Acetylcholine
DF	Dominant frequency
RA	Right atria
LA	Left atria
ERP	Effective refractory period
CV	Conduction velocity

Wavelength	ERP×CV
FFT	Fast Fourier transformation
PS	Phase singularity
CBC	Carbamylcholine
ATR	Atrial tachycardia-induced remodeling
ICR	Ion channel remodeling
EC_{50}	Concentration for half-maximal effect
E_K	Potassium reversal potential
E_{max}	Maximal effect
V_{max}	AP upstroke velocity
$[Cmdn]_{max}$	Cytoplasmic Ca^{2+}-buffering by calmodulin
$[Trpn]_{max}$	Cytoplasmic Ca^{2+}-buffering by troponin
$[Csqn]_{max}$	JSR Ca^{2+}-buffering by calsequestrin
$SR_{(Iup,Ileak,Irel)}$	All Ca^{2+} fluxes between the SR and cytoplasm
$[K^+]_i$	Intracellular potassium concentration
$[Na^+]_i$	Intracellular sodium concentration
$[Ca^{2+}]_i$	Intracellular calcium concentration
$[Cl^-]_i$	Intracellular chloride concentration
I_{ion}	Total transmembrane ionic current
I_{stim}	Stimulus current
I_{Na}	Fast sodium current
I_{K1}	Inward rectifier current
I_{to}	Transient outward current

I_{Kr}	Rapid component of classical delayed rectifier current
I_{Ks}	Slow component of classical delayed rectifier current
I_{Ca}	L-type calcium current
$I_{p,Ca}$	Sarcolemmal calcium pump current
I_{NaK}	Na^+,K^+-ATPase
I_{NaCa}	Sodium-calcium exchanger current
$I_{Cl,Ca}$	Calcium-activated chloride current
$I_{b,Na}$	Background sodium current
$I_{b,Ca}$	Background calcium current
$I_{b,Cl}$	Background chloride current
CT_{NaCl}	Na^+/Cl^- co-transporter
$I_{K(ACh)}$	ACh-activated potassium current
V	Transmembrane potential
C_m	Membrane capacitance
V_i	Volume of the intracellular cytoplasm
V_{up}	Volume of the SR uptake compartment
V_{rel}	Volume of the SR release compartment
C_0	Constant of integration
∇^2	Second-derivative Laplacian operator in space
I_{couple}	Coupling current between adjacent cells
Φ_{up}	Uptake flux from cytosolic Ca^{2+} pool to the NSR
$\Phi_{up(max)}$	Maximal value of Φ_{up}
K_{up}	Half-saturation constant for Φ_{up}

Φ_{leak}	Leakage flux between cytosolic Ca^{2+} pool and the NSR
$[Ca^{2+}]_{NSR}$	Ca^{2+} concentration in the NSR
$[Ca^{2+}]_{NSR(max)}$	Maximal $[Ca^{2+}]_{NSR}$
$[Ca^{2+}]_{JSR}$	Ca^{2+} concentration in the JSR
Φ_{rel}	Release flux from the JSR to the cytosolic Ca^{2+} pool
τ_{rel}	Activation time constant for Φ_{rel}
k_{rel}	Maximal release rate for Φ_{rel}
S_1	Basic stimulus
S_2	Premature stimulus
Φ_e	Extracellular potential
R_s	Series resistance

STATEMENT OF AUTHORSHIP

The following is a statement regarding the contributions of co-authors and myself to the papers included in this thesis.

Paper 1. I designed and performed the experiments, analyzed the data, formulated novel model currents and transporters, designed and performed model simulations, and wrote the manuscript. Rafael Ramirez provided model code and instruction on operation of the model. Denis Chartier provided valuable experimental assistance and teaching. Dr. Courtemanche supervised the formulation of mathematical expressions, data collection and simulations, and generated the initial idea. Dr. Nattel provided close supervision in all aspects, suggesting simulation protocols, clarifying the thought, and producing the final version of the manuscript.

Paper 2. I developed all models, designed and performed all simulation studies, participated in data analysis, and wrote the manuscript. Dr. Sun performed the experiments and performed much of the data analysis. Dr. Leblanc participated in discussing the data, providing suggestions, and reading the manuscript. Dr. Nattel provided close supervision in all aspects, generating the initial idea, clarifying the thought, and producing the final version of the manuscript.

Paper 3. I generated the initial idea, developed the model, designed and performed all simulations, performed all tissue-level experiments and data analysis, and

wrote the manuscript. Dr. Zou formulated the electrogram and FFT code and participated in simulation analysis. Dr. Vigmond provided parallelized 2D code, participated in discussing and processing data, and reading the manuscript. Dr. Wang participated in discussing the data. Dr. Leon supervised the implementation of the 2D model, discussed the simulations, provided suggestions, and assisted in finalizing the manuscript. Dr. Nattel provided close supervision in all aspects, clarifying the thought, and producing the final version of the manuscript.

Paper 4. I designed, performed, and analyzed all simulations and wrote the manuscript. Dr. Zou provided code and performed the phase singularity measurements. Dr. Leon assisted in model development and reading the manuscript. Dr. Nattel provided close supervision in all aspects, generating the initial idea, clarifying the thought, and producing the final version of the manuscript.

CHAPTER 1 INTRODUCTION

1 Mechanisms of Atrial Fibrillation

1.1 Overview

The heart is a mechanical pump that is electrically activated. The pump is divided into four muscle chambers, consisting of two atria and two ventricles. The atria receive blood from the venous circulation, and contraction of the atria and hydrostatic forces deliver blood to the much larger and more powerful ventricles that pump into the arterial circulation. Muscle chambers are composed of myocytes (size dimensions on the order of 10×100 μm) that are mechanically and electrically coupled on all sides, forming a mechanical and electrical syncytium (size dimensions on the order of 10×10 cm). With each heart beat, waves of transmembrane electrical depolarization propagate across this substrate, stimulating muscle contraction and the generation of mechanical force. At the single cell level, the electrical impulse is called an action potential. Cellular contraction occurs during the action potential, and the cell is refractory to additional excitation during this time. At the tissue level, cellular action potentials combine to form excitatory wavefronts. Each cell must generate an action potential to participate in contraction and transmission of the activation waves. While atrial and ventricular tissue share many similarities, important cellular and structural differences give each chamber-type unique electrical and mechanical properties. Furthermore, while neighboring cells and tissues are relatively homogeneous, cellular and structural differences form the basis of electrical and mechanical heterogeneity throughout the myocardium (1).

Cardiac rate is finely tuned to the body's needs by physiological control of the cardiac pacemaker function of the sinoatrial (SA) node, which maintains a rate of about

60/min at rest and can fire as rapidly as 180-200/min at peak exercise (1). The SA node first activates the atria, and then activation proceeds to the atrioventricular (AV) node, which transmits the impulse to activate the ventricles. Atrial fibrillation (AF) is characterized by rapid and irregular (400-600/min) atrial activation, which manifests as continuous, irregular atrial activation on the electrocardiogram (2). If each atrial impulse conducted to the ventricles, the extremely rapid ventricular rate would lead to ineffective cardiac contraction and death. To prevent this, the AV node provides a filtering function, restricting the ventricular rate to ~150/min during AF (1). Cardiac anatomy and electrical activity in sinus rhythm (panel A) and during AF (panel B) are depicted schematically in figure 1.

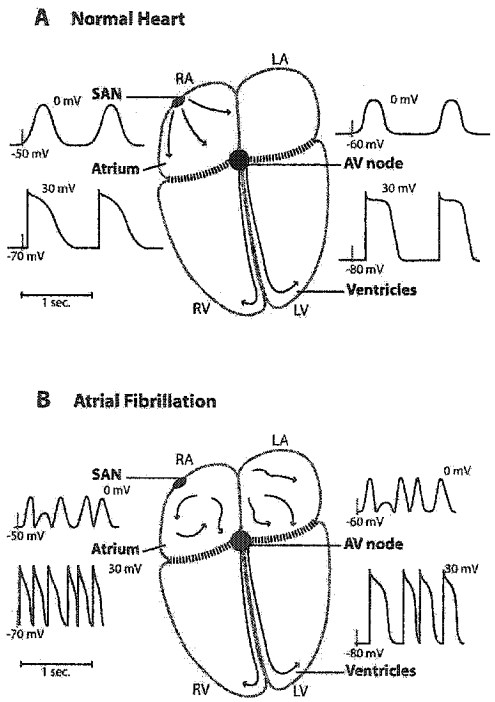

Figure 1. Schematic diagram of electrical activity during normal rhythm (**A**) and AF (**B**). Representative action potentials are shown from the sinoatrial node (SAN), atrium, AV node and ventricles. RA=right atrium, LA=left atrium, RV=right ventricle, LV=left ventricle.

1.2 The Epidemiology of Atrial Fibrillation

1.2.1 Incidence and Prevalence

AF is the most common sustained tachyarrhythmia, and will become more common with aging of the population (3-5). AF presently occurs in 0.4% of adults and 2-4% of those over 60 (6; 7). The prevalence of AF per 1000 persons is around 2-3 in those aged 25 to 35 years, 30-40 at ages 55 to 64, and 50-90 at ages 62 to 90. The Framingham study examined the precursors, occurrence, and prognosis of AF in a 22- to 30-year follow-up of a cohort of 5209 men and women in the 30- to 62-year range at the time of entry (4; 8-11). The incidence of AF was observed to be higher in men, and to increase with age in both sexes. The overall chance of developing AF over 2 decades was 2%.

1.2.2 Associated Diagnoses

AF is most frequently associated with other cardiovascular diseases, although a wide range of conditions may give rise to the arrhythmia. The majority of cases of chronic AF are related to cardiovascular abnormalities. The presence of cardiovascular disease increases the likelihood of AF three- to five-fold, with coronary artery disease doubling the risk of AF from 4% to 8%. AF also occurs in 6% to 23% of cases of myocardial infarction. Although it is not an independent risk factor and infrequently prompts patients to seek medical attention, it does suggest more extensive infarction and ventricular dysfunction, and is associated with increased mortality (12-14). An increased incidence of AF is also observed in patients with ischemic heart disease, as may occur in the contexts of atrial infarction, congestive heart failure, and mitral regurgitation. In rheumatic heart disease, the risk of AF is increased eight-fold in men and 27-fold in men

and women, respectively. Hypertension increases the risk of developing AF four- and cardiac failure by ~10-fold, and AF occurs in 5% to 40% of cases of coronary artery bypass grafting and cardiac valvular surgery (15; 16). In contrast to these associations, the Framingham study also showed no cardiovascular disease was discernable in 16.6% of men and 6% of women developing AF, although some showed signs of nonspecific abnormalities or intraventricular conduction delays (8).

AF frequently occurs in the setting of advanced pulmonary disease, as hypoxia, respiratory acidosis, cor pulmonale, pericarditis, neoplasm, increased catecholamines, and sympathomimetic drugs all predispose to AF (17; 18). Surprisingly, AF rarely complicates pulmonary embolism, as the National Co-operation Study of Urokinase for Pulmonary embolism found that only 3% of patients with pulmonary embolism had AF despite extensive hemodynamic compromise (19). In contrast, AF was also reported to occur in up to 15% of patients following thoracotomy performed in association with surgery for lung cancer (20).

The most important noncardiovascular causes of AF are alcohol and hyperthyroidism (20). Chronic drinkers may develop patchy inflammatory lesions (21) and high doses of alcohol can subsequently precipitate AF (22-25). Overt hyperthyroidism precipitates AF in approximately 10% to 20% of patients. This occurs more frequently in the elderly (26-28) where the classical clinical features of hyperthyroidism may be absent, and AF may be the presenting feature of this disease. Although a relatively uncommon cause of AF, hyperthyroidism is important to consider, since conversion and long-term maintenance of sinus rhythm is likely if antithyroid treatment is initiated early (28-30). Other rare causes of AF include infections (ie,

pneumonia and empyema), anesthetic agents, electrolyte disturbances (such as hypokalemia, hypocalcemia, hypomagnesemia), and metabolic abnormalities (such as hypothermia, hypoxia and hypoglycemia). Also drugs for respiratory disease such as β_2 agonists, sympathomimetic cold remedies, antihistamines, and coffee can precipitate AF (31; 32). Finally, extreme accelerating forces, as may occur in military aircraft, have been known to initiate attacks (25). Alternately, AF has been terminated by a catapult launch from an aircraft carrier, though it was commented that this "is probably not a clinically useful modality" (33).

1.2.3 Prognosis and Complications of Atrial Fibrillation

AF is a cause of significant morbidity and mortality, principally because of thromboembolic complications. AF is responsible for more than 85% of systemic thromboembolism from the heart (34), with more than two thirds of all clinical embolic events lodging in the brain (35; 36). AF is associated with a 4.8-fold increased risk of stroke in the absence of oral anticoagulation (9), with the risk increasing 17-fold when AF is associated with rheumatic mitral valve disease. The proportion of strokes associated with AF increases with age, from about 7% at ages 50 to 59 to 36% at ages 80 to 89. The risk of peripheral embolism is also increased in AF, occurring at approximately 2% per year compared to 4% to 6% per year for strokes. The combined results of recent antithrombotic trials in AF have aided risk stratification, though prophylaxis is a subject of ongoing debate. The incidence of pulmonary embolism is also increased in AF (36), although most atrial emboli are too small to cause significant pulmonary compromise.

The normal atrioventricular node generally suppresses the induction of ventricular tachyarrhythmias by the rapid and irregular rates of AF. However, AF may cause syncope and cardiac arrest in some patients with very abnormal ventricular function, as in hypertrophic cardiomyopathy (37). When impaired AV conduction leads to slow and irregular rates during AF or following conversion from AF, the long QT syndrome may result and initiate ventricular tachyarrhythmias, including ventricular fibrillation in some patients with the Wolff-Parkinson-White syndrome. Marked atrioventricular block during AF can cause syncope due to long pauses in cardiac contraction. Profound bradycardia can also occur after the termination of AF in patients with the sick sinus syndrome.

AF may provoke a dangerous acute deterioration in additional situations. Decreased cardiac output secondary to AF may induce ischemia in organs with compromised perfusion, and unstable angina can also be provoked by AF, as a rapid ventricular response increases myocardial oxygen demand. Patients with mitral stenosis or in whom left ventricular relaxation is limited because of hypertrophy or infiltration are especially dependent on atrial systole to supplement ventricular filling. In addition, a sustained rapid ventricular rate during AF can give rise to left ventricular dysfunction, although this effect appears to be reversible when the arrhythmia is terminated or the ventricular rate controlled (38; 39). AF with a poorly controlled ventricular rhythm may give rise to a variety of undesirable symptoms, including angina, palpitations, dyspnea, syncope, dizziness, and fatigue.

To summarize, atrial fibrillation came to be called the "darling arrhythmia" during the 1990s, fostering intense interest clinically and experimentally, as clinicians and researchers sought to understand its mechanisms and control its impact (40). As Waktare

and Camm pointed out, "AF causes numerous deleterious effects and is still difficult to treat. Our therapeutic choices are currently expanding but the long-term restoration of sinus rhythm can still not be the goal for all. The important principles are to investigate and treat appropriately from the outset to minimize the chances of adverse events and maximize the chances of maintaining sinus rhythm. Without treatment, AF begets trouble" (41). Achieving appropriate treatments may depend on our understanding of the mechanisms of AF.

1.3 Cellular Basis for AF—Action Potential

As mentioned in Section 1.1, arrhythmias are a multicellular phenomena that ultimately depend on the electrophysiological properties of individual cells. In response to excitatory stimuli, each cell generates an action potential, which represents a rapid increase in transmembrane potential followed by a more gradual return to baseline. Briefly, the sarcolemmal membrane forms a resistive barrier that permits the selective flow of ions through membrane-spanning channels, or pores. There are many different kinds of ion channels, each with characteristic time- and voltage-dependent kinetics and nonlinear restitution properties, and these selectively conduct various ionic species (primarily sodium (Na^+), potassium (K^+), and calcium (Ca^{2+})). During each cardiac cycle, action potentials arise from this transmembrane ion flow and resulting "bioelectricity". Action potentials have a characteristic shape, although there is considerable morphologic variability between atrial cell types (see Fig. 11 of Ref. (42)) and in various physiological and pathological contexts (see Section 1.5).

A variety of ionic currents are responsible for the action potential. I_{K1} is responsible for the resting K^+-conductance that sets the resting potential, normally between –70 and –80 mV. A large Na^+-current (I_{Na}) brings the cell from its resting potential to a value in the range of +40 mV, providing the electrical energy for cardiac conduction. The cell then partially repolarizes via a transient outward K^+-current, I_{to}, followed by a flatter portion of the action potential, the plateau, maintained by inward L-type Ca^{2+}-current (I_{Ca}). Time-dependent activating K^+-currents that show little inactivation ("delayed-rectifiers", I_K) repolarize the cell. Human atrial I_K has 3 components: an "ultra-rapid" component, I_{Kur}, a "rapid" component, I_{Kr}, and a "slow" component, I_{Ks}. An inward pacemaker current, I_f, is particularly important in spontaneously automatic cells like those in the sino-atrial and atrio-ventricular nodes. Intracellular concentrations of Na^+ and K^+ are relatively stable over each cardiac cycle, except for free intracellular [Ca^{2+}] which rises sharply during the depolarized phase of the AP, and diastolic relaxation ensues when cytosolic Ca^{2+} is reduced by uptake into the sarcoplasmic reticulum and by extrusion via the Na^+,Ca^{2+}-exchanger (NCX). NCX is electrogenic, exchanging 3 Na^+ ions for each Ca^{2+} (one net positive charge in the direction of Na^+ transport per cycle), and produces an inward current during Ca^{2+} extrusion. Ionic equilibrium is also maintained by the Na^+,K^+-ATPase, which removes 3 Na^+ ions while returning 2 K^+ ions with each pump cycle. This activity is also electrogenic, resulting in a net outward current that contributes to repolarization (1).

1.4 Mechanisms of AF

1.4.1 AF Based on Reentry—Early Developments

AF was first described William Harvey in 1628, as an "undulating atrial movement". This phenomenon also came to be known as "arrhythmia perpetua" (McKenzie), "pulsus irregularis perpetuus" (Hering), and "delirium cordis" (Wenckebach). However, as this activity was not understood, AF was not associated with its clinical correlates until many years later. Centuries after the initial observation (1906 to 1909), independent reports of the relationship between an irregular pulse and the characteristic electrocardiographic appearance of AF was made worldwide by Lewis, Rothberger and Winterberg, and Cushny and Evans (43-46). Today, AF is diagnosed by the same electrocardiographic features.

The electrophysiological basis of AF has been ascribed to reentrant mechanisms, where electrical activity conducts along circular circuit trajectories rather than in planar waves (47). Reentry was first conceived based on the concept of circus movement. The possibility of a circus movement of the cardiac impulse was first mentioned by McWilliam in 1887 (48) and was demonstrated in 1908 by Mayer (49) in rings cut from the bells of *Medusae*. In 1913, Mines suggested that reentrant processes underlying fibrillation required that the length of the excitation wave be shorter than the column of muscle on which it occurred (50). In 1914, Both Mines (51) and Garrey (52) presented concepts of fibrillation as maintained by multiple-simultaneous-reentrant circuits (Fig. 2[left]). In 1925, Lewis (Fig. 2[middle]) proposed instead that a single or small number of sources of stable reentrant activity maintain AF (53). Garrey published a detailed

review of the state of knowledge regarding AF in 1924 (47). Garrey viewed AF as arising when "the impulse is diverted into different paths, weaving and inter-weaving through the tissue mass, crossing and recrossing old paths again to course over them or to stop short as it infringes on some barrier of refractory tissue." Although he presented a consensus supporting the multiple-functional-reentry-circuit concept of AF, he pointed out alternative views of AF as caused by atrial hyperexcitability (one or more rapidly discharging ectopic foci) or to a single, dominant mother wave with fibrillatory conduction. These notions of mechanisms underlying AF are portrayed schematically in figure 2.

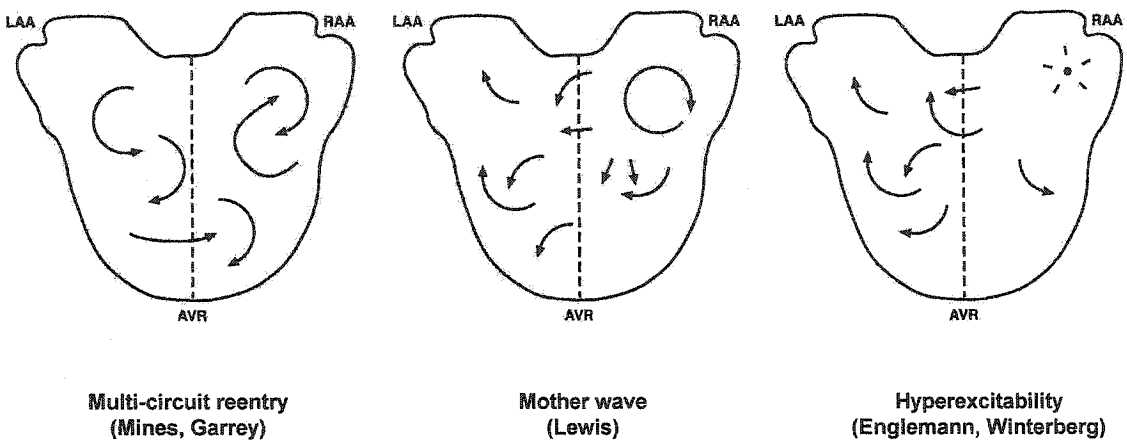

Figure 2. Schematic representations of mechanistic conceptualizations of atrial fibrillation proposed by investigators in the early twentieth century. The atria are unfolded with a dashed line indicating the position of the septum. LAA, left atrial appendage; RAA, right atrial appendage; AVR, atrioventricular ring. (Reproduced with permission from Ref. (54)).

1.4.2 Mechanisms of Reentry Initiation

Although the SA node is the intrinsically fastest pacemaker, various areas of the heart can show similar automaticity. Abnormally discharging cellular foci may produce ectopic

impulses that may initiate spontaneously-sustained reentry circuits or act independently as arrhythmia generators in the absence of stable reentry. In the case of automaticity, pacemaker activity results from a change in the balance of cardiac currents in the resting (diastolic) phase of the AP, such that inward currents predominate and lead to progressive depolarization. When the membrane reaches the threshold potential, the cell fires. If the slope of diastolic repolarization is increased in a region outside the sinus node, for example, the cell will reach threshold earlier and generate ectopic action potentials. Abnormal focal activity can also arise from arrhythmogenic afterdepolarizations (for details, see Ref. (1)). Haissaguerre et al. demonstrated the importance of pulmonary vein foci in the initiation of AF (55). While the pulmonary veins are the most common source of focal activity, arrhythmogenic foci can also arise from the ligament of Marshall (a venous remnant of the left atrium) (56) and the superior vena cava (57). Reentry arises from abnormal impulse propagation between different zones of tissue. Following initial depolarization of an action potential, Na^+ channels are inactivated and the cell cannot be re-fired until the cell repolarizes to a potential (about –60 mV) at which Na^+ channels recover from inactivation, (the "refractory period", often abbreviated RP).

The refractory period is often variable, even in connected tissue segments. An ectopic complex arising during the refractory period of one zone of connected tissues will initially fail to activate adjacent, refractory myocardium, but may propagate via an alternative pathway to return to the previously refractory zone when its refractory period has expired, causing reactivation at this site. Under appropriate conditions, this can result in repetitive reactivation of the 2 tissue areas in sequence, causing a tachyarrythmia. Reentry can occur in a single circuit, producing rapid, regular firing, or multiple unstable

reentry circuits can simultaneously co-exist, producing more irregular (fibrillatory) activity. Refractory period is clearly a key determinant of reentry. Long refractory periods make it more likely that circulating impulses will encounter still-refractory tissue and die out. Note that even in the presence of an appropriate substrate for reentry, a trigger is needed in the form of a premature activation to initiate reentry.

1.4.3 Mechanisms of Reentry

1.4.3.1 Closed-Circuit Reentry

Multiple-circuit reentry clearly plays an important role in AF. The precise mechanisms involved in multiple-circuit reentry and the underlying determinants have been the subject of considerable development. Mines considered that reentry occurs in "closed circuits in the myocardium" (Fig. 3[left]) (50). The center of these circuits is generally inexcitable as this region may consist of anatomical obstacles like the venae cavae or pulmonary veins, or regions of inexcitability caused by heart disease. More recently, Wu et al. demonstrated that even the atrial microstructure may also act as anatomical pathways for closed circuit reentry, as reentry may occur around loops formed by pectinate muscle bundles (58). These specialized tissue geometries may stabilize reentry in the vertical plane, such that emanating activity appears to arise from a spontaneously discharging focal source, as described by Garrey (47) (Section 1.4.1). Because the size of the circuit is fixed, reentry depends critically on a circuit time that is greater than the refractory period (the circuit time equals the path length divided by conduction velocity). The refractory period determines whether reentry can be maintained, as ongoing reentry

requires that the refractory period be less than the circuit time, but does not directly affect circuit time or tachycardia rate.

1.4.3.2 Leading-Circle Reentry

Garrey acknowledged that closed-circuit reentry is a limited concept as it does not account for the dynamic nature of reentry in arrhythmias like AF, in which the reentry substrate appears functional rather than fixed (47) (Section 1.4.1). Allessie et al. presented the first detailed conceptual model of functional reentry with supporting experimental observations in 1977 (59). According to Allessie's "leading-circle" conceptualization (Fig. 3[middle]), reentry is maintained in a leading circle, which establishes itself in the smallest circuit that can maintain continuous activity where the center (core region, defined in Section 1.4.7) of the reentry circuit is continuously invaded by centripetal impulses from the circulating reentrant wave and is thus continuously excited. This minimum circuit size for reentry is given by the wavelength, a concept first presented by Mines (50) and later quantified by Wiener & Rosenblueth (60) as the product of conduction velocity and refractory period (discussed in detail in Section 1.6.1). A change in conduction velocity causes the reentrant impulse to move concentrically based on the path length traveled in one refractory period; increased conduction velocity moves the wave outwards, to travel in a larger orbit, whereas decreased conduction velocity allows the wave to move inwards to a smaller path. Because the circuit time equals the refractory period (by definition in a path equal to the wavelength), refractory period is the sole determinant of circuit time and tachycardia rate.

1.4.3.3 Spiral-Wave Reentry

More recently, spiral waves rotating around an organizing center have been discovered in different types of excitable media, including autocatalytic chemical reactions and various biological systems (61), and it may be that functional reentry in cardiac muscle is also the result of similar spiral waves. Davidenko et al. used a potentiometric dye in combination with CCD (charge-coupled device) imaging technology to demonstrate spiral waves in ventricular muscle (62). Spirals were observed to anchor to small anatomic structures or drift to other sites. Activity was very regular when spirals were anchored and irregular during drift. It was later demonstrated that a single rapidly moving spiral rotor is sufficient to produce electrocardiographic patterns that are indistinguishable from fibrillation (63). Spiral wave reentry has also been demonstrated in atrial tissue (64-66), where a single meandering spiral also gave rise to AF-like electrograms (64; 67). Meander, also in human tissues, was attributed to rate adaptation of the atrial refractory period (64; 64; 65), as this meant that the distribution of excitable tissue available for reentry was continually changing. As indicated in Fig. 3[right], spiral wave reentry differs from the other models in that the core region (defined in Section 1.4.7) is fully excitable but unexcited (66; 68; 69).

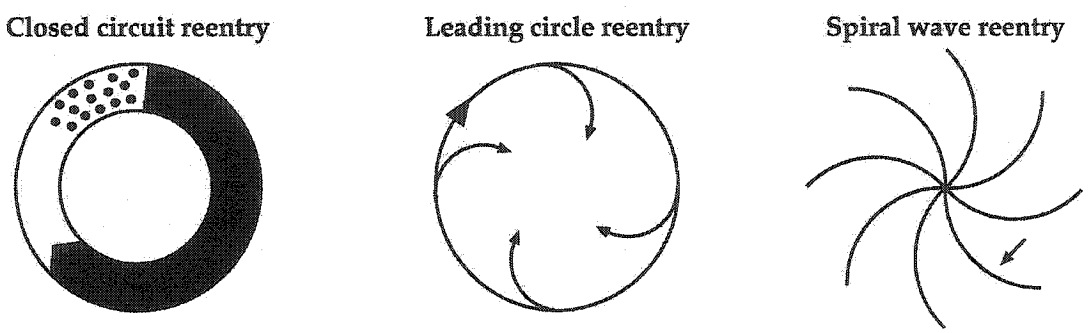

Figure 3. Schematic diagrams of closed-circuit reentry [*left*], leading-circle reentry [*middle*], and spiral-wave reentry [*right*] (Reproduced with permission from Ref. (54)).

1.4.4 Multiple Wavelet Hypothesis of AF

In 1959, Moe & Abildskov showed that AF could be produced by experimental paradigms of both multiple circuit reentry and rapid activity, and they suggested that either type of mechanism might cause clinical AF (70). The concept of reentry was further developed by the "multiple wavelet hypothesis" of AF, put forward by Moe et al. in 1962 (71). In this conceptualization, Moe developed the notion of wavelets of electrical excitation and the importance of spatial heterogeneity of refractory period in AF. This concept differed from previous multiple-circuit-reentry notions in that, rather than thinking of reentry waves making complete revolutions, it was believed that propagation during AF involves multiple independent wavelets circulating through functionally refractory tissue. Moe's original description was worded as follows: "Orderly spread of excitation will no longer be possible; the grossly irregular wavefront becomes fractionated as it divides about islets or strands of refractory tissue, and each of the daughter wavelets may now be considered as independent offspring. Such a wavelet may accelerate or decelerate as it encounters tissue in a more or less advanced state of recovery. It may become extinguished as it encounters refractory tissue; it may divide again or combine with a neighbor; it may be expected to fluctuate in size and change in direction" (70). Fibrillation was thought to be a random process sustained by the ongoing multiplication of wavelets, with fully developed fibrillation being a state in which many such randomly wandering wavelets coexist.

1.4.4.1 Moe Computer Model of AF

When the "multiple wavelet hypothesis" was first circulated, the experimental techniques necessary to test the proposed mechanism were not available. To evaluate his hypothesis,

Moe et al. developed a simple cellular automaton computer model of canine atrial tissue and cholinergic AF in the early 1960s (72). The model contained 992 tissue-units (each 4 mm in diameter) joined to simulate a 12.4×12.8 cm atrial sheet. Units were programmed with rate dependence of the absolute refractory period using time-dependent functions, and refractory period heterogeneity was randomly distributed. In control, conduction velocity was ~80 cm/s and conduction time ~160 ms (about twice typical experimental values). Moe acknowledged that this substrate bore only a limited resemblance to atrial tissue electrophysiology and recognized severe limitations to the computer representation and capacity, yet he believed the model to be sufficient to test the postulated mechanism of AF. The strength of the model was that it displayed sustained fibrillatory activity. AF in the model arose from the ongoing fractionation of multiple activation wavefronts into independent daughter wavelets. Wavelets would randomly collide, mutually annihilate, or coalesce in a self-perpetuating and ceaselessly-changing turbulent process that was reentrant in nature. As postulated, the model predicted that AF is a totally random process resembling Brownian motion. Being random, sustained AF was thought to represent a probability phenomenon dependent on the total number of wavelets present at any one time. Any factor increasing the number of wavelets would aid in maintaining AF while factors decreasing the wavelet count would tend to terminate AF. The model predicted that 23 to 40 wavelets were needed for sustained AF. A representative simulation from the original Moe model of AF is shown in figure 4.

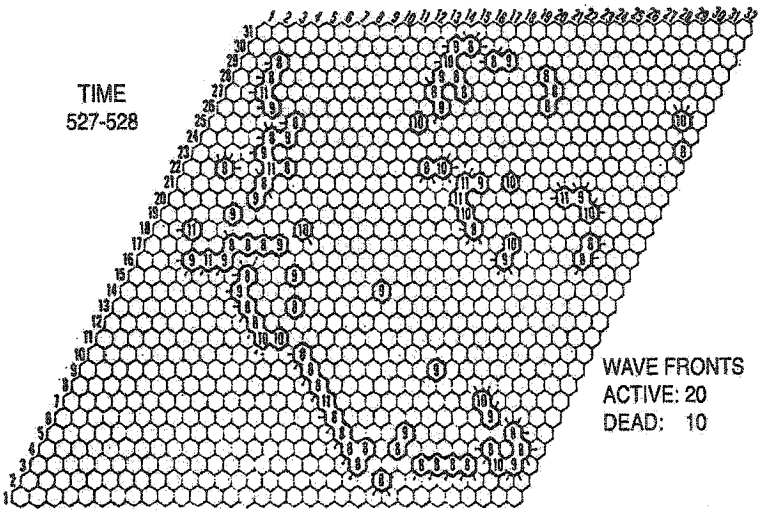

Figure 4. Representative simulation of AF from the original Moe computer model of AF (Reproduced with permission from Ref. (72)).

Following the presentation of this computer model in 1964 (72), Moe's multiple wavelet hypothesis (71), having some preliminary theoretical support but lacking any experimental validation, came to provide the most widely accepted mechanistic description of AF. Despite its many successes, the Moe model is now known to contain several serious limitations. Beyond the nonphysiologic cellular automaton tissue substrate, fibrillation depended on erroneous refractory period and conduction properties. Maximal refractory period heterogeneity gradients were permitted between adjacent units, because the smoothing of refractoriness gradients caused by physiological cell-to-cell coupling did not exist in the model. Conduction velocity dropped to 20 cm/s during the relative refractory period (30 ms fixed duration), slowing propagation to extremely low levels and creating a nonphysiologic conduction velocity heterogeneity during repeated stimulation. Asynchronous activity was further exaggerated by these nonuniformities, as cells excited early underwent a greater shortening of the refractory

period than those that responded later. These properties suggest that AF in the model was misrepresented, and that certain model predictions are likely to be misleading. While this does not disprove the multiple wavelet mechanism, the need for experimental observations supported by a more realistic mathematical model is clear.

1.4.5 Primary Generator-Sources Hypothesis of AF

Moe's multiple wavelet hypothesis and model predictions have been called into question in recent years. In 1998, Jalife et al. presented a new unifying hypothesis for the electrophysiological basis of AF (73). The postulated mechanism was based on a wealth of experimental data from multiple levels of study, including wavelet mapping and frequency analysis of electrograms, together with theoretical studies using more sophisticated mathematical models. It was surmised that "sustained AF depends on the uninterrupted periodic activity of discrete reentrant sites. The shorter reentrant circuits act as dominant frequency sources that maintain the overall activity. The rapidly succeeding wavefronts emanating from these sources propagate through both atria and interact with anatomic and/or functional obstacles, leading to the phenomenon of 'vortex shedding' and to wavelet formation. Some of such wavelets may shrink and undergo decremental conduction, others may be annihilated by collision with another wavelet or a boundary, and still others may curl to create new vortices. The end result would be the fragmentation of the periodic wavefronts into multiple independent daughter wavelets, giving rise to new wavelets, and so on in the ceaseless, globally aperiodic motion that characterizes fibrillatory conduction" (73). The phenomenon of vortex shedding is analogous to the formation of eddies in hydrodynamical systems (e.g., fluid waves

interacting with a physical obstacle in their path, as occurs in the ascending aorta during systole when the left ventricle rapidly expels blood through the aortic valve) (74). This hypothesis is fundamentally different from the multiple wavelet hypothesis, as stable sources imply that the multiplication of wavelets is not essential for AF maintenance, and that there is an intrinsic organization embedded in the complex dynamics of AF.

1.4.6 Experimental Observations of AF Mechanisms

1.4.6.1 Preliminary Support for Multiple Wavelet Hypothesis of AF

Experimental support for the multiple wavelet hypothesis had to await about 20 years. In 1985, Allessie et al. mapped the spread of excitation in canine atria during ACh-induced atrial fibrillation and demonstrated 4 to 6 coexisting wavelets giving rise to turbulent atrial activity in vivo (75). These investigators estimated that sustained AF in the dog required 4 to 6 wavelets. Other data in dogs (76) as well as humans (77; 78) provided insights into the characteristics of wavefront propagation. While these results were presented as demonstrations of the multiple wavelet mechanism, wavelet counts were substantially less than the 23 to 40 predicted by Moe's computer model (72), and no rigorous quantitative tests were performed to determine whether this number was critical and whether the arrhythmia terminates when the number decreases to less than 5 or 6. Nevertheless, a large body of experimental literature has appeared in which the mechanism of sustained fibrillation is assumed to be that described by the multiple wavelet hypothesis (79-86).

1.4.6.2 Recent Support for Primary Generator—Sources Hypothesis of AF

The following sections review recent experimental findings. While multiple independent wavelets are commonly observed, significant organization often appears to underlie global activity. This latter finding suggests a stable source generating AF, although a multiple wavelet mechanism cannot be excluded in all cases.

1.4.6.2.1 Mapping of Wavelets and Sources

Chen et al. have provided the most in depth experimental quantification of the initiation, propagation, and termination of wavelets produced by wavebreak during AF (87). A novel phase analysis technique was used to characterize wavelets in a sheep model of cholinergic AF (40% of atrial area observed), on the basis of wavelet phase singularities. Briefly, a phase singularity is defined as a point around which an arbitrarily small neighborhood contains all phases of a waveform (88). A phase singularity may be thought of as the point on the edge of a wavebreak where the depolarizing front and repolarization tail meet, located at the instantaneous center of rotation of reentry circuits (87). It was found that the majority of phase singularities were short-lived. The mean phase singularity (n=554) lifespan was 19.5±18.3 ms with a range that varied from 8.33 to 200 ms. Most (98%) of phase singularities lasted for <1 rotation (~85 ms). It was also found that the number of waves that entered the mapping field (15.7±1.6) significantly exceeded the number that exited (9.7±1.5). If wavebreak and the resulting wavelets were maintaining AF, the number of wavelets exiting the field of view would have been expected to exceed the number entering. Finally, the spatial distribution of wavebreaks was compared to the Poisson distribution, which is characteristic of randomly occurring events. A significant difference was found in all four left-right atrial pairs analyzed,

indicating that the patterns of wavebreak were non-randomly distributed in space (87). Taken together, these results suggested that AF was not sustained by the multiple wavelet mechanism in this model, but was more likely the result of high-frequency organized waves.

Schuessler et al. first demonstrated experimental AF arising from a single, relatively stable circuit, where the maintenance of AF was associated with a significant level of organization (89). In an in vitro study of cholinergic AF, the number of circuits and wavelets increased with increasing [ACh], but activity was only sustained at high concentrations when a single, relatively stable circuit emerged and dominated activity. The wavelet count was greatest following stabilization. These data suggest that ACh potentiates breakup while exerting a considerable organizing influence on fibrillatory dynamics, and that AF maintenance may depend on the strength of the organizing effect. A similar organizing influence is evident in the findings of Kumagai et al., where an interdependence between unstable and short-lived circuits (ie, mother waves) and resulting daughter wavelets was observed (90). Ongoing breakup of unstable circuits formed multiple independent wavelets that were continuously re-forming unstable circuits.

Similarly, using a combination of high-resolution video imaging with Langendorff-perfused sheep hearts (n=6), Skanes et al. identified sequences of temporally periodic wave fronts propagating with similar spatial patterns of propagation (spatiotemporal periodicity) emanating from relatively stable sources generating AF (91). In the majority of cases, periodic waves were seen to enter the mapping area from the edge of the field of view. In specific examples, sources of periodic activity were seen as

rotors in the epicardial sheet or as periodic breakthroughs most likely representing transmural pectinate muscle reentry. Sources were localized to the left atria and spatiotemporal periodicity was detected in the right atria in only 60% of cases, indicating that activity was much less organized at sites distal to the source. It was concluded that reentry in anatomically or functionally determined circuits forms the basis of spatiotemporal periodic activity during AF. Likewise, Mandapati et al. analyzed optical recordings of dynamics during 35 episodes of ACh-related AF in Langendorff-perfused sheep hearts (n=7) (92). Sources of AF were visualized as periodic rotors in the posterior left atria (n=14 episodes), with the mean core (defined in Section 1.4.7) perimeter and area measuring 10.4±2.8 mm and 3.8±2.8 mm^2, respectively. Spatiotemporally periodic propagation patterns were observed in the surrounding tissue. It was concluded that stable microreentrant sources are the most likely underlying mechanism of AF in this model. Elsewhere, observations of AF arising from spiral wave sources demonstrate that spiral wave meander may amplify the turbulence of fibrillation (65; 67).

1.4.6.2.2 Frequency Analysis of AF Electrograms and Signals

Frequency analysis using fast Fourier transforms (FFTs) of electrograms or optical signals (potentiometric dye fluorescence) recorded during AF has been widely used in conjunction with direct visualization to gain insights into global AF dynamics. Briefly, FFTs show the relative contributions of all frequencies involved in a complex waveform. FFT power spectra are displayed with frequency (Hz) along the horizontal axis and the power content of each frequency represented by the vertical axis (as may be seen in Fig. 3 of Ref. (92)). Those frequencies making the greatest contributions appear as discrete spectral peaks. The dominant frequency is the peak with greatest power amplitude, and

corresponds to the primary rate generating the waveform. Bandwidth refers to the range of frequency content. Spectra bounded by a small number of closely spaced peaks are said to be narrow-banded. The waveform arising from a single, uninterrupted periodic frequency represents the simplest case of maximal organization. In this scenario, the dominant frequency is the slowest peak, with faster peaks occurring in integer multiples of the dominant frequency. These faster peaks represent higher harmonics of the dominant frequency, and each occurs at progressively decreasing power over the physiologically relevant range (typically <60 Hz). Such spectra may arise from periodic waveforms in cardiac tissue (see Fig. 5B of Ref. (92)), where the uniform rate is evidenced by the lack of significant power between the harmonics. In contrast, the spectral profile of a totally random waveform is broad-banded and indistinct, with no discernable dominant frequencies or harmonics.

Skanes et al. computed FFTs of both electrograms and optical signals recorded during AF (91). Spectral profiles displayed a narrow-banded range of frequency content containing multiple discrete peaks with a single dominant frequency in all cases (mean, 9.4±2.6 Hz; cycle length, 106±26 ms). The cycle length of spatiotemporally periodic waves correlated with the dominant frequency of their respective optical pseudo-electrograms (left-atria: R^2=0.99, slope=0.94 [95% CI, 0.88 to 0.99]; right-atria: R^2=0.97, slope=0.92 [95% CI, 0.80 to 1.03]), and the dominant frequency of the left atrial pseudo-electrogram alone correlated with that of the global bipolar atrial electrogram (R^2=0.76, slope=0.75 [95% CI, 0.52 to 0.99]). In specific examples, sources of periodic activity were seen as rotors in the epicardial sheet or as periodic breakthroughs that most likely represented transmural pectinate muscle reentry (discussed Section 1.4.3.1). However, in

the majority of cases, periodic waves were seen to enter the mapping area from the edge of the field of view. It was concluded that reentry in anatomically or functionally determined circuits forms the basis of spatiotemporally periodic activity during AF, and that the cycle length of sources in the left atria determines the dominant peak in the frequency spectra in this experimental model (91).

Mandapati et al. extended these techniques, using an interactive offline approach for rapid preliminary identification of the dominant frequencies of 14 electrogram sites throughout the atria, a biatrial electrogram, and pseudoelectrograms of each optical recording (92). This permitted identification of the site with highest dominant frequency, which was most likely to contain the generator region. A roving electrode was then used to carefully explore the atrial endocardium/epicardium in the vicinity of the highest dominant frequency site. The specific site of origin of the periodic activity was determined as: 1. the source/site possessing a rapid periodic electrogram, with 2. its FFT revealing a single peak. As discussed above, this latter criterion refers to the purity of the signal, implying that activity at that site was driven, without interference, by only one frequency, as would be expected at a site immediately adjacent to a primary source. All 35 AF episodes were analyzed in this way. Mean left and right atrial dominant frequencies were 14.7±3.8 and 10.3±2.1 Hz, respectively, demonstrating that activity was most rapid in the left atria. Spatiotemporal periodicity was seen in the left atria during all episodes. In 5 of 7 experiments, a single site having periodic activity at the highest dominant frequency was localized, most often to the posterior left atria (80%), near or at the pulmonary vein ostium. A representative experiment is depicted in Figs. 4 & 5 of Ref. (92). Figure 5 shows an optically recorded activation map of a reentrant source in the left

atria, with nearby action potentials (and corresponding FFT analyses) revealing periodic activity at surrounding sites. Figure 4 shows electrograms and FFTs recorded at sites throughout the atria. All frequency spectra contained discrete peaks, suggesting spatiotemporally periodic activation at that location. Electrograms were regular (flutter-like) and dominant frequencies were fastest near the primary source at the base of the left atria. Signals were increasingly disorganized, yet generally narrow-banded, and became progressively slower at distal sites as not all conduction pathways were able to capture the rapid rate of the source in a 1:1 manner.

Berenfeld et al. provided a systematic quantification of the spatial distribution of dominant frequencies of local excitation on the epicardium of the right atrial free wall and left atrial appendage of the isolated sheep heart during AF (93). Video movies of the right and left atria were obtained and spectral analyses performed on movie signals to construct dominant frequency maps. These studies demonstrated that AF may be characterized by multiple discrete domains with distinct dominant frequencies on the atrial epicardium. Acceleration of AF at increased ACh concentrations increased the number of domains and the dominant frequency variance, indicating an increase in turbulent aperiodic behavior. The left atrial activity was faster and more homogenous, with a smaller number of dominant frequency domains compared to the right atria, suggesting that the sources for the impulses were localized to the left atria. Consistent with results elsewhere (91; 92), spectral profiles at individual sites were either highly organized or narrow-banded. These data revealed, for the first time, hidden organization, independent of the activation sequences or nature of electrograms. This finding suggested

that AF results from high-frequency impulses that undergo spectral transformations, with more transformations (implying greater heterogeneity) at faster rates (93).

In a related study, Karagueuzian et al. introduced two bipolar and one quadripolar electrode catheters with interelectrode distances of 1 cm into canine right atrium through the left internal jugular vein, positioned in the high, mid, and low atrial endocardial surface under fluoroscopic control (94). Recordings were made during AF, and it was found that electrogram morphology changed over time at a given site. FFTs showed peaks mostly below 15 Hz that were either discrete (narrow banded) with clear harmonic components, or had continuous (broad banded) spectra that changed in a time and site dependent manner. Phase plane plots (plot of voltage versus rate of change of voltage) varied with respect to time and location, however the morphology of these plots often inscribed well-defined structure, suggesting dynamics compatible with deterministic chaos, rather than random dynamics. The absence of discernable structure in certain cases is compatible with a multiple wavelet mechanism and consistent with studies by Mandapati et al. (discussed above), where evidence of spatiotemporal periodicity was only observed in 60% of cases (92).

Jalife et al. performed computer simulation studies to gain insights into possible mechanisms accounting for differences between left and right atrial electrogram spectral profiles (73). It was assumed that the underlying mechanism of AF may be a highly periodic stationary source located somewhere in the left atrium, and that the complicated anatomy of the atria play an integral role in the development of fibrillatory conduction. This scenario was represented in a mathematical model by mimicking the insertion of a major pectinate muscle into the anterior wall of the right atria. The three-dimensional

model (60×60×60 elements) consisted of a one-dimensional bundle (plane wave propagation in a thick bundle) attached to a two-dimensional sheet (as is shown in Fig. 2 of Ref. (73)). The sheet was large enough to avoid boundary effects at the edges. Modified FitzHugh-Nagumo kinetics were assigned to each element (95; 96). Briefly, the FitzHugh-Nagumo model provides a highly simplified AP representation that does not involve formulations of individual ionic currents, with the advantage that large multicellular systems remain computationally tractable on a single-processor workstation. Studies were conducted to evaluate the effects of periodic stimulation applied at the top edge of the bundle as the impulses propagated downstream to invade the two-dimensional sheet. It was found that as the period of stimulation and the bundle area was decreased, the sheet responded less frequently because of block of certain impulses at the input junction. The input:output frequency ratios changed from 1:1, when the bundle was thick and the stimulation period was low, to 4:3, 3:2, or 2:1, when the bundle was relatively thin and the stimulation frequency was high. In this way, with the exception of the harmonic at ~16.8 Hz, the dominant frequency corresponded to the fastest rate, and the largest secondary peaks fell at lower frequencies in integer ratios of the dominant frequency. These results demonstrate how a single source (with a single period) may generate narrow-banded frequency profiles in distant regions with additional frequencies arising by virtue of intermittent block at junctional sites, offering a mechanistic explanation for qualitatively similar frequency spectra observed experimentally (as in Fig. 4 of Ref. (92)). Alternately, Gray et al. have shown that the Doppler phenomenon provides a robust explanation for the narrow-banded frequency spectra characteristic of

fibrillation arising from a single rapidly meandering spiral, as may underlie AF (see Section 1.4.3.2) (63).

1.4.6.2.3 Statistical Studies of Randomness of AF Dynamics

Other investigators have applied rigorous statistical methods to provide evidence that AF is not totally random. For example, Botteron and Smith demonstrated that closely spaced bipolar recordings of atrial activation during human AF could be cross-correlated over considerable distances (97). These authors fit the relationship between activations at various points into a single decaying monoexponential function to derive the so-called "activation space constant," defined as the distance over which activation sequences remain well correlated. The mean space constant was 2.6 cm (range, 1.5 to 6 cm) and was stable over time during a given episode of AF. These results strongly suggested that there was spatial organization over appreciable distances in the atrial endocardium during fibrillation. Additional evidence for organization in AF has been presented by Rosenbaum and Cohen, who quantitatively characterized the degree of atrial electrical synchrony in patients with AF (98). Signal-averaged FFTs of multiple electrogram segments of AF demonstrated a broad range of atrial synchrony. Consistent with these studies, Gerstenfeld et al. have demonstrated transient "linking" during 1-minute episodes of AF in humans (99). The term linking had previously been applied to the behavior of macroreentrant circuits, whereby the fate of each successive impulse in the circuit was functionally linked to the electrophysiologic sequelae of the previous beat (94; 100). Using recordings acquired by orthogonal endocardial catheters, Gerstenfeld et al. (99) calculated mean vectors for each electrogram. Two successive electrograms were considered to be "linked" if their direction varied by <30°. Episodes of six successively

linked electrograms were considered evidence of transient linking during AF. Recordings from most patients demonstrated that the number of linked electrograms ranged from 6 to 14. By statistical analysis, this was considered strong evidence for linking over multiple cycles during AF.

1.4.6.2.4 Localization and Properties of Primary Sources

Studies by Skanes et al. (91) and Mandapati et al. (92), discussed in Sections 1.4.6.2.1 and 1.4.6.2.2, demonstrated AF arising from a discrete periodic source with complex patterns of conduction block and wavelet activity, where periodic sources were often localized to the left atria. Based on these results, Mansour et al. hypothesized that impulses emanating from sources in the left atria produce local activation at progressively lower frequencies as they propagate away from these sources, resulting in a frequency gradient between the left and right atria (101). In such a case, interatrial pathways such as Bachmann's bundle and the inferoposterior pathway, which runs along the coronary sinus, would be expected to act as preferential routes for left-to-right propagation of fibrillatory impulses. FFTs of optical and bipolar electrode recordings were performed with the use of a sheep model of cholinergic AF. At baseline, a left-to-right decrease in dominant frequencies occurred along Bachmann's bundle and the inferoposterior pathway, resulting in a baseline gradient of 5.7±1.4 Hz. Left-to-right impulse propagation was present in 81±5% and 80±10% of cases along each pathway, respectively. Increasing ACh concentration resulted in an acceleration of left atrial frequencies, with a resultant increase in the frequency gradient from 4.9±1.8 to 8.9±1.8 Hz. Ablation of both pathways decreased right atrial dominant frequencies from 10.9±1.2 to 9.0±1.5 Hz, without affecting left atrial dominant frequencies (16.8±1.5 Hz versus 16.9±1.8 Hz) (101). Taken

together, these results demonstrated for the first time that fibrillatory conduction away from left atrial sources result in a left-to-right frequency gradient, strongly supporting the hypothesis that AF is the result of high-frequency periodic sources in the LA with fibrillatory conduction away from such sources. In a study addressing the ionic basis for why the left atria may support faster frequencies than the right atria, Li et al. demonstrated that left atrial myocytes tend to have larger I_{Kr} current, and therefore shorter refractory period (102). This would permit higher rates of activation in the left atria, and may explain why reentry circuits in the left atria often dominate AF. This latter result raises the interesting possibility that drugs targeting I_{Kr} channel blockade (ie, dofetilide) may specifically destabilize reentrant sources in the left atria, thereby profoundly alter AF and contributing uniquely to AF termination.

Morillo et al. obtained similar results in a canine model of chronic AF induced by 6 weeks of continuous rapid atrial pacing at 400/min (103). Right atrial ERP was significantly shortened after pacing, from 150±8 to 127±10 ms (cycle length 400 ms) and from 147±11 to 123±12 ms (cycle length 300 ms). This finding, together with increased atrial area (40%), was highly predictive of sustained AF (88%). Mean AF cycle length was significantly shorter in the left atria (81±8 ms) compared with the right atria (94±9 ms), with an area of the posterior left atria consistently having the shortest cycle length (74±5 ms). Additionally, AF was terminated and no longer inducible in 9 of 11 dogs after serial cryoablation of this area. These results strongly suggest that a discrete source in the left atria may also be driving AF, thereby adding to findings in Refs. (91; 92; 101), as AF mechanisms in this pathological context may well be similar to cholinergic AF (see Sections 1.5.1 & 1.5.2).

The left atrium is also implicated in containing sources driving clinical AF. In 11 patients with chronic AF (AF duration 8.0±4.5 years), the mean AF cycle length ranged from 129 to 169 ms in the right atria and from 114 to 139 ms in the left atria (104). Regular and repetitive activation was found in the left atria of 7 of 11 patients, and AF disappeared in 10 patients (AF-free rate, 91%) following a simple ablation procedure exclusively targeting the left atria. In a related study, 10 patients with chronic AF were all found to have regular and repetitive activation originating in the left atria (105). Interestingly, two patterns of repetitive activation in 2 patients and three patterns in 1 patient appeared alternately during the observation period, suggesting an evolution in the behavior of the source or that multiple sources with intrinsically different properties were sharing generator function. In contrast to the repetitive activation in the left atria, the activation sequence of the right atria was described as extremely complex and chaotic. In 7 of 10 patients, the same pattern of right atrial activation was never repeated during the observation period. In 2 patients, revolution of repetitive activation in the right atrium sporadically appeared, but the pattern of activation immediately deteriorated to a complex and chaotic pattern (105). Similarly in the context of mitral valve disease, the left atria acted as an electrical driving chamber, with both dominant repetitive activation and sporadic complex activation in different patients (106). The latter observations suggested that some ongoing process of self-organization was occurring in regions distal to the source. Similarly, in 9 patients (age, 38±7 years) suffering from paroxysmal AF, Jais et al. determined that all arrhythmias were due to a single focus firing irregularly and exhibiting a consistent and centrifugal pattern of activation (107). Six of 9 foci were located in the left atrium at the ostium of the right pulmonary veins (n=5) and at the

ostium of the left superior pulmonary vein (n=1). All patients were successfully treated by radiofrequency ablation of generator-type foci. Based on similar findings in a canine model of chronic AF, Wu et al. concluded that the faster rate in the left atria may be due to the close proximity of the left atria to AF sources associated with the pulmonary veins and the ligament of Marshall (108).

1.4.6.2.5 Insights into AF Mechanisms from the Surgical Treatment of AF

In his recent editorial, R. Schuessler comments on evidence for a multiple wavelet mechanism versus a generator-based mechanism of AF obtained from the surgical treatment of AF (109). Indeed it was Moe's multiple wavelet mechanism (71; 72), with additional observations (110), that provided the scientific rationale for the maze procedure by this group (111). Subsequently, Cox et al. (112) reported excellent long-term results, with >90% of patients free after >10 years of follow-up. Briefly, the maze procedure consists of a series of atrial incisions that channels sinus node activation of both atria into an approximately normal sequence, while attempting to eliminate sufficient space for any reentry to occur. The maze procedure has been performed at an increasing number of institutions worldwide, with 80% to 90% of patients rendered AF free (113-116). Interestingly, both the Mayo Clinic (114) and the combined Japanese experience (116) found an increased failure rate for the maze procedure with increased left atrial size. These results suggest that if the left atria is large enough, even after the maze procedure, an adequate substrate remains for the initiation and maintenance of AF. Although application of only right atrial incisions in patients with AF has resulted in little

success in the general population, the right atrial maze procedure is effective in eliminating AF in patients with isolated tricuspid disease and enlarged right atrium (114).

While these observations seem consistent with the multiple wavelet hypothesis, they may also be explained by focal mechanisms. It is not entirely clear why atrial size would affect single-source AF caused by stable microreentrant circuits or other nonreentrant mechanisms. A number of studies demonstrated that many such foci are within the pulmonary veins and that, in some cases, very limited ablation eliminates AF (117). It has also been shown that a source within a vein may continue to activate rapidly after isolation from the body of the atria, as it did when it was generating fibrillation in the intact atria (118). Other observations by Schuessler et al. may explain why tissue size and shape are sometimes important in the context of focal sources (109). While intraoperatively mapping a patient with AF originating from a single source, the site of the source was observed to change. It did not migrate, but spawned an additional source several centimeters away. Both sources were present for two cycles, before the second site became dominant. Likewise, Nitta et al. reported as many as four different "focal" sources within a few minute period (119). This suggests that within the generator region of AF, new reentrant sources may develop and assume dominance. Except for the period of transition, a single quasi-stable source drives fibrillation. If this model is correct, then atrial size would be important, because increasing size would increase the number of possible sources that can develop, increasing the probability that a source will persist and sustain AF. In cases where individual sources are intrinsically unstable, the focal mechanism of AF is somewhat analogous to the multiple wavelet mechanism in that focal AF would be more stable when there is ongoing multiplication of potential sources.

Schuessler (109) raised many unanswered questions regarding the nature of sources, such as: What are the life times of a source? What causes the transition from one source to the next? What contributes to the stability of a source? Is pure multiple wavelet AF possible? These questions remain for future experimental and theoretical evaluation.

1.4.7 Biophysics of Wavelet Formation and Behavior

With the mechanisms of AF generation and the resulting formation and propagation of individual wavelets in mind, local electrophysiological dynamics during AF may be understood in terms of the biophysical properties of excitable media. Assuming that somewhere in the atria there exists a dominant reentrant source that radiates high frequency impulses into a heterogeneous myocardium, emanating wavefronts encounter both functional (e.g. a region of cell with relatively long refractory period) and anatomical (e.g. a scar) obstacles, causing wavebreak (break points also known as "phase singularity" points). Such points of incidental wavebreak are necessary for reentry initiation and the formation of independent wavelets (wavefront fragments bordered by two phase singularities) (87).

In the case of anatomical obstacles, wavebreak occurs against the obstacle and the two broken ends of the wavefront proceed to circumnavigate the obstacle. As discussed by Jalife et al., when excitability is sufficiently high (as occurs when sodium channels are fully functional and the cycle length of the source is sufficiently slow) the two broken ends of the wavefront come back together and fuse such that the wavefront recovers its previous shape and moves on (120). No reentry or wavelet formation results in this case. Alternately, when excitability is sufficiently low, due to sodium channel inhibition or a

sufficiently rapid excitation frequency, the free ends may not re-fuse (ie, vortex shedding by obstacle). In this case, curling of the two free ends may initiate functional reentry consisting of two counterrotating waves (figure-of-eight reentry), provided the distance between the two phase singularities is sufficiently large such that the rotations continue successfully without mutually annihilating. Functional obstacles, which may be residual regions of refractoriness from preceding wavefronts, behave similarly to anatomic obstacles, as broken wavefronts also circumnavigate these regions and either fuse or form counterrotating reentry waves. In the latter case, the initiation of reentry may be facilitated by repolarization of the obstacle during the time of circumnavigation, such that the area occupied by the original obstacle becomes part of the reentry pathways.

Why wavefront rotation occurs at phase singularity points may be understood in terms of the reaction-diffusion events driving wavefront propagation. Potential gradients provide energy for propagation, and arise from the potential difference between excited cells and downstream refractory tissue. The size of the gradient is proportional to the amplitude of the AP upstroke. This is largely determined by the magnitude of the fast sodium current (I_{Na}), which is also a primary determinant of conduction velocity and the safety factor for successful propagation (121). At the point of wavebreak (the phase singularity point), all phases of the action potential become singular, or are indistinguishable. Consequently there is no driving force for propagation at the tips of broken waves, such that forward propagation abruptly stops while proceeding at progressively higher velocities along the wavefront as the distance from the phase singularity increases. The wave thus develops a convex curvature that reaches a maximum at the phase singularity. At this point, the curvature is so steep that activation

of the tissue ahead fails and the wave begins to rotate (122). The phase singularity therefore acts effectively as a pivoting point and leads to the formation of a rotor. The trajectory of the phase singularity is theoretically limited by a critical curvature for propagation, which determines the smallest possible size of the core (area circumscribed by the trajectory of a phase singularity) (68; 122; 123). For a given value of intercellular resistance and coupling anisotropy, the critical curvature is a consequence of the magnitude of the source-to-sink potential gradient, where larger sources allow for greater wavefront curvature as sufficient propagation energy is available for conduction to a larger sink region. For this reason, sodium channel inhibition, by reducing the size of the source, is associated with an increase in core size (123) (see Section 1.6.4). During AF, phase singularities often follow wider reentry pathways than predicted by conduction theory, as residual refractory tissue from the previous reentry cycle may act as a functional obstacle, forcing the circuit into a larger trajectory.

In this way, AF dynamics in the periphery of generator regions are determined by patterns of wavebreak, where every break results in the formation of two phase singularity points which tend to counterrotate. The actual evolution of each phase singularity is determined by regions of variable refractoriness or excitability (largely a function of the excitation history), preferential conduction pathways defined by tissue geometry and fiber orientation, the distance between related phase singularity points (often determined by the size of the obstacles from which they form), and the presence of tissue borders. Although the direction of changes at each instant in time may be anticipated based on the relative contributions of these effects, it is readily apparent why the prediction of propagation patterns during AF is difficult (short term), or essentially

impossible (long term). It is also not surprising that while the dynamics of AF may be very complex and seemingly random, activity may also be significantly organized. In fact, the complicated anatomy and heterogeneous electrophysiology of the atria may dictate that repetitive activations seen during AF are constrained to preferred routes of propagation.

1.4.8 Utility of Historical Concepts

Aspects of many historical paradigms of fibrillation (Section 1.4.3) are consistent with recent observations of AF mechanisms. Situations giving rise to Mines' closed-circuit reentry (50) may arise around macro-type structural obstacles (64), may be created by sutures or scars (124; 125), or may arise naturally from valve orifices (126) and the great veins (127). Activity tends to be very regular, or flutter-like rather than AF-like, although wavefronts emanating from these stable circuits may breakup into independent wavelets as occurs during AF (87; 89). The pulmonary veins are highly arrhythmogenic (107; 128; 129), likely supporting AF as focal sources of hyperexcitability and by anchoring closed circuits. Garrey's functionally-determined circuits (47) are also recognized to be of great importance, but often in the context of drifting spiral waves (65; 67) and Lewis' mother-wave AF mechanism (87; 91; 92), rather than true multiple-circuit AF, and these functional circuits may at times be stabilized by closed circuits around atrial microstructures such as the pectinate muscle bundles (58; 130). Apart from the initial report of the leading circle mechanism (59), a reentry circuit that continually produces centripetal wavelets has not been observed elsewhere, and high-density mapping data have been presented that provide direct evidence for the presence of spiral wave reentry

with an unexcited but excitable core (66). However, the rate of functional reentry during AF (as indicated by the AF cycle length) is directly related to the refractory period (131). This is consistent with predictions of the leading-circle model (132), and hence our understanding of AF has benefited from this conceptualization. Thus, modern observations of AF mechanisms represent very new insights into very old ideas, raising new questions while demonstrating the relevance of old ones.

1.5 Physiological and Pathological Determinants of AF

Sustained AF is known to occur in the context of high vagal tone (acute physiological alteration), chronic AF (chronic pathological alteration), and congestive heart failure (chronic pathological alteration). While many of the mechanistic observations reported in the preceding sections were made in the setting of vagal AF, as experimental models of this type are readily obtainable, others, including many clinical findings, were made in the context of sustained atrial tachycardia or chronic AF. While fibrillation in each context may share mechanistic similarities, AF may also be fundamentally different between contexts.

1.5.1 Vagally-mediated AF

Cholinergic mechanisms have long been known to play an important role in the occurrence and maintenance of AF. In 1914, Rothberger & Winterberg showed that vagal stimulation converted atrial flutter into fibrillation (133), and Garrey cited the work of numerous investigators who established in the early twientieth century the AF-promoting

role of vagal-nerve activation (47). Vagally-related AF is primarily mediated by the induction of an acetylcholine (ACh)-activated repolarizing potassium current ($I_{K(ACh)}$), causing AP shortening and abolished AP rate adaptation (134). Abolished rate adaptation implies that even at slow rates, AP duration (and therefore refractory period) is very short. Shortening at all rates increases the proportion of excitable tissue, thereby predisposing to the initiation of AF while enabling the atrial substrate to support sustained fibrillation.

Evaluated in terms of distributed properties, these changes manifest as a progressive decrease in atrial effective refractory period that occurs in a spatially heterogeneous way (135; 136), thereby producing functional obstacles sufficient to cause wavebreak at rapid rates. Increases in refractoriness heterogeneity appear to be particularly important in the AF-promoting effects of vagal stimulation (131; 137). ACh is also known to accelerate the rate of reentry and AF (59; 67; 89; 93; 101). A 0.1 μM increase in ACh concentration may increase the global dominant frequency from 9.8 to 13.7 Hz (~250 ms cycle length speedup) (93). This change was associated with a clear increase in the number of dominant frequency domains in the right atria, while the left atria seemed more able to sustain high frequencies without fractionation. The atrial repolarization heterogeneity-promoting effects of vagal stimulation may be caused by patchy distribution of vagal nerve terminals and acetylcholine receptors; however, unmasking of underlying cellular action potential heterogeneity by reducing the space constant may also play an important role (138). The vagally mediated decrease in refractory period reduces the wavelength and the size of potential reentry circuits, so that AF more resembles multiple-circuit reentry (132; 138-140) (wavelength theory discussed

in Section 1.6.1). These vagally-mediated changes increase the duration of induced AF, with moderate vagal stimulation often permitting AF to be sustained indefinitely. In addition, vagal stimulation greatly promotes the initiation of AF by single premature atrial activations. This action also appears to depend both on refractoriness shortening at the site of premature impulse generation and on heterogeneous effects that cause the premature wave front to block in a region with a lesser degree of refractoriness abbreviation (131).

1.5.2 Chronic Tachycardia-related AF

A particularly important recent development in our understanding of the mechanisms of AF was the demonstration that AF alters the atrial electrophysiological milieu in a way that promotes its own maintenance. Wijffels et al. (141) very elegantly demonstrated that, when AF is maintained in goats by electrical-burst stimulation whenever sinus rhythm supervenes, the interval between spontaneous reversions increases progressively from several seconds to hours or even days when AF is maintained for up to 2 weeks (see Fig. 4 of Ref. (54)). The ~10-fold atrial rate increase caused by AF is the primary stimulus to remodeling, and similar changes are produced by any form of sufficiently-rapid atrial tachycardia (141). Wijffels et al. have very descriptively coined this self-promoting phenomenon "AF begets AF" (141).

The basis for the self-promoting nature of AF arises from a compensatory process called "electrical remodeling" (142). A 10-fold increase in atrial rate substantially increases cellular Ca^{2+}-loading (143). Progressive Ca^{2+}-loading threatens cell viability: the cell responds to minimize the impact of increased rate on intracellular Ca^{2+} load.

Short-term defense mechanisms include voltage- and intracellular [Ca^{2+}]-dependent inactivation of I_{Ca} (144). Over the longer term, decreases in mRNA encoding the pore-forming I_{Ca} α-subunit occur (145-147), decreasing I_{Ca} (148-150). Both short- and long-term decreases in I_{Ca} reduce Ca^{2+}-entry and help to prevent Ca^{2+} overload. Since I_{CaL} is a key contributor to the action potential plateau, reduced I_{Ca} decreases APD, thereby promoting the induction and maintenance of AF by multiple-circuit reentry(151). In addition to sarcolemmal changes in Ca^{2+} transport, subsarcolemmal Ca^{2+}-handling is also impaired following rapid pacing (152). Ca^{2+}-handling alterations decrease systolic Ca^{2+}-release, in association with altered concentrations of intracellular Ca^{2+}-handling proteins (147; 153). I_{Na} also appears decreased, possibly contributing to slowly-developing atrial conduction slowing that may help to promote AF (154; 155). I_{to} is decreased (148; 150; 156) and I_{K1} may be altered (150; 156). These findings suggest the idea that these alterations may represent an adaptation to preserve overall intracellular ionic homeostasis. Overall, I_{Ca} is reduced by 69% and I_{to} by 65% in dogs subjected to 42 days of rapid atrial pacing, resulting in AP shortening and totally abolished rate adaptation (148). Presently it is not clear whether sarcolemmal ion channel alterations fully account for abolished rate adaptation or whether subsarcolemmal alterations are also involved.

Evaluated in terms of distributed properties, AF-related remodeling manifests as a progressive decrease in atrial effective refractory period (thus tending to decrease the wavelength for reentry), and a progressive decrease in the AF cycle length, an indicator of refractory period during AF (103; 141; 151; 157). Changes induced by remodeling are spatially heterogeneous, increasing the heterogeneity in atrial refractory properties (158). As in vagally-mediated AF, the combination of decreased wavelength and increased

heterogeneity would be expected to promote multiple-circuit reentry, and epicardial mapping studies have provided evidence for a progressive increase in the number of apparent reentry waves during AF as atrial tachycardia-induced remodeling develops (151). In this way, the AF-promoting changes resulting from tachycardia-induced remodeling are qualitatively similar to ACh-related alterations during vagally-mediated AF (Section 1.5.1): refractory period is shortened and rate adaptation is abolished, while the spatial heterogeneity of refractory period is increased. This suggests that, although the cellular mechanisms underlying these alterations are entirely different, the tissue-level mechanisms of AF induction and maintenance in these contexts likely share many qualitative similarities.

1.5.3 Congestive Heart Failure (CHF)-related AF

CHF is one of the strongest clinical predictors of AF (159). CHF is a ventricular pathology that may be induced in canine models by rapid ventricular pacing at ~230/min for 35 days (160). This ventricular manipulation impacts on the atria, inducing remodeling different from that produced by atrial tachycardia. Li et al. found that the density of I_{Ca} is reduced by approximately 30%, I_{to} by approximately 50%, and I_{Ks} by approximately 30% without altering their voltage dependencies or kinetics (160). CHF also increased transient inward NCX current by approximately 45%. Despite these extensive changes, the AP duration of atrial myocytes was not altered at slow rates but was increased at faster rates, paralleling in vivo refractory changes. Histological examination revealed extensive interstitial fibrosis (connective tissue occupying 12.8±1.9% of the cross-sectional area) in CHF dogs compared with control (0.8±0.3%)

and dogs subjected to rapid atrial pacing to mimic chronic AF (0. 9±0.2%) (161), and CHF dogs had a substantial increase in the heterogeneity of conduction during atrial pacing (heterogeneity index in CHF dogs, 2.76±0.16 versus 1.46±0.10 for control and 1.51±0.06 for RAP dogs; $P<0.01$) owing to discrete regions of slow conduction. These changes enhanced atrial arrhythmogenicity, as the duration of AF induced by burst pacing increased (from 8±4 seconds in control dogs to 535±82 seconds; $P<0.01$), similar to the effect of 1 week of rapid atrial pacing (713±300 seconds) (161). Similarly in CHF patients, sclerotic patches and diffuse fibrotic displacement of the cardiac muscle are commonly found in those most vulnerable to AF (162). CHF-related AF appears, at least in some instances, to arise from a single macro-reentrant circuit (163). This result contrasts with the promotion of multiple circuit reentry in the contexts of vagally-mediated AF and chronic tachycardia-related AF, as CHF-related AF seems to arise from increased interstitial fibrosis, rather than effects on AP properties and the refractoriness distribution. These differences may imply variability in the efficacy of antiarrhythmic drugs and the mechanisms of pharmacological AF termination between contexts.

1.6 Pharmacological Antiarrhythmic Therapy

1.6.1 Wavelength Theory

To terminate AF, antiarrhythmic drugs attempt to block cellular ion channels, changing AP properties (Section 1.3) so as to influence multicellular wavefront dynamics (Section 1.4.6) and disrupt the mechanisms of fibrillation (Sections 1.4.4 & 1.4.5). Classical goals of pharmacological antiarrhythmic therapy are rooted in the concept of the wavelength of

reentry. The concept of wavelength is not limited to leading-circle reentry (Section 1.4.3.2) but is central to all reentry processes discussed above. The wavelength (WL), or minimal path length required to support reentry, is the product of the conduction velocity (CV) and refractory period (ERP) (164), i.e. WL=ERP×CV (50; 60; 165). The wavelength is thought to represent the space occupied by functional reentry circuits, and therefore determines the number of circuits that may be accommodated in a given size of atria at any one time. If the wavelength during AF is relatively large, the reentrant circuits would be large and tend to mutually annihilate, making fibrillation short-lasting. If the wavelength during fibrillation is short (i.e. slowing of CV or shortening of ERP), reentry circuits would be accommodated and fibrillation would tend to be stable. Wavelength theory accurately predicts the stability of AF in the contexts of vagally-mediated AF (Section 1.5.1) and chronic tachycardia-related AF (Section 1.5.2), as ERP (and therefore wavelength) is markedly shortened in both cases (164). Classical notions of pharmacological antiarrhythmic therapy predict that interventions causing the greatest increase in the wavelength will be most effective in terminating AF (132). Consequently, the primary goal of antiarrhythmic therapy is often to prolong AP duration, thereby increasing ERP and the wavelength of reentry to terminate AF.

1.6.2 Classification of Antiarrhythmic Drugs

The Vaughan Williams classification scheme defines 4 classes of antiarrhythmic drugs based on drug action, which may be effective in both atrial and ventricular tissue. Class I and III drugs are effective in AF termination, with the AF terminating efficacy of class I drugs being somewhat greater than that of class III agents (166). Class III drugs block K^+

channels, and consistent with classical WL theory, this directly prolongs the ERP to terminate AF. Alternately, class III drugs may be used to prevent arrhythmia induction by reducing the proportion of excitable tissue available for reentry initiation (see Section 1.4.3). Class III drugs may target a variety of channels and channel combinations (I_{to}, I_{Kur}, I_{Kr}, I_{Ks}, and I_{K1} [Section 1.3]), each with variable AP-prolonging potential. Class III drugs also offer the possibility of treating AF while minimizing effects on ventricular electrophysiology, as I_{Kur} is expressed in atrial, and not ventricular myocytes. However, class III drugs are severely limited in AF, as many agents display "reverse use dependence", meaning that channel blocking potency is reduced at the rapid rates of AF.

To date, Class I drugs have been the most clinically successful, yet also the most poorly understood class of AF terminating drugs (166). Class I drugs block the fast sodium channels (I_{Na}), thereby reducing electrophysiological excitability (Section 1.3). This reduces the upstroke velocity and amplitude of the action potential and conduction velocity, and may manifest as a widening of the QRS complex on the electrocardiogram (167). Decreased excitability may suppress spontaneous premature contractions, decreasing the likelihood of reentry initiation. In contrast to class III drugs, class I agents may benefit from "use dependence", meaning that channel blocking potency is enhanced at the rapid rates of AF (1; 168; 169). It is possible that sodium channel blockade accumulates very rapidly during AF, with rapid unbinding of class I agents following AF termination such that the level of channel inhibition at the time of termination would be difficult to assess.

1.6.3 Effects of Class I Drugs on Arrhythmia Dynamics

The success of class I drugs is surprising because these agents may convert AF without changing (125; 170; 171) or while decreasing the wavelength of reentry (82; 172). Class I efficacy may instead be due to decreased excitability rather than wavelength alteration (82; 125; 171-173). Class I drugs consistently prolong ERP (79; 80; 125; 171-175) and may reduce vagally-enhanced ERP heterogeneity (176), thereby countering fibrillation. However, the effects of class I agents on ERP may not parallel AP changes, as AP duration may be decreased (177), unchanged (80; 174; 175), or increased (140; 175; 177-179) by the drug. ERP increases exceeding AP prolongation may be due to the development of "postrepolarization refractoriness" (80; 175). Experimental findings indicate that class I drugs may increase circuit size and reduce wavefront density, thereby slowing and organizing AF prior to cardioversion (123; 125; 174; 176; 180). For example, in sheep ventricle Mandapati et al. determined that TTX may decrease wavefront density by ~40% and that block may increase the core area of spiral wave reentry, thereby increasing the rotation period and slowing and organizing associated electrograms (123). It was demonstrated that these changes were due to decreased excitability, comparable to what occurs during ischemia. Additionally, many investigators have shown that sodium channel blockade also increases the variability in reentry cycle lengths (80; 125; 140; 170; 171; 173). It is also known that the combination of rapid rate and strong sodium channel inhibition may result in conduction failure and regions of block along the reentry pathway (122; 173; 175; 181; 182), thereby forcing circuits into larger trajectories. Block generally resulted in regions having a low safety factor for propagation (173; 175), as are associated with sharply turning wavefronts

(181), transitions from longitudinal to transverse conduction (182), and with associated with changes in wavefront curvature (122). Presently it is not clear how these changes contribute to AF termination. Alternately, it may be that some changes potentiate or negate the AF-terminating actions of other effects.

1.6.4 Biophysical Consequences of Sodium Channel Inhibition

The effects of sodium channel blockade on local electrophysiogical mechanisms may be understood in terms of biophysical principles described above in Section 1.4.7. Propagation occurs when the current provided by excited cells (the source) is sufficient to excite downstream cells (the sink). Sodium channel blockade decreases the magnitude of I_{Na}, thereby decreasing cellular excitability and reducing the available source (183). In a one-dimensional fiber, the source is adequate for propagation when a minimal length of the fiber is simultaneously excited (184-186). Propagation may proceed in the presence of sodium channel inhibition, but conduction velocity is reduced secondary to the reduced excitability. In two-dimensional tissue, propagation occurs when a minimal area is simultaneously excited (122). When the excited area is relatively large, propagation may spread to more cells at rest, and the curvature of the wavefront is proportionately arched. As the net excitation is decreased, the wavefront curvature flattens to reduce the size of the downstream sink seen by the wavefront (122; 187). This is highly relevant to spiral wave behavior because the wavefront curvature becomes very pronounced close to the spiral wave tip. In control conditions, the critical radius of curvature is relatively small and the spiral wave rotates rapidly around a small core. After sodium channel blockade, the critical curvature becomes large and the path followed by the spiral wave

tip during one complete rotation is longer, resulting in increased size of the core and a prolongation of the reentry period (123). Similarly, decreased excitability may explain why sodium channel inhibition sometimes results in regions of block during transitions from transverse to longitudinal propagation (122; 181; 182), as the safety factor for propagation is characteristically lower in the longitudinal direction (121; 188-191).

1.7 Mathematical Models of Cardiac Electrophysiology

The most widely accepted mechanistic description of AF is based on the predictions of the relatively primitive Moe computer model (72). Today, the predictions of this model contradict many experimental observations of AF, however experimental studies also remain inconclusive. The development of more sophisticated mathematical models of atrial electrophysiology have provided many important insights into AP properties and the mechanisms of AF, and may form the basis of a more realistic model of AF that accounts for experimental observations.

1.7.1 Development of Mathematical Models of the Cardiac AP

The first mathematical model of the AP was developed by Hodgkin and Huxley in the 1950s to simulate the electrical behavior of the squid giant axon (192). Although the electrophysiology of the cardiac cell is more complicated than that of nerve axons, early efforts to mathematically represent the electrical activity of the cardiac cell were motivated by the success of the Hodgkin-Huxley equations. As discussed by Guan et al., the construction of cardiac cell models has progressed through three stages of

development, with increasingly complex formulations arising from a growing body of quantitative electrophysiological data (193). At the first stage, models of cardiac electrophysiology were derived mainly from the original Hodgkin-Huxley equations through some simple theoretical modifications (194; 195). At the second stage, the development of experimental techniques and clinical and laboratory research of cardiac electrophysiology had yielded a large amount of quantitative data about the biophysical mechanisms underlying the cardiac action potential. Consequently early models were perfected gradually, although the main characteristics of the Hodgkin-Huxley equations still remained (196; 197). For example, the McAllister-Nobel-Tsien (MNT) model of Purkinje fiber electrical activity (196) includes many ionic currents and is more complicated, but it inherits the assumption of the Hodgkin-Huxley model that the electrical activity is merely determined by the ionic channels.

The third stage of model development was marked by the establishment of the DiFrancesco-Noble (DN) model of cardiac myocyte electrophysiology (198). The DN model was the first to include changes in ionic concentrations and the activity of ionic pumps and exchangers, in addition to the activity of sarcolemmal ionic channels. DiFrancesco & Nobel simplified the very detailed cardiac cell into a system with three main components: ion channels and pumps which are responsible for the transmembrane ion exchange; ionic concentrations of sodium (Na^+), potassium (K^+), and calcium (Ca^{2+}) which are the primary ionic species; and the subcellular calcium sequestering and release activity of the sarcoplasmic reticulum. The incorporation of concentration changes into the cardiac electrical model was an important development because such changes occur rapidly in the small volume of the cardiac cell and may have profound effects on AP

properties. The interactions between these three main components were described by a system of 16 first-order ordinary differential equations (198). The establishment of the original DN model spawned the development of numerous other dynamic cardiac models patterned after the DN formulation. The incorporation of concentration changes was an especially important development as changes may occur rapidly in the small volume of the cardiac cell. Well-known third generation models include the human atrial myocyte models by Nygren et al. (199) and Courtemanche et al. (200), canine atrial myocyte model by Ramirez et al. (42), rabbit atrial myocyte model by Lindblad et al. (201), rabbit sinoatrial node model by Demir et al. (202), the ventricular myocyte models of Nordin et al. (203) and the phase II Luo and Rudy (LR2) model (204), and the bullfrog atrial myocyte (205) and SA node (206) models by Rasmusson et al. Models by Jafri et al. (207) and Winslow et al. (208) are also similar as they represent the Luo and Rudy equations with modified subcellular Ca^{2+}-handling.

These models represent the cell membrane as a capacitor connected in parallel with variable resistances (ion channels) and batteries (driving forces) following the original Hodgkin-Huxley formalism for an excitable membrane. In this formalism, each ionic current is proportional to the product of the driving force and the appropriate membrane conductance, which in turn is governed by gating functions with activation and inactivation variables. The activation and inactivation variables are represented as probabilities of ion channel opening, varying between 0 and 1, and are generally voltage- and time-dependent.

The rate of change in the transmembrane potential (V) is given by

$$\frac{dV}{dt}=\frac{-(I_{ion}+I_{stim})}{C_m} \quad 1.$$

where I_{stim} is the stimulus current and I_{ion} is the total transmembrane ionic current. C_m is the total membrane capacitance (~100 pF). For example, the model of the canine atrial AP by Ramirez et al. (42) consists of a system of 27 coupled first order ordinary differential equations, and I_{ion} is given by

$$I_{ion}=I_{Na}+I_{K1}+I_{to}+I_{Kur,d}+I_{Kr}+I_{Ks}+I_{Ca}+I_{Cl,Ca}+I_{p,Ca}+I_{NaCa}+I_{NaK}+I_{b,Na}+I_{b,Ca}+I_{b,Cl} \quad 2.$$

I_{ion} includes contributions from the fast sodium current (I_{Na}), the inward rectifier (I_{K1}) and transient outward (I_{to}) potassium currents, and the rapid (I_{Kr}) and slow (I_{Ks}) components of the classical delayed rectifier potassium current. L-type calcium current (I_{Ca}), a sarcolemmal calcium pump current ($I_{p,Ca}$), the sodium-potassium pump current (I_{NaK}), the sodium-calcium exchanger (I_{NaCa}), a calcium-activated chloride current ($I_{Cl,Ca}$), and background sodium ($I_{b,Na}$), calcium ($I_{b,Ca}$), and chloride ($I_{b,Cl}$) currents also contribute. Membrane currents are modulated by the subcellular activity. AP simulations may be performed with V computed by numerical time integration of Eqn. 2. Simulations are typically performed with I in pA and V in mV.

1.7.1.2 Insights from Third-Generation Atrial AP Models

Third generation cellular models have been used to address questions that are difficult to focus on experimentally and have given numerous insights into atrial AP properties that contribute importantly to the dynamics of AF. For example, the model of the bullfrog atrial cell by Rasmussen et al. (205) was compared to their previous model of the bullfrog

SA node (206) to show how the presence or absence of certain transmembrane currents can change AP characteristics and consequently alter the relative influence of the various transporter- and channel-mediated currents. Also Lindblad et al. developed a model of the rabbit atrial cell, and utilized the equations to provide a qualitative prediction of the intracellular Ca^{2+} concentration transient during the AP and to illustrate the interactions between membrane currents that underlie repolarization in the rabbit atrial myocyte (201).

AP heterogeneity is strongly associated with the occurrence of AF (2). Wang et al. identified three types of APs on the basis of morphology, ranging from type 1, a rectangular AP with a positive plateau, through type 2, a spike-and-dome AP with a plateau at ~0 mV, to type 3, a triangular AP with little plateau (209). These patterns have been observed by others (2; 210-215), with no difference in $I_{Ca,L}$ density found between cell types (210). In their human model, Courtemanche et al. showed that variations in I_{to} alone are able to generate many of the variations in AP morphology observed experimentally, consistent with experimental findings (200; 211). AP shapes ranged from a triangular morphology for large I_{to}, through a spike-and-dome morphology at intermediate I_{to} conductances, to a rectangular morphology for small I_{to} (200). In contrast, variations in I_{Kur} and $I_{Ca,L}$ alone could not reproduce the rectangular morphology observed only in the presence of a small I_{to}. In this way, the model demonstrated that experimentally-observed differences in ionic currents were sufficient to account for AP changes, and demonstrated that individual membrane currents, like I_{to}, cannot be considered independently of other currents. Similarly, in their model of the canine atrial

AP, Ramirez et al. showed that regional variations in ionic currents account for regional AP differences (42).

Rate dependence of AP duration and refractoriness is also an essential property of atrial cells that is central to patterns of excitability and propagation in the atria during AF (Section 1.4.3.2). Courtemanche et al. also used a modeling approach to determine the ionic basis of rate adaptation (200). This phenomenon was found to arise from a synergistic action between $I_{Ca,L}$ and I_K. Rate-dependent shortening of $I_{Ca,L}$ alone was observed, lowering the plateau potential and significantly accelerated late repolarization. Second, a rate dependent increase in available I_K alone was observed. This reduced the plateau level, thereby attenuating I_K activation such that terminal repolarization was unchanged. Together, the combined effects on $I_{Ca,L}$ and I_K lowered the plateau potential and accelerated late repolarization, thereby accounting for the total rate-dependent AP shortening (200). It has also been shown that block of $I_{Ca,L}$ by nifedipine may abolish AP rate dependence (216). Simulations of pharmacologic levels of block (90% reduction of $I_{Ca,L}$ conductance) reproduced this result. In the model, when $I_{Ca,L}$ was strongly inhibited, the plateau level was lowered to the point where I_K activation is greatly reduced and can no longer contribute to rate adaptation. Rate-adaptation is abolished in patients with chronic AF and dogs subjected to tachycardia-induced atrial remodeling (see Section 1.5.2 above). As discussed, remodeling is associated with 69 and 65% reductions in the densities of I_{Ca} and I_{to} currents, respectively (148). Rate adaptation persisted in the Ramirez model following these manipulations, suggesting that sarcolemmal effects are unable to fully account for the pathologic loss of rate adaptation in the disease state (42).

Antiarrhythmic drug therapy has benefited from recent advances in molecular electrophysiology, as the development of more selective ion channel blockers for therapeutic use is now possible. However, more information is needed about the effects of blocking specific channels on repolarization in normal human atrium and in atrial cells of patients with atrial fibrillation. In a subsequent study, Courtemanche et al. used their human model to explore the effects of class III channel blockade on the normal and AF-modified AP (AFAP), constructed by incorporating known remodeling-induced current reductions (217). Effects were not dramatic for single current blockade. I_{to} blockade failed to prolong both the normal AP and AFAP, and I_{Kur} block prolonged the AFAP by 12%. I_{Kr} block by 90% prolonged APD by 38 and 34% in the normal AP and AFAP, respectively. Interestingly, inhibition of both I_{Kr} and I_{Kur} produced a supra-additive effect on AP duration, dramatically delaying repolarization under both normal and AF conditions. These observations illustrate the importance of secondary current alterations in the response of the AP to single channel blockade, having potentially important implications for the development of improved antiarrhythmic drug therapy for AF (217). A similar synergistic interaction was found during simulation of class III drug effects in the human atrial cell model by Nygren et al (199). Thirty percent block of the sustained outward K^+ current (I_{sus}) increased AP duration by 15%, compared with 5% prolongation following 30% block of the transient outward K^+ current (I_t). Combined bock of I_{sus} and I_t by 40% increased AP duration by 27%.

1.7.1.3 Potential Mathematical Limitation of Third-Generation Cardiac AP Models

Third generation cellular models are finely tuned to reproduce electrophysiological behavior observed experimentally during periods of short duration. Yet despite their

many successes, the accuracy of such models may be limited. The original DN model was noted to produce a continual cycle-by-cycle (transient) accumulation (K^+) or depletion (Na^+, Ca^{2+}) of intracellular ionic species (198). AP morphology and the pre- and post-cycle values of the ionic concentrations were not constant as would be expected of steady-state behavior. Transient changes were negligible over a few cardiac cycles, but departures from the pre-stimulus initial concentrations were cumulative and became substantial over many cycles. Guan et al. (193) noted that the original DN equations are mathematically dependent (Jacobian is singular), and therefore that model fixed points are unstable. Varghese et al. (218) showed that there exists a conservation principle latent in model equations that may permit certain mathematical features to cause computational difficulties and erroneous model performance. Although the abnormal behavior may occur only when parameters are outside the zone of physiologic interest, it was argued that these features may introduce erroneous behavior and instabilities within the physiologically realizable range. Consequently, the validity of beat-to-beat changes in model AP properties has been questioned, as this property may impose strict limitations on model accuracy (199; 219). It follows that a more realistic model of AF (where many cardiac cycles occur rapidly) based on a 3rd generation cellular model may be significantly influenced by these instabilities, and would therefore be erroneous.

1.7.2 Mathematical Models of Cardiac Tissue

Despite potential mathematical limitations, detailed cellular models may provide a basis for realistic models of cardiac tissue, where refractoriness properties arise from cellular dynamics given by a system of differential equations, rather than estimates made by time-

dependent algebraic functions, as in the original Moe model (72). Briefly, such distributed models consist of a continuous grid of individually-calculated cardiac cells, interconnected by resistances representing gap junctions (as in Refs. (220-223)). Cellular coupling and propagation is given by the cable equation for reaction-diffusion systems

$$\frac{dV}{dt} = \frac{-(I_{ion} + I_{stim})}{C_m} + D \cdot \nabla^2 \qquad 3.$$

in one, two, or three space dimensions, where ∇^2 is the second-derivative Laplacian operator in space. In this case, numerical integration is performed using a finite difference approximation to the Laplacian. D is the diffusion constant determined by gap junction resistance, surface-to-volume ratio, and membrane capacitance (224; 225). D should be selected such that the longitudinal conduction velocity is physiological and the grid size should be selected such that the overall activation time is representative of the tissue from which the cellular model is derived. Directional differences in the value of D should be assigned to establish a representative transverse conduction heterogeneity.

In a series of seminal papers, Spach et al. clearly established the discontinuous nature of propagation in cardiac muscle (188-191). Continuous cable theory seems to apply along muscle bundles in the longitudinal direction, while high-resistance membranes and decreased gap junction connections (226) separate bundles transversely. Directional changes in AP properties resulting from structural discontinuities are inconsistent with a two- or three-dimensional extension of cable theory, which predicts that action potential shape is not dependent on the direction of propagation. Based on these findings, Leon et al. developed a more realistic representation of cardiac tissue by

repeatedly employing Eqn. 3 in one dimension to form an assembly of parallel cables, connected transversely by simple resistive elements (227), and found that this representation was sufficient to account for the observations of Spach et al (121). This assembly also addresses the computational challenges posed by large multicellular models as highly efficient algorithms may be developed for the cable network, facilitating effective multi-processor parallel computing (228).

1.7.2.1 Mechanisms of Reentry & Fibrillation Evaluated In Cardiac Tissue Models

Cardiac tissue models have given many important insights into the mechanisms of impulse propagation, reentry, and fibrillation. Spiral wave excitation around an unexcited but excitable core, as described in Section 1.4.3.3, is the mechanism of reentry in these computational substrates (68; 222; 229). Analogous to the studies by Spach et al. (discussed in the previous section), demonstrating how wavefronts propagating through a tissue syncytium generate APs that are different from those in isolated cells, Beaumont et al. demonstrated how reentry waves in the myocardium have additional properties to those of planar propagation (222). Using a two-dimensional sheet of Luo & Rudy I cells (230), it was demonstrated that the core exerts a strong electrotonic influence that effectively abbreviates AP duration (and thus wavelength) in its immediate surroundings. This effect was responsible for the stabilization and perpetuation of activity in the vicinity of the core, while tissue in the periphery is unable to capture in a 1:1 manner resulting in wavebreak. This electrotonic effect may explain how sustained stable reentry occurs in preparations whose wavelength (space occupied by activation wave), measured during plane wave propagation in the longitudinal direction of cardiac fibers, may be about three times larger than the size of the preparation (68; 231), and may also have

important implications for antiarrhythmic agents targeting wavelength prolongation (Section 1.6.2), as drugs would have to counteract this effect.

1.7.2.1.1 The Role of Functional Obstacles

Numerous theoretical studies have reached similar conclusions on the mechanisms of spiral wave breakup into independent wavelets of activity, as occurs during AF (229; 232-236) (see Section 1.4.3.3). These analyses identified the importance of rate adaptation of the AP in the formation of functional obstacles. This property results in variable recovery properties along the spiral wavefront such that there are regions where the activation front contacts regions of refractory tissue from the previous excitation, promoting spiral wave meander and breakup. The biophysical properties of wavebreak and wavelet formation were as described for wavefront interactions with functional obstacles in Section 1.4.7.

Nygren et al. (237) further investigated the conditions for breakup by comparing activity in tissue models based on the most realistic cellular models of the human atrial AP by Nygren et al. (199) and Courtemanche et al (200). As these models were published in the same year, they are largely based on the same data and might therefore be expected to be quite similar. However, the Courtemanche model displayed substantial rate-dependent adaptation of the AP duration while the Nygren model did not, and consequently recovery was homogeneous in the Nygren model but inhomogeneous in the Courtemanche model. Because of this difference, the Nygren model supported very stable and periodic reentrant activity, while the Courtemanche model exhibited less-stable, aperiodic behavior. The inhomogeneities in the Courtemanche model caused reentrant activity to drift off the sheet and also lead to conditions that support wavebreak

and other phenomena associated with high-frequency oscillations, as occur during fibrillation. Reentrant activity in the Nygren model resembled that of the Courtemanche model when ionic currents were adjusted such that the Nygren AP was similar to the Courtemanche AP. This study clearly demonstrated how breakup and fibrillation result from AP properties acting in a tissue syncytium, and how the relevance of individual ionic currents to AF is determined by the relative contribution to AP properties (237). These latter results are in agreement with the conclusions of Qu et al (238).

Modeling studies have also quantified the extent of AP rate-adaptation necessary for spiral wave breakup in terms of AP restitution. Briefly, restitution refers to the fact that AP duration depends on the previous diastolic interval (rest period between repolarization and the next excitation), and the restitution hypothesis states that it is the slope of the restitution curve (plot of AP duration versus the previous diastolic interval) that is the main determinant of wavebreak (239). As demonstrated by Courtemanche, if the tissue or model substrate is characterized by a restitution curve with slope <1, perturbations (e.g., a premature stimulus) will initially disrupt the dynamics, but reentry will then converge back to the stable equilibrium over subsequent cycles (234). In contrast, if the system has a restitution curve with slope >1, a small perturbation may rapidly become amplified, resulting in wavebreak along the spiral wave arm and spiral wave breakup (240). Similarly, Qu et al. have demonstrated that the steepness of conduction velocity restitution plays an important role in spiral wave stability (223). In contrast to these predictions, wavebreak has been observed in the absence of meander and restitution fluctuations, indicating that the restitution principles may not fully explain spiral wave breakup in all cases (241). Alternately, it may be that the protocol used to

measure restitution significantly influences the shape and predictions of the restitution curve (242).

1.7.2.1.2 The Role of Anatomic Obstacles

Mathematical models of cardiac tissue have also been used to gain insights into the mechanisms of vortex shedding by anatomical obstacles (Section 1.4.5). These studies showed that obstacles can lead to arrhythmias under conditions of decreased excitability, as may occur with sodium channel inhibition or decreased excitability (243-245). To further probe the relationship between excitability and obstacle-related arrhythmogenesis, Starobin et al. explored conditions for new wavelet formation after collision of a plane wave with an obstacle in an otherwise homogeneous excitable medium. By quantifying the balance of charge available in the wavefront and the excitation charge requirements of adjacent medium, critical medium parameters defining conditions for wavefront-obstacle separation were determined analytically (244). Detachment was more likely when obstacle boundaries were sharp. In a related study, wavefront-obstacle separation was observed to occur within a small boundary layer of the order of the wavefront thickness. Conditions for separation were determined by the relationship between reaction-diffusion flows within this boundary layer (243). In essence, wavefront-obstacle detachment occurs when the wavefront has insufficient diffusion current to maintain attachment at the edge of the obstacle, resulting in the formation of a phase singularity.

1.7.2.2 Mechanisms of Antiarrhythmic Drugs Evaluated in Cardiac Tissue Models

Mathematical models have also been used extensively to predict the effects of channel-blocking antiarrhythmic drugs. Joint proarrhythmic and antiarrhythmic effects have been identified in simulations of both potassium (class III) and sodium (class I) channel

blockade. While these observations are intriguing, it remains difficult to evaluate the relative contributions of competing pro- or anti-AF influences without a realistic model of sustained AF.

1.7.2.2.1 Studies of Potassium Channel Bockade

Starmer et al. demonstrated a proarrhythmic response to potassium channel blockade (221). During reentry, potassium channel blockade produced the expected increase in the wavelength of reentry (Section 1.6.1), however as the wavelength approached the perimeter of the unexcited core, reentry became unstable and began to drift (221). This was sufficient to convert a monomorphic ECG pattern to a torsade-like pattern. Similarly, Qu et al. found that blocking K^+ conductance converted a quasiperiodic spiral wave meander to chaotic meander, and then to spiral breakup with fully developed spatiotemporal chaos (223). This was directly attributed to an increased slope of the AP duration restitution curve (see Section 1.7.2.1.1). Chay also found that potassium channel blockade promotes cycle length oscillations in a ring model of cardiac tissue (246; 247) Taken together, these studies predict that while class III drugs may prevent the induction of reentry, wavelength-prolonging effects may promote fibrillation once reentry is initiated. These instability and breakup mechanisms are consistent with model studies elsewhere (Section 1.7.2.1.1), where interactions between successive reentry cycles lead to spiral wave fractionation into independent wavelets as wavefronts collided with inhomogeneous regions. In contrast, bretylium (class III agent) has been shown to flatten the restitution curve, preventing wavebreak and fibrillation in ventricular tissue (248). Unfortunately bretylium is not effective in atrial tissue.

1.7.2.2.2 Studies of Sodium Channel Bockade

Starmer et al. (220) predicted that slowly unbinding sodium channel blockers (encainide and flecainide) exert both an antiarrhythmic effect by delaying the vulnerable window (time when premature stimuli results in unidirectional block and reentrant activation) and a proarrhythmic effect by increasing the duration of the vulnerable period (time when premature contractions may initiate reentry) (Section 1.4.2). It was concluded that the price for increased antiarrhythmic efficacy (suppressed premature contractions) is an increased proarrhythmic vulnerability to unsuppressed premature contractions (220). In contrast to potassium channel blockade, Qu et al. observed that blocking sodium conductance slowed the spiral wave and shifted the system to a longer diastolic interval where the slope of the AP restitution curve was shallower, which tended to stabilize the spiral wave to a quasiperiodic meander pattern (238). Similarly, numerical studies by Chay et al. (246; 247) and others (174) found the sodium channel inhibition stabilized reentry, thereby stabilizing arrhythmic activity once initiated.

1.8 Rationale for Present Studies

Despite almost 120 years of research and speculation, the mechanisms of AF remain poorly understood. Since the early 1960s, the multiple wavelet hypothesis, tested using a primitive computer model but lacking experimental support, has dominated both experimental and clinical understandings of AF mechanisms. Today, experimental observations of AF question the multiple wavelet mechanism, and antiarrhythmic drug efficacy conflicts with classical notions of antiarrhythmic mechanisms. These results

underscore the inadequacy of the present understanding. Detailed mathematical models of cellular electrophysiology and tissue-level electrophysiological dynamics have recently been developed, providing important insights into mechanisms contributing to AF, yet no realistic model of sustained AF has been put forward. A more realistic computer model of AF is needed that accounts for experimental observations and elucidates the mechanisms of AF maintenance and termination by antiarrhythmic drugs. Such a unifying model may enable rapid progress towards controlling this complicated and debilitating arrhythmia.

The goal of the work described by this thesis was to improve our understanding of the basic mechanisms of AF and the mechanisms of antiarrhythmic drug action with the use of highly-realistic mathematical models of atrial electrical activity. I elected to use as a starting point a mathematical model of the canine atrial action potential developed in our laboratory (Ramirez et al., 2000) (42). This choice was based on the fact that extensive experimental observations are available for dog atria at the ionic, cellular, and tissue levels, and that there are extensive data available regarding arrhythmia mechanisms and impulse propagation during AF in the dog. Before proceeding to analyze AF itself, I addressed two important unresolved issues in the cellular model: 1. the stability and physiological nature of time-dependent properties of action potentials during prolonged simulations, and 2. the potential role of Ca^{2+}-handling abnormalities in the reduced rate-adaptation characteristic of AF associated with tachycardia-induced remodeling. I then went on to use the cellular model to create a simulated 2-dimensional sheet of atrial tissue that can be considered representative of a normal atrium. With the use of experimental data that I played a role in obtaining, I incorporated cholinergic effects on atrial ionic

currents and action potentials, and developed a mathematical model of AF, which shares many features with experimental observations of cholinergic AF in the dog and other species. The model was used to obtain insights into the mechanisms by which vagal nerve stimulation promotes AF. Finally, I used my model of cholinergic AF to investigate the mechanisms by which pure Na^+-channel blockade can terminate the arrhythmia. Once again, the results parallel experimental observations and provide the first clear mechanistic explanation of their basis.

The experimental portions of this thesis are presented as papers describing these four specific series of studies:

1. Time-dependent transients in an ionically-based mathematical model of the canine atrial action potential.

[James Kneller, Rafael Ramirez, Denis Chartier, Marc Courtemanche, and Stanley Nattel. Time-dependent transients in an ionically-based mathematical model of the canine atrial action potential. *Am J Physiol Heart Circ Physiol* 2002;282:H1437-51.]

2. Remodeling of Ca^{2+}-handling by atrial tachycardia: evidence for a role in loss of rate-adaptation.

[James Kneller, Hui Sun, Normand Leblanc, and Stanley Nattel. Remodeling of Ca(2+)-handling by atrial tachycardia: evidence for a role in loss of rate-adaptation. *Cardiovasc Res.* 2002;54:416-26.]

3. Cholinergic atrial fibrillation in a computer model of a 2-dimensional sheet of canine atrial cells with realistic ionic properties.

[James Kneller, Renqiang Zou, Edward J. Vigmond, Zhiguo Wang, L. Joshua Leon, and Stanley Nattel. Cholinergic atrial fibrillation in a computer model of a 2-dimensional sheet of canine atrial cells with realistic ionic properties. *Circ Res*. 2002;90:e73-e87.]

4. Mechanisms of AF termination by pure sodium blockade in an ionically-realistic mathematical model.

[James Kneller, Renqiang Zou, L. Joshua Leon, and Stanley Nattel. Mechanisms of AF termination by pure sodium blockade in an ionically-realistic mathematical model. *Circ Res.* (submitted)]

CHAPTER 2 TIME-DEPENDENT TRANSIENTS IN AN IONICALLY-BASED MATHEMATICAL MODEL OF THE CANINE ATRIAL ACTION POTENTIAL.

As discussion in Section 1.7.1.3, 3rd generation cardiac AP models display beat-to-beat changes in intracellular ionic concentrations and other state variables. Equation singularity is a common feature of 3rd generation cardiac AP models, and therefore equation fixed points are unstable in models of this type (193). The equation singularity has been shown to imply the existence of a conservation principle latent in model equations that may permit certain mathematical features to cause computational difficulties and erroneous model performance (218). It is presently unclear if the beat-to-beat changes are an artifact of these mathematical limitations, or if they reflect underlying physiological processes. Prior to developing cellular models of atrial pathologies related to AF and a multicellular model of AF, model transients were characterized and evaluated for validity.

Am J Physiol Heart Circ Physiol 282: H1437–H1451, 2002.
First published November 29, 2001; 10.1152/ajpheart.00489.2001.

Time-dependent transients in an ionically based mathematical model of the canine atrial action potential

JAMES KNELLER, RAFAEL J. RAMIREZ, DENIS CHARTIER,
MARC COURTEMANCHE, AND STANLEY NATTEL
Research Center, Montreal Heart Institute, Montreal, Quebec H1T 1C8, Canada

Received 4 June 2001; accepted in final form 20 November 2001

Kneller, James, Rafael J. Ramirez, Denis Chartier, Marc Courtemanche, and Stanley Nattel. Time-dependent transients in an ionically based mathematical model of the canine atrial action potential. *Am J Physiol Heart Circ Physiol* 282: H1437–H1451, 2002. First published November 29, 2001; 10.1152/ajpheart.00489.2001.—Ionically based cardiac action potential (AP) models are based on equations with singular Jacobians and display time-dependent AP and ionic changes (transients), which may be due to this mathematical limitation. The present study evaluated transients during long-term simulated activity in a mathematical model of the canine atrial AP. Stimulus current assignment to a specific ionic species contributed to stability. Ionic concentrations were least disturbed with the K^+ stimulus current. All parameters stabilized within 6–7 h. Inward rectifier, Na^+/Ca^{2+} exchanger, L-type Ca^{2+}, and Na^+-Cl^- cotransporter currents made the greatest contributions to stabilization of intracellular $[K^+]$, $[Na^+]$, $[Ca^{2+}]$, and $[Cl^-]$, respectively. Time-dependent AP shortening was largely due to the outward shift of Na^+/Ca^{2+} exchange related to intracellular Na^+ (Na_i^+) accumulation. AP duration (APD) reached a steady state after ~40 min. AP transients also occurred in canine atrial preparations, with the APD decreasing by ~10 ms over 35 min, compared with ~27 ms in the model. We conclude that model APD and ionic transients stabilize with the appropriate stimulus current assignment and that the mathematical limitation of equation singularity does not preclude meaningful long-term simulations. The model agrees qualitatively with experimental observations, but quantitative discrepancies highlight limitations of long-term model simulations.

ionic drift; action potential transients; atrial fibrillation; electrophysiology; ion channels and transporters

THE ESTABLISHMENT of the original DiFrancesco-Noble (DN) model of cardiac myocyte electrophysiology spawned the development of numerous other dynamic models patterned after the DN formulation (5). These models explicitly include transmembrane ion channels and pumps, the intracellular calcium sequestering and release activity of the sarcoplasmic reticulum (SR), and changing intracellular ionic concentrations. The incorporation of concentration changes into the cardiac electrical model was an important development because such changes occur rapidly in the small volume of the cardiac cell and can have profound effects on action potential (AP) properties.

Dynamic models are finely tuned to reproduce electrophysiological behavior observed experimentally during observation periods of short duration. However, the original DN model was noted to produce a continual cycle-by-cycle (transient) accumulation (K^+) or depletion (Na^+, Ca^{2+}) of intracellular ionic species (5). AP morphology and the pre- and postcycle values of the ionic concentrations were not constant as would be expected of steady-state behavior. Transient changes were negligible over a few cardiac cycles, but departures from the prestimulus initial concentrations were cumulative and became substantial over many cycles. Guan et al. (9) noted that the original DN equations are mathematically dependent (Jacobian is singular), and therefore that model fixed points are unstable. Varghese and Sell (32) showed that there exists a conservation principle latent in model equations that may permit certain mathematical features to cause computational difficulties and erroneous model performance. Although the abnormal behavior may occur only when parameters are outside the zone of physiological interest, it was argued that these features may introduce erroneous behavior and instabilities within the physiologically realizable range. Consequently, the validity of extended time simulations has been questioned (6, 26).

Time-dependent changes (transients) in ionic concentrations and APs following rate changes are well documented in the experimental literature (2, 7, 11–15, 27, 31, 38). Transients in mathematical models of the AP may represent artifacts of the system of equations used or may reflect physiological processes. We were unable to identify previous studies that characterized in detail time-dependent model transients and that compared model and experimentally observed AP transients. In the present study, electrophysiological transients in an ionic model of the canine atrial AP were studied with the following objectives: *1*) to determine whether dynamic models reach stability during sustained pacing at a fixed rate; *2*) to investigate the effects of stimulus current assignment; *3*) to investi-

Address for reprint requests and other correspondence: S. Nattel, Research Center, Montreal Heart Institute, 5000 Belanger St. E., Montreal, Quebec H1T 1C8, Canada (E-mail: nattel@icm.umontreal.ca).

The costs of publication of this article were defrayed in part by the payment of page charges. The article must therefore be hereby marked "*advertisement*" in accordance with 18 U.S.C. Section 1734 solely to indicate this fact.

gate the ionic basis of AP transients in the model; and 4) to compare experimental and model AP transients.

METHODS

Model Implementation

Model transients were studied in the Ramirez-Nattel-Courtemanche (RNC) model of the canine atrial AP (28). The RNC model is composed of 23 coupled first-order ordinary differential equations and accounts for intracellular concentrations of potassium ($[K^+]_i$), sodium ($[Na^+]_i$), calcium ($[Ca^{2+}]_i$), and chloride ($[Cl^-]_i$).

The rate of change in the transmembrane potential (V) is given by

$$\frac{dV}{dt} = \frac{-(I_{ion} + I_{stim})}{C_m} \quad (1)$$

in time, where I_{ion} and I_{stim} are the total transmembrane ionic and stimulus currents, respectively, and C_m is the total membrane capacitance. Numerical integration was performed using a modified Euler method. After completion of the Cl^- transport formulation (described below), the total transmembrane ionic current is given by

$$I_{ion} = I_{Na} + I_{K1} + I_{to} + I_{Kur,d} + I_{Kr} + I_{Ks} + I_{Ca} + I_{Cl,Ca} + I_{p,Ca} + I_{NaCa} + I_{NaK} + I_{b,Na} + I_{b,Ca} + I_{b,Cl} \quad (2)$$

I_{ion} includes contributions from the fast sodium current (I_{Na}), the inward rectifier (I_{K1}) and transient outward (I_{to}) potassium currents, the rapid (I_{Kr}) and slow (I_{Ks}) components of the classical delayed rectifier potassium current, L-type calcium current (I_{Ca}), a sarcolemmal calcium pump current ($I_{p,Ca}$), the Na^+-K^+-ATPase current (I_{NaK}), the Na^+/Ca^{2+} exchanger (I_{NaCa}), and a calcium-activated chloride current ($I_{Cl,Ca}$), and background sodium ($I_{b,Na}$), calcium ($I_{b,Ca}$), and chloride ($I_{b,Cl}$) currents also contribute. The RNC AP most closely resembles right atrial pectinate muscle APs, because ionic current formulations were based on data from cells isolated from this region (16, 28). Shorter APs would be expected from a left atrial AP model, because I_{Kr} is typically larger in the left atria (17).

All simulations were performed with I in picoamps, V in millivolts, and C_m = 100 pF. A fixed time step of 5 and 20 μs was used in the presence and absence of stimulation, respectively. For reasons discussed in *Stimulus Current Assignment* (see RESULTS), all simulations were performed with the stimulus current attributed to potassium unless stated otherwise. All simulations were performed using double-precision arithmetic on Unix PC workstations.

Model Modification

In the RNC model, $I_{Cl,Ca}$ brings Cl^- into the cell during each cycle. The magnitude of this current increases with increasing $[Ca^{2+}]_i$. However, the RNC equations do not provide for Cl^- efflux (as noted). The interdependence of membrane currents ($I_{Cl,Ca}$, Na^+-K^+ pump, and Na^+/Ca^{2+} exchanger) implies that the beat-to-beat accumulation of Cl^- simultaneously induces transients in all ionic concentrations, and consequently absolute stability is not possible. Because other dynamic models do not account for $[Cl^-]_i$, this limitation was overcome by developing a model of myocyte pH and Cl^- regulation based on physiological processes as described by Baumgarten and Duncan (1). The net ionic movement of Cl^- was formulated as an inward electroneutral Na^+-Cl^- cotransporter and constant Cl^- efflux through a leakage pathway, in addition to $I_{Cl,Ca}$.

The electroneutral Na^+-Cl^- cotransporter was empirically formulated with a Hill function and is given by

$$CT_{NaCl} = g_{CT}\left(\frac{\Delta_{CT}^n}{\Theta_{CT}^n + \Delta_{CT}^n}\right) \quad (3)$$

where the conductance of the cotransporter (g_{CT}) = 0.115, $\Theta_{CT}^n = E_{Na} - E_{Cl}$ (where E_{Na} is the equilibrium potential of Na^+ and E_{Cl} is the equilibirium potential of Cl^-), Δ_{CT}^n = 87.8251 and n = 4.

The background leakage current ($I_{b,Cl}$) is given by

$$I_{b,Cl} = g_{b,Cl}(V - E_{Cl}) \quad (4)$$

where the conductance of the $I_{b,Cl}$ ($g_{b,Cl}$) = 0.0018.

Because of the lack of kinetic data in the literature, $g_{b,Cl}$ was approximated as twice the mean of the RNC background conductances. The cotransporter parameters were chosen to balance the magnitude of the leakage current at rest with rapid kinetics as intracellular pH is tightly regulated. The original RNC equations were based on short-term (several second) simulations. I_{Ca} was reduced to 30% of mean experimental values to obtain physiological AP durations (APDs). When we performed longer-term simulations, we found that the RNC parameters provided APDs that were too short, and that K^+ currents had to be corrected [maximal I_{to} conductance (g_{to}) and $I_{Kur,d}$ conductance ($g_{Kur,d}$) were reduced to 25 and 75% of original RNC values] to provide values closer to experimental observations. Conductance changes, CT_{NaCl}, and $I_{b,Cl}$ were incorporated into the RNC equations to obtain the modified RNC (mRNC) model. Initial conditions for the mRNC model were obtained from the RNC initial conditions by allowing the revised equations to equilibrate for >5 min at rest (Table 1). Although the ionic mechanisms necessary for long-term stability were present following these modifications, it was noted that the equation singularity remained in the mRNC model. Therefore, the mRNC fixed points were also unstable and the equations still possessed the latent conservation principle as described.

Experimental Techniques for AP Recording

Adult mongrel dogs (n = 16) of either sex (20–32 kg) were anesthetized with pentobarbital sodium (30 mg/kg iv), and their hearts were quickly removed and immersed in Tyrode solution at room temperature and equilibrated with 100% O_2. The Tyrode solution contained (in mM) 126 NaCl, 5.4 KCl, 1.0 $MgCl_2$, 0.33 NaH_2PO_4, 1.0 $CaCl_2$, 10 dextrose, and 10 HEPES, pH was adjusted to 7.4 with NaOH. The right atrium was dissected free, and the right coronary artery was cannulated and perfused with Krebs solution at 37°C and equilibrated with 5% O_2-95% CO_2 to maintain the pH between 7.35 and 7.40. The Krebs solution contained (in mM) 120 NaCl, 3.8 KCl, 1.2 $CaCl_2$, 1.2 $MgSO_4$, 1.2 KH_2PO_4, 25 $NaHCO_3$, and 5.5 dextrose. Any leaks from arterial branches were ligated, and the tissue was perfused at 10–12 ml/min throughout the experiment to approximate normal flow in the canine right atrium (34).

Preparations were stimulated with square-wave pulses (4 ms) delivered at 1.5 to 2 times diastolic threshold through bipolar Teflon-coated silver electrodes. The standard microelectrode techniques used in the present study have been described in detail elsewhere (24). Cellular membrane potentials were recorded from the endocardium using glass microelectrodes filled with 3 M KCl (8–20 MΩ resistance) coupled to an Axoclamp 2B amplifier (Axon Instruments; Foster City, CA). Signals were converted into digital form by a Digidata

Table 1. *Initial conditions for mRNC model*

Symbol	Definition	Resting Value
V	Transmembrane potential	−82.72 mV
M	I_{Na} activation variable	0.002256
H	I_{Na} fast inactivation variable	0.9750
J	I_{Na} slow inactivation variable	0.9843
D	I_{Ca} activation variable	5.448×10^{-6}
F	I_{Ca} voltage-dependent inactivation variable	0.9999
x_r	I_{Kr} activation variable	8.647×10^{-7}
x_s	I_{Ks} activation variable	0.01853
$[Na^+]_i$	Intracellular sodium concentration	13.86 mM
$[Ca^{2+}]_i$	Intracellular calcium concentration	1.310×10^{-4} mM
$[K^+]_i$	Intracellular potassium concentration	136.9 mM
$[Cl^-]_i$	Intracellular chloride concentration	29.95 mM
$[Ca^{2+}]_{up}$	Ca^{2+} concentration in network SR	1.869 mM
$[Ca^{2+}]_{rel}$	Ca^{2+} concentration in junctional SR	1.869 mM
o_a	I_{to} activation variable	0.07351
o_i	I_{to} inactivation variable	0.9978
q_{Ca}	Ca^{2+} flux-dependent $I_{Cl,Ca}$ activation gating variable	0.0
u_a	$I_{Kur,d}$ activation variable	0.06039
u_i	$I_{Kur,d}$ inactivation variable	0.9987
f_{Ca}	I_{Ca} Ca^{2+}-dependent inactivation variable	0.6536
$[Ca^{2+}]_{Cmdn}$	Ca^{2+}-bound calmodulin concentration	2.347×10^{-3} mM
$[Ca^{2+}]_{Trpn}$	Ca^{2+}-bound troponin concentration	8.933×10^{-3} mM
$[Ca^{2+}]_{Csqn}$	Ca^{2+}-bound calsequestrin concentration	6.916 mM
u	Activation gating variable for I_{rel}	0.0
v	Ca^{2+} flux-dependent I_{rel} inactivation gating variable	1.0
w	Voltage-dependent I_{rel} inactivation gating variable	0.9993

Symbols were adopted from Ramirez et al. (28).

1200 series analog-to-digital converter (Axon Instruments) and displayed on a Pentium PC using Axotape version 2.0 software (Axon Instruments). Tissues were paced continuously at 400-, 300-, and 200-ms basic cycle lengths (BCLs) for 35 min at each BCL. AP recordings were obtained in each preparation from a minimum of five impalements 0–5, 15–20, and 30–35 min from the onset of stimulation at each BCL. A 5-min rest period followed stimulation at each BCL. During this time, preparations that did not beat spontaneously were paced at 1 Hz, and further control recordings were made to ensure the stability of the preparation. The 35-min pacing duration was chosen to allow measurement of the largest possible transients at three rates without compromising the viability of the tissues. Because results depended on the shape of the waveforms, precautions were taken to ensure that the stimulus current did not interfere. Each stimulus site was located at least several millimeters from the impaled cell (39). In addition, an interval of constant rest potential between the stimulus artifact and the recorded AP was confirmed (30). Light tension was applied to stabilize the preparations as needed. APD to 90% (APD_{90}) and 50% (APD_{50}) repolarization were measured with custom-made software and confirmed manually. Only recordings demonstrating <3% variation in interbeat end-diastolic potential were analyzed.

Statistical comparisons were performed on raw data with an exponential regression mixed-model analysis as described by Glantz and Slinker (8). Analysis of variance was applied for statistical comparison, with Bonferroni's correction used for post hoc tests. SAS release 6.12 (Cary, NC) was used to perform all statistical analyses. The level of statistical significance was set at $P < 0.05$.

RESULTS

Comparison of RNC and mRNC Ionic Transients

Figure 1 shows ionic transients in the RNC and mRNC models over 10 h of simulated pacing at 2 Hz. For reasons discussed below, simulations in both models were performed with the stimulus current attributed to K^+. Ionic concentrations were sampled 2 ms before each AP upstroke. The RNC concentrations did not stabilize, because $[K^+]_i$ (Fig. 1*A*) and $[Cl^-]_i$ (Fig. 1*D*) displayed long-term linear increases that were clearly nonphysiological, and $[Na^+]_i$ (Fig. 1*B*) and $[Ca^{2+}]_i$ (Fig. 1*C*) failed to reach a constant value. These ongoing changes would be expected to eventually cause model failure. In contrast, the mRNC concentrations stabilized following monotonic increases in $[Na^+]_i$, $[Ca^{2+}]_i$, and $[Cl^-]_i$. $[K^+]_i$ initially decreased and then reversed, increasing to a steady state after 4 h. In both models, as $[Ca^{2+}]_i$ plateaued, Cl^- influx through $I_{Cl,Ca}$ approached a constant value. RNC $[Cl^-]_i$ steadily increased (no Cl^- efflux mechanism) and forced transients in all ionic species. The initial mRNC $[Cl^-]_i$ increase was greater as CT_{NaCl} brought Cl^- into the cell before $I_{b,Cl}$ could compensate. Cotransport with Na^+ also caused a larger initial increase in $[Na^+]_i$ (and therefore in $[Ca^{2+}]_i$ by reduced forward-mode Na^+/Ca^{2+} exchange) in the mRNC model.

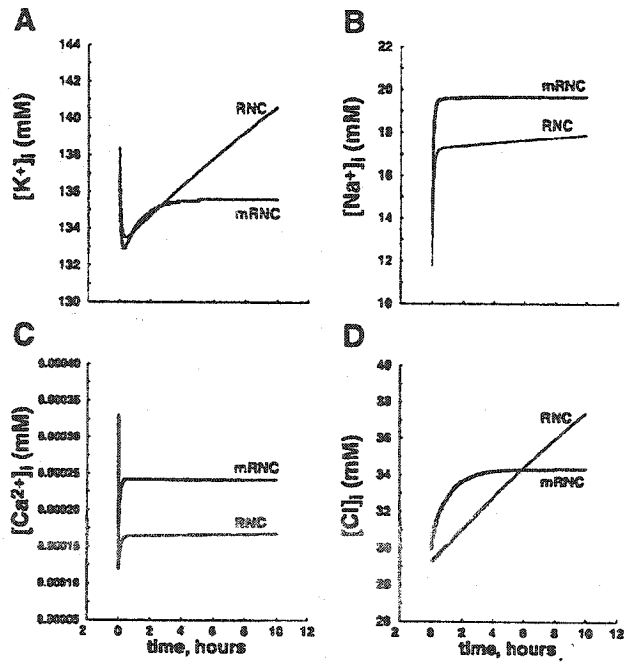

Fig. 1. Steady-state model ionic transients. Transients in intracellular concentrations of K^+ ($[K^+]_i$; *A*), Na^+ ($[Na^+]_i$; *B*), Ca^{2+} ($[Ca^{2+}]_i$; *C*), and Cl^- ($[Cl^-]_i$; *D*) are shown over 10 h of pacing at 2 Hz. Ramirez-Nattel-Courtemanche (RNC) concentrations failed to reach constant values. All modified RNC (mRNC) concentrations stabilized.

Although all mRNC concentrations appeared to be unchanging after 7 h of pacing, it was not clear whether the model system had reached absolute stability. To determine whether perfect stability was attained, numerical integration of all K^+ currents and the AP waveform (measured to six significant figures) was performed after each hour of pacing for up to 10 h. All changes ceased between 6 and 7 h (not shown), confirming that model equations had reached absolute stability as suggested by the ionic concentrations (Fig. 1). In this way, the addition of Cl^- transporters was sufficient for the mRNC model to stabilize during sustained pacing, despite the inherent equation instabilities. The mRNC model was used for all subsequent simulations.

To ensure convergence of the integration scheme, the 10-h ionic transients were computed with two and four times reductions of the time step. No differences in $[K^+]_i$ were found between all time steps after 5 h. No differences between the 2.5- and 1.25-μs time steps were found for $[Na^+]_i$ after 5 h, and results with either differed from those with the 5-μs time step by <0.05%. $[Ca^{2+}]_i$ and $[Cl^-]_i$ displayed slightly greater departures, but both converged toward the 5-μs solution. Overall, the 2.5- and 1.25-μs solutions differed from those with the 5-μs time step by <0.35% at all times, demonstrating that appreciable numerical error did not accumulate during the long pacing simulations and that the transients were indeed a property of the equation system.

Stimulus Current Assignment

The RNC stimulus current delivers 58 pC/pF over the first 2 ms of each cycle (28). Simulations shown in Fig. 1 were conducted with this current attributed to K^+. Both models featured reversal of the $[K^+]_i$ transient following 40 min of pacing, after which RNC $[K^+]_i$ continued to increase in a linear fashion while mRNC $[K^+]_i$ plateaued. The effect of stimulus current assignment on model transients and stability was therefore investigated. Ten-hour pacing simulations at 2 Hz were conducted as before, with the stimulus current attributed to either Na^+, Ca^{2+}, or Cl^- (I_{stim} substituted into *Eqs. 9*, *10*, or *11* below, respectively). Concentrations were sampled 2 ms before each AP upstroke. Results are shown in Fig. 2. Although the model remained stable, the magnitude and time course of all transients were influenced by each assignment. Overall, the K^+ ionic stimulus assignment least perturbed all ionic species, and stable concentrations were reached in the shortest time. Relative to the K^+ assignment, the Na^+ assignment caused a greater $[Na^+]_i$ increase, allowed a greater $[K^+]_i$ depletion, and caused a greater $[Ca^{2+}]_i$ departure from baseline. The Ca^{2+} assignment caused maximal $[Na^+]_i$ and $[Ca^{2+}]_i$ transients and the most extensive $[K^+]_i$ depletion of all cationic assignments. The Cl^- assignment caused severe $[K^+]_i$ and $[Cl^-]_i$ depletion. When the stimulus current was not attributed to any ion (i.e., I_{stim} absent in *Eqs. 8–11* below), the model became very unstable.

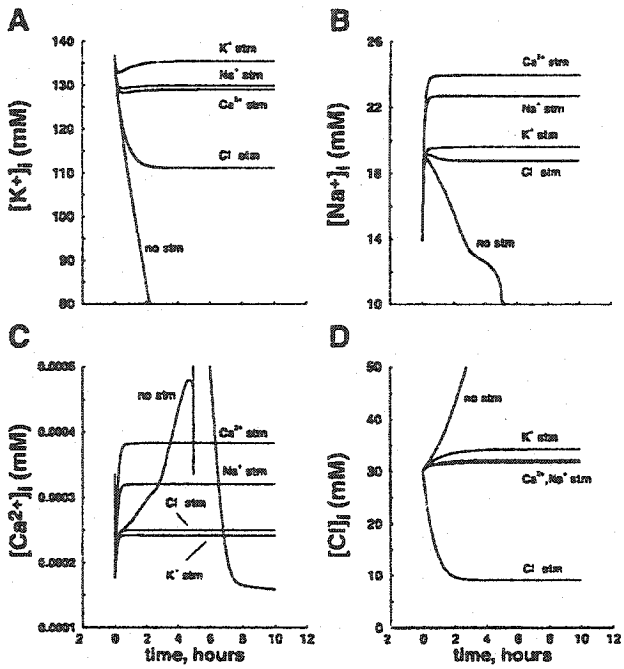

Fig. 2. Effects of stimulus current assignment on ionic transients. For each stimulus assignment (stm), resulting $[K^+]_i$ (*A*), $[Na^+]_i$ (*B*), $[Ca^{2+}]_i$ (*C*), and $[Cl^-]_i$ (*D*) ionic transients are shown. All transients were altered by each assignment. Stimulus with K^+ current assignment caused the smallest overall displacements.

$[K^+]_i$ and $[Na^+]_i$ were depleted to <0.5% and 20% of prestimulus baseline during 10 h, respectively, and $[Cl^-]_i$ increased to over 600% of baseline. $[Ca^{2+}]_i$ also increased to over 500% of initial values midway through the simulation, but returned to near baseline after 10 h.

Ionic Basis of $[K^+]_i$ Transient Reversal

Figure 2 shows that the $[K^+]_i$ transient reversal only occurs when the stimulus is attributed to K^+. Because this phenomenon is well documented experimentally (7, 11–15) and in human tissues (27), additional simulations were conducted to determine the ionic mechanisms underlying the reversal. The quantity of charge carried by each K^+ current was calculated by numerical integration over one cycle after each minute of sustained stimulation. Figure 3*B* shows summated K^+ influx (I_{NaK}, I_{stim}) and efflux (I_{to}, $I_{Kur,d}$, I_{Kr}, I_{Ks}, I_{K1}). The combined magnitudes of K^+ efflux currents initially exceeded the magnitude of K^+ influx and $[K^+]_i$ decreased (Fig. 3*A*). Over this time the magnitude of I_{NaK} gradually increased while outward K^+ currents decreased, attenuating the transient to achieve a local minimum between 13.4 and 20 min when K^+ influx and efflux were balanced. I_{NaK} then continued to increase, and with supplementation by I_{stim} influx eventually exceeded efflux and $[K^+]_i$ changes reversed. Thus slow I_{NaK} adaptation accounted for the $[K^+]_i$ transient reversal, as previously postulated (11–15, 27). At the time of each integration, APD_{90} and APD_{50} were measured to within 0.5 ms. After the onset of

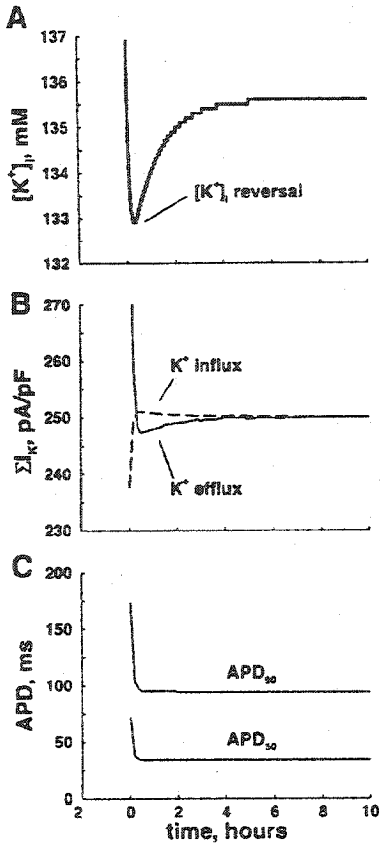

Fig. 3. Ionic mechanism of $[K^+]_i$ transient reversal. After the onset of stimulation, $[K^+]_i$ decreased (*A*) over many cycles because combined efflux currents (*B*) exceeded Na^+-K^+-ATPase current (I_{NaK}) influx. I_{NaK} gradually increased such that the direction of change in $[K^+]_i$ reversed. Steady state was attained when influx and efflux were balanced. Action potential duration (APD) reduction (*C*) occurred very early and stabilized before $[K^+]_i$.

stimulation, both APD_{90} and APD_{50} declined monotonically to steady state, with APD_{90} changes ceasing when $[K^+]_i$ was within 1 mM of stabilization.

Unstable Fixed Points and Conservation Principle

It is not presently known whether ionic transients in models of this type are significantly influenced by the equation singularity and are therefore artifacts of the mathematical formulation. Before we compared model and experimental transients, the unstable fixed points of the mRNC equations and presence of the latent conservation principle were evaluated.

To demonstrate the fixed-point instability, initial $[K^+]_i$ was decreased by 30, 60, and 90 mM, and the model was allowed to seek steady state by simulating 10 h without stimulation. If model fixed points were stable, concentrations would return to (or at least tend toward) the original unperturbed initial concentrations. The responses of all ionic species to the perturbations are shown in Fig. 4. It can be seen that the initial values of $[K^+]_i$ (Fig. 4*A*) were perturbed, whereas the profiles of $[Na^+]_i$ (Fig. 4*B*), $[Ca^{2+}]_i$ (Fig. 4*C*), and $[Cl^-]_i$ (Fig. 4*D*) began at the same initial values. Each transient reached a new steady-state concentration (fixed point) with displacement proportional to the $[K^+]_i$ perturbation. The responses of $[K^+]_i$ and $[Cl^-]_i$ were monotonic, whereas $[Na^+]_i$ and $[Ca^{2+}]_i$ changes reversed early in the simulation. This behavior resulted from the equation singularity and demonstrates the strict dependence of model solutions on initial conditions.

The basic conservation principle (32) is given by

$$\alpha_0^{-1}\partial_t u = \sum_{i=1}^{6} \alpha_i^{-1}\partial_t w_i \qquad (5)$$

where u is the voltage, w is a concentration variable, and $\alpha_0 = C_m - 1$, $\alpha_1 = \alpha_2 = (V_iF) - 1$, $\alpha_3 = (-V_iF) - 1$, $\alpha_4 = (2V_iF) - 1$, $\alpha_5 = (2V_{up}F) - 1$, and $\alpha_6 = (2V_{rel}F) - 1$.

The explicit form for the mRNC equations is given by

$$V = \frac{V_iF}{C_m}\left([Na^+]_i + [K^+]_i - [Cl^-]_i + 2[Ca^{2+}]_i + \frac{2V_{up}}{V_i}[Ca^{2+}]_{up} + \frac{2V_{rel}}{V_i}[Ca^{2+}]_{rel}\right) + C_0 \qquad (6)$$

where V_i is the volume of the intracellular cytoplasm, and V_{up} and V_{rel} are the volumes of the SR uptake and release compartments, respectively. C_0 is a constant of integration.

This conservation principle explicitly states that the potential difference between the inside and outside of

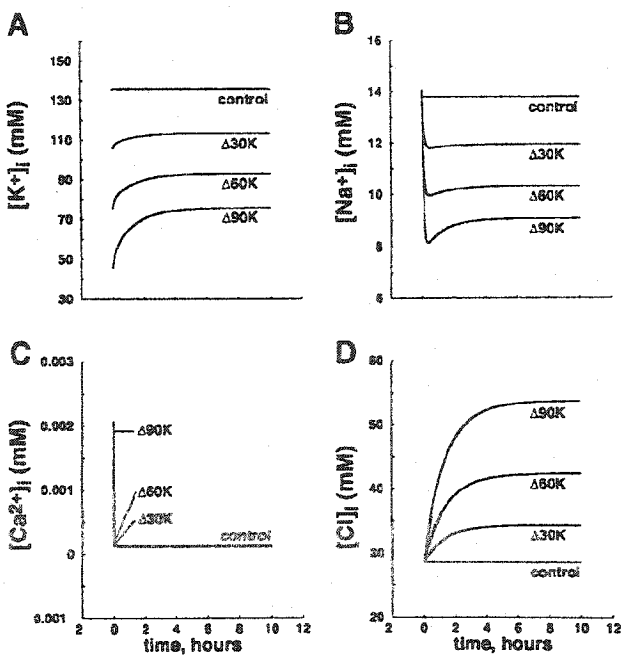

Fig. 4. Unstable fixed points arising from mRNC equation singularity. Initial $[K^+]_i$ was decreased by 30, 60, and 90 mM (*A*), and model equations were allowed to seek steady state by simulating 10 h without stimulation. At steady state, ionic transients were displaced in proportion to the $[K^+]_i$ perturbations. Δ30K, Δ60K, and Δ90K indicate transients resulting from $[K^+]_i$ decreases of 30, 60, and 90 mM, respectively.

the cell is regulated by the flow of ions through the cell membrane. It is readily apparent from *Eq. 6* that membrane potential may remain constant as long as the total intracellular charge is conserved, regardless of the ionic composition. In this way, the principle predicts that the unstable fixed points demonstrated by the displaced ionic transients in Fig. 4 would have appeared stable (i.e., transients would have returned to original unperturbed initial concentrations) if each $[K^+]_i$ decrease was offset with an equal but opposite increase in another cationic species.

This prediction was used to demonstrate the presence of the latent conservation principle in the mRNC equations. The initial value of $[K^+]_i$ was decreased by 30, 60, and 90 mM as before, with each charge deficit offset by increasing initial $[Na^+]_i$ by 30, 60, and 90 mM, respectively. The model was again allowed to seek steady state over 10 h without stimulation. The responses of all concentrations to the perturbations are shown in Fig. 5. It can be seen that $[Ca^{2+}]_i$ (Fig. 5*C*) and $[Cl^-]_i$ (Fig. 5*D*) responded to the $[K^+]_i$ (Fig. 5*A*) and $[Na^+]_i$ (Fig. 5*B*) offsets with departures proportional to the displacement magnitudes. As expected, all transients returned completely to the original unperturbed initial conditions over 10 h (except for the response of $[Cl^-]_i$ to the 90 mM perturbations, which returned to within >99% of the initial $[Cl^-]_i$ value). The responses

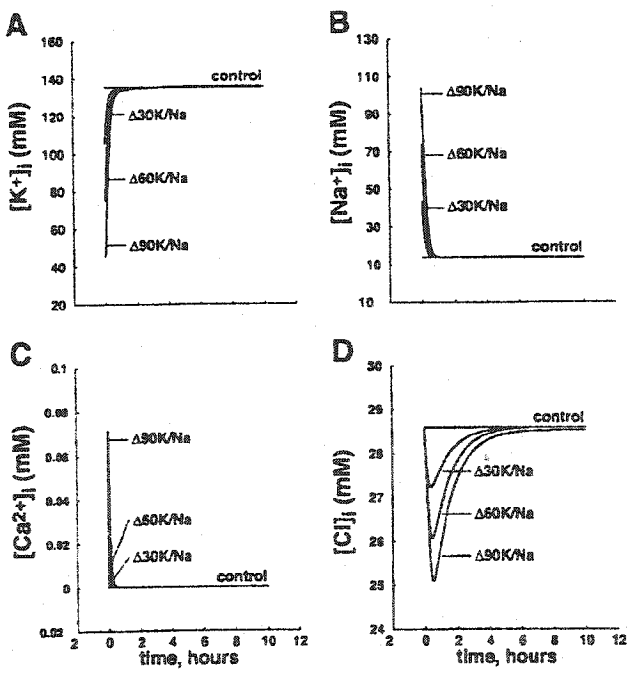

Fig. 5. Conservation principle latent in the mRNC equations. Initial $[K^+]_i$ was decreased by 30, 60, and 90 mM along with offsetting initial $[Na^+]_i$ increases of 30, 60, and 90 mM, respectively. Model equations were allowed to seek steady state by simulating 10 h without stimulation as before. Although the perturbations caused large initial displacements of $[K^+]_i$ (*A*), $[Na^+]_i$ (*B*), $[Ca^{2+}]_i$ (*C*), and $[Cl^-]_i$ (*D*), original initial concentrations were eventually recovered by all ionic species. Δ30K/Na, Δ60K/Na, and Δ90K/Na indicate transients resulting from initial $[Na^+]_i$ and $[K^+]_i$ displaced by 30, 60, and 90 mM, respectively.

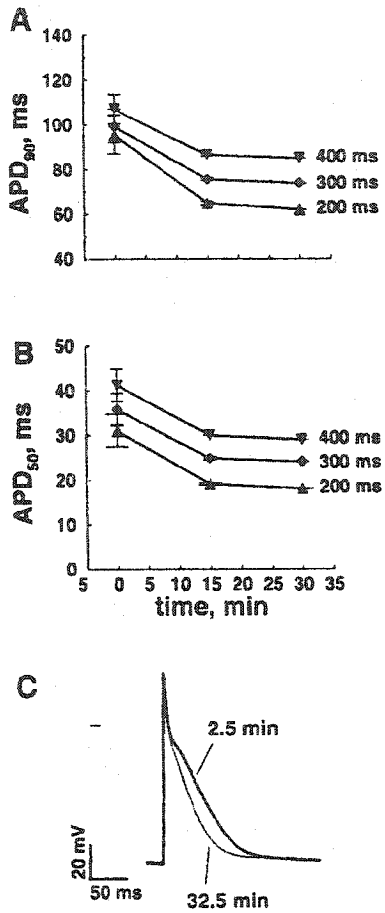

Fig. 6. Pacing-induced model AP transients with K^+ stimulus assignment. APD at 90% (APD_{90}; *A*) and and 50% repolarization (APD_{50}; *B*) reductions are shown, with representative APs [300 ms basic cycle length (BCL)] from the 0–5 and 30–35 min pacing intervals (*C*). Marker at *left* indicates 0 mV.

of $[Na^+]_i$ and $[K^+]_i$ were monotonic, whereas $[Ca^{2+}]_i$ and $[Cl^-]_i$ reversed early in the simulation before returning toward baseline.

Model AP Transients

AP transients occurring simultaneously with ionic changes were measured using an experimentally reproducible simulation protocol. The mRNC model was paced at BCLs of 400, 300, and 200 ms for 35 min, and APs were collected among 0–5, 15–20, and 30–35 min of pacing. In this way, model performance was evaluated over 5,250, 7,000, and 10,500 cycles for the 400-, 300-, and 200-ms pacing BCLs, respectively, totaling 750, 1,000, and 1,500 APs per recording interval. Results with the stimulus current assigned to K^+ are shown in Fig. 6. Changes were similar at all rates, and APs were close to steady state after 35 min. Reductions at a BCL of 200 ms were 34 and 13 ms for APD_{90} and APD_{50}, respectively, with 91% and 92% of the change occurring during the initial 15 min. To investigate the effects of alternate stimulus current assignment on AP transients, simulations were repeated with the stimu-

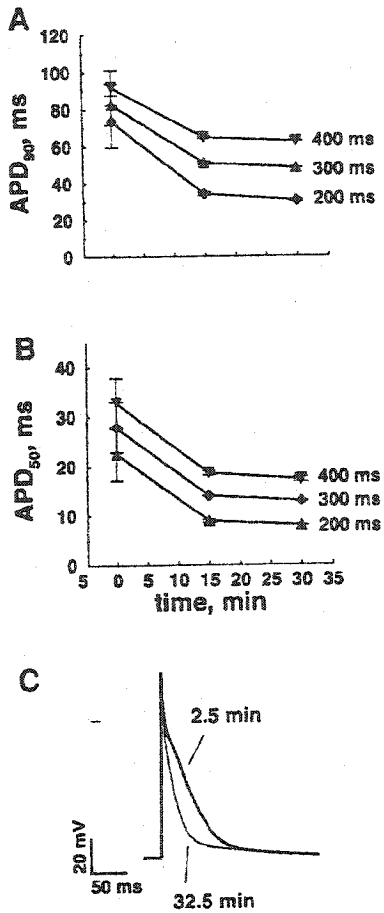

Fig. 7. Pacing-induced model AP transients with Na^+ stimulus assignment. APD_{90} (*A*) and APD_{50} (*B*) reductions are shown, with representative APs (300 ms BCL) from the 0–5 and 30–35 min pacing intervals (*C*). Marker at left indicates 0 mV.

lus current assigned to Na^+ (Fig. 7). APs were substantially shorter at all time points, and reductions were somewhat more extensive. Reductions at a BCL of 200 ms were 35 and 15 ms for APD_{90} and APD_{50}, respectively, with 91% and 94% of the change occurring during the initial 15 min. Although reductions were similar, APs were significantly shorter and less physiological (Fig. 12) than for the K^+ stimulus current assignment. We therefore used K^+ stimulus assignment for all further analyses of mechanisms of activity-related ionic and AP transients in the model.

Ionic Basis of Model AP Transients

The model was used to investigate the electrophysiological basis of the AP reductions. The transients in ion concentrations and ionic currents associated with the AP changes in Fig. 6 were determined. $[Na^+]_i$ (Fig. 8*B*) and $[Cl^-]_i$ (Fig. 8*D*) increased monotonically. $[K^+]_i$ (Fig. 8*A*) initially decreased, stabilized, and began to increase after 17 (BCL 400 ms) and 25 (BCL 200 ms) min. $[Ca^{2+}]_i$ (Fig. 8*C*) increased following an early rapid decline. As with the AP changes, all ionic transients were greater at faster rates and did not completely stabilize within the pacing interval. Each concentration evolved along an exponential time course as suggested by the statistical analyses of experimental results.

The origin of the ionic transients was investigated. For the accumulation or depletion of ionic species the following inequality must hold

$$\int_{\text{cycle}} \sum I_i \neq 0 \qquad (7)$$

where $i = K^+$, Na^+, Ca^{2+}, or Cl^-. ΣI_i is the per-cycle sum of the charge carriers contributing to each concentration and is obtained by summing the relevant charge carriers from *Eq. 2* with stoichiometric scaling of the pump and exchanger currents. For each ionic species, ΣI_i is given by (with I_{stim} attributed to K^+)

$$\sum I_K = -I_{to} - I_{Kur,d} - I_{Kr} - I_{Ks} - I_{K1} + 2I_{NaK} - I_{stim} \qquad (8)$$

$$\sum I_{Na} = -I_{Na} - I_{b,Na} - 3I_{NaCa} - 3I_{NaK} + CT_{NaCl} \qquad (9)$$

$$\sum I_{Ca} = -I_{Ca} - I_{b,Ca} - I_{p,Ca} + 2I_{NaCa} + SR(I_{up}, I_{leak}, I_{rel}) \qquad (10)$$

$$\sum I_{Cl} = I_{Cl,Ca} + I_{b,Cl} + CT_{NaCl} \qquad (11)$$

where $SR(I_{up}, I_{leak}, I_{rel})$ includes all Ca^{2+} fluxes between the SR and cytoplasm. Positive currents were defined as positive charge effluxes from the intracellular volume. The expressions for each charge carrier and the activity of the SR are fully described in Ref. 28.

To attain steady state at each stimulus rate, the cell attempts to remove the inequality in *Eq. 7*. Because

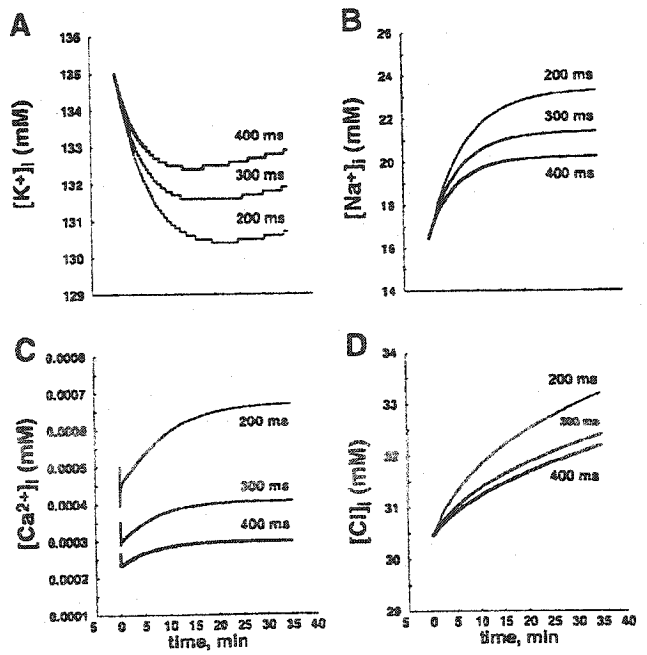

Fig. 8. Ionic transients associated with time-dependent mRNC APD reductions during stimulation at cycle lengths indicated. Over the 35-min pacing interval, $[K^+]_i$ (*A*) decreased, whereas $[Na^+]_i$ (*B*), $[Ca^{2+}]_i$ (*C*), and $[Cl^-]_i$ (*D*) increased.

certain charge carriers play only minor roles in the cardiac cycle, an equivalent contribution of each to ΣI_i of *Eq. 7* would not be expected. The currents that carried the greatest quantity of charge were most responsible for the magnitude of ΣI_i and the resulting ionic transients. The greatest changes in current magnitude toward this end contributed most to neutralizing the concentration drift. To determine the total charge carried by all membrane currents and the functional changes in current magnitude over the pacing interval, numerical time integration of each current in *Eqs. 8–11* was performed over one 300-ms cycle after 2.5 and 32.5 min of pacing. Integration results and the corresponding ΣI_i are given in Tables 2–5. In the tables, Δ indicates the magnitude of the contribution of functional changes to ionic stabilization. ΣI_i indicates the overall charge imbalance at each time point, and $\Delta\Sigma I_i$ indicates the magnitude of combined functional changes toward ionic stabilization.

K^+ and 35-min transients. All K^+ currents (Table 2) adjusted toward a new $[K^+]_i$ steady state, except the stimulus current, which has a fixed magnitude in the RNC model. The largest K^+ current was efflux by I_{K1} after 2.5 and 32.5 min. Over the pacing interval, reduced efflux by $I_{Kur,d}$ contributed most toward $[K^+]_i$ stabilization, although reduced effluxes by I_{K1} and I_{to} were also important to limiting $[K^+]_i$ depletion. In Table 2, negative ΔI for membrane currents indicates that current magnitude decreased during the pacing interval. Positive $\Delta\Sigma I_K$ indicates increased conservation of intracellular K^+.

Na^+ and 35-min transients. All Na^+ charge carriers (Table 3) adjusted toward a new $[Na^+]_i$ steady state, with the exception of $I_{b,Na}$. The largest Na^+ charge carrier at both times was efflux by I_{NaK}. The greatest contributor to the pacing-induced increase in $[Na^+]_i$ was I_{NaCa}, and functional changes in the balance of reverse-mode I_{NaCa} exchange also contributed most toward $[Na^+]_i$ stabilization. In Table 3, negative $\Delta\Sigma I_{Na}$ indicates decreased accumulation of intracellular Na^+.

Ca^{2+} and 35-min transients. For Ca^{2+} (Table 4), I_{Ca} and $I_{p,Ca}$ adjusted toward a new $[Ca^{2+}]_i$ steady state, whereas I_{NaCa} and $I_{b,Ca}$ opposed it. The overall magnitude of I_{NaCa} preferentially attenuated in favor of establishing a new $[Na^+]_i$ steady state. The largest Ca^{2+} current was efflux by I_{NaCa} after 2.5 and 32.5 min. Reduced influx by I_{Ca} contributed most toward establishing a new $[Ca^{2+}]_i$ steady state. The immediate drop following the onset of stimulation was due to large Ca^{2+} efflux carried by I_{NaCa}. The preceding train of conditioning pulses at 1 Hz before the onset of rapid stimulation reduced this early redistribution. The greater final magnitude of $[Ca^{2+}]_i$ at shorter BCLs evinced the rate dependence of Ca^{2+} loading. SR fluxes were balanced during each cycle, and a net SR flux did not contribute appreciably to the Ca^{2+} overload. In Table 4, negative $\Delta\Sigma I_{Ca}$ indicates decreased accumulation of intracellular Ca^{2+}.

Cl^- and 35-min transients. Finally, the magnitudes of all Cl^- charge carriers (Table 5) adjusted toward establishing a new $[Cl^-]_i$ steady state, except $I_{Cl,Ca}$, which was constrained to increase with increasing $[Ca^{2+}]_i$, thereby contributing to the delayed $[Cl^-]_i$ steady state seen in Fig. 8. The largest Cl^- charge carriers were influx by CT_{NaCl} at both times. Increased efflux by $I_{b,Cl}$ also contributed most toward establishing a new $[Cl^-]_i$ steady state, although decreased influx by CT_{NaCl} was only slightly less important. Compared with other functional changes contributing to charge balance, adjustment of Cl^- charge carriers were of minor importance. In Table 5, negative $\Delta\Sigma I_{Cl}$ indicates decreased accumulation of intracellular Cl^-.

Contribution of concentration transients to AP reduction. To determine the relative contribution of each 35-min concentration transient (Fig. 8) to pacing-induced AP reduction, the 2.5-min AP was computed after clamping initial concentrations with values sampled 2 ms before the AP upstroke after 32.5 min of pacing (BCL 300 ms). Results are shown in Fig. 9. The addition of rapid pacing-induced changes in $[K^+]_i$ (1.5% decrease) prolonged the 2.5-min measurement of APD_{90} by 1 ms (1.0% prolongation) but did not change APD_{50} (Fig. 9*A*). Pacing-induced changes in $[Na^+]_i$ (18% increase) accounted for 100% and 121% of the overall APD_{50} and APD_{90} reductions, respectively (Fig.

Table 2. *Total charge carried by potassium currents over one cycle after 2.5 and 32.5 min of pacing*

Time	I_{to}	$I_{Kur,d}$	I_{Kr}	I_{Ks}	I_{K1}	$2I_{NaK}$	I_{stim}	ΣI_K
32.5	14.4	31.9	2.82	0.286	131.4	124.8	−58	1.99
2.5	17.4	46.9	5.52	0.518	138.1	121.8	−58	−28.6
Δ	−3.0	−15.0	−2.7	−0.232	−6.7	3.0	0	30.6

Values are measured in pC/pF. Δ, Difference between 32.5 and 2.5 min; ΣI_K, net K^+ decrease during each cycle; $\Delta\Sigma I_K$, overall change toward ionic stability. Basic cycle length (BCL) was at 300 ms. See text for additional definitions.

Table 3. *Total charge carried by sodium currents over one cycle after 2.5 and 32.5 min of pacing*

Time	I_{Na}	$I_{b,Na}$	$3I_{NaK}$	$3I_{NaCa}$	CT_{NaCl}	ΣI_{Na}
32.5	−54.3	−24.1	187.2	−91.8	17.2	0.2
2.5	−56.1	−24.0	182.6	−118.8	19.4	35.7
Δ	1.8	−0.1	4.6	27.0	−2.2	−35.5

Values are measured in pC/pF at 300 ms BCL. Δ, Difference between 2.5 and 32.5 min; ΣI_{Na}, net Na^+ increase during each cycle; $\Delta\Sigma I_{Na}$, overall change toward ionic stability. See text for additional definitions.

Table 4. *Total charge carried by calcium currents and SR concentrations changes over one cycle after 2.5 and 32.5 min of pacing*

Time	I_{Ca}	$I_{b,Ca}$	$I_{p,Ca}$	$2I_{NaCa}$	I_{up}	$I_{up,leak}$	I_{rel}	ΣI_{Ca}
32.5	−46.3	−59.7	44.4	−61.2	0.584	0.256	3.773	0.4
2.5	−61.3	−59.0	40.4	−79.2	0.517	0.226	3.339	0.7
Δ	15	−0.7	4.0	18	0.067	0.03	0.434	−0.3

Calcium current changes are measured as pC/pF and sarcoplasmic reticulum concentration changes are in mM at 300 ms BCL. Δ, Difference between 2.5 and 32.5 min; ΣI_{Ca}, net Ca^{2+} increase during each cycle; $\Delta\Sigma I_{Ca}$, overall change toward ionic stability.

Table 5. *Total charge carried by chloride currents over one cycle after 2.5 and 32.5 min of pacing*

Time	$I_{Cl,Ca}$	$I_{b,Cl}$	CT_{NaCl}	ΣI_{Cl}
32.5	1.99	−17.0	17.2	2.2
2.5	1.61	−13.7	19.4	7.31
Δ	0.38	−3.3	−2.2	−5.11

Values are measured as pC/pF at 300 ms BCL. Δ, Difference between 2.5 and 32.5 min; ΣI_{Cl}, net Cl^- increase during each cycle; $\Delta\Sigma I_{Cl}$, overall change toward ionic stability.

9*B*). The reduction of APD_{90} was beyond that of the 35-min AP because these effects were augmented in the absence of the APD-preserving $[K^+]_i$ decrease and $[Ca^{2+}]_i$ change. Because $[Ca^{2+}]_i$ is not constant over the AP and changes in Ca^{2+} handling strongly affect the $[Ca^{2+}]_i$ time course, myoplasmic $[Ca^{2+}]_i$ changes (24.7% increase) and changes in SR uptake (13.5% increase) and release (18.1% increase) compartments were also included. APD_{50} was unchanged, whereas APD_{90} was prolonged by 3 ms (3.1% prolongation). Pacing-induced changes in $[Cl^-]_i$ (13.5% increase) did not alter APD. It was thus concluded that pacing-induced increased $[Na^+]_i$ contributes significantly to AP shortening, whereas changes in $[K^+]_i$ and Ca^{2+} handling oppose this effect. This result is consistent with Fig. 7, where the Na^+ stimulus assignment markedly shortened APD relative to the K^+ assignment, because of greater cell intracellular Na^+ loading with Na^+ as the stimulus current and a consequent outward shift in I_{NaCa}.

Contribution of functional current changes to AP reduction. To determine the relative contribution of the pacing-induced $I_{Ca,L}$ decrease to AP shortening, it was first necessary to determine the changes in calcium handling at 32.5 min without the influence of the abbreviated 32.5-min AP waveform. This was accomplished by computing the 32.5-min calcium transient ($[Ca^{2+}]_i$ changes during single AP) with clamping of the 2.5-min AP waveform. $I_{Ca,L}$ underlying the 2.5-min AP with clamping of the modified calcium transient (for $I_{Ca,L}$ only) is shown in Fig. 10*A*. The peak magni-

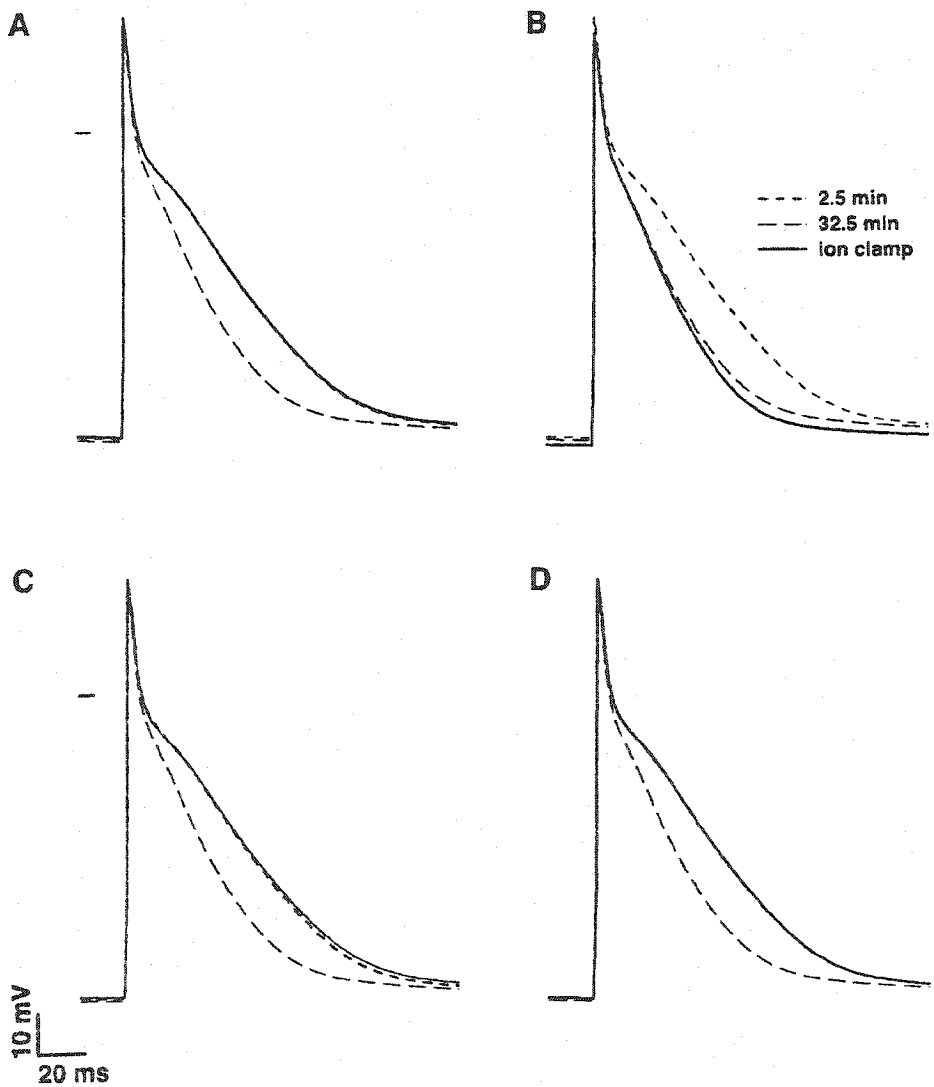

Fig. 9. Effects of rate-related ionic concentration changes on APs. Results were obtained by substituting 32.5-min values for intracellular concentration of each species (K^+ in *A*, Na^+ in *B*, Ca^{2+} in *C*, and Cl^- in *D*) into the equations for the AP at 2.5 min. For Ca^{2+}, 32.5-min Ca^{2+}-handling parameters were also substituted, because intracellular Ca^{2+} during the AP is determined largely by Ca^{2+} handling in the sarcoplasmic reticulum.

tude of the current was slightly reduced due to increased $[Ca^{2+}]_i$-induced inactivation of $I_{Ca,L}$, a mechanism consistent with experimental studies (20, 21). These changes were not sufficient to alter APD_{50} or APD_{90} of the 2.5-min AP (Fig. 11*A*). To determine the relative contribution of I_{NaCa} changes to the pacing-induced AP reduction, the 2.5-min exchanger current was computed with clamping of the modified calcium transient (used for $I_{Ca,L}$ above) and 32.5-min $[Na^+]_i$, both for I_{NaCa} only, producing the current and AP changes illustrated in Figs. 10*B* and 11*B*, respectively. The 2.5-min AP was significantly shortened by the I_{NaCa} changes occurring at 32.5 min, accounting for 83% and 104% of APD_{90} and APD_{50} reduction, respectively. Clearly, I_{NaCa} changes contributed importantly to rate-dependent APD alterations. To determine the relative contribution of the pacing-induced I_{NaK} increase to the corresponding AP reduction (BCL 300 ms), the 2.5-min AP was computed with the 32.5-min values of $[K^+]_i$ and $[Na^+]_i$ clamped for I_{NaK} only. The

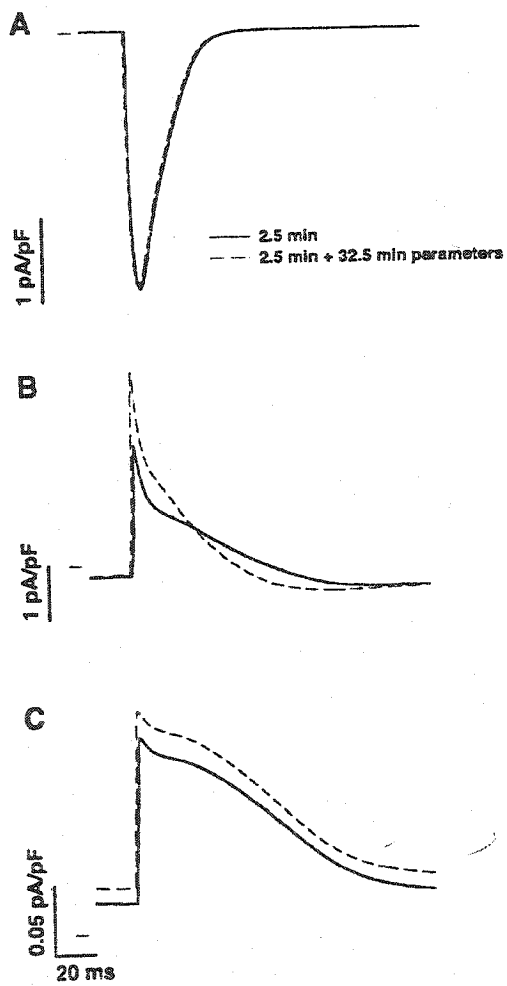

Fig. 10. Effects of current parameters at 32.5 min on current during 2.5 min AP. *A*: $I_{Ca,L}$; *B*: I_{NaCa}; *C*: I_{NaK}. For each current, the defining parameters at 32.5 min were substituted into the 2.5-min AP equations, indicating the effects of pacing-induced parameter changes on current during the AP.

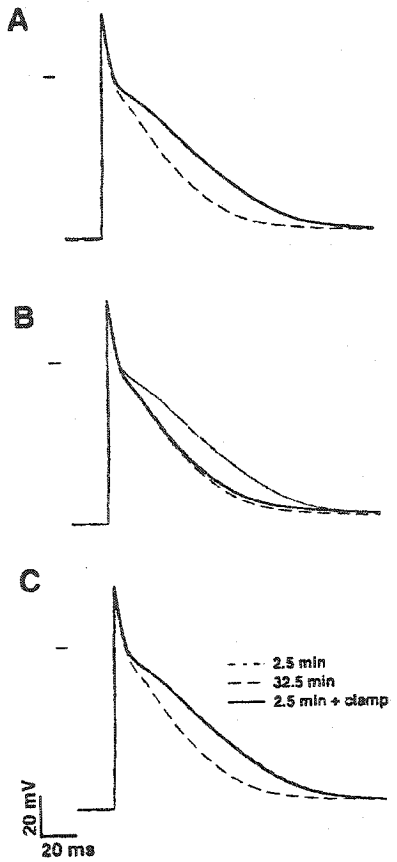

Fig. 11. Effects of pacing-induced changes in each current on the AP. Currents obtained in Fig. 10 were substituted individually into the AP at 2.5 min. *A*: $I_{Ca,L}$ clamp; *B*: I_{NaCa} clamp; *C*: I_{NaK} clamp. Resulting AP indicates the effect that pacing at 32.5 min had on the AP via the current indicated. Results show that I_{NaCa} played the largest role, in itself accounting for most of the rate-related AP changes.

altered I_{NaK} waveform and resulting AP changes are shown in Figs. 10*C* and 11*C*, respectively. APD_{50} of the 2.5-min AP was unchanged, whereas the increased net outward current (also Tables 2 and 3) accounted for 4.2% of APD_{90} reduction. Analysis of other currents showed that they changed minimally between 2.5 and 32.5 min and did not contribute significantly to AP alterations over this interval.

Experimental and Model AP Transients

Experiments were conducted to determine how AP transients in this species-specific dynamic AP model (Figs. 6 and 7) compare with tissue transients. Figure 12 shows experimental results expressed as the mean ± 95% confidence interval (Fig. 12, *A* and *B*). Representative APs from the 0–5 and 30–35 min recording intervals during pacing at BCL 300 ms are also shown (Fig. 12*C*). Mean APD and maximum diastolic potentials were within the standard ranges for canine atrial APs established by Wang et al. (33). Over the 35-min pacing interval, mean reductions of 10.3 and 12.8 ms were observed for APD_{90} and APD_{50}, respectively, with 79% and 75% of the change occurred dur-

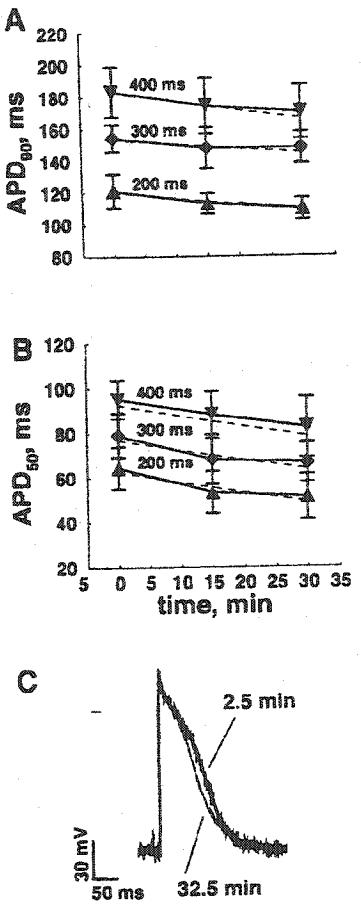

Fig. 12. Pacing-induced experimental AP transients. APD_{90} (*A*) and APD_{50} (*B*) reductions are shown with representative APs (300 ms BCL) from the midpoint of 0–5 and 30–35 min pacing intervals (*C*). Marker at *left* indicates −20 mV.

ing the initial 15 min. APD_{90} and APD_{50} decreased exponentially at all pacing BCLs ($P < 0.001$), suggesting that reductions were tending toward steady state. Time constants ranged from 150 to 600 min, and regression results are plotted as dashed lines along with the data in Fig. 12. Compared with these experimental data, model transients (Figs. 6 and 7) were initially more extensive but approached steady state faster than their experimental counterparts. Overall, model (Fig. 6) and experimental transients were of a comparable order when the model stimulus assignment was attributed to K^+, but model transients were quantitatively larger.

DISCUSSION

We have shown that dynamic models with unstable fixed points may stabilize, provided complete homeostatic mechanisms for all ionic species are present, including the stimulus charge. Model stability depended on the assignment of the stimulus current, and K^+ stimulus assignment produced the smallest perturbations in the equilibrium of all ionic species. Model AP transients agreed qualitatively with experiments, and therefore were not appreciably influenced by potential model artifacts due to unstable fixed points. AP reduction was due to changes in the Na^+/Ca^{2+} exchanger function related to accumulation of intracellular Na^+. APD reduction was opposed by transient changes in $[K^+]_i$ and $[Ca^{2+}]_i$.

Comparison With Previous Cardiac Models

The 1985 version of the DN model was the first to explicitly include concentration changes (5). Consequently, the DN equations became unstable because pacing gave rise to progressive changes in intracellular ionic concentrations. Varghese and Sell (32) later showed that model equations possess a hidden conservation principle, and Guan et al. (9) showed that dynamic model equations are singular. These findings provided a theoretical basis for the equation instabilities, because these mathematical features imply that model fixed points are inherently unstable.

Ionic drift is a common property of ionic models based on the original DN formulation scheme (5). Similar models include the human atrial myocyte models by Nygren et al. (26) and Courtemanche et al. (3), rabbit atrial myocyte model by Lindblad et al. (18), rabbit sinoatrial node model by Demir et al. (4), the ventricular myocyte models of Nordin (25) and the phase II Luo and Rudy (LR2) model (19), and the bullfrog atrial myocyte model by Rasmusson et al. (29). Models by Jafri et al. (10) and Winslow et al. (37) are also similar because they represent the Luo and Rudy equations with modified subcellular Ca^{2+} handling.

None of these earlier models monitored $[Cl^-]_i$. Lindblad et al. (18) included a formulation for $I_{b,Cl}$, but $[Cl^-]_i$ was held constant such that Cl^- fluxes did not disturb the ionic equilibrium. Nygren et al. (26) added a small electroneutral flux of Na^+ to achieve long-term ionic homeostasis. It was suggested that this flux could be accounted for by a cotransport system with Cl^- similar to the one implemented in the present study; however, these mechanisms were not modeled. Because these other models account for only $[K^+]_i$, $[Na^+]_i$, and $[Ca^{2+}]_i$, ionic equilibrium may theoretically be attained by I_{NaK} and I_{NaCa}. Rather than fixing $[Cl^-]_i$, we chose to provide for $[Cl^-]_i$ equilibrium by formulating an empirical model of Cl^- transport based on physiological mechanisms. This allowed changes in $I_{Cl,Ca}$ to influence the ionic transients.

Transients in these earlier models were qualitatively similar to those of the mRNC model. In the model by Lindblad et al. (18), a small increase in $[Na^+]_i$ was noted over each pacing cycle, and a slow downward drift of $[Na^+]_i$ followed the termination of pacing. Rasmusson et al. (29) reported that $[Na^+]_i$ decreased over 2 min in the absence of stimulation. $[Na^+]_i$ increased and $[K^+]_i$ decreased over 40 s of pacing, and the magnitude of the transients was greater at faster rates. In the LR2 model, $[K^+]_i$ was reported to decrease, whereas $[Ca^{2+}]_i$ and $[Na^+]_i$ increased during 60 s of pacing at 2 Hz (19). The transients were used to illustrate the redistribution of ions that may result from

overdrive and cause suppression of pacemaker cells. In the model by Courtemanche et al. (3), it was noted that the ionic balance was disturbed by periodic stimulation and that slow changes in intracellular ionic concentrations still persisted after several minutes. Initial transients were attributed to kinetic rate adaptation of the currents and dissipated over a few seconds. The small subsequent slow changes in ionic concentrations resulted in slow changes in the shape of the AP. To ensure that the AP morphology took into account kinetic adaptation at the specified frequency but did not include the effects of concentration changes, simulation results were presented after 12 s of pacing from rest. Similarly, Demir et al. (4) showed results after simulation of at least eight cycles. To avoid the effects of concentration changes on model results, Nygren et al. (26) added a small electroneutral inward flux of Na^+ (discussed above), and Dokos et al. (6) modified the maximum I_{NaK} and time constant for uptake of intracellular calcium of the original DN equations.

In the model by Nordin (25), $[Na^+]_i$ was monitored over 50 min of sustained pacing. Pacing was initiated at 1 Hz for 10 min and was then increased without interruption to 2 and 4 Hz for 10 min at each rate. $[Na^+]_i$ markedly increased and then began to plateau during each interval. At 30 min, pacing was slowed to 2 Hz and then 1 Hz for 10 min at each rate. $[Na^+]_i$ decreased along an exponential time course as the stimulus rate was slowed and returned to baseline after stimulation was stopped. The Nordin model also generated a fourfold increase in the size of myoplasmic $[Ca^{2+}]_i$ transients as the stimulation rate increased and diastolic $[Ca^{2+}]_i$ more than doubled. The role of the ionic transients on AP shortening was also studied. As in the mRNC model, $[Na^+]_i$-independent AP shortening over several minutes of stimulation at rapid rates was caused in part by a reduction of Ca^{2+} current secondary to increased myoplasmic $[Ca^{2+}]_i$ (25). AP shortening was largely caused by an outward shift of I_{NaCa} as $[Na^+]_i$ increased (25).

Comparison With Experimental Findings

The models discussed above displayed transients that agree qualitatively with previous experimental observations. Increased rate has been shown to result in a transient loss of $[K^+]_i$ in isolated preparations of cardiac tissue (11, 13) from whole heart preparations in vitro (7) and from heart in vivo (27). Kline et al. (11) also reported that membrane potential became more negative, reflecting increased Na^+-K^+ pump activity as predicted by the mRNC model (Table 2). Using K^+ selective electrodes in canine Purkinje fibers, Kline et al. (11) measured an extracellular K^+ concentration ($[K^+]_o$) displacement of 0.5 mM and return to baseline after ~5 min. With similar techniques, Kunze (12) measured a $[K^+]_o$ transient change of ~0.95 mM over 12 min (BCL 300 ms) in rabbit atria. In the frog ventricle, reversals were reported to occur over ~17–60 min depending on type of tissue preparation (13). These data and the time course of $[K^+]_i$ changes in the mRNC model (Figs. 3 and 8) were of the same order. Pacing-induced increases in $[Na^+]_i$ and $[Ca^{2+}]_i$ have been measured experimentally (14, 15), and rate-dependent increases in $[Ca^{2+}]_i$ have been observed (31). Transient increases in $[Na^+]_i$ were recognized to be closely related to $[K^+]_i$ changes (11, 12, 14); however, $[Na^+]_i$ was not quantified in these studies. Measurement of pacing-related $[Ca^{2+}]_i$ increases in canine atria (31) expressed $[Ca^{2+}]_i$ as a fluorometric ratio ($R_{400/500}$), preventing quantified comparison with the model. APD decreases were measured over 3 h (38) and 4 h (2) of pacing in the atria of Langendorff-perfused rabbit hearts. APD was shortened by 14–17 ms after 4 h of pacing (BCL 333 ms) (2). Consistent with the AP transients measured in the present study, no steady-state AP was reached in either case. Although APs recorded from intact tissue may not be directly comparable to models formulated to represent single cells, tissue preparations are advantageous because single isolated cell action potentials are difficult to maintain in stable conditions for prolonged periods because of deterioration in cell viability, and because the enzymes needed to isolate cells damage ionic currents. As such, tissue level experiments may provide a more reliable physiological comparison for long-term model performance. Although modifications to artificially stabilize model concentrations (6, 26) demonstrate that the overall model formulation is such that equilibrium can be reasonably maintained, the results of the present study suggest that such changes may not be appropriate.

Stimulus Current Assignment

None of the models discussed indicate that the stimulus current was assigned to an ionic species, the balance of which is explicitly included in the model. This is also true of the Courtemanche model (as noted) published by our laboratory (3). Results of the present study indicate that assignment of the stimulus current is necessary for model stability and that the choice of the stimulus charge-carrying ion affects the magnitude of the transients.

There is no experimental evidence on which to allocate the stimulus current carrier for model simulations. The most likely charge carriers are K^+ and Na^+, which are the cations that are by far the most concentrated in the intracellular and extracellular compartments, respectively. The resting ionic concentrations in the heart favor Na^+ as an inward current carrier. However, during impulse propagation, cell-to-cell coupling is effected by pore-forming gap junctions, which are highly permeable to intracellular cations. Because K^+ is by far the most concentrated mobile intracellular ionic species, it is likely that K^+ movement plays an important role in excitatory cell-to-cell transmission. In addition, when a portion of the membrane is depolarized, the adjacent membrane may respond by depolarization via local movement of subsarcolemmal K^+. The results with Na^+ as the charge carrier (Fig. 7) resulted in unphysiologically short action potentials, because Na^+ loading during activity favored reverse-

mode outward I_{NaCa} (Figs. 9–11). Because attributing the stimulus current to K^+ reproduced experimental observations of $[K^+]_i$ changes (Fig. 2), because the K^+ assignment best preserved the intracellular ionic equilibrium (Fig. 2), and because AP transients were most physiological for the K^+ stimulus carrier (Fig. 6), K^+ stimulus attribution was the preferred assignment. Assignment of stimulus to an ionic species is necessary for stability. Physiologically, the stimulus current may actually be carried by more than one ionic species; however, in the absence of knowledge about the relative participation of different ionic species, it is reasonable and practical to attribute stimulus current to a single ionic species for long-term simulations. It is possible that lack of stability in related models may be corrected by the appropriate stimulus current assignment.

Novel Aspects and Potential Significance

The present study demonstrated that: *1*) tissue and model transients are of the same order; *2*) any distortion arising from dynamic model equation instabilities is not likely to be major; *3*) dynamic models may reach absolute stability during sustained pacing, provided they contain complete homeostatic mechanisms for all ionic species; *4*) assignment of the stimulus current contributes importantly to model stability during maintained activity; *5*) K^+ is likely the most appropriate stimulus current assignment; and *6*) slow rate-related APD changes are likely related to intracellular Na^+ accumulation and outward I_{NaCa} augmentation. To our knowledge, our study is the first to examine systematically long-term time-related ionic and AP transients in a DN-type AP model. Our results suggest that model equations formulated to reproduce short-term electrophysiological behavior may also reproduce longer-term changes in myocyte electrophysiology.

Sustained rapid pacing is known to induce electrophysiological remodeling, mimicking chronic atrial fibrillation (AF) (22, 35). Tachycardia-induced remodeling shortens APD and abolishes AP rate adaptation, thereby enhancing atrial arrhythmogenicity ("AF begets AF") (35, 36). In atrial myocytes of dogs atrially paced at 400 beats/min for 6 wk, Yue et al. (40) found that the densities of I_{Ca} and I_{to} were progressively decreased by 69 and 65%, respectively, as a result of downregulation of mRNA encoding I_{Ca} and I_{to} α-subunits (41). The most extensive remodeling occurred early and gradually attenuated toward the end of the pacing period. In contrast, no remodeling of I_{Kr}, I_{Ks}, I_{K1}, $I_{Kur,d}$, or $I_{Cl,Ca}$ was found. The present study provides insights into the functional events following the onset of rapid pacing. Results here indicate that ionic transients cause short-term APD reductions (over 30 min) that precede remodeling per se. These functional changes may contribute to early AF-promoting effects of atrial tachycardia (23).

Potential Limitations

Both the model simulations and experimental observations showed time-dependent decreases in APD over 15–30 min of observation. However, there were quantitative differences between experimental observations (Fig. 12) and model simulations (Fig. 6), with changes being larger and faster in the model. In addition, model APDs were somewhat shorter than experimental values. A number of factors may have contributed to these discrepancies.

Agreement between model and experiment was theoretically limited. The explicit form of the conservation principle (*Eq. 5*) includes a constant of integration, C_0. The physical significance of C_0 may be understood by recognizing that the conservation principle is Faraday's principle

$$V = \frac{\Delta Q}{C_m}, \Delta Q = \Sigma Q_o - \Sigma Q_i$$

where Q_0 is extracellular charge and Q_i is intracellular charge rewritten in terms of ionic concentration. Here, Q_o is fixed, and ΣQ_i changes throughout the cardiac cycle. Although the model accounts for the concentrations of the ionic species predominantly responsible for the AP, other ionic species (e.g., HCO_3^-, SO_4^{2-}, PO_4^{3-}, and Mg^{2+}) are found within the cardiac myocyte as well as extracellularly. C_0 contains the combined effect of additional ionic species and may be expressed as

$$C_0 = \frac{(\Sigma Q_0^{\text{unknown}} - \Sigma Q_i^{\text{unknown}})}{C_m} \quad (12)$$

where Q_0 and Q_i indicate extracellular and intracellular charge, respectively. The presence of these additional ionic species in physiological systems necessarily implies discrepancies with model results.

It was recognized, as discussed above, that experimental AP recordings were made from a tissue syncytium, whereas the model represents an isolated cell. The role of one-dimensional propagation effects was investigated by modifying *Eq. 1* to obtain the reaction-diffusion system

$$\frac{dV}{dt} = \frac{-(I_{ion} + I_{stim})}{C_m} + D\nabla^2 V \quad (13)$$

in time and one space dimension, where $D = 0.001$ cm^2/ms and ∇^2 is the second-derivative Laplacian operator in space.

The finite difference equation resulting from *Eq. 13* is

$$V_j^{n+1} = V_j^n - \Delta t \frac{(I_{ion} + I_{stim} + I_{couple})}{C_m} \quad (14)$$

where V_j^n is the voltage at time step n and location j. Δt and Δx are the time and space discretization steps fixed at 5 μs and 0.025 cm, respectively. I_{couple} is the coupling current between adjacent cells with a 3-point central difference approximation to the Laplacian given by

$$I_{couple} = -D\frac{C_m}{\Delta x^2}(V^n_{j+1} - 2V^n_j + V^n_{j-1}) \qquad (15)$$

Preliminary cable simulations with I_{couple} attributed to K^+ revealed that transients were augmented in coupled segments, and that the net charge carried by I_{couple} was nearly 30 times less than I_{stim}. The finding that reduced net stimulus current augmented the ionic transients is consistent with the exaggerated transients observed in the single cell when the stimulus current was not assigned (Fig. 2). Although it may have been meaningful to study model stability and fully characterize model transients in the context of propagation, this was not done for reasons of computational tractability. Wall time required to pace a 50-cell cable for 1 h was on the order of weeks, and simulations of this type may not be parallelized. It would be expected that transients in a propagated model would also reach absolute stability, although substantially more time would likely be required in a distributed system.

We assumed that extracellular ionic concentrations were constant. This is a reasonable assumption for isolated cells. However, the type of experimental preparation may influence ionic transients (13), and in a multicellular preparation ion accumulation/depletion phenomena can occur and contribute to rate-related changes. Also, biochemical and molecular changes may occur in vivo that are not reproduced in the purely ionic mathematical model. Finally, the experimental recording method also includes potential artifacts, including possible tissue ischemia during perfusion with crystalloid solutions that have limited oxygen-carrying capacity and tissue damage during isolation and experimental preparation.

The authors thank Wei Han and Drs. Hui Sun and Danshi Li for assistance with the experimental preparations.

This research was funded by grants from the Canadian Institutes of Health Research (CIHR), the Mathematics of Information Technology and Complex Systems (MITACS) Network of Centers of Excellence, a CIHR MD, PhD Studentship (to J. Kneller), and the Merck Pharmacology Fellowship Program.

REFERENCES

1. **Baumgarten CM and Duncan SWN.** Regulation of Cl^- activity in ventricular muscle: Cl^-/HCO_3^- exchange and Na^+-dependent Cl^- cotransport. In: *Heart Function and Metabolism*, edited by Dhalla NS. Boston, MA: Nijhoff, 1987, p. 117–131.
2. **Costard-Jackle A, Goetsch B, Antz M, and Franz MR.** Slow and long-lasting modulation of myocardial repolarization produced by ectopic activation in isolated rabbit hearts. Evidence for cardiac "memory." *Circulation* 80: 1412–1420, 1989.
3. **Courtemanche M, Ramirez RJ, and Nattel S.** Ionic mechanisms underlying human atrial action potential properties: insights from a mathematical model. *Am J Physiol Heart Circ Physiol* 275: H301–H321, 1998.
4. **Demir SS, Clark JW, Murphey CR, and Giles WR.** A mathematical model of a rabbit sinoatrial node cell. *Am J Physiol Cell Physiol* 266: C832–C852, 1994.
5. **DiFrancesco D and Noble D.** A model of cardiac electrical activity incorporating ionic pumps and concentration changes. *Philos Trans R Soc Lond B Biol Sci* 307: 353–398, 1985.
6. **Dokos S, Celler BG, and Lovell NH.** Modification of DiFrancesco-Noble equations to simulate the effects of vagal stimulation on in vivo mammalian sinoatrial node electrical activity. *Ann Biomed Eng* 21: 321–335, 1993.
7. **Gilmore JP and Gerlings ED.** Influence of interstimulus interval on myocardial potassium balance. *Am J Physiol* 217: 136–141, 1969.
8. **Glantz SA and Slinker BK.** Nonlinear regression. In: *Primer of Applied Regression and Analysis of Variance*. New York: McGraw Hill, 1990, p. 464–468.
9. **Guan S, Lu Q, and Huang K.** A discussion about the DiFrancesco-Noble model. *J Theor Biol* 189: 27–32, 1997.
10. **Jafri MS, Rice J, and Winslow RL.** Cardiac Ca^{2+} dynamics: the roles of ryanodine receptor adaptation and sarcoplasmic reticulum load. *Biophys J* 74: 1149–1168, 1998.
11. **Kline RP, Cohen I, Falk R, and Kupersmith J.** Activity-dependent extracellular K^+ fluctuations in canine Purkinje fibres. *Nature* 286: 68–71, 1980.
12. **Kunze DL.** Rate-dependent changes in extracellular potassium in the rabbit atrium. *Circ Res* 41: 122–127, 1977.
13. **Lamb JF and McGuigan JA.** Potassium fluxes in quiescent and beating frog ventricle. *Nature* 205: 1115–1116, 1965.
14. **Langer GA.** Ion fluxes in cardiac excitation and contraction and their relation to myocardial contractility. *Physiol Rev* 48: 708–755, 1968.
15. **Langer GA.** Sodium exchange in dog ventricular muscle. Relation to frequency of contraction and its possible role in the control of myocardial contractility. *J Gen Physiol* 50: 1221–1239, 1967.
16. **Li D, Melnyk P, Feng J, Wang Z, Petrecca K, Shrier A, and Nattel S.** The effects of experimental heart failure on atrial cellular and ionic electrophysiology. *Circulation* 101: 2631–2638, 2000.
17. **Li D, Zhang L, Kneller J, and Nattel S.** Potential ionic mechanism for repolarization differences between canine left and right atrium. *Circ Res* 88: 1168–1175, 2001.
18. **Lindblad DS, Murphey CR, Clark JW, and Giles WR.** A model of the action potential and underlying membrane currents in a rabbit atrial cell. *Am J Physiol Heart Circ Physiol* 271: H1666–H1696, 1996.
19. **Luo CH and Rudy Y.** A dynamic model of the cardiac ventricular action potential. II. Afterdepolarizations, triggered activity, and potentiation. *Circ Res* 74: 1097–1113, 1994.
20. **Mentrard DG, Vassort G, and Fischmeister R.** Calcium-mediated inactivation of the calcium conductance in caesium-loaded frog heart cells. *J Gen Physiol* 83: 105–131, 1984.
21. **Mitchell MR, Powel T, Terrar DA, and Twist VW.** Influence of a change in stimulation rate on action potentials, currents and contractions in rat ventricular cells. *J Physiol (Lond)* 364: 113–130, 1985.
22. **Morillo CA, Klein GJ, Jones DL, and Guiraudon CM.** Chronic rapid atrial pacing. Structural, functional, and electrophysiological characteristics of a new model of sustained atrial fibrillation. *Circulation* 91: 1588–1595, 1995.
23. **Nattel S.** Atrial electrophysiological remodeling caused by rapid atrial activation: underlying mechanisms and clinical relevance to atrial fibrillation. *Cardiovasc Res* 42: 298–308, 1999.
24. **Nattel S.** Relationship between use-dependent effects of antiarrhythmic drugs on conduction and V_{max} in canine cardiac Purkinje fibres. *J Pharmacol Exp Ther* 241: 282–288, 1987.
25. **Nordin C.** Computer model of membrane current and intracellular Ca^{2+} flux in the isolated guinea pig ventricular myocyte. *Am J Physiol Heart Circ Physiol* 265: H2117–H2136, 1993.
26. **Nygren A, Fiset C, Firek L, Clark JW, Lindblad DS, Clark RB, and Giles WR.** Mathematical model of an adult human atrial cell: the role of K^+ currents in repolarization. *Circ Res* 82: 63–81, 1998.
27. **Parker JO, Chiong MA, West RO, and Case RB.** The effect of ischemia and alterations of heart rate on myocardial potassium balance in man. *Circulation* 42: 205–217, 1970.
28. **Ramirez RJ, Nattel S, and Courtemanche M.** Mathematical analysis of canine atrial action potentials: rate, regional factors, and electrical remodeling. *Am J Physiol Heart Circ Physiol* 279: H1767–H1785, 2000.
29. **Rasmusson RL, Clark JW, Giles WR, Robinson K, Clark RB, Shibata EF, and Campbell DL.** A mathematical model of

electrophysiological activity in a bullfrog atrial cell. *Am J Physiol Heart Circ Physiol* 259: H270–H389, 1990.
30. **Spach MS, Miller WT III, Geselowitz DB, Barr RC, Kootsey JM, and Johnson EA.** The discontinuous nature of propagation in normal canine cardiac muscle. Evidence for recurrent discontinuities of intracellular resistance that affect the membrane currents. *Circ Res* 48: 39–54, 1981.
31. **Sun H, Chartier D, Leblanc N, and Nattel S.** Intracellular calcium changes and tachycardia-induced contractile dysfunction in canine atrial myocytes. *Cardiovasc Res* 49: 751–761, 2001.
32. **Varghese A and Sell GR.** A conservation principle and its effect on the formulation of Na-Ca exchanger current in cardiac cells. *J Theor Biol* 189: 33–40, 1997.
33. **Wang ZG, Pelletier LC, Talajic M, and Nattel S.** Effects of flecainide and quinidine on human atrial action potentials. Role of rate-dependence and comparison with guinea pig, rabbit, and dog tissues. *Circulation* 82: 274–283, 1990.
34. **White CW, Marcus ML, and Abboud FM.** Distribution of coronary artery flow to the canine right atrium and sinoatrial node. *Circ Res* 40: 342–347, 1977.
35. **Wijffels MC, Kirchhof CJ, Dorland R, and Allessie MA.** Atrial fibrillation begets atrial fibrillation. A study in awake and chronically instrumented goats. *Circulation* 92: 1954–1968, 1995.
36. **Wijffels MC, Kirchhof CJ, Dorland R, Power J, and Allessie MA.** Electrical remodeling due to atrial fibrillation in chronically instrumented conscious goats: roles of neurohumoral changes, ischemia, atrial stretch, and high rate of electrical activation. *Circulation* 96: 3710–3720, 1997.
37. **Winslow RL, Rice J, Jafri S, Marban E, and O'Rourke B.** Mechanisms of altered excitation-contraction coupling in canine tachycardia-induced hear failure. II. model studies. *Circ Res* 84: 571–586, 1999.
38. **Wood MA, Mangano RA, Schieken RM, Baumgarten CM, Simpson PM, and Ellenbogen KA.** Modulation of atrial repolarization by site of pacing in the isolated rabbit heart. *Circulation* 94: 1465–1470, 1996.
39. **Woodbury JW and Crill WE.** On the problem of impulse conduction in the atrium. In: *Nervous Inhibition*, edited by Florey E. New York: Pergamon, 1961, p. 124–135.
40. **Yue L, Feng J, Gaspo R, Li G, Wang Z, and Nattel S.** Ionic remodeling underlying action potential changes in a canine model of atrial fibrillation. *Circ Res* 81: 512–525, 1997.
41. **Yue L, Melnyk P, Gaspo R, Wang Z, and Nattel S.** Molecular mechanisms underlying ionic remodeling in a dog model of atrial fibrillation. *Circ Res* 84: 766–784, 1999.

CHAPTER 3 REMODELING OF CA2+-HANDLING BY ATRIAL TACHYCARDIA: EVIDENCE FOR A ROLE IN LOSS OF RATE-ADAPTATION.

As discussed in Section 1.5.2, rapid atrial pacing induces a remodeling process in atrial myocytes and tissues, as occurs in chronic AF. In canine atria, 42 days of pacing at 400/min results in AP shortening and totally abolished AP rate adaptation (148). Sarcolemmal changes include 69% and 65% reduction of I_{Ca} and I_{to}, respectively (148), and subsarcolemmal Ca^{2+}-handling is also impaired (152). Given the prominent role of I_{Ca} in determining AP duration and rate adaptation, and the role of the intracellular Ca^{2+} transient in the inactivation of I_{Ca}, both sarcolemmal and subsarcolemmal changes could contribute significantly to the pathologic changes in the AP. In the original Ramirez paper (42), sarcolemmal changes alone were found to be inadequate to explain the loss of APD rate-adaptation caused by atrial tachycardia-remodeling. This study, entitled "Remodeling of Ca^{2+}-handling by atrial tachycardia: evidence for a role in loss of rate-adaptation", used a mathematical modeling approach to investigate the relative contributions of sarcolemmal and intracellular remodeling to the AP alterations, with the notion that alterations in intracellular Ca^{2+} handling might contribute significantly.

ELSEVIER

Cardiovascular Research 54 (2002) 416–426

Cardiovascular Research

www.elsevier.com/locate/cardiores

Remodeling of Ca^{2+}-handling by atrial tachycardia: evidence for a role in loss of rate-adaptation

James Kneller[1], Hui Sun[1], Normand Leblanc, Stanley Nattel*

Departments of Medicine and Physiology, Research Center, Montreal Heart Institute, University of Montreal, and Department of Pharmacology, McGill University, 5000 Belanger Street East, Montreal, Quebec, Canada H1T 1C8

Received 15 August 2001; accepted 21 January 2002

Abstract

Background: Loss of rate-dependent action potential (AP) duration (APD) adaptation is a characteristic feature of atrial tachycardia-induced remodeling (ATR). ATR causes sarcolemmal ion-channel remodeling (ICR) and changes in Ca^{2+}-handling. The present studies were designed to quantify Ca^{2+}-handling changes and then to apply a mathematical AP model to assess the contributions of Ca^{2+}-handling abnormalities and ICR to loss of APD rate-adaptation. **Methods:** Indo-1 fluorescence was used to measure intracellular Ca^{2}-transients and whole-cell patch-clamp to record APs in atrial myocytes from control dogs and dogs subjected to atrial pacing at 400/min for 6 weeks. A previously developed ionic model of the canine atrial AP was modified to reproduce measured Ca^{2+}-transients of control and ATR myocytes. **Results:** In control, APD to 95% repolarization (APD_{95}) decreased by 91 ms experimentally and by 88 ms in the model over the 1–6 Hz range. In ATR myocytes, APD_{95} failed to decrease over the 1–6 Hz range. Ca^{2+}-handling abnormalities in ATR myocytes included slowed upstroke, decreased amplitude and strong single-beat post-rest potentiation. Unaltered Ca^{2+}-handling properties included caffeine-releasable Ca^{2+}-stores and Ca^{2+}-transient relaxation before and after exposure to the sarcoplasmic reticulum Ca^{2+}-ATPase (SERCA) inhibitor cyclopiazonic acid (CPA). Including ICR alone in the model accounted for loss of APD_{50} rate-adaptation; however, KR alone reduced APD_{95} rate-adaptation by only 19% to 71 ms. When both ICR and Ca^{2+}-handling changes were incorporated, APD_{95} rate-adaptation decreased to 6 ms, accounting for experimental observations. **Conclusion:** ICR alone does not fully account for loss of APD rate-adaptation with atrial remodeling: Ca^{2+}-handling changes appear to contribute to this clinically significant phenomenon.

Keywords: Arrhythmia (mechanisms); Calcium (cellular); Remodeling; SR (function); Supraventr. arrhythmia

1. Introduction

Atrial fibrillation (AF) is the most common arrhythmia in clinical practice [1]. Investigators have recently developed realistic animal models of AF related to the phenomenon of atrial tachycardia-induced remodeling, by which 'AF begets AF' [2,3]. Remodeling plays an important role in the pathophysiology of AF [4]. Loss of APD and refractoriness rate-adaptation are among the most universally recognized functional changes caused by atrial tachycardia-induced remodeling (ATR) [2–6].

Chronic tachypacing induces specific ion channel remodeling (ICR). L-type Ca^{2+} current ($I_{Ca,L}$) and transient outward current (I_{to}) are down-regulated by rapid pacing, with other plateau currents remaining unaltered [7–9]. Inhibition of $I_{Ca,L}$ with nifedipine reproduces the AP-shortening and loss of rate-adaptation caused by remodeling [7]; however, the concentration of nifedipine used (10 μM) reduces $I_{Ca,L}$ by over 90%, whereas atrial tachycardia decreases $I_{Ca,L}$ by about 69% [7]. The intracellular Ca^{2+}-transient, resulting from sarcolemmal Ca^{2+} entry and Ca^{2+}-triggered Ca^{2+}-release from the sarcoplasmic reticulum (SR), is also reduced in atrial myocytes of rapidly-paced dogs [10], and there is experimental evidence that tachycardia-induced changes in Ca^{2+}-handling contribute

*Corresponding author. Tel.: +1-514-376-3330x3990; fax: +1-514-376-1355.

E-mail address: nattel@icm.umontreal.ca (S. Nattel).

[1]Both authors contributed equally.

Time for primary review 36 days.

0008-6363/02/$ – see front matter
PII: S0008-6363(02)00274-2

to AP abnormalities [11]. We recently developed an ionically based mathematical model of the canine atrial AP and found that pacing-induced ICR fails to account fully for the loss of rate-adaptation produced by remodeling [12]. The Ca^{2+}-handling properties of the latter model, which we will refer to as the Ramirez–Nattel–Courtemanche (RNC) model, were based on data from the literature, rather than direct measurements. The failure of ICR to reproduce lack of rate-adaptation in the RNC model may have been due to inaccuracies in the Ca^{2+}-handling representation, to the lack of a representation of tachycardia-induced Ca^{2+}-handling abnormalities, or to other missing elements. The present study was designed to obtain data with which atrial Ca^{2+}-handling could be more precisely defined, to modify the RNC model to reproduce experimental Ca^{2+}-transients, and to evaluate the role of tachycardia-induced ICR and changed cellular Ca^{2+}-handling in APD rate-maladaptation.

2. Methods

2.1. Animal model, cell isolation and solutions

Animal-handling procedures followed guidelines of the Canadian Council on Animal Care and conformed with the *Guide for the Care and Use of Laboratory Animals* published by the US National Institutes of Health (NIH Publication No. 85-23, revised 1996). Under sterile conditions, a tined pacemaker lead was inserted in the right atrial appendage, connected to a pacemaker in a subcutaneous pocket in the neck and used to pace the atria at 400/min for 6 weeks to produce ATR [7]. On study days, dogs were anesthetized with 30 mg/kg pentobarbital i.v., the heart removed via right lateral thoracotomy and left atrial myocytes isolated from six control and six paced dogs as previously described [7,10]. Cells were superfused with Tyrode's solution containing (mM) NaCl 136, KCl 5.4, $MgCl_2$ 1.0, $CaCl_2$ 1.8, NaH_2PO_4 0.33, glucose 10, and HEPES 10, pH adjusted to 7.4 with NaOH at 36 °C. APs were recorded in current-clamp mode [7].

2.2. Recording of intracellular Ca^{2+}-transients

Myocytes were incubated in indo-1 acetoxymethyl ester (Molecular Probes, 5 μM) for 10–12 min in 100 μM Ca^{2+}-containing Tyrode's solution at room temperature. Myocytes were then superfused with Indo-free solution for >40 min to wash out extracellular indicator and allow for intracellular deesterification. Background and cell autofluorescence were cancelled by zeroing the output of the photomultiplier tubes using cells without indo-1 loading. Cell exposure to ultraviolet light from a mercury-arc lamp was controlled by an electronic shutter (Optikon T132, Vincent Associates) between the arc lamp and epifluorescence attachment of a Nikon Diaphot epifluorescence microscope. Only a portion of the cell (~15 μm diameter) was exposed to UV light. The dye was excited at 340 nm and the emitted fluorescent light (>380 nm) was relayed to the microscope and processed by a spectral microfluorometer (Sycamore Scientific) equipped with a charge-coupled camera (Pulnix America TM-440). The emitted light was split by dichroic mirrors and passed through narrow band-pass (±10 nm) filters centered at 400 and 500 nm. Light intensity was detected with matched photomultiplier tubes (Hamamatsu R2560HA). The ratio of the two fluorescent signals (400/500 nm) was filtered at 60 Hz and digitized at 1 kHz (TL-1-125 LabMaster, Axon). In this study, Indo-1 ratios were converted to Ca^{2+} concentrations ($[Ca^{2+}]_i$) by performing an in vivo calibration using the following relationship [13]:

$$[Ca]_i = K_d \cdot \beta \left[\frac{R - R_{min}}{R_{max} - R} \right] \quad (1)$$

where K_d (844 nM) is the in vivo dissociation constant of Indo-1 [14]. R_{min} and R_{max} are, respectively, the minimum and maximum Indo-1 ratios determined by exposing atrial myocytes to a Tyrode's solution containing 100 nM ionomycin, and either 10 mM EGTA (no added Ca^{2+}) or 5 mM Ca^{2+} (saturating Ca solution), and F_0/F_s is the ratio of the maximum to minimum fluorescent intensities measured at 500 nm. In five myocytes, $R_{min} = 0.755$, $R_{max} = 2.933$, and $F_0/F_s = 1.452$.

A 1-min rest period separated episodes of field stimulation and Ca^{2+}-transient recording. In some experiments, Ca^{2+}-transients were induced by applying 10 mM caffeine with a temperature-controlled fast-flow system after stopping stimulation at 2 Hz following the attainment of steady state. Only one cell was studied for each cell aliquot added to the bath. In other experiments, Ca^{2+}-transients were studied before and after the addition of 100 μM cyclopiazonic acid (CPA) to inhibit SR Ca^{2+}-ATPase.

2.3. Model development and implementation

Ionic currents were modeled as detailed in Ramirez et al. [12]. The time-derivative of the membrane potential (V) is given by:

$$\frac{dV}{dt} = \frac{-(I_{ion} + I_{stim})}{C_m} \quad (2)$$

where I_{ion} and I_{stim} are transmembrane total ionic and stimulus currents, respectively, and C_m is membrane capacitance.

$$I_{ion} = I_{Na} + I_{K1} + I_{to} + I_{Kur,d} + I_{Kr} + I_{Ks} + I_{Ca} + I_{Cl,Ca} + I_{p,Ca} + I_{NaCa} + I_{NaK} + I_{b,Na} + I_{b,Ca} + I_{b,Cl} \quad (3)$$

where I_{Na}, I_{K1}, $I_{Kur,d}$, I_{Kr}, I_{Ks}, I_{Ca} are sodium, inward-rectifier, ultra-rapid delayed rectifier, rapid and slow delayed-rectifier and Ca^{2+} currents, respectively, $I_{p,Ca}$ is sarcolemmal calcium pump, I_{NaK} is sodium–potassium

pump, I_{NaCa} is sodium–calcium exchanger, $I_{Cl,Ca}$ is calcium-activated chloride, $I_{b,Na}$, $I_{b,Ca}$, $I_{b,Cl}$ are background sodium, calcium and chloride currents, respectively. The model constantly monitors intracellular $[Na^+]$, $[K^+]$, $[Ca^{2+}]$ and $[Cl^-]$.

Sarcoplasmic reticulum (SR) Ca^{2+}-handling is described as illustrated in Fig. 1, with network SR (NSR) subserving Ca^{2+}-uptake and junctional SR (JSR) governing release. Model parameters include cytoplasmic Ca^{2+}-buffering by calmodulin ($[Cmdn]_{max}$) and troponin ($[Trpn]_{max}$) and JSR Ca^{2+}-buffering by calsequestrin ($[Csqn]_{max}$). An uptake flux (Φ_{up}) moves Ca^{2+} from the cytosolic Ca^{2+} pool to the NSR. Φ_{up} depends on $[Ca^{2+}]_i$, and is governed by a maximal value ($\Phi_{up(max)}$) and half-saturation constant (K_{up}). Φ_{leak} depends on NSR $[Ca^{2+}]$ ($[Ca^{2+}]_{NSR}$), and is a function of $\Phi_{up(max)}$ and maximal $[Ca^{2+}]_{NSR}$ ($[Ca^{2+}]_{NSR(max)}$). A transfer flux (Φ_{tr}) moves Ca^{2+} from NSR to JSR. Φ_{tr} depends on the inter-compartment $[Ca^{2+}]$ gradient ($[Ca^{2+}]_{NSR}-[Ca^{2+}]_{JSR}$) and is governed by a transfer time-constant (τ_{tr}). A release flux (Φ_{rel}) corresponds to Ca^{2+}-release from JSR to cytoplasm. Φ_{rel} is closely coupled to sarcolemmal Ca^{2+} channels and is activated by Ca^{2+} flux into the cytoplasm with activation time constant τ_{rel}. Φ_{rel} also depends on the $[Ca^{2+}]$ gradient between JSR and cytoplasm ($[Ca^{2+}]_{JSR}-[Ca^{2+}]_i$), and has a maximal release rate (k_{rel}). Φ_{rel} inactivation gating is both flux and voltage dependent. The parameters defining Ca^{2+}-handling were altered from the RNC model as described below and shown in Fig. 2, to create agreement with experimental Ca^{2+}-transient recordings. Numerical integration of Eq. (3) was carried out using a fixed time step of 5 μs. All simulations were performed using double-precision arithmetic on Unix PC workstations.

Group data are expressed as mean±S.D.

3. Results

3.1. Experimental Ca^{2+}-transients and results of the RNC model

Fig. 3 shows representative recordings of Ca^{2+}-transients measured in cells from a control dog (panel A) and a dog subjected to rapid pacing (panel B) stimulated at 2 Hz following a 1-min rest period. Both control and paced cells showed post-rest potentiation, but the control cell showed a biphasic staircase in contrast to low uniform-amplitude Ca^{2+} signals in the paced cell. For comparison, the RNC model was paced from rest at 2 Hz under control conditions (panel C) and after incorporating known pacing-induced ICR (panel D). Post-rest potentiation was observed in both cases while subsequent Ca^{2+}-transients declined monotonically. The RNC post-rest pulse was reduced by ~200 nM and steady-state peak concentrations were 2.5-fold lower than mean control data (Fig. 4C). After ICR, the RNC post-rest pulse was ~300 nM greater than in ATR (Fig. 6E), while the 60th peak agreed well with experiment.

The RNC Ca^{2+}-handling model adopts SR buffer concentrations and binding constants from earlier models of guinea pig [15] and bullfrog [16] cardiac APs, and clearly fails to reproduce Ca^{2+}-transients in dog atrial myocytes. Our first objective was therefore to produce a revised control model (designated '*r*-Ctl') to match experimental observations. SR constants were adjusted to reproduce quantitatively the biphasic post-rest staircase in control cells (Fig. 4A). Modifications (Fig. 2) included: (for uptake) 20% increase in $\Phi_{up(max)}$; 60% increase in $[Ca^{2+}]_{NSR(max)}$; 86% reduction of K_{up}; (for transfer) 33% reduction in τ_{tr}; and (for release) 40% increase in τ_{rel}.

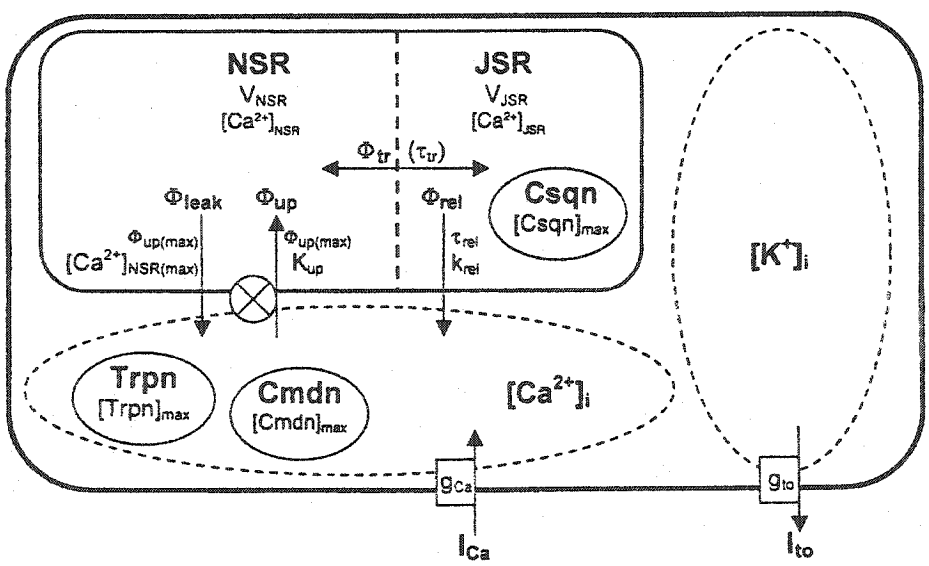

Fig. 1. Schematic representation of key components of the Ca^{2+}-handling model (bold). For description and definition of abbreviations, see text. Model constants involved in each process are shown next to each.

site of action	constant	RNC value	r-Ctl	ICA+SR
sarcolemma	g_{Ca}	0.264 nS/pF	↔	69%↓
	g_{to}	0.10507 nS/pF	$3.964 \cdot 10^{-2}$ nS/pF	65%↓
	g_{K1}	0.15 nS/pF	0.18 nS/pF	↔
myoplasm	$[Cmdn]_{max}$	0.045 mM	↔	↔
	$[Trpn]_{max}$	0.35 mM	↔	↔
SR uptake (Φ_{up})	V_{NSR}	1109.52 μm^3	↔	↔
	$\Phi_{up(max)}$	0.005 mM/ms	0.006 mM/ms	↔
	K_{up}	$9.2 \cdot 10^{-4}$ mM	$1.288 \cdot 10^{-4}$ mM	↔
SR leak (Φ_{leak})	$[Ca^{2+}]_{NSR(max)}$	15 mM	24 mM	76.25%↓
SR transfer (Φ_{tr})	τ_{tr}	180 ms	120 ms	328.6%↑
SR release (Φ_{rel})	V_{JSR}	96.48 μm^3	↔	↔
	τ_{rel}	8 ms	11.2 ms	128.6%↑
	k_{rel}	30 ms^{-1}	↔	↔
	$[Csqn]_{max}$	10 mM	↔	↔

↔ = no change, ↑ = increase, ↓ = decrease

Fig. 2. Ca^{2+}-handling parameters in RNC model, alterations made to agree with experimental Ca^{2+}-transient recordings (*r*-Ctl) and alterations in SR Ca^{2+}-handling required to reproduce altered Ca^{2+} transients in remodeled cells.

Consistent with routine experimental procedure, all simulations were preceded by 2 min of pacing at 2 Hz followed by a 1-min rest period. The Ca^{2+}-transients generated by the *r*-Ctl model during pulsing at 2 Hz are shown in Fig. 4B. The *r*-Ctl Ca^{2+} peaks differed from mean experimental data by less than 5% at each pulse (Fig. 4C). These adjustments required small modifications of K^+ currents to maintain physiological APD_{50} (a 62% reduction in I_{to}) and APD_{95} (a 20% increase in I_{K1}). In the original RNC

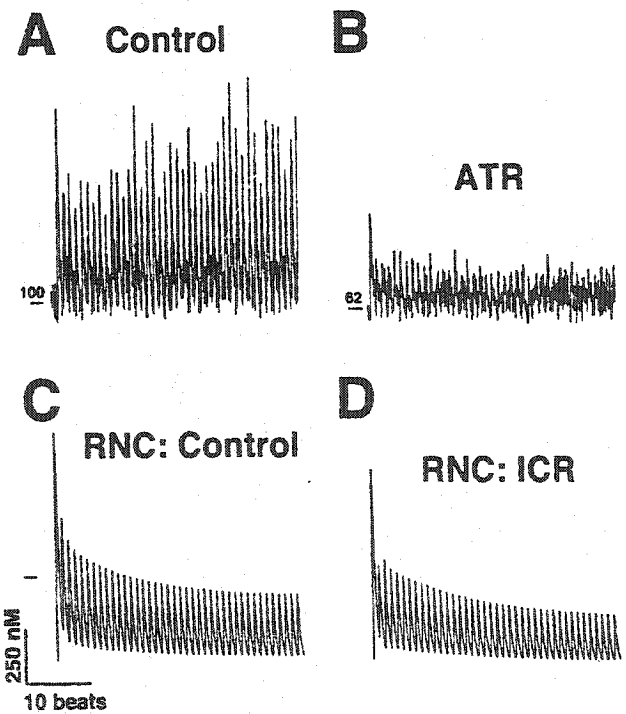

Fig. 3. Sequential Ca^{2+} transients from a control (A) and remodeled (B) cell. RNC model simulations of a control cell (C) and a cell incorporating pacing-induced ICR (D). The short horizontal marker at left of CaT simulations in panel C indicates an intracellular Ca^{2+} level of 500 nM.

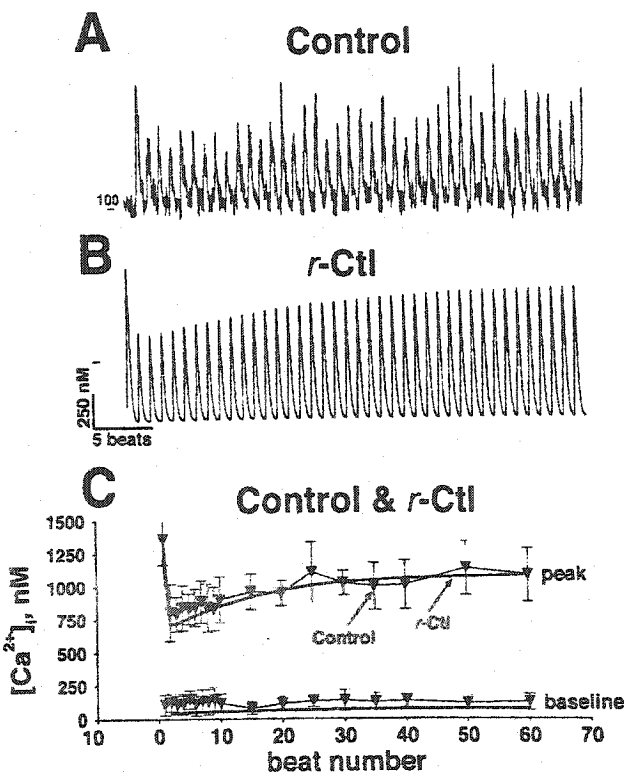

Fig. 4. Ca^{2+}-transients from a control cell (A), simulations with the *r*-Ctl model (B) and (C) comparison of Ca^{2+}-transients (CaTs) measured in five control cells (mean±S.D.) and corresponding model simulation (curve). The short horizontal marker at left of CaT simulations in panel B indicates an intracellular Ca^{2+} level of 500 nM.

model, $I_{Ca,L}$ was decreased by 70% from experimental values in order to produce physiological APDs [12], but K^+ currents were left at experimental values. Therefore, an adjustment in K^+ currents of an order less than those of $I_{Ca,L}$ was deemed reasonable.

3.2. Effects of rapid pacing on Ca^{2+}-handling and model parameters

To determine the parameter modifications of *r*-Ctl necessary to reproduce the Ca^{2+}-handling abnormalities caused by remodeling, we studied several specific aspects of Ca^{2+}-handling in paced myocytes. First, we examined SR Ca^{2+}-stores by rapid application of 10 mM caffeine. Fig. 5A shows representative Ca^{2+}-transients at 2 Hz. At steady-state, a caffeine puff was applied via a fast-flow system that exchanged the extracellular milieu of the cell within 500 ms. Mean caffeine-induced $[Ca^{2+}]$ peaks averaged 958±17 nM in five control cells and 887±21 nM in seven paced cells (P=NS), indicating no change in releasable Ca^{2+}. Fig. 5B shows the kinetics of Ca^{2+}-transient rise and decay in a control and remodeled myocyte. The rate of Ca^{2+}-rise was clearly decreased by pacing (from 0.016 to 0.012/ms in the cells shown). The relaxation time-course (quantified as the time for 50% decrease in the Ca^{2+}-transient based on an exponential fit to transient decay) was not altered, measuring 207 and 212 ms in the cells shown. Similar results were obtained in a total of five control and five paced cells. Thus, Ca^{2+}-release was slowed by remodeling, but the kinetics of Ca^{2+} removal were unaltered. We then studied Ca^{2+}-transient decay kinetics before and after 100-μM CPA. Fig. 5C shows Ca^{2+}-transients at 0.5 Hz before and after CPA in representative control and paced cells. CPA slowed Ca^{2+}-transient relaxation, but there were no relaxation kinetic differences between control and remodeled cells. The 50% relaxation time averaged 244±13 and 257±16 ms in five control and five paced cells (P=NS) before CPA and 486±44 vs. 505±40 ms, respectively (P=NS) after CPA exposure. These results suggest that Na^+, Ca^{2+} exchange (NCX) function and SERCA are unaltered by chronic tachycardia, consistent with previous molecular studies [17,18].

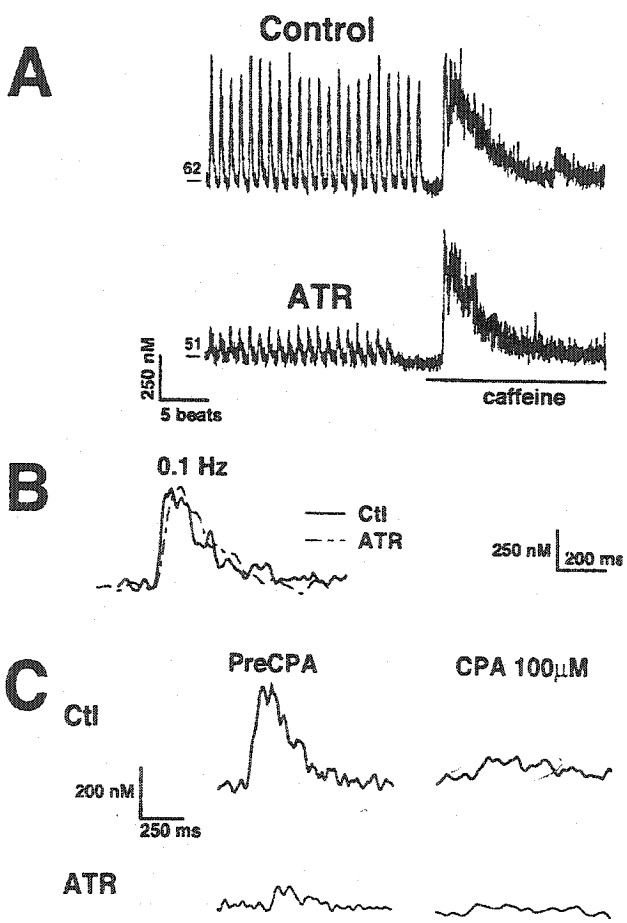

Fig. 5. Examples of caffeine-induced Ca^{2+}-transients (A), Ca^{2+}-transients during steady-state 0.1-Hz stimulation (B) and Ca^{2+}-transients before and after CPA (C).

Based on the observations in remodeled myocytes, we determined the parameter alterations of the *r*-Ctl model needed to reproduce Ca^{2+}-transient reductions in paced cells, assuming that releasable SR Ca^{2+} stores, Ca^{2+}-uptake rate, NCX and SERCA function are unaltered and Ca^{2+}-release rate is reduced. The required changes are summarized in Fig. 2, and included a 76.3% reduction in $[Ca^{2+}]_{NSR(max)}$, a 328.6% increase in τ_{tr}, and a 128.6% increase in τ_{rel}. Slowing of Φ_{rel} kinetics were needed to match experimentally observed decreases in the Ca^{2+}-transient rise rate. This alteration may reflect disruption of the close coupling of L-type Ca^{2+}-channels and JSR Ca^{2+} release channels, or of channels selective to monovalent ions countering Ca^{2+}-release [19–21]. $[Ca^{2+}]_{NSR(max)}$ reduction accounted for the abolished positive post-rest staircase, and implies changed JSR leak. While this change appears as a decrease in maximum SR Ca^{2+}-uptake capacity in the model, it may also represent reduced leakiness of ryanodine receptors in the disease state. The large increase in τ_{tr} was primarily responsible for the reduced Ca^{2+}-transient amplitude. These changes are consistent with observations of cardiac myolysis and SR fragmentation resulting from AF [22]. The slowing in intra-SR transfer may represent reduced recycling of intra-SR Ca^{2+}, thought to be associated with impaired SR function and the conversion of rest-potentiation to rest-depression in canine myocytes as discussed by Hryshko et al. [23] and depicted schematically in Fig. 9 of Ref. [24].

The model incorporating pacing-induced Ca^{2+}-handling alterations will be referred to as the SR-only model, and the model incorporating only ICR will be termed the ICR-only model. The model incorporating both will be termed the ICR+SR model. Fig. 6 shows beat-to-beat changes in Ca^{2+}-transients recorded from a paced cell (Fig. 6A), along with simulations incorporating Ca^{2+}-

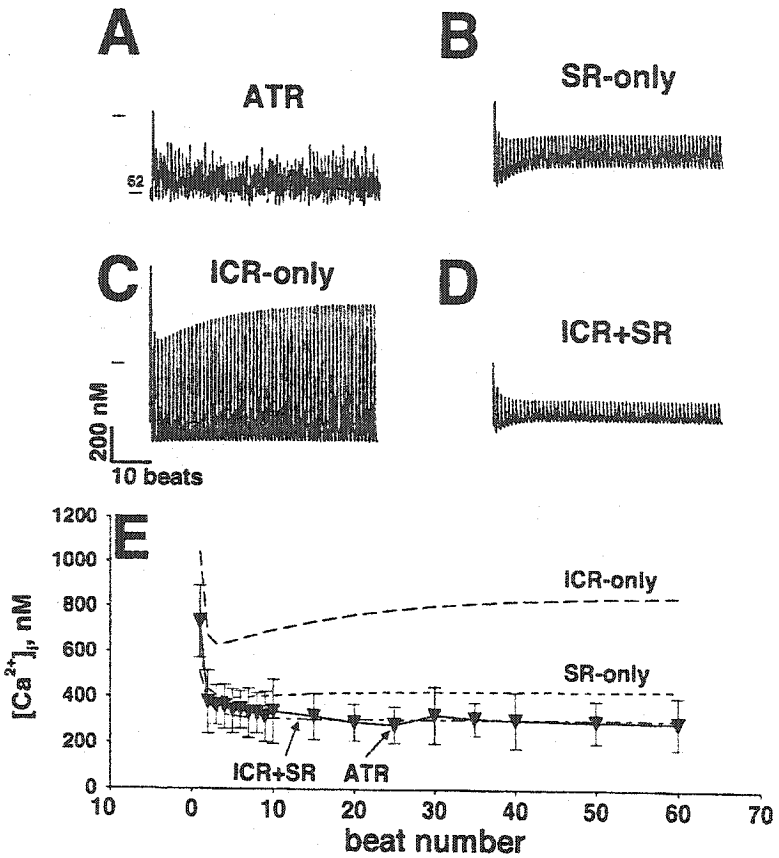

Fig. 6. Ca^{2+}-transients recorded in an ATR cell (A) compared with SR-only (B), ICR-only (C) and ICR+SR (D) models. (E) Experimental Ca^{2+}-transients from 5 ATR cells (mean±S.D.) along with simulations (curves). The short horizontal marker at left of CaT simulations in panel C indicates an intracellular Ca^{2+} level of 500 nM.

handling abnormalities in the SR-only model (Fig. 6B), the ICR-only model (Fig. 6C), and the ICR+SR model (Fig. 6D). Fig. 6E shows mean experimental data from five ATR cells, along with quantitative representations of simulation results. ICR-only fails to account for pacing-induced Ca^{2+}-transient changes. The agreement was better with the SR-only model, but remained imperfect. Steady-state ICR-only and SR-only peaks were approximately 80 and 41% of *r*-Ctl, respectively, consistent with the findings of Bers et al. [25], where NCX was estimated to account for about 30% of Ca^{2+} removal from the cytoplasm during relaxation, with SR-uptake accounting for the remaining 70%. In the model, both are ~10% higher than these estimates as each also contributes to the other. In the ICR-only model, reduced trigger Ca^{2+} from remodeled I_{Ca} was nevertheless sufficient to induce a large response from the normal SR, while in the SR-only model, normal I_{Ca} was unable to elicit a substantial release from the dysfunctional SR. This property of the ICR-only model contributes both to the persistence of a positive staircase in Fig. 6, and to the persistence of AP rate-adaptation in the absence of SR abnormalities (Fig. 8). The combined ICR+SR model agreed well with experimental data, differing by less than 11% at each pulse.

Fig. 7A and B show individual normalized experimental Ca^{2+}-transients at 1 Hz under control and remodeled conditions. Fig. 7C and D show corresponding simulations with the *r*-Ctl model and the combined ICR+SR model, respectively. There is clearly good agreement with recordings for both Ca^{2+}-transient amplitude and kinetics, unlike the ICR-only model (Fig. 7E).

3.3. Tachycardia-induced changes in APD rate-adaptation

Fig. 8 shows representative APs at 1 and 6 Hz from a control (panel A) and ATR (panel B) cell. The control AP displayed a prominent plateau and significant rate-adaptation, while the paced cell showed the triangular morphology, APD abbreviation, and abolished APD rate-adaptation characteristic of tachycardia-induced remodeling. These morphologic features and associated properties were reproduced in the *r*-Ctl (panel C) and ICR+SR (panel D) models, respectively. Panels E–F show APD to 50% (APD_{50}) repolarization from 1 to 6 Hz ($n=25$ cells each group). APD_{50} in the *r*-Ctl model paralleled experimental results at all rates. APD_{50} rate-adaptation over 1–6 Hz was 24 ms in the *r*-Ctl model compared to 32 ms in experiment

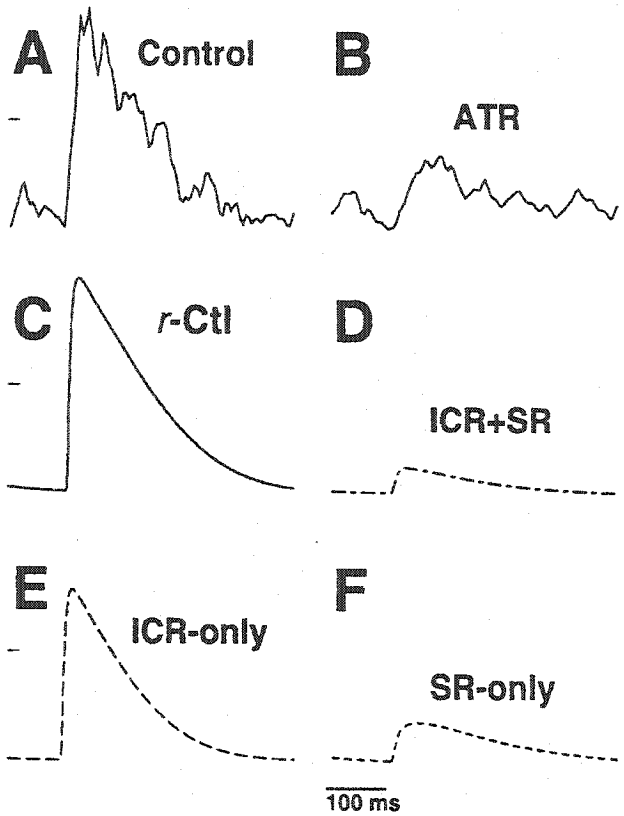

Fig. 7. Examples of single Ca^{2+}-transients recorded from control (A) and remodeled (B) cells, and results of simulations with *r*-Ctl (C), ICR + SR (D), ICR-only (E) and SR-only (F) models. Markers at left indicate 50% of control amplitude.

(panel E). APD_{50} rate-adaptation was abolished in paced cells and reduced to 5 ms in the ICR + SR model (panel F). ICR-only accounted for 79% of the diminished APD_{50} rate-adaptation, as I_{Ca} reduction was responsible for much of the triangular AP morphology. Rate-adaptation was preserved in the SR-only model because the APD_{50}-shortening effect of rate-dependent I_{Ca} inactivation remained, although somewhat offset by potentiation of I_{Ca} secondary to decreased Ca_i^{2+}-induced inactivation. However, in combination with ICR, SR dysfunction contributed importantly to the ICR + SR result.

Panels G–H show APD to 95% (APD_{95}) repolarization from 1 to 6 Hz. APD_{95} in the *r*-Ctl model closely matched experimental data at all rates but was slightly prolonged at 6 Hz (panel G). APD_{95} rate-adaptation over 1–6 Hz was 91 ms in control, compared to 88 ms in the *r*-Ctl model. APD_{95} rate-adaptation was abolished in paced cells and reduced by over 90% (to 6 ms) in the ICR + SR model, which closely approximated the paced group (panel H). APD_{95} was reduced in the ICR- and SR-only models (panel H), but rate-adaptation persisted, with shortening by 71 and 20 ms, respectively, over the 1–6 Hz range. APD_{95} shortening in the ICR-only model was due to persistent rate-dependent I_{Ca} reduction, since I_{Ca} was incompletely down-regulated by ICR. In the SR-only model, AP morphology changes occurred because of reduced Ca_i^{2+}-dependent inactivation of I_{Ca}. This raised the plateau voltage and prolonged the plateau, thereby increasing I_{Kr} by ~61% relative to control, and had a net effect to decrease APD_{95} rate-adaptation. The ICR-only and SR-only models accounted for 19 and 78% of APD_{95} rate-adaptation reduction, respectively. Loss of rate-adaptation in ICR + SR arose from the balance of decreased I_{Ca}-related effects on the APD in ICR and plateau I_{Ca} potentiation by reduced Ca_i^{2+}-dependent I_{Ca} inactivation with SR abnormalities and resulting I_{Kr} recruitment. These results indicate that both ICR and SR dysfunction contribute to ATR-induced loss of APD rate-adaptation, and taken together can account fully for loss of rate-adaptation.

4. Discussion

We developed a mathematical model of the canine atrial AP by modifying Ca^{2+}-handling terms based on experimental Ca^{2+}-transient recordings in control and remodeled cells. The model reproduces changes in APD rate-adaptation in remodeling, suggesting that Ca^{2+}-handling changes contribute to tachycardia-induced atrial repolarization abnormalities.

4.1. Significance and mechanisms of tachycardia-induced loss of APD rate-adaptation

A reduction in atrial refractoriness rate-adaptation is a finding characteristic of tachycardia-induced atrial remodeling [2,26] and is observed in patients with AF [5,6]. Loss of rate-adaptation causes marked refractory period reduction at the long basic cycle lengths of sinus rhythm [2,5,26]. Clinical AF is generally initiated by premature complexes during sinus rhythm, making refractory periods at longer cycle lengths a critical determinant of vulnerability to AF [27]. Thus, APD reduction and loss of APD rate-adaptation are potentially important contributors to the enhanced vulnerability for AF following remodeling.

Li et al. [28] demonstrated a central role of transmembrane Ca^{2+} current in human atrial APD rate-adaptation. In their human AP model, Courtemanche et al. [29] showed that rate-adaptation arose from a synergistic interaction between I_{Ca} and I_K. At fast rates, available I_{Ca} was decreased while I_K was increased, lowering the plateau and accelerating late repolarization, respectively [29]. The central role of I_{Ca} was further supported by evidence that rate-adaptation in normal canine atrial cells is abolished by 10 μM nifedipine [7]. Loss of rate-adaptation was reproduced in the RNC and Courtemanche models when I_{Ca} was reduced by 90%, simulating pharmacological blockade [12,29]. When I_{Ca} is strongly decreased, the plateau level is lowered to the point where I_K activa-

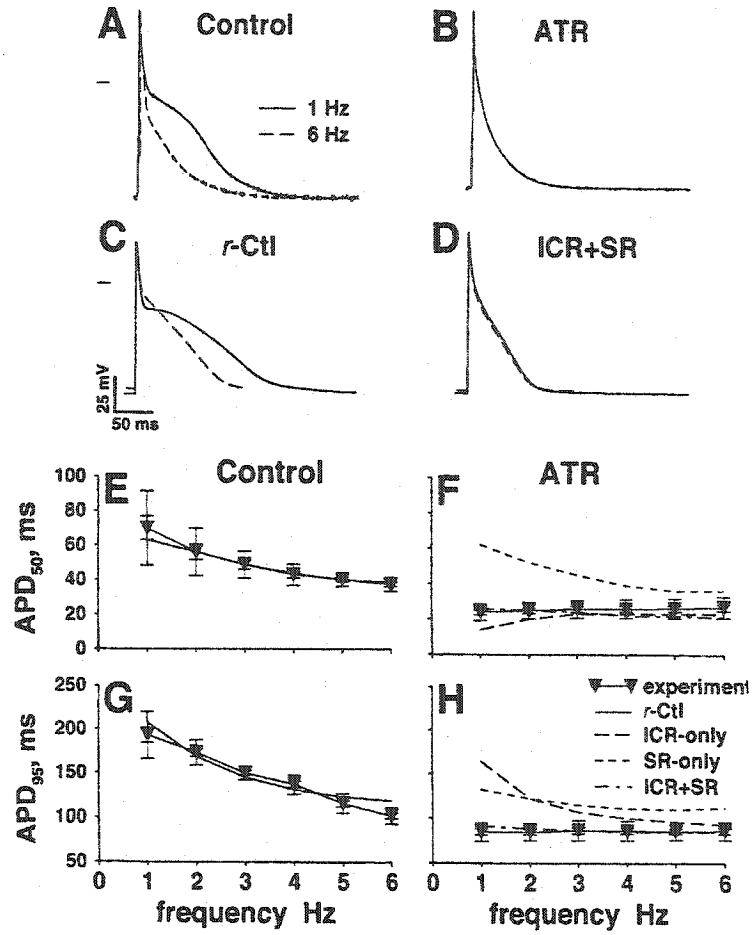

Fig. 8. Examples of APs recorded from control (A) and remodeled (B) cells at 1 and 6 Hz, along with simulated APs with *r*-Ctl (C) and ICR + SR (D) models. (E–H) Experimental mean data and corresponding model simulations. Markers at left indicate 0 mV.

tion is greatly reduced and can no longer contribute to rate-adaptation [29]. Tachycardia-induced I_{Ca} reduction in canine atria [7] is quantitatively similar (69% decrease) to the 63% atrial Ca^{2+} current density reduction in AF patients [8]. Both are less than the 90% I_{Ca} reduction that abolishes APD rate-adaptation in experimental [7] and modeling studies [12,29], indicating that additional mechanisms contribute to loss of rate-adaptation. Hara et al. [11] showed that ryanodine restores the AP plateau in remodeled atria, suggesting that changes in SR Ca^{2+}-handling may play a significant role. The present study suggests that tachycardia-induced ICR is insufficient in itself to account for loss of rate-adaptation, but that the combination of ICR and changes in SR Ca^{2+}-handling does explain loss of APD rate-dependence.

4.2. Comparison of Ca^{2+}-handling abnormalities in remodeled atria and other cardiac pathologies

Congestive heart failure (CHF) is also well-known to cause AP remodeling [30,31] and Ca^{2+}-handling abnormalities. Ventricular Ca^{2+}-transients are prolonged, exhibiting reduced amplitude, slowed relaxation, and blunted frequency-dependence [32] while tissues [30,31,33] and cells [34,35] from failing human ventricles exhibit AP prolongation. Sarcolemmal NCX mRNA and protein levels are increased in CHF [32,36,37]. Ventricular ryanodine receptor mRNA decreases have been noted in some studies of terminal CHF [38,39], but no change in receptor protein level has been demonstrated [40]. Reduced SERCA2a mRNA [36,41–45] expression has been a common finding in CHF. Phospholamban mRNA is consistently reduced [32,41,46], but not necessarily phospholamban protein [37,41,47]. Winslow et al. [48] developed a mathematical model of the failing human ventricular AP with a detailed representation of subcellular Ca^{2+}-handling. They found that changes in Ca^{2+}-handling contribute importantly to AP prolongation in heart failure.

Although some features of Ca^{2+}-transients in atrial remodeling resemble those in CHF (reduced amplitude, loss of positive staircase), others are quite different (minimal or no change in Ca^{2+}-transient relaxation in atrial remodeling). Whereas NCX is prominently up-regulated in CHF, it is unchanged by atrial pacing [17,18,49]. SERCA

expression is reduced in some clinical studies of AF patients [49–51] and unchanged in others [18]. Ryanodine receptors, phospholamban and calsequestrin are unaltered in AF [18,49,51]. The present results indicate that, as in CHF, Ca^{2+}-handling abnormalities in remodeled atrial cells contribute to physiologically relevant changes in AP properties. For both pathologies, diminished $[Ca^{2+}]_i$-induced inactivation of L-type Ca^{2+} current was an important determinant of AP properties.

4.3. Novel findings and potential significance

The present study is the first to evaluate quantitatively the respective roles of ICR and Ca^{2+}-handling abnormalities in the tachycardia-induced loss of atrial APD rate-adaptation. In order to achieve these objectives, we formulated the first atrial AP model incorporating Ca^{2+}-handling formulations based on direct recordings of Ca^{2+}-transients. Our results point to the importance of Ca^{2+}-handling in governing the canine atrial AP and in understanding the electrophysiological basis of tachycardia-mediated changes in AP properties. Our results are consistent with experimental AP studies in atrial tachycardia remodeling [7,11], and give insights into underlying mechanisms. Because of the clinical importance of remodeling for AF [52,53], these insights have potential clinical relevance.

4.4. Potential limitations

The focus of this study was on the role of Ca^{2+}-transient changes in AP properties. A key objective of the model was to reproduce quantitative experimental measurements of Ca^{2+}-transients under control and paced conditions. This was done in a realistic mathematical model of the canine atrial AP that implements a widely accepted representation of the SR. It was recognized that the idea of 'uptake' and 'release' compartments is a hypothetical construct used to explain the delay between relaxation due to Ca^{2+} sequestration by the SR and availability of Ca^{2+} for release [54]. We acknowledge that Ca^{2+} leak from the SR may arise from the ryanodine receptor itself, allowing more Ca^{2+} to flow during diastole. What was modeled as a change in JSR leakage may correspond to altered release processes. These may also be thought of as SR release channels recovering from inactivation [54]. A more sophisticated representation would require much more extensive mechanistic and quantitative experimental studies including single Ca^{2+} channel analysis, beyond the scope of this study. Despite these limitations, the present approach to model development was consistent with known mechanisms. Solutions were unique and optimized to faithfully reproduce experimentally recorded Ca^{2+}-transients under a variety of conditions. The AP is a sarcolemmal phenomenon arising from trans-membrane processes, and the modulation of these processes produced by the Ca^{2+}-transient depends on the cytosolic transient per se, not on the specifics of the Ca^{2+}-handling process that produce the measured Ca^{2+}-transient. Therefore, even if the same Ca^{2+}-transients were produced by a different set of Ca^{2+}-handling alterations, the results would not change our conclusions, which depend on altered Ca^{2+}-transient effects on APs and not how Ca^{2+}-transient changes are achieved. The validity of the results is evinced by the quantitative agreement between experimental and model Ca^{2+}-transients and APD in both control and ATR conditions.

Acknowledgements

This work was supported by the Canadian Institutes of Health Research (CIHR), the Heart and Stroke Foundation of Quebec and the Mathematics of Information Technology and Complex Systems (MITACS) Network. Dr Leblanc is a Fonds de la Recherche en Sante du Quebec Research Scholar. James Kneller is supported by a CIHR MD, PhD Studentship and by a Merck Pharmacology Fellowship. The authors thank Diane Campeau for secretarial assistance.

References

[1] Kannel WB, Wolf PA. Epidemiology of atrial fibrillation. In: Falk RH, Podrid PJ, editors, Atrial fibrillation: mechanisms and management, New York: Raven Press, 1992, pp. 81–92.
[2] Wijffels MC, Kirchhof CJ, Dorland R et al. Atrial fibrillation begets atrial fibrillation. A study in awake chronically instrumented goats. Circulation 1995;92:1954–1968.
[3] Wijffels MC, Kirchhof CJ, Dorland R et al. Electrical remodeling due to atrial fibrillation in chronically instrumented conscious goats: roles of neurohumoral changes, ischemia, atrial stretch, and high rate of electrical activation. Circulation 1997;96:3710–3720.
[4] Nattel S, Li D, Yue L. Basic mechanisms of atrial fibrillation—very new insights into very old ideas. Annu Rev Physiol 2000;62:51–77.
[5] Attuel P, Childers R, Cauchemez B et al. Failure in the rate adaptation of the atrial refractory period: its relationship to vulnerability. Int J Cardiol 1982;2:179–197.
[6] Boutjdir M, Le Heuzey JY, Lavergne T et al. Inhomogeneity of cellular refractoriness in human atrium: factor of arrhythmia? Pacing Clin Electrophysiol 1986;9:1095–1100.
[7] Yue L, Feng J, Gaspo R et al. Ionic remodeling underlying action potential changes in a canine model of atrial fibrillation. Circ Res 1997;81:512–525.
[8] Van Wagoner DR, Pond AL, Lamorgese M et al. Atrial L-type Ca^{2+} currents and human atrial fibrillation. Circ Res 1999;85:428–436.
[9] Bosch RF, Zeng X, Grammer JB et al. Ionic mechanisms of electrical remodeling in human atrial fibrillation. Cardiovasc Res 1999;44:121–131.
[10] Sun H, Gaspo R, Leblanc N et al. Cellular mechanisms of atrial contractile dysfunction caused by sustained atrial tachycardia. Circulation 1998;98:719–727.

[11] Hara M, Shvilkin A, Rosen MR et al. Steady-state and nonsteady-state action potentials in fibrillating canine atrium: abnormal rate adaptation and its possible mechanisms. Cardiovasc Res 1999;42:455–469.
[12] Ramirez RJ, Nattel S, Courtemanche M. Mathematical analysis of canine atrial action potentials: rate, regional heterogeneity, and electrical remodeling. Am J Physiol 2000;279:H1767–H1785.
[13] Grynkiewicz G, Poenie M, Tsien R. A new generation of Ca^{2+} indicators with greatly improved fluorescence properties. J Biol Chem 1985;260:3440–3450.
[14] Bassani JWM, Bassani RA, Bers DM. Calibration of indo-1 and resting intracellular $[Ca]_i$ in intact rabbit cardiac myocytes. Biophys J 1995;68:1453–1460.
[15] Luo CH, Rudy Y. A dynamic model of the cardiac ventricular action potential. II. Afterdepolarizations, triggered activity, and potentiation. Circ Res 1994;74:1097–1113.
[16] Rasmusson RL, Clark JW, Giles WR et al. A mathematical model of electrophysiological activity in a bullfrog atrial cell. Am J Physiol 1990;259:H370–H389.
[17] Yue L, Melnyk P, Gaspo R et al. Molecular mechanisms underlying ionic remodeling in a dog model of atrial fibrillation. Circ Res 1999;84:776–784.
[18] Van Gelder IC, Brundel BJ, Henning RH et al. Alterations in gene expression of proteins involved in the calcium handling in patients with atrial fibrillation. J Cardiovasc Electrophysiol 1999;10:552–560.
[19] Hals GD, Stein PG, Palade PT. Single channel characteristics of a high conductance anion channel in 'sarcoballs'. J Gen Physiol 1989;93:385–410.
[20] Coronado R, Rosenberg RL, Miller C. Ionic selectivity, saturation, and block in a K^+-selective channel from sarcoplasmic reticulum. J Gen Physiol 1980;76:425–446.
[21] Coronado R, Miller C. Decamethonium and hexamethonium block K^+ channels of sarcoplasmic reticulum. Nature 1980;288:495–497.
[22] Ausma J, Wijffels M, Thone F et al. Structural changes of atrial myocardium due to sustained atrial fibrillation in the goat. Circulation 1997;96:3157–3163.
[23] Hryshko LV, Kobayashi T, Bose D. Possible inhibition of canine ventricular sarcoplasmic reticulum by BAY K 8644. Am J Physiol 1989;257:H407–H414.
[24] Hryshko LV, Bouchard R, Chau T, Bose D. Inhibition of rest potentiation in canine ventricular muscle by BAY K 8644: comparison with caffeine. Am J Physiol 1989;257:H399–406.
[25] Bers DM, Bridge JHB, Spitzer KW. Intracellular Ca transients during rapid cooling contractures in guinea-pig ventricular myocytes. J Physiol 1989;417:537–553.
[26] Gaspo R, Bosch RF, Talajic M et al. Functional mechanisms underlying tachycardia-induced sustained atrial fibrillation in a chronic dog model. Circulation 1997;96:4027–4035.
[27] Wang J, Liu L, Feng J et al. Regional and functional factors determining induction and maintenance of atrial fibrillation in dogs. Am J Physiol 1996;271:H148–H158.
[28] Li GR, Nattel S. Properties of transmembrane Ca^{2+} current at physiologic temperatures relevant to the action potential in human atrial myocytes. Am J Physiol 1997;272:H227–H235.
[29] Courtemanche M, Ramirez RF, Nattel S. Ionic mechanisms underlying human atrial action potential properties: insights from a mathematical model. Am J Physiol 1998;275:H301–H321.
[30] Coltart DJ, Meldrum SJ. Intracellular action potential in hypertrophic obstructive cardiomyopathy. Br Heart J 1972;34:204.
[31] Gwathmey JK, Copelas L, MacKinnon R et al. Abnormal intracellular calcium handling in myocardium from patients with end-stage heart failure. Circ Res 1987;61:70–76.
[32] O'Rourke B, Kass DA, Tomaselli GF et al. Mechanisms of altered excitation–contraction coupling in canine tachycardia-induced heart. I. Experimental studies. Circ Res 1999;84:562–570.
[33] Vermeulen JT, McGuire MA, Opthof T et al. Triggered activity and automaticity in ventricular trabeculae of failing human and rabbit hearts. Cardiovasc Res 1994;28:1547–1554.
[34] Beuckelmann DJ, Nabauer M, Erdmann E. Intracellular calcium handling in isolated ventricular myocytes from patients with terminal heart failure. Circulation 1992;85:1046–1055.
[35] Beuckelmann DJ, Nabauer M, Erdmann E. Alterations of K^+ currents in isolated human ventricular myocytes from patients with terminal heart failure. Circ Res 1993;73:279–285.
[36] Flesch M, Schwinger RH, Schiffer F et al. Evidence for functional relevance of an enhanced expression of the $Na(+)$–Ca^{2+} exchanger in failing human myocardium. Circulation 1996;94:992–1002.
[37] Reinecke H, Studer R, Vetter R et al. Cardiac Na^+/Ca^{2+} exchange activity in patients with end-stage heart failure. Cardiovasc Res 1996;31:48–54.
[38] Brillantes AM, Allen P, Takahashi T et al. Differences in cardiac calcium release channel (ryanodine receptor) expression in myocardium from patients with end-stage heart failure caused by ischemic versus dilated cardiomyopathy. Circ Res 1992;71:18–26.
[39] Go LO, Moschella MC, Watras J et al. Differential regulation of two types of intracellular calcium release channels during end-stage heart failure. J Clin Invest 1995;95:888–894.
[40] Meyer M, Schillinger W, Pieske B ét al. Alterations of sarcoplasmic reticulum proteins in failing human dilated cardiomyopathy. Circulation 1995;92:778–784.
[41] Schwinger RH, Bohm M, Schmidt U et al. Unchanged protein levels of SERCA II and phospholamban but reduced Ca^{2+} uptake and $Ca(2+)$-ATPase activity of cardiac sarcoplasmic reticulum from dilated cardiomyopathy patients compared with patients with nonfailing hearts. Circulation 1995;92:3220–3228.
[42] Feldman AM, Weinberg EO, Ray PE et al. Selective changes in cardiac gene expression during compensated hypertrophy and the transition to cardiac decompensation in rats with chronic aortic banding. Circ Res 1993;73:184–192.
[43] Zarain-Herzberg A, Afzal N, Elimban V et al. Decreased expression of cardiac sarcoplasmic reticulum $Ca(2+)$-pump ATPase in congestive heart failure due to myocardial infarction. Mol Cell Biochem 1996;163–164:285–290.
[44] Hasenfuss G, Reinecke H, Studer R et al. Relation between myocardial function and expression of sarcoplasmic reticulum $Ca(2+)$-ATPase in failing and nonfailing human myocardium. Circ Res 1994;75:434–442.
[45] Kiss E, Ball NA, Kranias EG et al. Differential changes in cardiac phospholamban and sarcoplasmic reticular $Ca(2+)$-ATPase protein levels. Effects on Ca^{2+} transport and mechanics in compensated pressure-overload hypertrophy and congestive heart failure. Circ Res 1995;77:759–764.
[46] Linck B, Boknik P, Eschenhagen T et al. Messenger RNA expression and immunological quantification of phospholamban and SR-$Ca(2+)$-ATPase in failing and nonfailing human hearts. Cardiovasc Res 1996;31:625–632.
[47] Movsesian MA, Karimi M, Green K et al. $Ca(2+)$-transporting ATPase, phospholamban, and calsequestrin levels in nonfailing and failing human myocardium. Circulation 1994;90:653–657.
[48] Winslow RL, Rice J, Jafri S et al. Mechanisms of altered excitation–contraction coupling in canine tachycardia-induced heart failure. II. Model studies. Circ Res 1999;84:571–586.
[49] Brundel BJ, van Gelder IC, Henning RH et al. Gene expression of proteins influencing the calcium homeostasis in patients with persistent and paroxysmal atrial fibrillation. Cardiovasc Res 1999;42:443–454.
[50] Ohkusa T, Ueyama T, Yamada J et al. Alterations in cardiac sarcoplasmic reticulum Ca^{2+} regulatory proteins in the atrial tissue of patients with chronic atrial fibrillation. J Am Coll Cardiol 1999;34:255–263.
[51] Lai LP, Su MJ, Lin JL et al. Down-regulation of L-type calcium channel and sarcoplasmic reticular $Ca(2+)$-ATPase mRNA in human atrial fibrillation without significant change in the mRNA of

ryanodine receptor, calsequestrin and phospholamban: an insight into the mechanism of atrial electrical remodeling. J Am Coll Cardiol 1999;33:1231–1237.
[52] Zipes DP. Atrial fibrillation. A tachycardia-induced atrial cardiomyopathy. Circulation 1997;95:562–564.
[53] Nattel S. Atrial electrophysiological remodeling caused by rapid atrial activation: underlying mechanisms and clinical relevance to atrial fibrillation. Cardiovasc Res 1999;42:298–308.
[54] Yue DT, Burkhoff D, Franz MR, Hunter WC, Sagawa K. Post-extrasystolic potentiation of the isolated canine left ventricle. Circ Res 1985;56:340–350.

CHAPTER 4 CHOLINERGIC ATRIAL FIBRILLATION IN A COMPUTER MODEL OF A 2-DIMENSIONAL SHEET OF CANINE ATRIAL CELLS WITH REALISTIC IONIC PROPERTIES.

As discussed in Section 1.4.4, Moe's multiple wavelet hypothesis (71) and classical computer model (72) have shaped clinical and experimental conceptions of AF since the early 1960s. However, recent experimental work has raised questions about the multiple wavelet mechanism, suggesting a discrete "driver region" underlying AF. The present study addressed the need for a more realistic computer model of AF that is consistent with experimental observations, thereby providing a unified conceptual framework to understand this complex process. I took advantage of the detailed ionic model of the canine atrial AP that I had worked with and improved in previous studies, in order to create a novel, realistic 2-dimensional mathematical model of canine atrial electrical activity.

UltraRapid Communication

Cholinergic Atrial Fibrillation in a Computer Model of a Two-Dimensional Sheet of Canine Atrial Cells With Realistic Ionic Properties

James Kneller, Renqiang Zou, Edward J. Vigmond, Zhiguo Wang, L. Joshua Leon, Stanley Nattel

Abstract—Classical concepts of atrial fibrillation (AF) have been rooted in Moe's multiple-wavelet hypothesis and simple cellular-automaton computer model. Recent experimental work has raised questions about the multiple-wavelet mechanism, suggesting a discrete "driver region" underlying AF. We reexplored the theoretical basis for AF with a 2-dimensional computer model of a 5×10-cm sheet of atrial cells with realistic ionic and coupling properties. Vagal actions were formulated based on patch-clamp studies of acetylcholine (ACh) effects. In control, a single extrastimulus resulted in a highly meandering unstable spiral wave. Simulated electrograms showed fibrillatory activity, with a dominant frequency (DF, 6.5 Hz) that correlated with the mean rate. Uniform ACh reduced core meander of the spiral wave by ≈70% (as measured by the standard deviation of spiral-wave tip position) and accelerated the DF to 17.0 Hz. Simulated vagally induced refractoriness heterogeneity caused wavefront breakup as accelerated reentrant activity in regions of short refractoriness impinged on regions unable to respond in a 1:1 fashion because of longer refractoriness. In 7 simulations spanning the range of conditions giving sustained AF, 5 were maintained by single dominant spiral waves. On average, 3.0±1.3 wavelets were present (range, 1 to 7). Most wavelets were short-lived and did not contribute to AF maintenance. In contrast to predictions of the multiple-wavelet hypothesis, but in agreement with recent experimental evidence, our model indicates that AF can result from relatively stable primary spiral-wave generators and is significantly organized. Our results suggest that vagal AF may arise from ACh-induced stabilization of the primary spiral-wave generator and disorganization of the heterogeneous tissue response. The full text of this article is available at http://www.circresaha.org. (*Circ Res.* 2002;90:e73-e87.)

Key Words: atrial fibrillation ■ mathematical model ■ reentry ■ vagus nerve

Since the early 1960s, Moe's multiple-wavelet hypothesis[1] and classical computer model[2] have provided the most widely accepted conceptual mechanistic description of atrial fibrillation (AF). AF was thought to arise from the ongoing fractionation of activation wavefronts causing multiplication of independent daughter wavelets. Wavelets would randomly collide, mutually annihilate, or coalesce in a self-perpetuating and ceaselessly-changing turbulent process. The model suggested that AF is a random process, with the maintenance of AF being a probabilistic phenomenon dependent on the total number of wavelets. Any factor that increased the number of wavelets would serve to perpetuate the arrhythmia, whereas any factor that decreased the total wavelet count would favor termination.

Recent experimental findings appear inconsistent with predictions of the multiple-wavelet hypothesis. High-resolution optical mapping of AF has provided evidence that AF is not random and that a critical number of wavelets may not be essential for AF maintenance.[3–5] Results in human[6–9] and experimental[3–5,10] studies suggest that local left atrial sources may play a critical role in AF. These data are consistent with the hypothesis first proposed by Lewis[11] that a single or small number of sources of stable reentrant wavefronts maintain AF.

Moe's computer model used time-dependent functions to represent excitability, conduction, and refractoriness in cellular automata arranged in a polygonal array to represent the atria. Ionic current properties are critical determinants of action potential waveform, dynamics, and phase-dependence, but were not included in Moe's model. Our laboratory has developed a realistic ionic model of the canine atrial action potential (AP), which we will term the Ramirez-Nattel-Courtemanche (RNC) model, and shown that it accounts for a variety of experimentally observed properties.[12,13] The objectives of the present study were as follows: (1) to develop a mathematical model of a 2-dimensional sheet of canine

Original received October 31, 2001; resubmission received March 15, 2002; revised resubmission received April 15, 2002; accepted April 16, 2002.

From the Research Center and Department of Medicine (J.K., R.Z., H.S., Z.W., S.N.), Montreal Heart Institute and University of Montreal; the Department of Pharmacology (J.K., S.N.), McGill University, Montreal, Quebec, Canada; and the Department of Electrical and Computer Engineering (E.J.V., L.J.L.), University of Calgary, Calgary, Alberta, Canada.

Correspondence to Dr Stanley Nattel, Research Center, Montreal Heart Institute, 5000 Belanger St E, Montreal, Quebec, Canada, H1T 1C8. E-mail nattel@icm.umontreal.ca

Circulation Research is available at http://www.circresaha.org

DOI: 10.1161/01.RES.0000019783.88094.BA

atrial tissue with realistic ionic, coupling, and propagation properties; (2) to incorporate a representation of ACh's ionic actions based on experimental observations to reproduce cholinergic effects on the AP; (3) to study the impact of varying intensity and distribution of ACh effects on reentrant arrhythmias in the model; and (4) to compare the determinants and properties of AF in the model with those in experimental studies.

Materials and Methods

Model Description and Implementation

The RNC model of the canine atrial AP was implemented.[12] The cell membrane is modeled electrically as a capacitor connected in parallel with variable resistors and batteries representing the ionic channels and driving forces. The total ionic current (I_{ion}) is given by the following:

$$(1)\quad I_{ion}=I_{Na}+I_{K1}+I_{to}+I_{Kur,d}+I_{Kr}+I_{Ks}+I_{Ca}+I_{ClCa}+I_{K(ACh)}+I_{p,Ca}+I_{NaCa}+I_{NaK}+I_{b,Na}+I_{b,Ca}+I_{b,Cl}$$

I_{ion} includes contributions from the fast sodium current (I_{Na}), the inward-rectifier K^+-current (I_{K1}), transient outward current (I_{to}), ultrarapid ($I_{Kur,d}$), rapid (I_{Kr}), and slow (I_{Ks}) delayed-rectifier K^+-current (I_K). Also included are the L-type Ca^{2+} current (I_{Ca}), a sarcolemmal Ca^{2+} pump current ($I_{p,Ca}$), the Na^+/K^+-ATPase current (I_{NaK}), the Na^+/Ca^{2+}-exchanger current (I_{NaCa}), a Ca^{2+}-activated Cl^- current (I_{ClCa}), and background Na^+ ($I_{b,Na}$) and Ca^{2+} ($I_{b,Ca}$) currents. A detailed tabulation of currents and their representation is provided in Ramirez et al[12]. An expression for the ACh-activated potassium current ($I_{K(ACh)}$) was formulated (described below) and included in Equation 1 to account for ACh effects.

The cellular model constantly monitors intracellular concentrations of Na^+, K^+, Ca^{2+}, and Cl^-. Sarcoplasmic reticulum (SR) Ca^{2+} handling is described using a 2-compartment model composed of network (NSR) and junctional (JSR) components subserving Ca^{2+} uptake and release, respectively. Ca^{2+} release from the JSR is induced by Ca^{2+} flux into the myoplasm, with close coupling between sarcolemmal I_{Ca} channels and subcellular I_{rel} channels. A formulation of a Na^+/Cl^- cotransporter and the background Cl^- current ($I_{b,Cl}$) were added to account for Cl^- flux,[14] and model g_{Ca} was increased by 25% to match AP measurements (Figure 2A). This adjustment was justified because the density of I_{Ca} in the original RNC model was scaled to 33% of experimental findings.[12]

For simulation studies of AF, a 2-dimensional rectangle of atrial tissue was modeled as previously described.[15] The tissue was composed of a network of 300 discrete cables representing muscle fibers. Each fiber may be viewed as a chain of myocytes that form a syncytium in the longitudinal direction. Fibers were 10 μm in diameter and had an axial resistivity of 390 $\Omega \cdot$ cm. Each was uniformly segmented into 600 segments of 167-μm length, such that the computational grid comprised 300×600 segments. Adjacent fibers were separated from one another by 167 μm and were connected transversely by fixed resistors (10 MΩ) placed 167 μm apart to form a brick-wall pattern of connections. Fiber resistivity and interfiber resistance values were chosen to match propagation characteristics observed experimentally.

The discretization factor (segment length per length constant) was kept lower than 0.1 to prevent numerical distortions.[16,17] The system of equations was solved as previously described.[18] To increase computational efficiency, voltage-dependent expressions involving exponentials were precomputed with a 50-μV resolution and stored in a table indexed by voltage.[19] A table with a resolution of $8.75 \cdot 10^{-7}$ mmol/L was also used to compute E_{Ca} from $[Ca^{2+}]_i$. Calculations were performed using a time step of 5 μs on 32 processors of a 64-processor Origin 2400 computer (Silicon Graphics) and 16 processors of an Enterprise 10000 (Sun). In this way, individual simulations of 5 seconds of activity (designated as "sustained AF" in Figures 6 and 7 and 10 through 12) requiring the solution of 4.14×10^6 coupled equations over 10^6 time steps could be accomplished in 12 to 18 hours, rather than the 5 to 7 days that would be necessary with a single processor.

This implementation achieved an atrial conduction velocity (CV) anisotropy ratio of ≈2.4:1 and a longitudinal CV of ≈100 cm/s, equal to the average of 5 measurements made from canine right atrial (RA) free wall, RA Bachmann's bundle, RA inferior wall, left atrial (LA) Bachmann's bundle, and LA free wall.[20] The computational substrate had dimensions of 5×10 cm, achieving an activation time during longitudinal propagation of ≈100 ms, compatible with experimental measurements.[20]

Two-Dimensional Simulation Protocols

Model effective refractory period (ERP) was measured by simulating the experimental protocols of Wang et al.[21] A square electrode, ≈0.8 mm per side, was used to best compare with the 2-pronged hook electrodes in experiments (each ≈0.5 mm per side). All stimuli were 180 μA/cm^2 in strength and 1 ms in duration. CV was calculated in the longitudinal direction between electrodes positioned 0.5 cm apart, and the proximal electrode was a sufficient distance from the stimulus site such that the wavefront was planar. Proximal segments were stimulated from rest at cycle lengths of 200 and 400 ms, and a single premature stimulus (S_2) was delivered after every 15 basic (S_1) stimuli. ERP was defined as the longest S_1-S_2 failing to initiate a propagated response. In the presence of increasing [ACh], the S_1-S_2 interval was initially set at the ERP of the preceding concentration and reduced such that ERP measurements were accurate within 0.5 ms. CV was measured from S_1 pulse trains at each concentration. The wavelength (ERP×CV), thought classically to represent the minimum path length for reentry and to determine the size of functional reentry circuits, was computed as previously defined.[21,22] Reentry was initiated using a cross-shock protocol.[23] An S_1 stimulus was applied along the uppermost cable, creating a wavefront propagating uniformly in the transverse direction. Before the recovery front reached the half-way point, an S_2 stimulus was applied to 1/4 of the sheet, establishing a single phase singularity and initiating reentry.

Potential Maps

For display purposes, propagating wavefronts over the entire computational substrate were visualized by constructing potential maps on a 25×50 pixel display grid, after verifying that observed activation patterns were not distorted by this approach. The transmembrane potential was sampled at the center of each 12×12 segment square on the computational grid after each millisecond. The visual display of static potential maps in Figures 4, 5, 6, 8, and 10 through 12 was enhanced in a postprocessing step using Image Magick software (Dupont). Corresponding movie supplements retained the original sampling resolution and can be found in the online data supplement available at http://www.circresaha.org.

Simulated Pseudounipolar Electrogram

A unipolar electrogram for a sheet of cells under conditions of uniform intracellular anisotropic resistivity (assuming the sheet was immersed in a bath of infinite size) was simulated as previously described.[17] The extracellular potential (Φ_e) is given by the following:

$$(2)\quad \Phi_e(P)=\frac{\rho_e}{4\pi}\sum_{i=1}^{M}\sum_{j=1}^{N}\frac{I_{ionti,j)}}{r_{i,j}V_s}$$

where M and N are the total numbers of segments in the longitudinal and transverse directions, respectively, and $r_{i,j}$ is the distance from the observation point (P) to the center of the volume element (V_s) at node i,j. The value of $\rho_e=100\ \Omega \cdot$ cm is close to that of 0.9% saline solution.[17]

Signal Analysis

To compare the frequency content of experimental and model electrograms, spectral analysis of signals was performed with fast

Fourier transformations (FFTs).[3-5] Content in the 0 to 60-Hz band was analyzed. Because it was possible to scale model results uniformly, FFTs of electrograms recorded at various observation points during the same simulation were normalized to the largest peak to facilitate comparison of the relative power of spectral peaks between sites. Activity was sampled at 1000 Hz (1 ms) for 5000 frames (≈5 seconds), providing a spectral resolution of 0.2 Hz.

Experimental Techniques for $I_{K(ACh)}$ Characterization

Single canine atrial myocytes were isolated as previously described.[24] The right atrium from adult mongrel dogs (20 to 26 kg) of either sex was dissected and mounted via the right coronary artery to a Langendorff perfusion system. Preparations were first perfused with Ca^{2+}-containing Tyrode's solution at 37°C and then with Ca^{2+}-free Tyrode's solution for 20 minutes at 12 mL/min, followed by the same solution containing collagenase (110 U/mL CLS II; Worthington Biochemical) and 0.1% BSA. Dispersed cells were stored in KB medium at 4°C.

The Tyrode's solution contained (in mmol/L) NaCl 136, KCl 5.4, $MgCl_2$ 1, $CaCl_2$ 1, NaH_2PO_4 0.33, glucose 10, and *N*-2-hydroxyethlypiperazine-*N'*-2-ethanesulfonic acid (HEPES) 5; pH 7.4 (NaOH). The KB medium contained (in mmol/L) KCl 20, KH_2PO_4 10, glucose 25, potassium glutamate 70, β-hydroxybutyric acid 10, taurine 20, EGTA 10, mannitol 40, and 0.1% albumin; pH 7.4 (KOH). The pipette solution contained (in mmol/L) GTP 0.1, K^+-aspartate 110, KCl 20, $MgCl_2$ 1, Mg-ATP 5, HEPES 10, EGTA 10, and phosphocreatine 5; pH 7.3 (KOH). I_{Na} contamination was prevented with a holding potential (HP) ≤−50 mV. Other currents were minimized by bath inclusion of 1 μmol/L dofetilide (to inhibit I_{Kr}), 20 μmol/L 293B (Aventis, I_{Ks}), 10 μmol/L glyburide (ATP-sensitive K^+ current), and 200 μmol/L Cd^{2+} (I_{Ca}).

Our patch-clamp techniques have been described in detail.[24] $I_{K(ACh)}$ was recorded with whole-cell voltage-clamp and an Axopatch 200B amplifier (Axon). Electrodes filled with pipette solution had tip resistances of 1 to 3 MΩ. Seal resistance averaged 15±1 GΩ. Capacitance and series resistance (R_s) were electrically compensated. Before R_s compensation, the capacitative time constant was 412±12 ms and R_s averaged 5.0±0.4 MΩ. After compensation, the time-constant was 111±4 ms (capacitance, 71±4 pF), and R_s 1.4±0.1 MΩ. Experiments were conducted at 36±1°C. Steady-state current was recorded during 300-ms voltage steps from a HP of −40 mV under control conditions and then with 0.02 (n=6 cells), 0.1 (n=8), 1 (n=18), and 10 μmol/L (n=6) ACh. These concentrations spanned the range of $I_{K(ACh)}$ activity; no $I_{K(ACh)}$ was elicited at 0.01 μmol/L and current was maximal at 10 μmol/L.

Experimental Determination of Cholinergic Effects on the AP

APs were recorded from intact atria using standard microelectrode techniques as described previously.[25] Adult mongrel dogs (n=7, 20 to 32 kg) were anesthetized with pentobarbital (30 mg/kg IV). Their hearts were removed, and the right atrium was dissected and perfused via the right coronary artery with Krebs' solution (37°C, pH 7.35 to 7.40, 95%-O_2/5% CO_2) containing (in mmol/L) NaCl 120, KCl 3.8, $CaCl_2$ 1.2, $MgSO_4$ 1.2, KH_2PO_4 1.2, $NaHCO_3$ 25, and glucose 5.5. Arterial leaks were ligated and the tissue perfused at 10 to 12 mL/min, approximating normal canine atrial flow.[26] Preparations were stimulated endocardially with square-wave pulses (4-ms), 1.5 to 2 times diastolic-threshold current. Glass microelectrodes were filled with 3 mol/L KCl (12 to 20 MΩ) and coupled to an Axoclamp 2B amplifier.

Endocardial APs were recorded after pacing to steady state at 0.1, 0.2, 1, 2, 4, and 6 Hz before and during perfusion with carbamylcholine (Sigma). Carbamylcholine was used to obtain reproducible dose-response relations as ACh is rapidly broken down by tissue cholinesterases. Carbamylcholine concentrations of 0.1 and 1 μmol/L were used, as the AP was maximally reduced at 1 μmol/L. The stimulus site was at least 1 cm from the impaled cell,[27] and an interval of constant resting potential between the stimulus artifact and the AP was confirmed.[28] Recovery of control AP morphology was confirmed on washout.

Terminology

The following terminology was used:

AF: defined by rapid and irregular electrograms with varying morphologies. Potential maps were required to demonstrate propagation along lines of block and ongoing wavefront breakup, which changed on a cycle-to-cycle basis.[4,5]

Wavebreak: a discontinuity that allows contact between a wavefront and its own repolarization tail. Wavebreak occurs after blockade along a wavefront while remaining segments continue to propagate.[4]

Phase Singularity (PS): a point around which any arbitrary neighborhood contains all phases of the waveform. It is often the point where the depolarizing front and repolarizing tail of a wavefront meet.[29] PSs arise from wavebreaks and are located at the instantaneous center of rotational activity.[4]

Rotor: a spiral wave of excitation rotating around a PS for 1 or more cycles.[4]

Chirality: the sense of rotation, clockwise or counterclockwise, around a PS.[4]

Core: area circumscribed by the trajectory of a PS. A small region of excitable but unexcited tissue around which a rotor rotates.[30]

Wavelet: segments of excitation wavefronts, regardless of size, flanked by 2 PSs or a PS and a boundary.[4]

All data are presented as mean±SD.

Results

$I_{K(ACh)}$ Formulation

Figure 1A shows $I_{K(ACh)}$ *I*-V relations and the model fit. The current was formulated as follows:

$$I=\left[a_0+\frac{a_1}{1+\exp\left[\frac{V+a_2}{a_3}\right]}\right](V-E_K) \quad (3)$$

Parameters were determined by nonlinear regression (10^{-6} error tolerance) at each concentration using the experimental reversal potential E_K and are listed in the Table.

The dose-response relation was determined using nonlinear regression and is given by the following:

$$E=E_{max}\left[\frac{1}{1+\frac{EC_{50}}{[ACh]^n}}\right], \quad (4)$$

where E_{max} is the maximal effect, EC_{50} is the concentration for half-maximal effect, and n is the binding order. The dose-response characteristics were best reproduced with $E_{max}=10$, $EC_{50}=9.13652$, and $n=0.47781$ (Figure 1B).

Expressed in pA/pF, $I_{K(ACh)}$ is given by the product of Equations 3 and 4 (as indicated in Equation 5):

$$I_{K(ACh)}=\left[\frac{10}{1+\frac{9.13652}{[ACh]^{0.477811}}}\right]\left[0.0517+\frac{0.4516}{1+\exp\left[\frac{V+59.53}{17.18}\right]}\right](V-E_K), \quad (5)$$

with the best-fit parameters at 1 μmol/L from the Table.

Figure 1C shows model $I_{K(ACh)}$ with accompanying APs at 1 and 6 Hz in control and with 0.003 μmol/L and 0.03 μmol/L ACh.

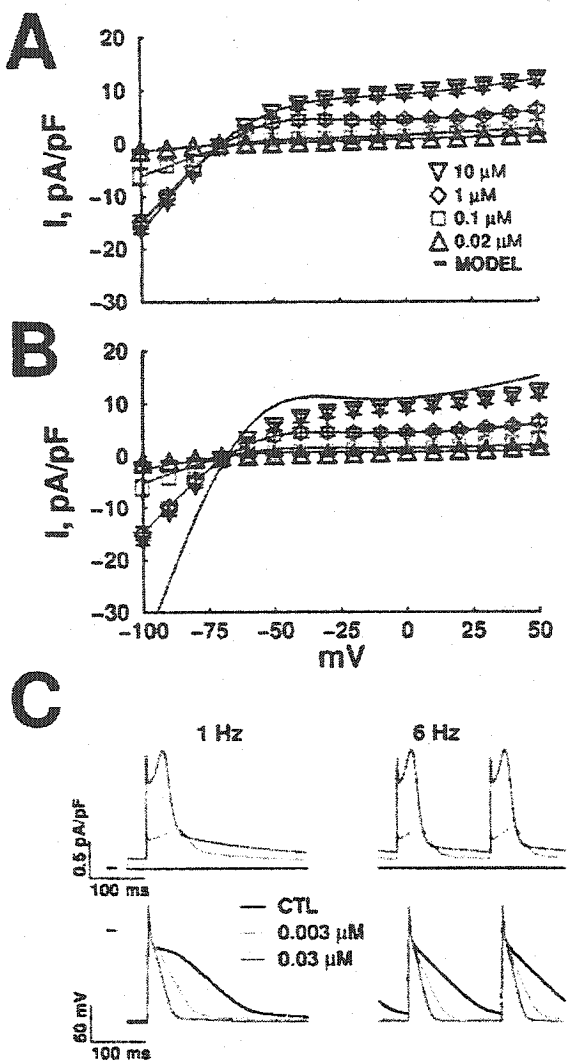

Figure 1. A, $I_{K(ACh)}$ *I*-V relations (data points are mean±SD) fit using Equation 3 (red curves). B, Data and model dose-response characteristics given by Equation 5. C, Model $I_{K(ACh)}$ (top) and APs (bottom) during 1 and 6 Hz as a function of [ACh]. Markers at left indicate 0 pA/pF (top) and 0 mV (bottom).

Experiment and Model AP Comparisons

Figure 2 compares experimental (left) and model (right) results. Mean AP durations (APDs) to 90% repolarization (APD_{90}) are shown in Figure 2A. Representative APs are shown in Figure 2B. ACh concentrations of 0.003 and 0.03 μmol/L had effects in the model similar to carbamylcholine (CBC) concentrations (0.1 and 1 μmol/L) producing moderate and strong APD abbreviation in tissue preparations and were therefore used in model simulations. Consequently, all model simulations were conducted within the range of ACh concentration over which the $I_{K(ACh)}$ *I*-V relation was in closest agreement with experiments (Figure 1B). Overall APD_{90} was reduced at maximum cholinergic stimulation by 81.7% and 73.8% in experiments and the model, respectively. APD rate adaptation (the difference in APD_{90} from 0.1 to 6 Hz) was substantial under control conditions (144 ms in experiments and 175 ms in the model; Figure 2C), but nearly abolished at maximal [ACh] (14 ms in experiments and 19 ms in the model; Figure 2D). Resting membrane potential was slightly hyperpolarized by $I_{K(ACh)}$. No significant ACh-dependent changes in AP amplitude and upstroke velocity (V_{max}) were discernible.

Equation 3 Coefficients for Each [ACh]

[ACh], μmol/L	a_0	a_1	a_2	a_3
0.02	$1.3384 \cdot 10^{-2}$	$2.2663 \cdot 10^{-2}$	$8.0253 \cdot 10^{1}$	$5.0714 \cdot 10^{0}$
0.1	$2.5400 \cdot 10^{-2}$	$1.4080 \cdot 10^{-1}$	$6.5730 \cdot 10^{1}$	$1.1690 \cdot 10^{1}$
1*	$5.1700 \cdot 10^{-2}$	$4.5160 \cdot 10^{-1}$	$5.9530 \cdot 10^{1}$	$1.7180 \cdot 10^{1}$
10	$9.6176 \cdot 10^{-2}$	$5.6040 \cdot 10^{-1}$	$6.3561 \cdot 10^{1}$	$2.3897 \cdot 10^{1}$

*1 μmol/L parameters used in Equation 5.

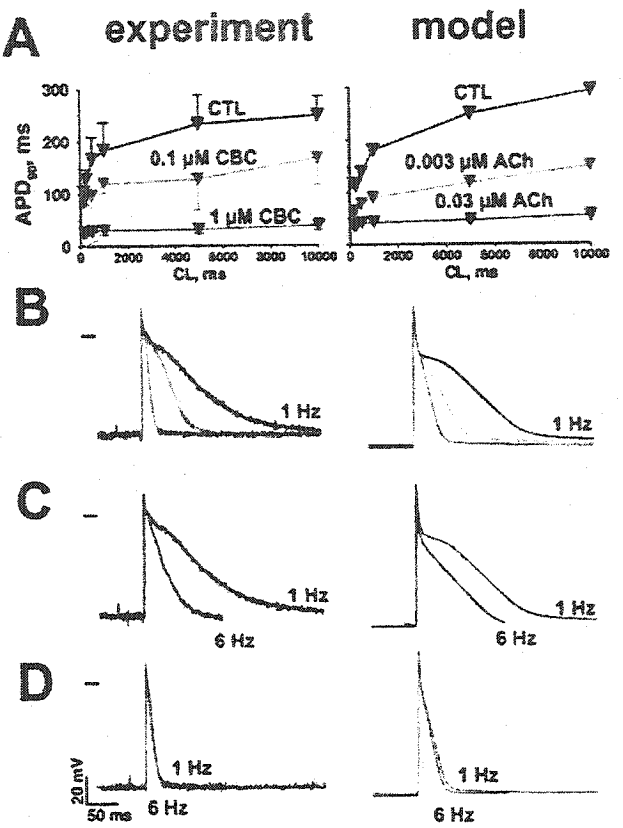

Figure 2. Comparison of experimental (left) and model (right) AP properties. A, Mean±SD experimental (n=7 dogs) and model AP duration, with representative experimental recordings (left) and model simulations (right) illustrating the dose response of AP changes (B), rate adaptation under control conditions (C), and abolition of rate-adaptation by ACh (D). CTL indicates control; CBC, carbamylcholine.

Experiment and Model Distributed Properties

Figure 3B compares in vivo measurements of canine atrial ERP at increasing levels of vagal stimulation in the 2-dimensional model as [ACh] was increased.[21] In the absence of ACh, the model ERP agreed well with experimental controls (166 versus 160 ms, respectively). Consistent with AP findings, ERP matched experimental data at maximal vagal stimulation (63 versus 60 ms, respectively). Like

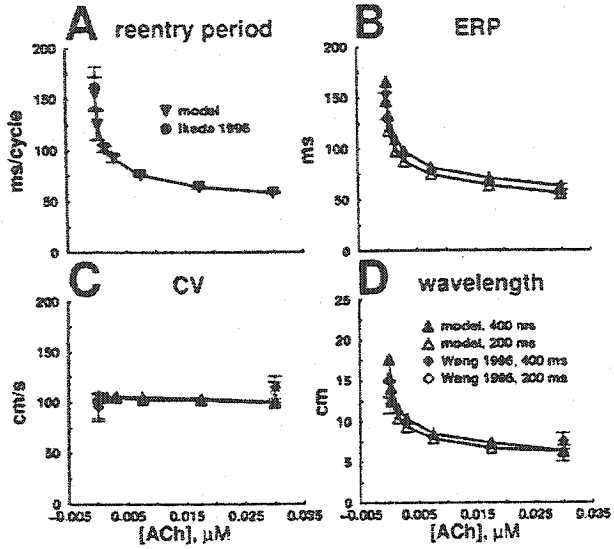

Figure 3. Comparison of model distributed properties at various [ACh] with experimental data at control and peak vagal effect from the literature, including ACh-induced acceleration of reentry cycle-length (A), ERP-shortening (B), unaltered CV (C), and wavelength reduction (D). Data are from Ikeda et al[34] and Wang et al.[21]

experimental data, model CV changes due to ACh were minimal (Figure 3C).[21,31] Associated wavelength reductions agreed quantitatively with experimental findings and paralleled ERP changes because CV was relatively constant (Figure 3D).[21]

ACh accelerates the rate of atrial reentry.[31–33] To evaluate this effect in the 2-dimensional model, reentry was initiated under control conditions (no ACh) and then with increasing [ACh]. The reentry period was determined from activation times in the upper left corner of the grid. In the absence of ACh, model reentry periods (Figure 3A) agreed with experimental controls.[34] The mean rate increased 2.7-fold across concentrations, whereas the SD decreased by 95%, indicating that ACh had accelerated and organized reentry.

Reentry in the Absence of ACh

Figure 4A shows a representative example at a single time point of a single reentry circuit under control conditions. Animation of activity in Figure 4A is also provided as an online-only movie (see online Movie 1). The rotor was unstable, propagating along a hypermeandering and irregular trajectory. The mean reentry cycle length was 155±16 ms (range, 132 to 195 ms), in agreement with previous measurements in isolated canine right atria (162±20 ms; range, 130 to 220 ms).[34] The cycle-to-cycle variability in position was quantified by plotting the trajectory of the rotor tip in 10 ms intervals (Figure 4B).[30] The standard deviation of the longitudinal position between cycles was 0.95 cm. The core area was calculated by dividing rotor-tip points into cycles (n=10) and constructing polygons traced by the tip for each cycle. The mean core area per cycle was thus determined to be 2.78±0.42 cm^2. Sustained activity was rare in the absence of ACh. In this example, the wave encountered the no-flux

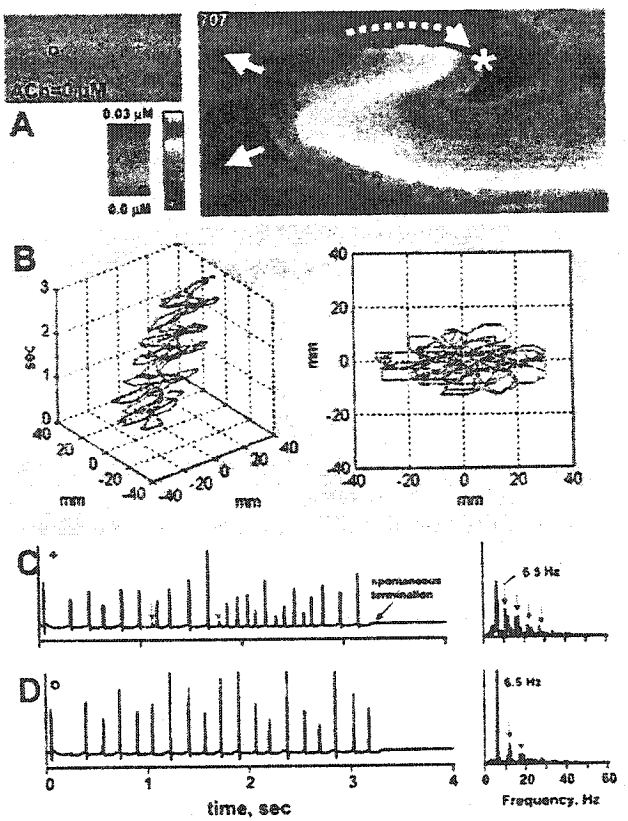

Figure 4. Unstable reentry under control conditions. A, Representative membrane potential map during activity (at time point indicated, in milliseconds). Asterisk indicates tip of the spiral; solid arrows, direction of wavefront propagation; and dashed arrow, chirality of the spiral. Trajectory of the tip of the spiral wave is plotted as a function of time (B, left) and in the space domain only (B, right). Electrograms shown from within the region of meander (C) and a distal region activated by wavefronts emanating from the spiral wave (D) are illustrated, along with corresponding FFTs. Blue arrows indicate higher harmonics of dominant frequencies.

boundary at the edge of the tissue substrate and terminated after ≈3 seconds of spontaneously sustained activity.

Electrograms were recorded within the region of reentry (Figure 4C) and at a more remote area (Figure 4D). In agreement with previous findings that a single meandering spiral is sufficient to produce AF-like electrograms,[31,34–36] electrogram complexes at both sites were rapid, irregular, and polymorphous. Activations at the distal site were irregular because of the nonuniform rate of reentry (Figure 4D). As observed experimentally,[34] signal polymorphism (variability in size and shape of electrograms) was greater in proximity to the spiral-wave core (Figure 4C). When the core drifted away from the recording site, electrical activity exhibited large-amplitude complexes. Return of the core again decreased signal amplitude. Large complexes were indicative of local activation, whereas deflections <10% of these were considered to be passive depolarizations (red arrows).[34] FFTs of electrograms revealed narrow-banded frequency content containing discrete peaks, with a dominant frequency (DF) at 6.5 Hz that correlated with the mean cycle length (Figures 4C and 4D). Higher-frequency peaks at decreasing power represent

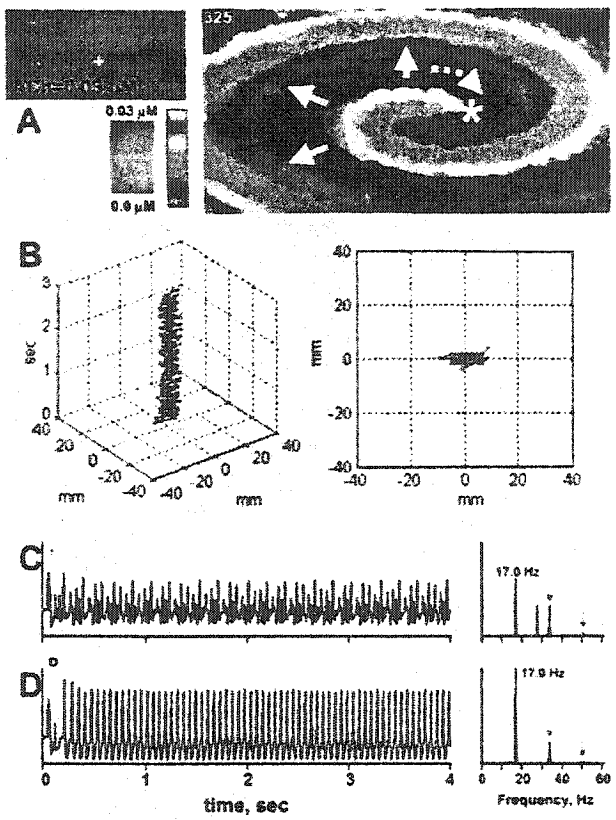

Figure 5. Organization of reentry by ACh. A, Representative membrane potential map during activity (time point indicated in milliseconds). Asterisk indicates tip of the spiral; solid arrows, direction of wavefront propagation; and dashed arrow, chirality of the spiral. Trajectory of the tip of the spiral wave is plotted as a function of time (B, left) and in space only (B, right). Electrograms are shown from within the region of meander (C) and from a distal region activated by emanating wavefronts (D), along with corresponding FFTs. Blue arrows indicate higher harmonics of dominant frequencies.

harmonics of the DFs (blue arrows). The notches that broaden each harmonic were attributed to meandering of the spiral wave pivoting point around an instantaneous center that drifts, with possible modulation by the Doppler phenomenon.[37,38] Comparison of Figures 4C and 4D indicates that spectral power was reduced in proximity to the spiral core.

Organization of Reentry by ACh

Figure 5A shows a single reentry circuit with 0.03 μmol/L ACh distributed uniformly over the computational substrate. Animation of activity in Figure 5A is also provided as an online-only movie (see online Movie 2). Reentry was organized into a stable stationary rotor (Figure 5B). The mean cycle length was 58±0.8 ms, a 2.7-fold rate increase from control (Figure 3A). Reflecting increased organization, the standard deviation of the position was 0.28 cm, reduced by 70% from control. The area of the core was 1.25±0.097 cm^2, reduced by ≈55% from control.

An electrogram within the spiral core (+, Figure 5C) and an example representative of activity at more distal locations (o, Figure 5D) are shown. Complexes were uniform and regular outside the core, characteristic of atrial flutter.[39] Within the core, meander of the spiral tip caused polymorphic activity. FFTs of electrograms reflected global organization. A dominant peak at 17.0 Hz correlated with the mean rate of reentry. Discrete peaks at higher harmonics were also seen (blue arrows). An additional peak at 28 Hz (Figure 5C) due to meandering of the spiral may be seen as a high-frequency wobble of the spiral core in the online Movies. This motion was not evident at the distal site (Figure 5D). Spectral power was markedly reduced within the core.

APD Heterogeneity and AF

Cholinergic effects are heterogeneously distributed in vivo.[40,41] To investigate the role of dispersion of APD and refractoriness in AF, ACh concentration was varied according to a sinusoidal distribution across the computational substrate. Equation 6 gives the distribution of ACh at position x, y as follows:

(6)
$$\mathrm{ACh}(x,y)=b_{\mathrm{ACh}}[1+B\cdot\sin(2\pi\cdot C\cdot x+\phi)\cdot\cos(2\pi\cdot C\cdot y)]$$

where $1\le x\le 600$ and $1\le y\le 300$ along the longitudinal and transverse dimensions, respectively, b_{ACh} represents baseline [ACh], B determines the relative amplitude of ACh oscillations around b_{ACh} with $0\le B\le 1$, and C controls the periodicity of the spatial distribution. $\Phi=0$ by default but was set to $\pi/2$ to initiate reentry when the heterogeneity was such that the S_2 stimulus encountered block in the transverse direction and failed to launch a rotating circuit.

Equation 6 created APD and consequently ERP gradients (graded changes from lowest to highest ACh concentrations). To obtain an estimation of spatial APD variation, the entire substrate was stimulated from rest at 6 Hz, and AP duration to −60 mV (APD_{-60}) was measured across the grid for the 10th pulse. APD_{-60} was used because −60 mV is the approximate voltage at which excitability is restored and APD_{-60} is therefore closely related to the ERP.

Reentry was simulated at varying [ACh] distributions (distance between lowest and highest concentrations) and a constant mean [ACh]. Figure 6 shows representative results. When [ACh] was closely distributed (Figure 6A; ≈0.67 cm), electrotonic influences limited APD variations; the spiral was distorted, but lines of block failed to form and no wavebreak resulted. Electrograms were regular, and associated FFTs confirmed a single discrete peak throughout the recording field. AF resulted when [ACh] gradients were distributed over larger distances (Figure 6B; 3.3 cm). Ongoing breakup into independent wavelets was observed. Electrograms were irregular and polymorphous. FFTs were disorganized, yet frequency content was narrow-banded with one or multiple discrete peaks, the largest of which correlated with mean frequency. Flutter-like activity was restored when the ACh distribution was sufficiently diffuse (Figure 6C; 10 cm).

The DFs were from 12.2 to 15.3 Hz, reflecting substantial ACh-induced acceleration of reentry relative to control (Figure 4), despite the absence of ACh in certain regions. In Figure 4A, stable reentry was possible at the rapid rate because electrotonic modulation shortened ERP in regions where ACh was absent. In Figure 4B, the greater dispersion of vagal effects decreased electrotonic modulation, and on-

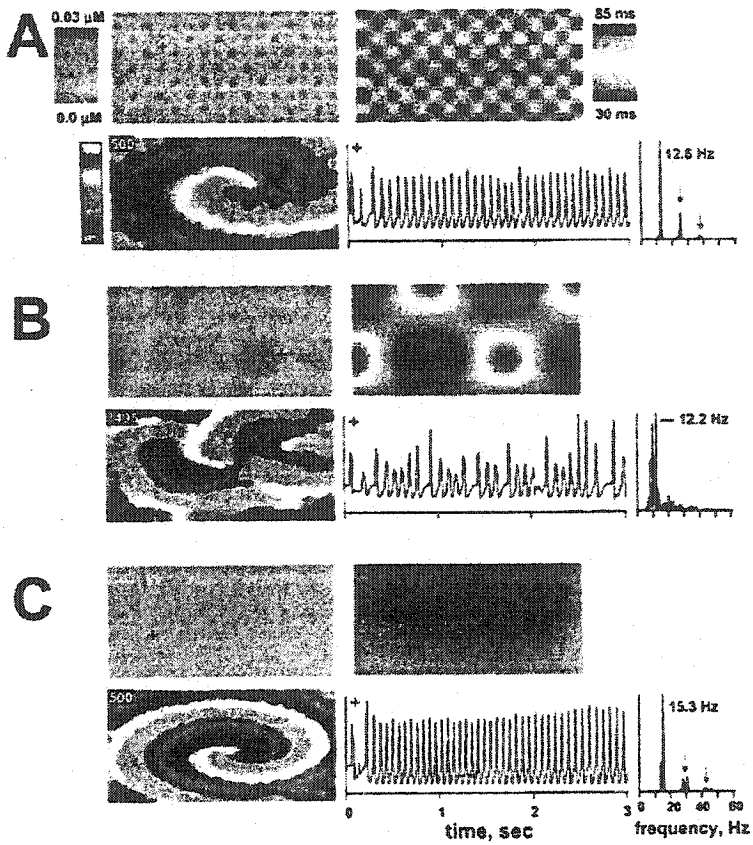

Figure 6. Effects of APD heterogeneity on reentry. Top left, ACh distribution, Top right, APD distribution. Bottom left, Membrane potential maps (at the times indicated in milliseconds); bottom right, electrogram simulations at the points given by the "+" symbols in the ACh distribution grids, with corresponding FFTs at the right. Blue arrows indicate higher harmonics of dominant frequencies. Reentry was stable and activation uniform when APD gradients were closely-distributed (A) or sufficiently diffuse (C). AF resulted when APD gradients were distributed at ≈3 cm (B).

going breakup occurred because reentry was faster in regions of high [ACh] with short ERP, causing wavefronts to impinge on zones of greater refractoriness in regions with low [ACh]. The spiral wave in Figure 4C rotated in a region of high [ACh] with a DF (15.3 Hz) close to the mean reentry rate for 0.015 μmol/L (≈67 ms; 14.9 Hz) uniform ACh (Figure 3A).

Baseline APD_{-60} values ranged between 28 and 81 ms in Figures 4A through 4C, with differences being greater at the largest distributions (smallest electrotonic attenuation). Although this analysis provides a useful approximation of the dispersion of repolarization, variations in local activation rate during AF change APD on a cycle-to-cycle basis: this adaptation is important to AF-like dynamics. At rapid rates of AF (DF ≈12.2 Hz), regions of block result in local episodes of 2:1 conduction that increase the range of APD_{-60} values. In contrast to the static APD_{-60} values shown in Figure 4B, APD_{-60} was 65±23.6 ms (range, 15 to 111 ms) in cells with 0 μmol/L ACh and 34.3±3.3 ms (range, 30.1 to 34.9 ms) in cells with 0.015 μmol/L.

Results in Figure 6 indicate that AF only occurred for certain heterogeneity conditions. Figure 7 shows an analysis of the relationship between the combinations of concentrations and spatial distributions and AF occurrence. Each entry in the graphic represents results from 1 of 67 simulations. The minimum [ACh] was 0 and the maximum for each simulation is shown on a logarithmic scale on the vertical axis, with [ACh] distributions (distances between maximum and minimum [ACh]) given on a logarithmic scale along the horizontal axis. "Sustained AF" was defined as AF >5 seconds. Conditions were classified as "fibrillatory" if AF-like activity was not sustained. Conditions were said to be "nonfibrillatory" when no wavebreak occurred. Fibrillatory distributions ranged from 1.25 to 2.5 cm at low [ACh] to 1.25 to 7.5 cm at high [ACh]. Sustained AF occurred only at high [ACh] when APD gradients were large and distributed between 1.88 and 5.0 cm (mean 3.33 cm). Results in Figure 7 suggest that the

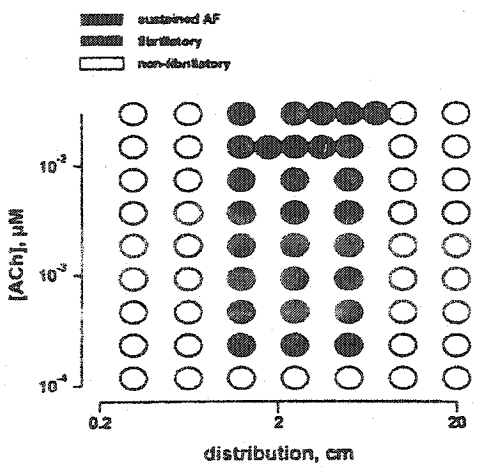

Figure 7. Role of [ACh] heterogeneity in the occurrence of AF at various combinations of [ACh] gradients and distributions. Each entry in the graphic presents results from 1 of 67 5-second simulations. The minimum [ACh] was 0 and the maximum for each simulation is shown on the vertical axis. Concentration distributions (distances between maximum and minimum concentrations) are on the horizontal axis.

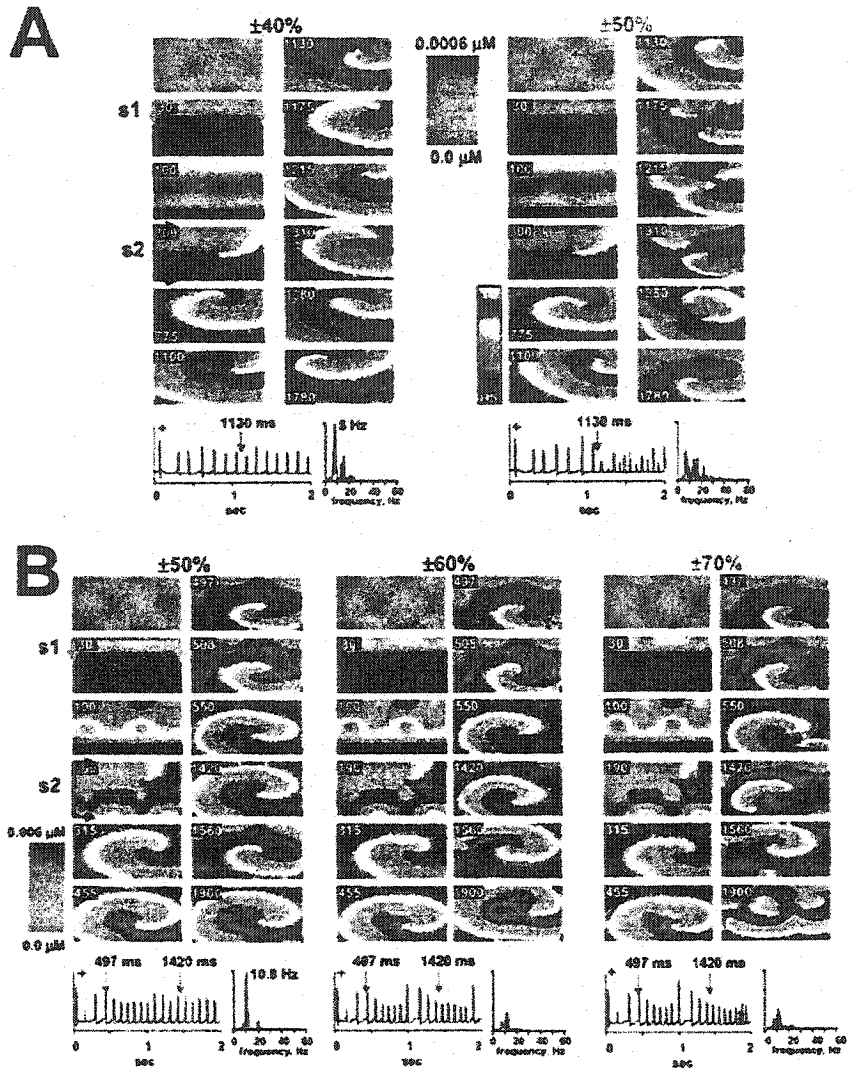

Figure 8. Role of [ACh] gradients as mean [ACh] increases. Effects of [ACh] at 0.0003 (A) and 0.003 µmol/L (B) were simulated and concentration oscillations imposed at ±10% increments of baseline. For each condition, potential maps show dynamics at identical times (ms) to illustrate changes. At increasing [ACh], larger [ACh] gradients were needed to induce wavebreak (±50% in A versus ±70% in B). Vertical red arrows indicate regions of instability and wavebreak.

ACh effect must be sufficiently strong to permit sustained AF, and that as ACh concentration increases, larger spatial distributions are needed for fibrillation. To determine the effect of higher ACh concentrations with smaller differences between peak and trough concentrations, 7 additional simulations were conducted with peak [ACh] of 0.03 µmol/L and trough [ACh] of 0.015 µmol/L (at all distributions); nonfibrillatory activity was observed in all cases (results not shown).

Vagal stimulation reduces mean ERP while increasing ERP heterogeneity in vivo.[42] Figure 8 illustrates the role of concentration gradients in ACh-related AF as cholinergic tone increases. Potential maps show the initiation of reentry, and subsequent activity at the simulation time (ms) indicated in the upper left corner. In Figure 8A, 0.0003 µmol/L mean [ACh] was distributed at 2.5 cm, and concentration oscillations (the difference between maximum and minimum [ACh]) were imposed in increments of ±10% of this baseline. When concentration oscillation amplitude was increased from ±40% (left panels) to ±50% (right panels), wavefront thinning (arrows) became clear at 1130 ms, resulting in a transition from flutter-like to AF-like dynamics (1175 ms). FFT alterations reflected the increased disorganization. Figure 8B shows results with a 10-fold increase in mean [ACh] (0.003 µmol/L). This time, a transition from flutter-like to AF-like behavior was observed when concentration oscillation amplitude was increased from ±60% to ±70%. Results at ±50% are also shown, as wavebreak (arrows) was clearly observed at ±60% (497 and 1420 ms), yet without a change in the overall activation pattern. The instabilities at ±60% were reflected in electrogram changes, although AF-like signals were only observed at ±70%. These results demonstrate that as baseline [ACh] increases, larger [ACh] oscillations are needed for fibrillation. DFs were at 8 Hz (Figure 8A) and 11 Hz (Figure 8B). These rates are comparable to the reentry rate at a homogeneous [ACh] (Figure 3A; cycle-lengths 125.4 and 92.5 ms, respectively) equivalent to the mean under each condition, indicating that mean concentrations were the primary determinants of DFs. Otherwise, spectral power was markedly reduced after breakup, suggesting frequency modulation by competing transient circuits. As in Figure 6, breakup occurred because reentrant activity

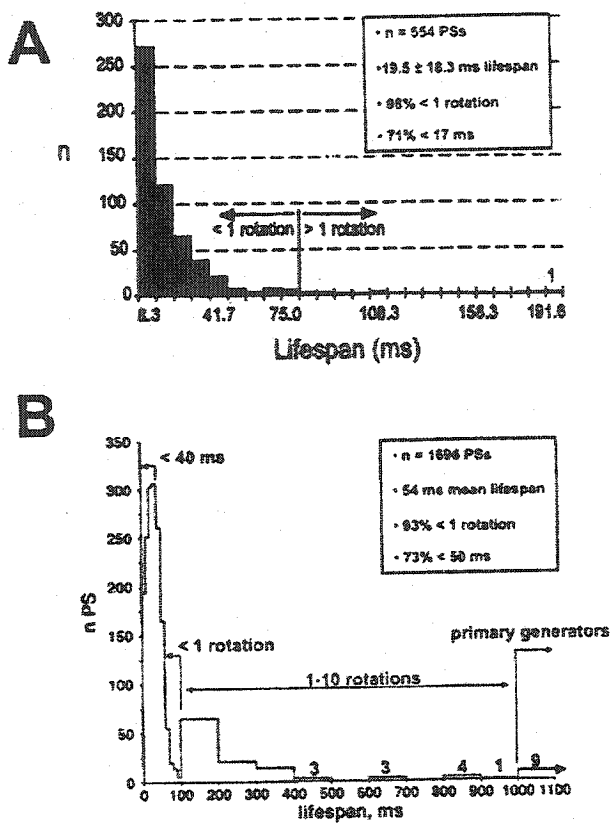

Figure 9. Analysis of lifespan of wavelet PSs during AF in milliseconds and rotations. Model results (B) are compared with experimental studies of Chen et al[4] (A).

propagated faster through regions of short refractoriness (higher [ACh]) and impinged on zones of prolonged refractoriness (lower [ACh]). Breakup occurred when ACh oscillations were sufficiently large that electrotonic modulation failed to bring refractory zones of low [ACh] regions within the accelerated reentry period.

PS Lifespan Analysis

Chen et al[4] used a novel phase analysis technique to characterize experimentally observed wavelets on the basis of PSs in a sheep model of cholinergic AF (Figure 9A). To compare results of our model with these data, manual measurement of PS (n=1696) lifespans was performed in the 7 simulations of sustained AF discussed above (Figure 9B). As in the experiments of Chen et al, the majority of PSs were short-lived: 93% lasted less than the average rotation period of reentry (≈95 ms), and 78% lasted <50 ms. PSs persisted for more than 1 rotation but less than 1 second (≈10 rotations) in 6.5% of cases. Nine PSs (≈0.5%) belonged to stable high-frequency circuits and acted as sources generating shorter-lived wavelets. Five of seven simulations with sustained AF were maintained by 1 PS lasting throughout the simulation (single-spiral AF). Two were maintained by a succession of long-lived PSs, with no more than 2 present simultaneously. On average, 3.0±1.3 wavelets were present at any one time.

Mechanisms of AF Maintenance

AF Maintained by a Single Spiral Wave

Figure 10 shows an example of AF maintained by a single spiral wave. The distribution of [ACh] (1.67 cm), an APD distribution map, electrogram recording sites, and a representative potential map during AF are shown (Figure 10A). Animation of activity in Figure 10A is also provided as an online-only movie (see online Movie 3). A functionally determined rotor with clockwise chirality was located near (+) and acted as a primary source of activity, generating impulses that fractionated into multiple independent wavelets along the heterogeneous substrate. Most died out without incidence. Several PSs with opposite chirality attached to functional anchors near the right border and persisted for 1 to 3 rotations. An average of 3.5±1.2 wavelets were simultaneously present, with 6 to 7 at times of peak disorganization (Figure 10D). Wavelets tended to multiply from the primary spiral and would at times coalesce to form a large unstable circuit, reducing the wavelet count to 1. These episodes of global organization were short-lived, however, as activity cycled through varying degrees of complexity. Sequences of spatiotemporal periodicity were evident throughout.

Representative examples of electrograms recorded near (+, Figure 10B) and distal to (o, Figure 10C) the primary circuit are shown. The irregular propagation patterns were associated with decreased electrogram amplitude and increased morphological variability at the distal site. Although the power of the major spectral peak was also reduced, DFs at both locations were the same (11.2 Hz) and correlated with the mean cycle length of the dominant circuit (89.3 ms), as expected for AF arising from a relatively stable periodic source. Frequency content was narrow-banded with discrete spectral peaks between 8.7 and 19.7 Hz. The DF was slower than the reentry rate with uniform ACh (Figure 3A; 13.1 Hz) at the same mean concentration (0.0075 μmol/L), indicating that heterogeneity slowed reentry. The reduced rate is due to anchoring and slowing of the dominant spiral about a functional obstacle and the effects of electrotonic modulation, through which influences from regions of low [ACh] increase APD in regions of high [ACh].

AF Maintained by Multiple Spiral Waves

AF sustained by multiple sources has also been observed, which may appear sporadically[8] or be spawned several centimeters away from the point of initiation.[6] Figure 11 shows an example of AF maintained by up to 2 spiral waves. The distribution of [ACh] (3.33 cm), an APD distribution map, electrogram recording sites, and a representative potential map of activity are shown (Figure 11A). Animation of activity in Figure 11A is also provided as an online-only movie (see online Movie 4). AF initially arose from a primary rotor below (+). This spiral failed to anchor, increasing the variability of the PS trajectory. Emanating impulses impinged on refractory tissue, fractionating into wavelets with variable chirality. This time, many more PSs completed multiple reentry cycles, competing with the primary spiral. At ≈2.5 seconds the initial primary spiral died out along the bottom right border, at the time indicated by the black vertical line in Figure 11C. A second generator of opposite chirality origi-

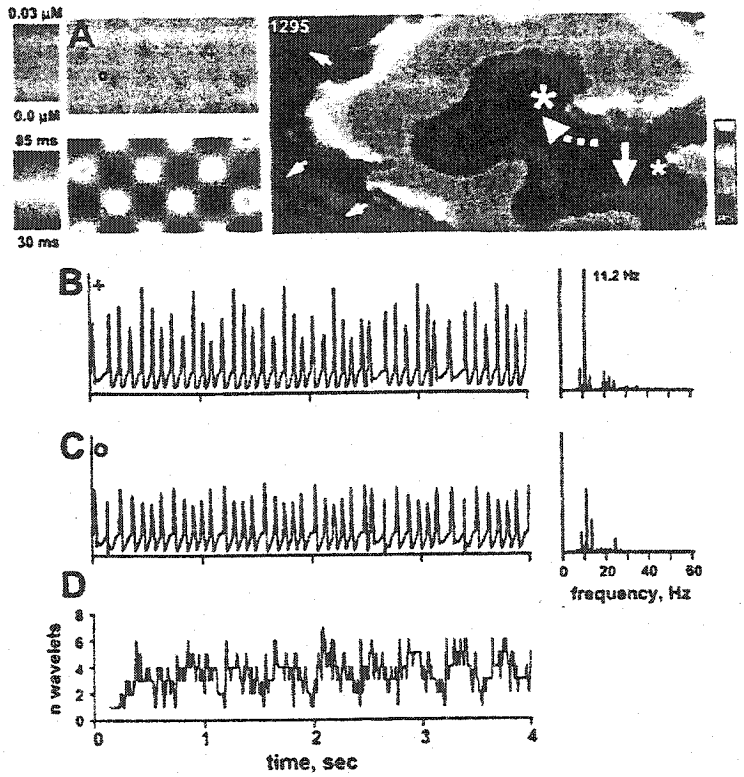

Figure 10. AF maintained by a single spiral wave. A, Top left, [ACh] over the grid; Bottom left, APD distribution; Right, a representative transmembrane potential map at one time point during AF. Asterisk indicates tip of the spiral; solid arrows, direction of wavefront propagation; and dashed arrow, chirality of the spiral. The larger symbols correspond to the primary spiral; smaller symbols to transient wavelets generated by the primary spiral. Electrograms were recorded near the source (B) and distally (C). Corresponding FFTs are at the right. D, Number of wavelets present at each time.

nated from wavebreak at ≈2.3 seconds, then assumed dominance and sustained fibrillation for the duration of the simulation (indicated as "generator 2" in Figure 11C). No appreciable difference in the reentry periods of the generator spirals was found. Figure 11A of the figure shows activity when both generator spirals coexisted. An average of 3.0±1.4 wavelets were simultaneously present, with as many as 7 at times of peak disorganization (Figure 11D). Sequences of

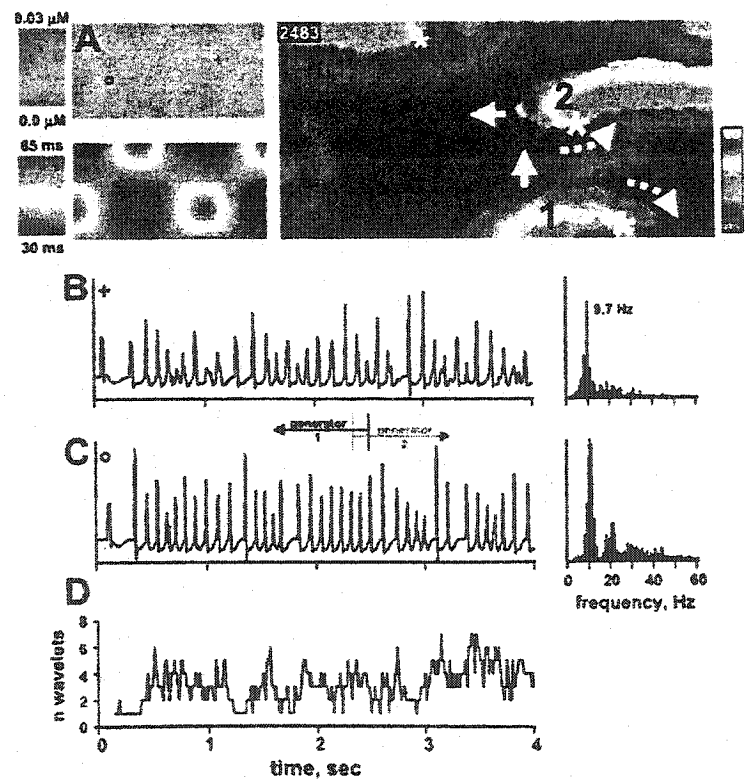

Figure 11. AF maintained by multiple spiral waves. A, Top left, [ACh] over the grid; Bottom left, APD distribution; Right, a representative transmembrane potential map at one time point during AF. Asterisk indicates tip of the spiral; solid arrows, direction of wavefront propagation; and dashed arrow, chirality of the spiral. In this example, one primary spiral maintained AF until 2.5 seconds of the simulation. This was then replaced by a second spiral originating from wavebreak at 2.3 seconds, which sustained AF for the rest of the simulation. Map in A was obtained at an instant when both the initial generator (1) and the second spiral (2) coexisted. Electrograms were recorded near the source (B) and distally (C). Corresponding FFTs are at the right. D, Number of wavelets present at each time.

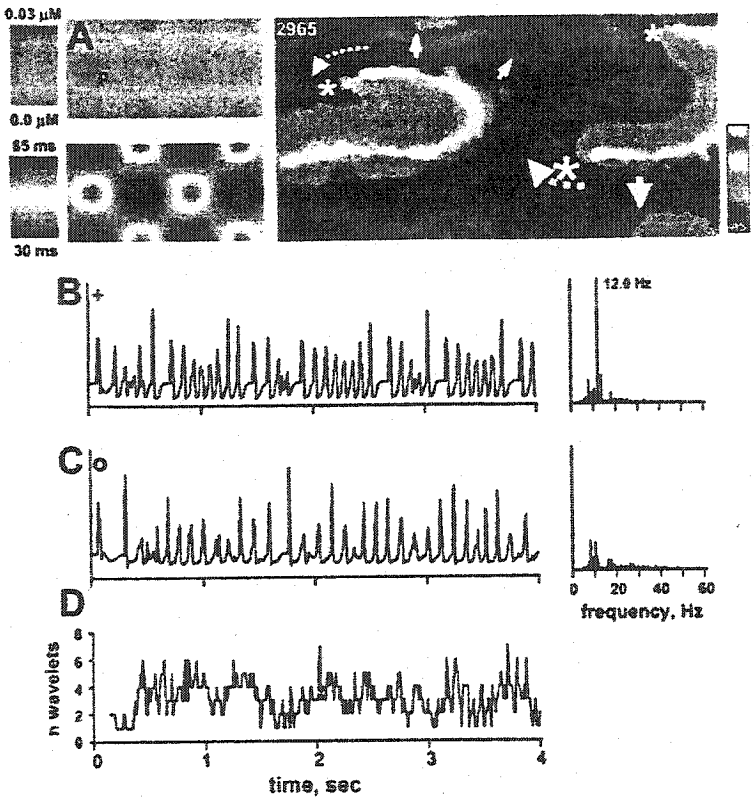

Figure 12. Apparent multiple-circuit AF. A, Top left, [ACh] over the grid; Bottom left, APD distribution; Right, a representative transmembrane potential map at one time point during AF. Asterisk indicates tip of the spiral; solid arrows, direction of wavefront propagation; and dashed arrow, chirality of the spiral. Larger symbols correspond to the primary spiral; smaller symbols to transient waves emanating from the primary spiral. Electrograms were recorded near the source (B) and distally (C). Corresponding FFTs are to the right. D, Number of wavelets present at each time.

spatiotemporally periodic propagation patterns arising from both generators were evident. Heterogeneity was such that the minimum path length for reentry of transient circuits was clearly not determined by the wavelength for all cycles, as calculated in Figure 3D and Wang et al[21] and Rensma et al.[22]

Electrograms recorded at all sites were characteristic of AF. Representative examples of electrograms recorded near (+, Figure 11B) and distal to (o, Figure 11C) the primary sources are shown. Matching DFs (9.7 Hz) in Figures 11B and 11C indicated that activity at both sites arose from the same generator-type spiral. The rate was slower than in Figure 10 because refractory regions were broader, increasing the cycle length around functional obstacles. The amplitude of signals near the primary sources was reduced by the proximity of the cores, whereas the spectral profile at the distal site was much less organized due to the competing influence of other transient spirals.

Apparent Multiple-Circuit AF

Figure 12 shows an example of AF maintained by a single spiral wave (≈2.8 cm dispersion), which gives the appearance of multiple-circuit AF. Figure 12A shows a representative potential map during AF and animation of activity is provided as an online-only movie (see online Movie 5). A single spiral-wave generator was located below (+) and persisted for the duration of the simulation, although numerous PSs completed multiple reentry cycles. The mechanism of breakup was the same as in other simulations of AF (Figures 6, 8, 10, and 11). On average, 3.1±1.2 wavelets were present. Electrograms recorded at all sites were characteristic of AF. Electrogram frequency content near the primary source (+, Figure 12B) was narrow-banded, with a dominant discrete peak (12.0 Hz) that corresponded to the mean period of the source (≈80 ms). DFs were greatly reduced in Figure 12C and lower frequencies were more prominent, reflecting a process of spectral transformation[43] between the generator region and the distal site. It might have been expected that the DF would fall between those in Figures 10 and 11, because the spatial dispersion of [ACh] in Figure 12 is intermediate between those in Figures 10 and 11. The DF was faster, however, likely because of the net effect of less electrotonically-mediated ERP increase in regions of high [ACh] than in Figure 10 (favoring an increased rate of reentry), smaller functional obstacles than in Figure 11, and less interference by competing transient circuits than when AF was maintained by multiple spirals (Figure 11).

Discussion

We have developed a mathematical model of canine atrial electrophysiology and cholinergic actions that reproduced experimentally observed AF dynamics. AF in the model is maintained by primary reentry sources, which are often single dominant spiral waves, but may also involve more than one spiral wave in succession with periods of overlap.

Model Studies of AF

Since the early 1960s, Moe's multiple-wavelet hypothesis[1] has shaped clinical and experimental conceptions of AF. To test his hypothesis, Moe et al[2] developed a simple cellular automaton computer model of canine atrial tissue and cholinergic AF containing 992 4-mm diameter tissue-units in a 12.4×12.8 cm atrial sheet. Under control conditions, CV was

≈80 cm/s and conduction time ≈160 ms (about twice typical experimental values). Units were programmed with rate dependence of the absolute refractory period. CV dropped to 20 cm/s during the relative refractory period (30 ms fixed duration), slowing propagation to extremely low levels during repeated stimulation. ERP heterogeneity was randomly distributed, permitting maximal ERP gradients between adjacent units, as electrotonic modulation was not incorporated.

Moe acknowledged that this substrate bore only a limited resemblance to atrial tissue electrophysiology and recognized severe limitations to the computer representation and capacity. The strength of the model was that it displayed sustained turbulent reentrant activity resembling fibrillation. Limitations included the nonphysiological determinants of the cellular-automaton substrate, totally random ERP distribution (impossible with physiological electrotonic interactions), and CV heterogeneity, on which fibrillation depended. The model suggested that AF is a totally random process maintained by the ongoing multiplication of wavelets, with 23 to 40 needed at any time.

Our model included a complete ionic representation of the canine atrial AP, ensuring that rate dependence and ACh-related changes in rate-dependent properties were realistic (Figure 2). Coupling properties were selected to ensure that important 2-dimensional properties including ERP, CV, CV anisotropy, and wavelength were physiological at all [ACh] used (Figure 3). These features enabled the model to reproduce experimental observations of AF, permitting meaningful analyses of potential underlying mechanisms.

Under control conditions, significant rate adaptation caused unstable reentry and meander that was sufficient to manifest as AF (Figures 4C and 4D), although spontaneous activity was generally self-terminating. Uniform ACh abolished rate adaptation (Figure 2D) and markedly reduced the wavelength (Figure 3D), thereby organizing reentry into a highly stable stationary circuit and flutter-like rhythm (Figure 5D). These results are consistent with the findings of Nygren et al,[44] who recently explored the role of rate adaptation in spiral-wave stability using models of the human atrial AP by Nygren et al[45] and Courtemanche et al.[46] The Courtemanche AP displayed substantial rate adaptation although the Nygren AP did not; consequently, the Nygren model supported very stable and periodic reentrant activity, whereas the Courtemanche model displayed less stable, aperiodic behavior with high-frequency oscillations as occur during AF.[44] Like the Courtemanche model, canine APs display substantial rate adaptation (Figure 2), yet are considerably shorter than human APs. Consequently, reentry properties in the present model are between the Nygren and Courtemanche models, and this intermediate level of stability contributed importantly to the dynamics of sustained AF (Figures 10 through 12).

Vagal discharge has long been known to promote AF by decreasing atrial ERP and increasing the spatial heterogeneity of refractoriness.[40,41] Heterogeneous [ACh] distribution in the model created repolarization gradients that forced the breakup of reentry, promoting global disorganization and AF. Liu et al[42] measured canine atrial ERP at 7 locations during vagal stimulation in vivo (2 cm between adjacent sites). Mean ERP was reduced from 110 to 83 ms and the SD between sites was increased from 9 to ≈17 ms. Our model results are consistent with these data, and predict the conditions that best promote cholinergic AF: sufficient [ACh] (Figure 7), appropriate [ACh] and APD gradients (Figure 6), and a need for larger [ACh] and APD spatial gradients with increasing mean [ACh] (Figure 8). The arrhythmogenicity of these conditions is potentiated by an ACh-induced increase in the rate of spiral rotation, causing activity to impinge on zones of greater refractoriness.

Comparison With Experimental Studies of Vagal AF

Sustained AF in the model was due to primary sources from which emanating activity formed spatiotemporally periodic patterns of wavelet propagation (Figures 10 through 12). Spectral analysis quantitatively reflected this organization, demonstrating that source frequencies may also be dominant at distal sites (Figures 10 and 11) or altered by spectral transformation along the heterogeneous myocardium (Figure 12). Both results are consistent with experimental studies of the spatial distributions of DFs during AF, demonstrating how activity at various sites may be related, despite seemingly random activity throughout. Berenfeld et al[47] demonstrated that AF arising from these mechanisms may be characterized by multiple domains with distinct DFs on the atrial epicardium, thereby revealing a hidden organization, independent of the activation sequences or nature of the electrograms. Some studies emphasize the spatial variability of spectral properties,[48,49] whereas others demonstrate that DFs may form large uniform domains[47] or be spectrally transformed,[50] depending on conditions between sites of comparison. As in these experimental studies, we noted a prominent underlying organization in AF, with the ability of vagal tone to promote sustained AF related both to stabilization of a primary spiral wave (which causes arrhythmia maintenance) and disorganization of propagation by repolarization gradients (which causes fibrillatory dynamics).

Schuessler et al[32] first demonstrated that ACh exerts an organizing influence on fibrillatory dynamics, and that AF maintenance depends on the strength of this effect. In an in vitro study of cholinergic AF, the number of circuits and wavelets increased with increasing [ACh], but activity was only sustained at high concentrations when a single, relatively stable circuit emerged and dominated activity. The wavelet count was greatest after stabilization. Skanes et al[5] further established organization during cholinergic AF, demonstrating that complex AF electrograms arose from a small number of dominant frequencies. Both Skanes et al[5] and Mandapati et al[3] located stable high-speed reentry circuits acting as high-frequency sources, and demonstrated spatiotemporal periodicity in the emanating wavefronts and wavelets. Flutter-like electrograms with the highest dominant frequencies were most commonly located in the left atria, with AF-like signals appearing distally and in the right atrium. Building on these results, Mansour et al[50] demonstrated that left atrial sources produce a left-to-right atrial frequency gradient, as wavefronts sometimes encounter local activity and not all conduc-

tion pathways (Bachmann's bundle, inferoposterior pathway) are able to capture in a 1:1 manner.

Indications from our model that multiple wavelets are a consequence of AF-generating mechanisms, rather than a cause of AF, agree with the wavelet analysis of Chen et al during cholinergic AF (Figure 9A).[4] In the latter study, the mean PS (n=554) lifespan was 19.5±18.3 ms with a range that varied from 8.33 (1 frame) to 200 ms. The number of waves that entered the mapping field (15.7±1.6) significantly exceeded the number that exited (9.7±1.5). If wavebreak and the resulting wavelets were maintaining AF, the number of wavelets exiting the field of view would have been expected to exceed the number entering. The distribution of surviving PSs was found to be nonrandom, as would occur for activity originating from primary sources.

In the 7 simulations of sustained AF, ongoing breakup of primary circuits formed wavelets that would collectively form unstable circuits (as in Figures 10 through 12), with on average ≈3 wavelets at any time. In canine cholinergic AF, Allessie et al[51] found an average of 3 wavelets (range from 0 to 5) present per atrium. Schuessler et al[32] observed 0 to 15, with 5.1±1.8 present during sustained AF. Liu et al[42] reported 3.3±0.3 wavelets at a time. Similarly, Kumagai et al[52] found an interdependence between unstable and short-lived reentrant circuits and resulting multiple daughter wavelets during experimental AF. Breakup of unstable circuits formed wavelets that were continuously re-forming unstable circuits. In keeping with the present work, the mechanism of fibrillation in these studies may be a ceaselessly correcting balance between organization and disorganization of complex dynamics. Although a perfect balance is never obtained, neither does a flutter-like rhythm or totally random activity ever gain lasting control. Organizing influences exerted by basal levels of ACh appear to be in constant competition with the disorganizing pressure of ACh-related heterogeneity, such that AF represents an ongoing process of breakup and self-organization. It may be the tendency of wavelets to coalesce, rather than to multiply, that is necessary for AF maintenance.

Our results support the notion that single reentrant sources (analogous to Lewis' "mother wave" concept[11]) may maintain AF, but also demonstrate that under certain conditions, AF may arise from more than one coexisting spiral wave, analogous to multiple-circuit reentry.[53,54] Moe's classic computer model of AF and multiple-wavelet hypothesis were contributions of fundamental importance, but were limited by the analytical and experimental methodologies available. Modern computing techniques and a wealth of experimental data allowed us to develop a more realistic computer model, which indicates that (1) AF may be maintained by primary sources that in many cases are single rotors, (2) global dynamics during AF are nonrandom, and (3) most wavelets are a consequence of AF-generating mechanisms, not a cause of AF.

Clinical AF is most commonly observed in the contexts of chronic AF and pathologies like congestive heart failure (CHF). Like cholinergic AF, tachycardia-induced remodeling in chronic AF decreases ERP and increases ERP heterogeneity.[55] Although the ionic mechanisms of action potential changes in tachycardia-remodeled atria are different from those in cholinergic AF,[56] comparable changes in action potential properties (decreased APD and APD rate adaptation, increased APD heterogeneity) suggest that basic mechanisms of AF maintenance may be similar. In contrast, CHF primarily alters the atrial substrate by promoting interstitial fibrosis; associated ionic remodeling, although substantial, minimally effects atrial ERP.[20,57] CHF-related AF appears to arise, at least in some instances, from a single macroreentrant source.[58] Further work is needed to evaluate quantitatively the potential mechanisms of AF based on substrates other than increased cholinergic tone.

Novel Findings and Potential Significance

The present model of AF in a 2-dimensional system with realistic atrial ionic and propagation properties agrees well with experimental observations and has important potential implications regarding AF mechanisms. To our knowledge, it is the first such model described. The model presents a tool that may be useful in the quantitative analysis of hypotheses regarding mechanisms of AF in defined pathological substrates. Weaker left-ventricular inward-rectifier (I_{K1}) rectification appears to stabilize single left-ventricular rotors underlying VF, whereas strong I_{K1} rectification in the right ventricle leads to rotor instability, termination, and wavebreaks.[59] Our model may similarly be useful in the evaluation of the role of specific ionic currents, providing insights into potential antiarrhythmic drug mechanisms and helping in the development of new antiarrhythmic agents. Preliminary data suggest that the model provides novel and potentially important insights into the mechanisms of Na^+ channel–blocking drug-induced AF termination.[60]

Potential Limitations

Our model representation of canine atrial tissue contains numerous simplifications. No area in the atria comprises a 2-dimensional 5×10 cm^2 sheet. Rather, the normal atria have substantial areas of conduction discontinuity, in particular in the septum[61] and the venae cavae. Although many experimental studies of AF have been performed in isolated, unfolded atrial preparations,[32,62] and are therefore more comparable with the present model, even these possess atrial microstructure that may contribute importantly to the stability of AF, as reentry may occur within or be anchored by pectinate muscle bundles projecting from the plane of the tissue.[63] In addition, the no-flux model boundary conditions in the model may protect vortices from terminating, thereby influencing the balance between source-type spirals and resulting wavelets.[59] Finally, it is possible that the mechanisms of AF may be different in tissues of larger dimension, which might more readily permit the coexistence of more than one primary spiral-wave generator. We have begun to examine this issue and have found that even in a 4-fold larger 2-dimensional sheet (10×20 cm), AF can be maintained by a single primary spiral wave, but that under different conditions activity resembles multiple-wavelet reentry with no long-lived spiral-wave sources. We selected the dimensions of the computational substrate for the present study to reproduce overall conduction times and tissue dimensions in normal dog

atria. A detailed evaluation of AF mechanisms in a much larger atrial substrate, as might for example occur with severe CHF, is potentially very interesting but goes beyond the scope of the present study.

Acknowledgments

The authors thank the Canadian Institutes of Health Research (CIHR), the Natural Sciences and Engineering Research Council (NSERC), and the Mathematics of Information Technology and Complex Systems (MITACS) Network for research funding. Our work was made possible through access to the infrastructure and resources generously funded by MACI, Multimedia Advanced Computational Infrastructure for Alberta. The authors also thank Dr Yves Léger and the "Réseau Québécois de Calcul de Haute Performance (RQCHP)" for providing essential computing resources. Sincere appreciation is extended to Annie Laprade for secretarial help with the manuscript. James Kneller was supported by a CIHR MD, PhD Studentship and a Merck Pharmacology Fellowship.

References

1. Moe GK. On the multiple wavelet hypothesis of atrial fibrillation. *Arch Int Pharmacodyn Ther.* 1962;140:183–188.
2. Moe GK, Rheinboldt WC, Abildskov JA. A computer model of atrial fibrillation. *Am Heart J.* 1964;67:200–220.
3. Mandapati R, Skanes A, Chen J, Berenfeld O, Jalife J. Stable microreentrant sources as a mechanism of atrial fibrillation in the isolated sheep heart. *Circulation.* 2000;101:194–199.
4. Chen J, Mandapati R, Berenfeld O, Skanes AC, Gray RA, Jalife J. Dynamics of wavelets and their role in atrial fibrillation in the isolated sheep heart. *Cardiovasc Res.* 2000;48:220–232.
5. Skanes AC, Mandapati R, Berenfeld O, Davidenko JM, Jalife J. Spatiotemporal periodicity during atrial fibrillation in the isolated sheep heart. *Circulation.* 1998;98:1236–1248.
6. Schuessler R. Does size matter? *J Cardiovasc Electrophysiol.* 2001;12: 875–876.
7. Jais P, Haissaguerre M, Shah DC, Chouairi S, Gencel L, Hocini M, Clementy J. A focal source of atrial fibrillation treated by discrete radiofrequency ablation. *Circulation.* 1997;95:572–576.
8. Harada A, Sasaki K, Fukushima T, Ikeshita M, Asano T, Yamauchi S, Tanaka S, Shoji T. Atrial activation during chronic atrial fibrillation in patients with isolated mitral valve disease. *Ann Thorac Surg.* 1996;61: 104–111; discussion 111–112.
9. Sueda T, Nagata H, Shikata H, Orihashi K, Morita S, Sueshiro M, Okada K, Matsuura Y. Simple left atrial procedure for chronic atrial fibrillation associated with mitral valve disease. *Ann Thorac Surg.* 1996;62: 1796–1800.
10. Morillo CA, Klein GJ, Jones DL, Guiraudon CM. Chronic rapid atrial pacing: structural, functional, and electrophysiological characteristics of a new model of sustained atrial fibrillation. *Circulation.* 1995;91: 1588–1595.
11. Lewis T. *The Mechanism and Graphic Registration of the Heart Beat.* 3rd ed. London, UK: Shaw & Sons; 1925:319–374.
12. Ramirez RJ, Nattel S, Courtemanche M. Mathematical analysis of canine atrial action potentials: rate, regional factors, and electrical remodeling. *Am J Physiol.* 2000;279:H1767–H1785.
13. Kneller J, Sun H, Leblanc N, Nattel S. Remodeling of Ca^{2+}-handling by atrial tachycardia: evidence for a role in loss of rate-adaptation. *Cardiovasc Res.* 2002;54:416–426.
14. Kneller J, Ramirez RJ, Chartier D, Courtemanche M, Nattel S. Time-dependent transients in an ionically based mathematical model of the canine atrial action potential. *Am J Physiol Heart Circ Physiol.* 2002; 282:H1437–H1451.
15. Vigmond EJ, Leon LJ. Computationally efficient model for simulating electrical activity in cardiac tissue with fiber rotation. *Ann Biomed Eng.* 1999;27:160–170.
16. Joyner RW. Effects of the discrete pattern of electrical coupling on propagation through an electrical syncytium. *Circ Res.* 1982;50:192–200.
17. Roberge FA, Vinet A, Victorri B. Reconstruction of propagated electrical activity with a two-dimensional model of anisotropic heart muscle. *Circ Res.* 1986;58:461–475.
18. Leon LJ, Roberge FA. Structural complexity effects on transverse propagation in a two-dimensional model of myocardium. *IEEE Trans Biomed Eng.* 1991;38:997–1009.
19. Victorri B, Vinet A, Roberge FA, Drouhard JP. Numerical integration in the reconstruction of cardiac action potentials using Hodgkin-Huxley-type models. *Comput Biomed Res.* 1985;18:10–23.
20. Li D, Fareh S, Leung TK, Nattel S. Promotion of atrial fibrillation by heart failure in dogs: atrial remodeling of a different sort. *Circulation.* 1999;100:87–95.
21. Wang J, Liu L, Feng J, Nattel S. Regional and functional factors determining induction and maintenance of atrial fibrillation in dogs. *Am J Physiol.* 1996;271:H148–H158.
22. Rensma PL, Allessie MA, Lammers WJ, Bonke FI, Schalij MJ. Length of excitation wave and susceptibility to reentrant atrial arrhythmias in normal conscious dogs. *Circ Res.* 1988;62:395–410.
23. Leon LJ, Roberge FA, Vinet A. Simulation of two-dimensional anisotropic cardiac reentry: effects of the wavelength on the reentry characteristics. *Ann Biomed Eng.* 1994;22:592–609.
24. Wang Z, Fermini B, and Nattel S. Rapid and slow components of delayed rectifier current in human atrial myocytes. *Cardiovasc Res.* 1994;28: 1540–1546.
25. Li D, Zhang L, Kneller J, Shi H, Nattel S. Ionic mechanism of repolarization differences between canine right and left atrium. *Circ Res.* 2001; 88:1168–1175.
26. White CW, Marcus ML, Abboud FM. Distribution of coronary artery flow to the canine right atrium and sinoatrial node. *Circ Res.* 1977;40: 342–347.
27. Woodbury W, Crill WE. On the problem of impulse conduction in the atrium. In: Florey E, ed. *Nervous Inhibition.* New York, NY: Pergamon Press; 1961:124–135.
28. Spach MS, Miller WT III, Geselowitz DB, Barr RC, Kootsey JM, Johnson EA. The discontinuous nature of propagation in normal canine cardiac muscle. *Circ Res.* 1981;48:39–54.
29. Winfree AT. Sudden cardiac death: a problem in topology. *Sci Am.* 1983;248:144–149, 152–157, 160–161.
30. Mandapati R, Asano Y, Baxter WT, Gray R, Davidenko J, Jalife J. Quantification of the effects of global ischemia on dynamics of ventricular fibrillation in isolated rabbit heart. *Circulation.* 1998;98:1688–1696.
31. Ikeda T, Wu T-J, Uchida T, Hough D, Fishbein MC, Mandel WJ, Chen P-S, Karagueuzian HS. Meandering and unstable reentrant wave fronts induced by acetylcholine in isolated canine right atrium. *Am J Physiol.* 1997;273:H356–H370.
32. Schuessler RB, Grayson TM, Bromberg BI, Cox JL, Boineau JP. Cholinergically mediated tachyarrhythmias induced by a single extrastimulus in the isolated canine right atrium. *Circ Res.* 1992;71:1254–1267.
33. Allessie MA, Bonke FI, Schopman FJ. Circus movement in rabbit atrial muscle as a mechanism of tachycardia. III. The "leading circle" concept: a new model of circus movement in cardiac tissue without the involvement of an anatomical obstacle. *Circ Res.* 1977;41:9–18.
34. Ikeda T, Uchida T, Hough D, Lee JJ, Fishbein MC, Mandel WJ, Chen PS, Karagueuzian HS. Mechanism of spontaneous termination of functional reentry in isolated canine right atrium: evidence for the presence of an excitable but nonexcited core. *Circulation.* 1996;94:1962–1973.
35. Ikeda T, Yashima M, Uchida T, Hough D, Fishbein MC, Mandel WJ, Chen PS, Karagueuzian HS. Attachment of meandering reentrant wave fronts to anatomic obstacles in the right atrium: role of the obstacle size. *Circ Res.* 1997;81:753–764.
36. Ikeda T, Czer L, Trento A, Hwang C, Ong JJC, Hough D, Fishbein MC, Mandel WJ, Karagueuzian HS, Chen P-S. Induction of meandering functional reentrant wave front in isolated human atrial tissues. *Circulation.* 1997;96:3013–3020.
37. Jalife J, Gray R. Drifting vortices of electrical waves underlie ventricular fibrillation in the rabbit heart. *Acta Physiol Scand.* 1996;157:123–131.
38. Gray RA, Jalife J, Panfilov AV, Baxter WT, Cabo C, Davidenko JM, Pertsov AM, Hogeweg P. Mechanisms of cardiac fibrillation. *Science.* 1995;270:1222–1223.
39. Slocum J, Sahakian A, Swiryn S. Computer discrimination of atrial fibrillation and regular atrial rhythms from intra-atrial electrograms. *Pacing Clin Electrophysiol.* 1988;11:610–621.
40. Ninomiya I. Direct evidence of nonuniform distribution of vagal effects on dog atria. *Circ Res.* 1966;19:576–583.
41. Ailessi R, Nusynowitz M, Abildskov JA, Moe GK. Nonuniform distribution of vagal effects on the atrial refractory period. *Am J Physiol.* 1958;194:406–410.
42. Liu L, Nattel S. Differing sympathetic and vagal effects on atrial fibrillation in dogs: role of refractoriness heterogeneity. *Am J Physiol.* 1997; 273:H805–H816.

43. Jalife J, Berenfeld O, Skanes A, Mandapati R. Mechanisms of atrial fibrillation: mother rotors or multiple daughter wavelets, or both? *J Cardiovasc Electrophysiol*. 1998;9:S2–S12.
44. Nygren A, Leon LJ, Giles WR. Simulations of the human atrial action potential. *Phil Trans R Soc Lond A*. 2001;359:1111–1125.
45. Nygren A, Fiset C, Firek L, Clark JW, Lindblad DS, Clark RB, Giles WR. Mathematical model of an adult human atrial cell: the role of K^+ currents in repolarization. *Circ Res*. 1998;82:63–81.
46. Courtemanche M, Ramirez RJ, Nattel S. Ionic mechanisms underlying human atrial action potential properties: insights from a mathematical model. *Am J Physiol*. 1998;275:H301–H321.
47. Berenfeld O, Mandapati R, Dixit S, Skanes AC, Chen J, Mansour M, Jalife J. Spatially distributed dominant excitation frequencies reveal hidden organization in atrial fibrillation in the Langendorff-perfused sheep heart. *J Cardiovasc Electrophysiol*. 2000;11:869–879.
48. Sih HJ, Sahakian AV, Arentzen CE, Swiryn S. A frequency domain analysis of spatial organization of epicardial maps. *IEEE Trans Biomed Eng*. 1995;42:718–727.
49. Karagueuzian HS, Khan SS, Peters W, Mandel WJ, Diamond GA. Non-homogeneous local atrial activity during acute atrial fibrillation: spectral and dynamic analysis. *PACE*. 1990;13:1937–1942.
50. Mansour M, Mandapati R, Berenfeld O, Chen J, Samie FH, Jalife J. Left-to-right gradient of atrial frequencies during acute atrial fibrillation in the isolated sheep heart. *Circulation*. 2001;103:2631–6.
51. Allessi MA, Rensma PL, Brugada J, Smeets JLRM, Penn O, Kirchhof CJHJ. Pathology of atrial fibrillation. In: Zipes DP, Jalife J, eds. *Cardiac Electrophysiology: From Cell to Bedside*. Philadelphia, Pa: W.B. Saunders Company; 1990:548–559.
52. Kumagai K, Khrestian C, Waldo AL. Simultaneous multisite mapping studies during induced atrial fibrillation in the sterile pericarditis model: insights into the mechanism of its maintenance. *Circulation*. 1997;95: 511–521.
53. Garrey WE. The nature of fibrillatory contraction of the heart: its relation to tissue mass and form. *Am J Physiol*. 1914;33:397–414.
54. Mines GR. On circulating excitations in heart muscles and their possible relation to tachycardia and fibrillation. *Proc Trans R Soc Can*. 1914;8: 43–53.
55. Fareh S, Villemaire C, Nattel S. Importance of refractoriness heterogeneity in the enhanced vulnerability to atrial fibrillation induction caused by tachycardia-induced remodeling. *Circulation*. 1998;98:2202–2209.
56. Yue L, Feng J, Gaspo R, Li GR, Wang Z, Nattel S. Ionic remodeling underlying action potential changes in a canine model of atrial fibrillation. *Circ Res*. 1997;81:512–525.
57. Li D, Melnyk P, Feng J, Wang Z, Petrecca K, Shrier A, Nattel S. Effects of experimental heart failure on atrial cellular and ionic electrophysiology. *Circulation*. 2000;101:2631–2638.
58. Li D, Benardeau A, Nattel S. Contrasting efficacy of dofetilide in differing experimental models of atrial fibrillation. *Circulation*. 2000;102: 104–112.
59. Samie FH, Berenfeld O, Anumonwo J, Mironov SF, Udassi S, Beaumont J, Taffet S, Pertsov AM, Jalife J. Rectification of the background potassium current: a determinant of rotor dynamics in ventricular fibrillation. *Circ Res*. 2001;89:1216–1223.
60. Kneller J, Leon J, Nattel S. How do class I antiarrhythmic drugs terminate atrial fibrillation? A quantitative analysis based on a realistic ionic model. *Circulation*. 2001;104(suppl II):II-5. Abstract.
61. Ho SY, Sanchez-Quintana D, Cabrera JA, Anderson RH. Anatomy of the left atrium: implications for radiofrequency ablation of atrial fibrillation. *J Cardiovasc Electrophysiol*. 1999;10:1525–1533.
62. Athill CA, Ikeda T, Kim YH, Wu TJ, Fishbein MC, Karagueuzian HS, Chen PS. Transmembrane potential properties at the core of functional reentrant wave fronts in isolated canine right atria. *Circulation*. 1998;98: 1556–1567.
63. Wu TJ, Yashima M, Xie F, Athill CA, Kim YH, Fishbein MC, Qu Z, Garfinkel A, Weiss JN, Karagueuzian HS, Chen PS. Role of pectinate muscle bundles in the generation and maintenance of intra-atrial reentry: potential implications for the mechanism of conversion between atrial fibrillation and atrial flutter. *Circ Res*. 1998;83:448–462.

CHAPTER 5 MECHANISMS OF AF TERMINATION BY PURE SODIUM BLOCKADE IN AN IONICALLY-REALISTIC MATHEMATICAL MODEL.

As discussion in Section 1.6.3, the sodium channel blockers (class I drugs) constitute the most successful class of antiarrhythmic drugs in AF termination, but the mechanisms of action are poorly understood. Using the realistic model of AF developed in the previous study, the present study investigated the effects of sodium channel inhibition on AF dynamics, providing clear insights into potential mechanisms of AF termination by pure Na^+-channel blockade.

Mechanisms of AF Termination by Pure Sodium Channel Blockade in an Ionically-Realistic Mathematical Model

James Kneller, Renqiang Zou, L. Joshua Leon, Stanley Nattel

Short Title: Mechanisms of AF Termination by I_{Na} Inhibition

Subject Codes: [5] Arrhythmias, clinical electrophysiology, drugs;

[130] Animal models of human disease.

Word count: 6,413

From the Research Center and Department of Medicine, Montreal Heart Institute and University of Montreal (J.K., R.Z., S.N.), Department of Pharmacology, McGill University (J.K., S.N.), Montreal, Quebec, Canada and Department of Electrical and Computer Engineering (L.J.L), University of Calgary, Calgary, Alberta, Canada.

Correspondence to Dr Stanley Nattel, Research Center, Montreal Heart Institute, 5000 Belanger St E, Montreal, Quebec, Canada, H1T 1C8. Tel.: 514-376-3330 ext: 3990; Fax: 514-376-1355, E-mail: nattel@icm.umontreal.ca

Abstract- The mechanisms by which Na^+-channel blocking antiarrhythmic drugs terminate atrial fibrillation (AF) remain unclear. Classical "leading-circle" theory suggests that Na^+-channel blockade should, if anything, promote reentry, and interpretation of experimental results is complicated by K^+-channel blocking actions of available class I drugs. We used an ionically-based mathematical model of vagotonic AF to evaluate the effects of applying pure I_{Na}-inhibition during sustained arrhythmia. Under control, AF was maintained by 1 or 2 dominant spiral-waves with fibrillatory propagation at critical levels of APD dispersion. I_{Na}-inhibition terminated AF in 5.6% of simulations at 30%-block, 22.2% at 50%-block, 33.3% at 60%-block, and 100% at 65%-block. During 1:1 conduction, I_{Na}-inhibition reduced action potential duration (by 13% at 4 Hz and 60% block), conduction velocity (by 37%), and reentry wavelength (by 24%). During AF, I_{Na}-inhibition increased the size of primary reentry spirals and reduced reentry rate (eg, dominant frequency decreased by 33% at 60% I_{Na}-inhibition), while decreasing generation of secondary-wavelets by wavebreak. Three mechanisms contributed to I_{Na}-block induced AF termination: 1) enlargement of primary spiral-wave generators so that they could no longer be accommodated on the computational substrate, 2) decreased effectiveness of primary spiral-wave tip anchoring, producing increased meander and extinction at boundaries, and 3) reduction in the number of secondary wavelets that could provide a new primary spiral-wave generator. We conclude that pure I_{Na}-inhibition terminates AF in this model, producing activation changes consistent with clinical and experimental observations. These results provide insights into previously-enigmatic mechanisms of class I antiarrhythmic drug-induced AF termination.

Key Words: atrial fibrillation # mathematical model # class I drugs # sodium channels

Introduction

Class I antiarrhythmic drugs terminate clinical atrial fibrillation (AF), but the electrophysiological mechanisms remain poorly understood (1). AF is generally considered to be a reentrant arrhythmia, and the stability of AF is classically related to the wavelength (164). The wavelength (product of refractory period and conduction velocity) is thought to represent the minimum pathlength for reentry and therefore to determine the size of functional reentry circuits (59). The most commonly-accepted mechanism for antiarrhythmic drug termination of AF is drug-induced wavelength increases that reduce the number of circuits that the atria may accommodate.

Experimental evidence has been presented suggesting that class I antiarrhythmic agents act on AF by changing the effective refractory period (ERP) and the wavelength (140; 164; 176). Recent data have challenged established notions of antiarrhythmic drug action by showing that potent Na^+-channel blockers can terminate AF without increasing the wavelength (171). Indeed, in some instances decreases in wavelength preceded termination, and the most characteristic electrophysiological change prior to AF termination was an increase in the temporal excitable gap (171).

It is difficult to determine experimentally whether pure Na^+-channel blockade can terminate AF, since Na^+-channel blockers used to terminate AF, including class IA agents like quinidine and class IC agents like flecainide and propafenone, also have important actions on K^+-channels (249-251). We recently developed a realistic mathematical model of cholinergic AF in a 2-dimensional sheet of canine atrial tissue with physiological ionic, coupling, and propagation properties (134). Pure Na^+-channel blockade can be mimicked in the model by reducing maximum I_{Na} conductance. This allows for a

theoretical exploration of the effects on AF of I_{Na}-inhibition in the absence of collateral effects on other ion channels. In the present study, we applied this approach to determine whether Na^+-channel blockade alone is sufficient to terminate AF in the model, and if so, to: 1) evaluate the relationship between the intensity of I_{Na}-inhibition and the likelihood of AF termination, 2) investigate the mechanism(s) of AF termination by I_{Na}-inhibition, and 3) relate any effects to associated changes in wavelength and other electrophysiological parameters.

Methods

Model Description and Implementation

The Ramirez-Nattel-Courtemanche (RNC) model of the canine atrial action potential (AP) was implemented (42). Total ionic current (I_{ion}) is given by

$$I_{ion}=I_{Na}+I_{K1}+I_{to}+I_{Kur,d}+I_{Kr}+I_{Ks}+I_{Ca}+I_{Cl,Ca}+I_{K(ACh)}+I_{p,Ca}+I_{NaCa}+I_{NaK}+I_{b,Na}+I_{b,Ca}+I_{b,Cl} \quad 1.$$

An expression for the ACh-activated potassium current ($I_{K(ACh)}$) is included to simulate vagal effects (134). For AF simulation, a 5×10 cm rectangle of atrial tissue was modeled as before (134). Myocytes were placed in 300 single cell-width cables representing muscle fibers, with each divided into 600 cell-segments, such that the computational grid was comprised of 300×600 cells. Fiber resistivity and inter-fiber resistance values were chosen to match experimental propagation characteristics. Other details of the model can be found in reference (134).

Calculations were performed with a time-step of 25 microseconds and up to 25 processors of a 64-processor Enterprise 10000 (Sun). In this way, simulations of 5

seconds of activity, requiring the solution of 4.14·106 coupled equations over 2·105 time steps, were accomplished in 12-18 hours.

Two-Dimensional Simulation Protocols

I_{Na}-block was modeled by scaling I_{Na} conductance (g_{Na}). A maximum I_{Na} reduction of 65% was used to compare with 60-70% sodium channel inhibition (estimated from drug-induced conduction slowing) terminating experimental AF (82; 171; 176).

Model ERP was measured by simulating experimental protocols (140; 176). All stimuli (180 μA/cm2, 1-ms duration) were applied via a 0.2×0.4-cm electrode, such that the stimulus strength was 1.5-2 times threshold at 65% block. Proximal segments were stimulated from rest at 200 and 400 ms cycle lengths (CLs) and a single premature stimulus (S_2) was delivered after every 15 basic (S_1) stimuli. ERP was defined as the longest S_1-S_2 failing to initiate a propagated response. Conduction velocity (CV) was calculated during S_1 pulse trains in the longitudinal direction. The wavelength (ERP×CV) was computed as previously defined (59; 164). APs were recorded from distal segments during S_1 pulse trains to study changes in waveform morphology and AP duration to -60 mV (APD_{-60}), the approximate voltage at which excitability is normally restored (217). Maximum phase-0 upstroke velocity (V_{max}) was computed at 10-ms resolution with Matlab v5.3.

Conditions for sustained AF were based on in vivo levels of vagally mediated ERP shortening and spatial heterogeneity (131; 137) achieved by varying ACh concentration (0-0.015 μmol/L) across the grid according to a sinusoidal distribution (134). Reentry

was initiated using a cross-shock protocol (134). The core area of primary-generator spirals was calculated by dividing rotor-tip points into cycles ($n \geq 10$) and constructing polygons traced by the tip for each cycle (134).

Potential Maps

Propagating wavefronts over the computational substrate were visualized by constructing potential maps (134). After each ms, transmembrane potential at the center of each 6 by 6 cell-square (the approximate size of a space constant) on the computational grid was sub-sampled to a 50×100 pixel display grid, providing color maps of transmembrane potential (252). Corresponding movie supplements are provided in the online data supplement at http://www.circresaha.org.

Signal Analysis

Unipolar electrograms were computed as previously (134). Spectral analysis of model electrograms was performed with fast Fourier transformations (FFTs). Spectral signals were normalized to the largest peak to facilitate inter-site comparison. Activity sampled at 1000 Hz (1 ms) for 5000 frames (~5 seconds) provided spectral resolution of 0.2 Hz.

Terminology

AF: defined by rapid and irregular electrograms with varying morphologies. Potential maps were required to demonstrate propagation along lines of block and ongoing wavefront breakup changing on a cycle-to-cycle basis (87).

Wavebreak: a discontinuity permitting contact between a wavefront and its own repolarization tail (87).

Phase Singularity (PS): a point around which all phases of the waveform are encountered, generally where the depolarizing front and repolarizing tail of a wavefront meet (87). PSs arise from wavebreaks, are located at the instantaneous center of rotational activity, and were detected by a computer algorithm with manual verification (252).

Rotor: a spiral-wave of excitation rotating around a PS for 1 or more cycles (87).

Chirality: the sense of rotation, clockwise or counterclockwise, around a PS (87).

Core: area circumscribed by the core-tip trajectory of a PS, consisting of excitable but unexcited tissue, around which a rotor rotates (252).

Wavelet: segments of excitation wavefronts flanked by 2 PSs or a PS and a boundary (87).

All data are presented as mean±SD.

Results

AF Termination Rates and Intensity of I_{Na}-Inhibition

We first defined 5 different [ACh]-distribution conditions that resulted in sustained AF. Varying degrees of I_{Na}-inhibition were then applied after ~500, 750 or 1000 ms of simulated sustained AF for each of the 6 conditions (90 simulations). I_{Na}-inhibition effects were related to intensity of Na^+-channel blockade. Moderate I_{Na}-inhibition (as little as 30%) could terminate AF, but 100% efficacy required 65%-block (Figure 1).

Effects of I_{Na}-inhibition on Distributed Properties

ERP increased slightly but progressively as I_{Na}-inhibition increased. ERP_{200} (ERP at 200 ms CL) increased from 146-187 ms at 65%-inhibition (Figure 2A), with values converging towards ERP_{400} at 65% block. I_{Na}-inhibition prolonged the reentry period (Figure 2B), closely paralleling ERP changes. Means and standard deviations of reentry period increased 29% and 190%, respectively, at the strongest I_{Na}-inhibition, in agreement with 29% and 200% increases caused by moricizine in canine atria (173), and indicating greater increases in reentry period variability than in period per se. The core area increased from 2.78±0.42 cm2 to 3.77±1.92 cm2 (P<0.01). CV (Figure 2C) progressively decreased with I_{Na}-inhibition, from 105-66 cm/s (37% reduction) at 65%-inhibition. The wavelength (Figure 2D) decreased progressively, from 17.3-13.0 cm.

Effects of Sodium Channel Block on AP Properties

Both APD and AP amplitude progressively decreased with I_{Na}-inhibition (Figure 3A). APD_{-60} decreases became particularly important at >40% inhibition (Figure 3B). APD abbreviation with increased ERP (Figure 2A) reflects post-repolarization refractoriness, typical of class I drugs (80; 175). As observed experimentally (80; 181), strong I_{Na}-inhibition (>50%) resulted in 2:1 capture in the model at rapid rates (Figure 3B). This result is consistent with the development of transient lines of block during intra-cardiac reentry (122; 173; 175; 181; 182), which may decrease the rate while increasing the variability of reentry by forcing circuits into larger trajectories for certain cycles, thereby promoting meander of spiral-core tips. APD rate-adaptation was not substantially altered by I_{Na}-inhibition (Figure 3C), indicating that this contribution to CL oscillations would be

maintained during reentry and AF (134; 253). Changes in V_{max} were qualitatively similar at 1 and 5 Hz, with a maximum decrease of ~70% (Figure 3D).

Mechanisms of AF Termination

To determine how I_{Na} inhibition terminated AF, we examined activity under identical conditions, first during sustained AF in the absence of I_{Na} inhibition, and then prior to and during I_{Na}-inhibition-induced AF termination. Figure 4A shows [ACh]-distribution, an APD-distribution map and representative membrane-potential maps during one sustained AF. Animation of activity is available as online-only Movie 1. At 100 ms, the propagating impulse from the last S_1 approached the inferior border. An S_2 delivered at the upper-left initated a horizontally-propagating wavefront in the excitable upper region of the substrate, which propagated around the refractory lower part of the grid, creating a PS at the asterisk and a reentering wavefront at 165 ms. This PS remained at the core-tip of a generator spiral-wave that maintained activity for ~2.4 seconds. Emanating impulses impinged on refractory tissue, fractionating into wavelets with variable chirality, with numerous counter-rotations between adjacent transient circuits. Short-lived spirals resulting from the 48/74 (65%) of attempted counter-rotations that were successfully-completed (~1 attempted per 68-ms interval) competed with the primary spiral-generator. Selected frames show examples of attempted counter-rotations ("Y"=success [475, 525, 2312, 3706 ms], "X"=failure [3145 ms]). The spatial gradient of APD_{-60} was 58 ms (range: 27-85 ms).

At ~2.5 seconds, the initial primary spiral died out along the bottom right border (Figure 4C). A second generator of opposite chirality originating from wavebreak at

~2.3 seconds then assumed dominance and sustained fibrillation for the duration of the simulation. An average of 2.7±1.4 wavelets were present, with up to 7 at times of peak disorganization (Figure 4D). Electrograms recorded near (+, Figure 4B) and distal to (o, Figure 4C) the primary sources are clearly fibrillatory, with DFs of 11.3 and 10.7 Hz respectively.

Figure 5A shows termination of the AF shown in Figure 4 by I_{Na}-inhibition (animation at online-only Movie 2). Conditions identical to those in Figure 4 were used, but 65% I_{Na}-inhibition was applied after ~900 ms. A single wavelet persisted following block (at 920 ms). Wavefront curvature was greatly expanded and the wavelet corresponding to the uppermost PS (smaller asterisk) promptly extinguished along the top boundary (1010 ms). The PS at the core-tip of the original primary-circuit (larger asterisk) followed a more linear trajectory than prior to I_{Na}-inhibition, rotating around a markedly enlarged core. Reentry failed along the top border (1336 ms) after nearly one complete cycle, terminating AF. In this case, I_{Na}-inhibition enlarged the primary spiral to the extent that it could no longer be accommodated by the tissue substrate, leading to rapid termination. The spatial APD gradient was reduced to 50 ms (range: 20-70 ms), representing a 15 ms reduction in the maximum value relative to control (Figure 4), and 8 ms decrease overall. No further wavebreak occurred as the enlarged circuit conducted slowly in the presence of decreased APD heterogeneity.

Figure 5B shows termination under the same AF conditions by a lesser degree (30%) of I_{Na}-inhibition (animation in online-only Movie 3). Circuits were enlarged and wavelets tended to coalesce, such that the number of successfully-completed counter-rotations was reduced to 12/35 (34%, versus 65% in control) prior to termination (~1

attempted per 103-ms interval), as fewer PSs were separated by the critical inter-PS distance needed for ongoing reentry (87). Enlarged daughter-wavelets interfered with the primary generator and the dominant PS died out along the bottom boundary at ~3.22 seconds. Other PSs present at this time blocked (3255 ms). Subsequent wavebreak produced a final spiral which failed to establish sustained generator function, completing 1 rotation prior to annihilation along the left boundary (3415 ms), terminating AF (3510 ms). The DF during AF decreased from 11.3 Hz (Figure 4B) to 10.7 Hz (Figure 5C) during 30% I_{Na}-inhibition. In this example, the spatial APD gradient (57 ms, range: 27-84 ms) was negligibly changed relative to control (Figure 4A); thus, wavelet alterations resulting in AF termination did not require reductions in APD heterogeneity.

Figure 6A shows an example of AF maintained by a single spiral wave in the absence of I_{Na}-inhibition (animation available in on-line Movie 4). A rotor with clockwise chirality located near (+) acted as the primary source of activity. The trajectory of the dominant PS is plotted in black on the APD distribution-map. A region of increased APD in a low-[ACh] zone served as a functional anchor for the generator spiral-wave tip. Wavelets tended to multiply from the primary spiral and would at times coalesce to form a large unstable circuit, reducing the wavelet count to 1. Several PSs with opposite chirality completed multiple reentry cycles near the right border. On average, 3.6±1.2 wavelets were present, with 7 at peak disorganization (Figure 6B). Electrogram activity was fibrillatory, but the underlying order imposed by the primary spiral-wave generator was evidenced by a discrete, narrowly-peaked FFT (Figure 6B).

Figure 6C shows termination of this AF by 60% I_{Na}-inhibition applied after ~750 ms of activity (animation: online-only Movie 5). I_{Na}-inhibition caused rapid termination

of the generator spiral-wave. A secondary wavelet generated counter-rotating spiral-waves (760, 1195, 1224 ms) that evolved through 4 cycles before one spiral (PS indicated by smaller asterisk) terminated against the lower boundary. The core-tip (PS indicated by larger asterisk) of the remaining spiral then sustained generator-function until termination. The trajectory of the initial spiral-wave generator is plotted on the APD distribution map (black–before I_{Na}-inhibition; black and white–after block). The tip-trajectory of the generator after block is shown in yellow. I_{Na}-inhibition greatly slowed reentry (Panel D, DF decreased from 11.2-7.1 Hz) and reduced the spatial APD gradient (Panel C, from 40 to 33 ms in this example). These reduced the anchoring effect of low-[ACh] zones and wavebreak against refractory tissue. Reduced anchoring, along with regions of transient conduction block, caused hyper-meandering of the primary-generator tip PS, continuing until the primary PS reached the lower boundary and extinguished after 20 cycles. Because of reduced wavebreak, other PSs were unable to assume generator function. Despite the increased meander of the generator spiral, the electrogram was more organized following I_{Na}-inhibition (panel D), indicating that wavebreak contributed significantly to the disorganized electrograms in control (Figure 6B). The area of core-tip meander, 2.0 cm^2 under control conditions, increased to 7.7 cm^2 with 60% I_{Na}-inhibition.

Organization of AF by I_{Na}-Inhibition

Figures 5 and 6C demonstrate how I_{Na}-inhibition may increase primary-circuit size, promote primary-circuit meander, and reduce wavefront density, thereby slowing and organizing AF prior to conversion. These changes occurred in all cases of AF termination

and agree with experimental observations of class I drugs (176; 180). Figure 7 illustrates the progression of changes caused by I_{Na}-inhibition in another case. Activity is shown under control conditions (Figure 7A), with 30% (Figure 7B) and 60% (Figure 7C) I_{Na}-inhibition applied at the times indicated.

Under control conditions, electrograms were fibrillatory with a DF of 10.3 Hz, and 3.5±1.5 (range, 1-7) wavelets. The trajectory of the dominant PS is shown in black. With 30% I_{Na}-inhibition, the fibrillation rate slowed to 9.4 Hz. The trajectories of the dominant spiral tip before (black) and after (yellow) blockade are shown, with the introduction of block marked by an orange dot. With 60% block, activity became flutter-like, with discrete spectral peaks including higher harmonics (arrows) of the dominant frequency. Block caused the generator to meander along an erratic course, before stabilizing in a region of low APD. The trajectories of the dominant spiral tip (large asterisk on potential map) before (black) and after (yellow) block are shown. In this example, 2 counter-rotating PSs (small asterisks on potential map) present at the time of block persisted for the duration of the simulation (green trajectories), stabilizing activity into a system of large, highly uniform counter-rotating circuits. The electrogram frequency was 6.4 Hz and the wavelet count was reduced to 2.3±1.4 (range, 1-5).

PS Lifespan Analyses

To obtain a quantitative index of the effect of I_{Na}-inhibition on activity during AF, we analyzed the lifespan of all PSs with the use of an automated algorithm (252). Simulations (5-seconds) were performed for each of 5 [ACh]-distributions associated with sustained AF and then repeated with 30% and 60% I_{Na}-block applied after 500 ms of

activity. PS-lifespans were measured between 500 and 4500 ms, and PS-lifespan histograms were constructed for all simulations under control (A), 30% I_{Na}-inhibition (B) and 60% I_{Na}-inhibition (C) conditions. Consistent with experiments (87), the mean lifespan of PSs lasting <1 second under control conditions was ~30 ms, with 90% lasting <50 ms. PSs lasting >1 second belonged to the tips of primary-generator spirals. After 30% I_{Na}-inhibition, the number of PSs was reduced by 37%. The number of short-lasting PSs was reduced- for example, 310 lasted <10 ms, compared to 420 under control conditions; however, PSs lasting <50 ms remained over 90% of the total. After 60% I_{Na}-inhibition, the total number of PSs was drastically reduced, to 3.6% of control. The mean lifespan was increased to 70 ms, with 70% lasting <50 ms.

Discussion

We applied a mathematical model of AF to evaluate the effects of pure I_{Na}-inhibition. We found that I_{Na}-inhibition terminated AF in a fashion consistent with the ability of I_{Na}-blockers to terminate clinical AF. Mechanisms contributing to termination included: 1) enlargement of primary spiral-wave generators so that they could no longer be accommodated by the substrate, 2) decreased effectiveness of spiral-wave tip anchoring in zones of greater refractoriness, increasing meander and causing extinction at boundaries, and 3) reduction in the number of daughter-waves (resulting from wavebreak) that could provide new primary spiral-waves to maintain AF should the initial generator-spiral be extinguished.

Comparison with Results of Previous Studies of AF Termination by Class I Antiarrhythmic Drugs

The major effects of I_{Na}-inhibition in the present study were a reduction in the number of wavelets due to decreased wavebreak, increased size and hyper-meander of the primary generator-spiral, slowing of reentry and dose-related AF termination (despite decreased wavelength), with 100% efficacy at 65% Na^+-channel blockade. Wijffels et al. showed that the class I drugs cibenzoline and flecainide terminate sustained AF in an AF-remodeled substrate, while prolonging the AF cycle length (AFCL) with a concomitant decrease in the wavelength (170; 171). AFCL was consistently prolonged relative to the ERP during AF (RP_{AF}), and the only change correlating consistently with AF termination was an increased temporal excitable gap (AFCL-RP_{AF}) (171). They suggested that the increased excitable gap might reduce the number of daughter wavelets due to decreased wavebreak, a phenomenon that was quite apparent in our model. The variability of AFCL values was increased by ~2-fold (cibenzoline) (171) and 4-fold (flecainide) (170), indicating a large drug-induced increase in reentry-rate variability prior to cardioversion. The model suggests that these large increases in variability may be due to hyper-meander of the spiral-wave generator that leads to termination by extinction at boundaries. The maximum conduction slowing caused by these drugs was 42-44%, corresponding to inhibition of 64% and 69% of Na^+-channels (254), in the same range as I_{Na}-inhibition associated with complete efficacy in the present study. Sinus rhythm was restored in 80% of goats treated with cibenzoline, but only 40% of goats receiving flecainide, suggesting differences possibly related to the AF substrate (atrial remodeling in the Wijffels study,

ACh in the present study). Nonlinear analysis showed slowing and increased organization of AF by cibenzoline prior to termination (255), similar to our results.

Several studies have examined the effects of class I antiarrhythmic agents in canine vagotonic AF, an experimental paradigm directly analogous to our model. Lidocaine terminates AF maintained by bilateral vagal nerve stimulation (256), making atrial electrograms broader, slower and more regular, as in our model (eg, see Figure 7). FFTs under control conditions showed broad-banded peaks in the range of 13 and 17 Hz, changing to a narrow-banded peak at ~7 Hz after lidocaine Flecainide and propafenone are also highly-effective in canine vagotonic AF (140; 176), organizing activity and increasing the size of reentrant circuits prior to termination. AF termination was attributed to increased wavelength in the latter studies, but estimated I_{Na}-inhibition was 55% by flecainide (176) and 68% by propafenone (140), within the range of I_{Na}-inhibition that effectively terminated AF in the present model. Experimental observations are thus consistent with the results of our model in showing that Na^+-channel blocking drugs terminate AF with high efficacy at concentrations producing substantial Na^+-channel blockade, with organization and slowing of atrial activity prior to termination.

Clinical observations with class I antiarrhythmic agents are also consistent with our model simulations. Flecainide and propafenone both increase AFCL prior to conversion (257). Cibenzoline transforms highly-disorganized atrial activity into much more organized activity prior to termination, in conjunction with a substantial increase in AFCL (180).

Theoretical Aspects

Gray et al. were the first to show experimentally substantial spatial and temporal organization during cardiac fibrillation (258). They suggested that ventricular fibrillation (VF) is maintained by a limited number of organized rotors that terminate upon collision with rotors of opposite chirality or by encountering a boundary condition. Chen et al. provided experimental evidence for the relevance of these considerations to mechanisms of AF (87). We previously showed that such theoretical considerations apply to AF in a computer model of vagotonic AF in a 2-dimensional cell-grid closely approximating canine atrial properties (134). In the present study, we find that the termination of AF by I_{Na}-inhibition in this computational model follows the principles of spiral-wave reentry and impulse propagation in excitable media.

Mandapati et al. showed that decreased excitability resulting from I_{Na} blockade or ischemia may expand reentry spirals, increasing the core area and reducing the wavefront density while slowing fibrillation (123). During conduction in excitable media, the safety factor, or source-to-sink ratio, determines propagation velocity (122). The excitation-front curves around functional or anatomical obstacles when the safety factor for conduction is sufficiently large that activated cells in the wavefront are able to excite more than one cell at rest (68). As I_{Na}-blockade decreases source current, the number of sink cells that can be activated decreases and wavefront curvature flattens (122; 187; 259). This effect is particularly significant close to spiral-core tips, where wavefront curvatures become increasingly pronounced. A relatively-large source enables the spiral to rotate rapidly around a small core (123). When the source is reduced by I_{Na} block, the critical curvature becomes large and the path followed by the spiral wave tip increases

(123), increasing core size and slowing reentry. I_{Na}-blockade stabilizes spiral-waves without terminating reentrant activity in a mathematical model of ventricular tissue, opposing breakup and destabilizing the spiral wave core, thereby promoting meander and increasing the size of reentry pathways (238).

Novel Insights into Mechanisms of AF Termination by Na^+-Channel Blockers

Experimental studies have pointed to spiral-wave reentry in atrial tissue (66; 69). They have shown that a variety of antiarrhythmic drugs with Na^+-channel blocking activity can terminate AF. Initial studies suggested that AF termination was due to increased wavelength (59; 140; 176; 260). More recent work has, however, shown that class I drugs can terminate AF while decreasing wavelength (170; 171). The experimental evidence is difficult to interpret because of accessory drug actions, including important K^+-channel blockade (249-251). In a computational model that mimics many properties of experimental vagotonic AF, we found that pure I_{Na}-inhibition terminates arrhythmic activity, with the likelihood of termination increasing with increasing Na^+-channel block. Effective AF termination in the model is seen at levels of Na^+-channel block occurring with doses of class I antiarrhythmic agents that effectively terminate experimental AF. Changes in atrial activation in the model (including slowing, organization and regularization of atrial activity) are similar to those observed experimentally and clinically. While wavelength increases could contribute to the AF-terminating ability of some class I agents, the present study indicates that pure I_{Na} inhibition can terminate AF without prolonging and in fact despite decreasing, the wavelength.

Our simulations therefore show, for the first time to our knowledge, that pure Na^+-channel inhibition can terminate AF, and that Na^+-channel inhibition can account for many of the effects of class I drugs on AF. Our studies also provide potential insights into the mechanisms by which Na^+-channel blockers may terminate AF. One mechanism is an increase in the critical angle of curvature of spiral-wave activity, which may enlarge the spiral-wave generators beyond the available substrate. This mechanism parallels suggestions based on observations of the effects of flecainide on activation in a rabbit model of 2-dimensional ventricular reentry (181). The second potential contributor, decreased formation of multiple daughter wavelets, has been postulated based on increases in the temporal excitable gap during experimental AF (171). The final mechanism for AF termination, increased meander of the spiral-wave causing termination by movement to a boundary condition has not, to our knowledge, previously been suggested. Boundary conditions exist at multiple atrial locations, including the atrio-ventricular valves, venae cavae, pulmonary veins and interatrial septum, which contains significant conduction discontinuities (261). Drift of the primary spiral-wave generator to a boundary, resulting in extinction as described by Gray et al. (258), could explain AF termination by class I antiarrhythmics at levels of I_{Na}-inhibition below those needed to enlarge the spiral beyond the capacity of the reentry substrate.

The observations of the present study may help to understand why class I antiarrhythmics terminate experimental and clinical atrial, but not ventricular, fibrillation. The effects of I_{Na}-inhibition on activation during ventricular fibrillation are qualitatively similar to those on AF, including increased organization with slowing and enlargement of reentrant rotors (123; 262). However, the ventricular mass is much greater than that of the

atrium, potentially making it much more difficult to enlarge rotors beyond the spatial capacity of ventricular tissue. In addition, boundary conditions are much more plentiful in the atria than the ventricles, making spiral-core drift to a boundary much more likely at the atrial level. Thus, Na^+-channel blockers slow, regularize and stabilize VF, while tending to terminate AF.

Potential Limitations

Our computational substrate is a 2-dimensional sheet of cells, and does not reproduce the complexities of 3-dimensional atrial geometry. Although the model reproduces well the features of vagal AF (134), and accounted for many experimentally-observed effects of I_{Na}-inhibition in the present work, it would be interesting to analyze atrial arrhythmia mechanisms and mechanisms of drug action in more complex models incorporating realistic atrial geometric features (263). Disease states and atrial remodeling may importantly change the atrial reentrant substrate (141; 161). Consequently, they may affect the response to antiarrhythmic agents, including Na^+-channel blockers, altering mechanisms of drug action. Further theoretical and experimental work to address this issue would be of considerable potential interest and importance.

Acknowledgements

The authors thank the Canadian Institutes of Health Research (CIHR), the Natural Sciences and Engineering Research Council (NSERC), and the Mathematics of Information Technology and Complex Systems Network for funding, the Multimedia Advanced Computational Infrastructure for Alberta and "Réseau Québécois de Calcul de

Haute Performance" for essential computing resources, and Annie Laprade for secretarial help with the manuscript. James Kneller was supported by a CIHR MD, PhD Studentship and a Merck Pharmacology Fellowship.

Lapran/publ/Circulation Research/Sodium.al.sn

Figure Legends

Figure 1. AF termination in relationship to intensity of I_{Na} inhibition.

Figure 2. Effects of I_{Na} inhibition on ERP (**A**), reentry period (**B**), CV (**C**), and wavelength (**D**).

Figure 3. Effects of I_{Na} inhibition on APs (**A**), APD_{-60}, with conduction block ("X") at fast rates and strong I_{Na}-inhibition (**B**), APD_{-60} rate-adaptation (**C**), and V_{max} (**D**).

Figure 4. AF in the absence of I_{Na}-inhibition. (**A**) Left: top, [ACh]-distribution; below, APD-distribution; other panels, selected potential maps show activity during sustained AF, at times indicated (ms). Asterisks indicate spiral tip, "y" successful and "x" failed reentry of counter-rotating spirals. Electrograms were recorded near the source (**B**) and distally (**C**). Corresponding FFTs are at the right. (**D**) Number of wavelets present at each time.

Figure 5. (**A**) Termination of the AF shown in Figure 4 by 65% I_{Na}-block. Left, second from top: APD distribution in the presence of I_{Na}-inhibition. Selected potential maps show activity prior to (890 ms) and after (920 ms) application of I_{Na}-block leading to termination. (**B**) Termination of the AF shown in Figure 4 by 30% I_{Na}-block. Left, second from top: APD distribution in the presence of I_{Na}-block. Selected potential maps show activity prior to (890 ms) and after (1064 ms) block leading to termination. (**C**) Electrogram recordings and FFTs for example shown in **B**. (**D**) Wavelet-count versus time during simulation in **B**.

Figure 6. (**A**) AF maintained by a single spiral wave. Left: top, [ACh]-distribution; second from top, APD_{-60}-distribution, with trajectory of the dominant PS (black). (**C**) Termination of AF in (**A**) by 60% I_{Na}-block. Selected potential maps show activity prior to (482 ms) and after (760 ms) block leading to termination. The tip trajectories of the initial spiral-wave generator (black-before I_{Na} inhibition; black and white-after block) and subsequent generator after block (yellow) are shown. (**B, D**) Electrograms near the generators with corresponding FFTs, and the total wavelet counts for each condition.

Figure 7. Progression of changes caused by I_{Na}-inhibition in another case of AF. Activity under control conditions (**A**), and with 30% (**B**) and 60% (**C**) I_{Na}-inhibition applied at the times indicated. A representative potential-map during AF, APD distribution map with trajectory of the dominant PSs, electrogram recordings with corresponding FFTs, and wavelet count are shown for each condition.

Figure 8. PS-lifespans during AF. Values for 1st 1000 ms (left column) and for PSs lasting <100 ms (right column) are shown for control (**A**) and with 30% (**B**) and 60% (**C**) I_{Na}-block.

FIGURE 1

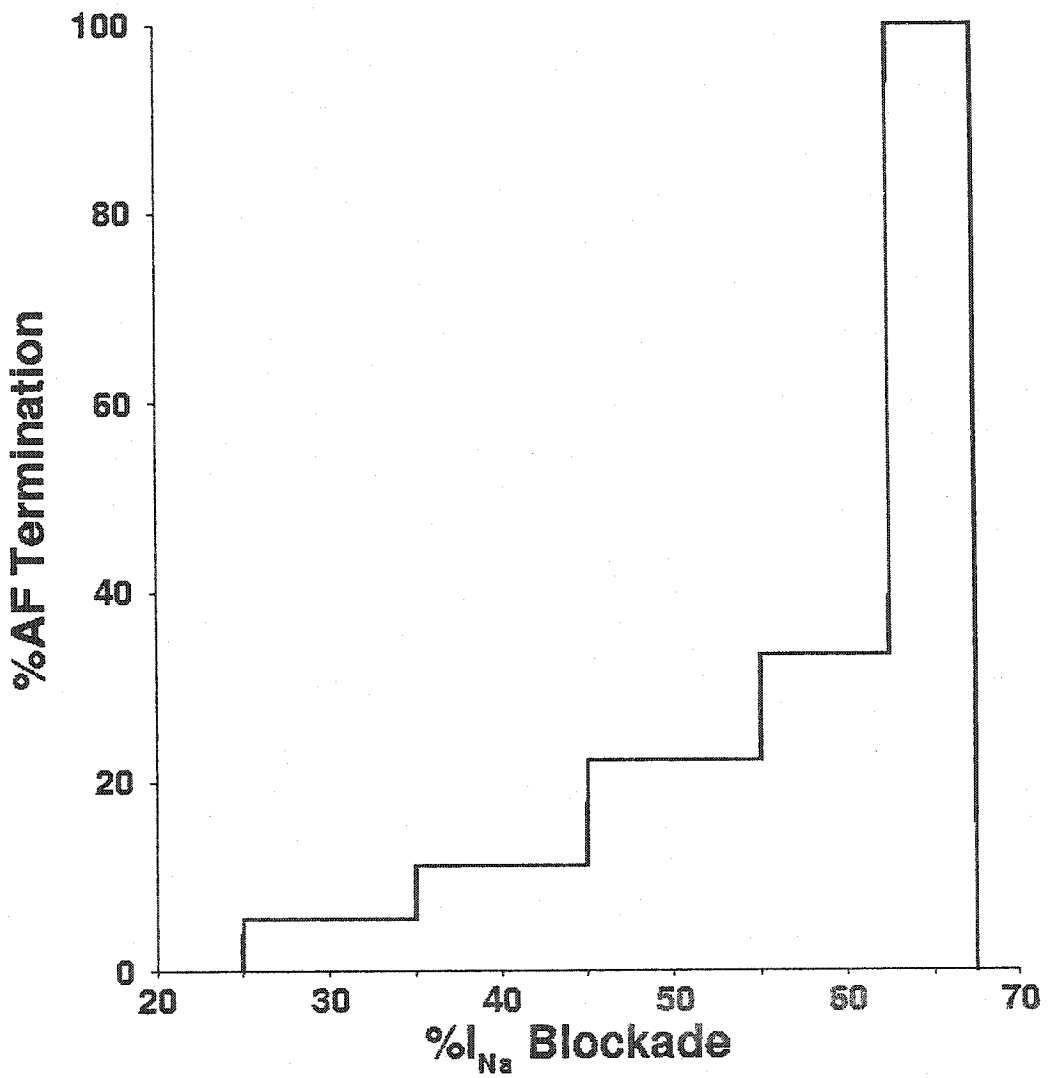

FIGURE 2

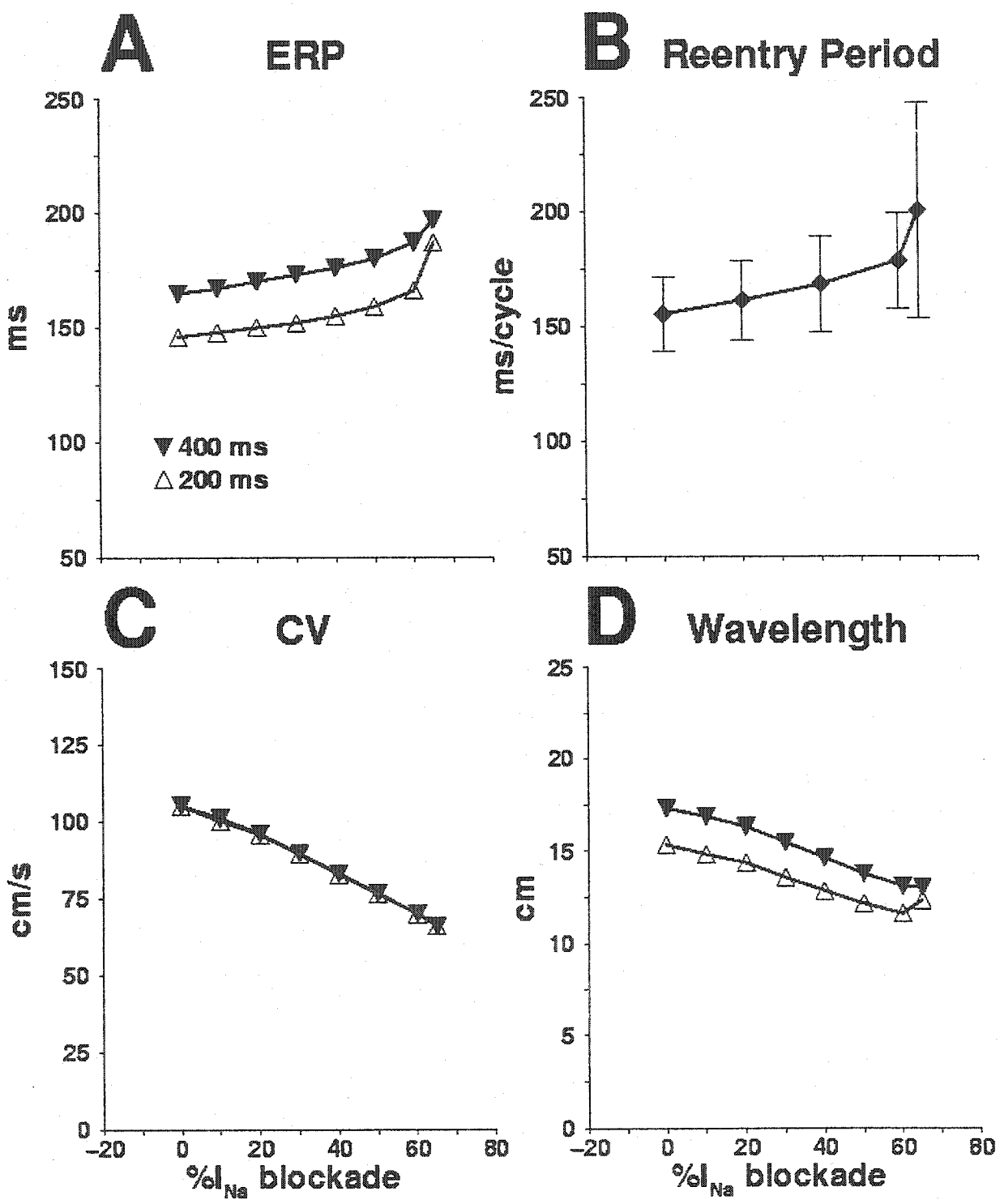
A
ERP
ms
250
200
150
100
50
▼ 400 ms
△ 200 ms
B
Reentry Period
ms/cycle
250
200
150
100
50
C
CV
cm/s
150
125
100
75
50
25
0
–20
0
20
40
60
80
%I$_{Na}$ blockade
D
Wavelength
cm
25
20
15
10
5
0
–20
0
20
40
60
80
%I$_{Na}$ blockade

FIGURE 3

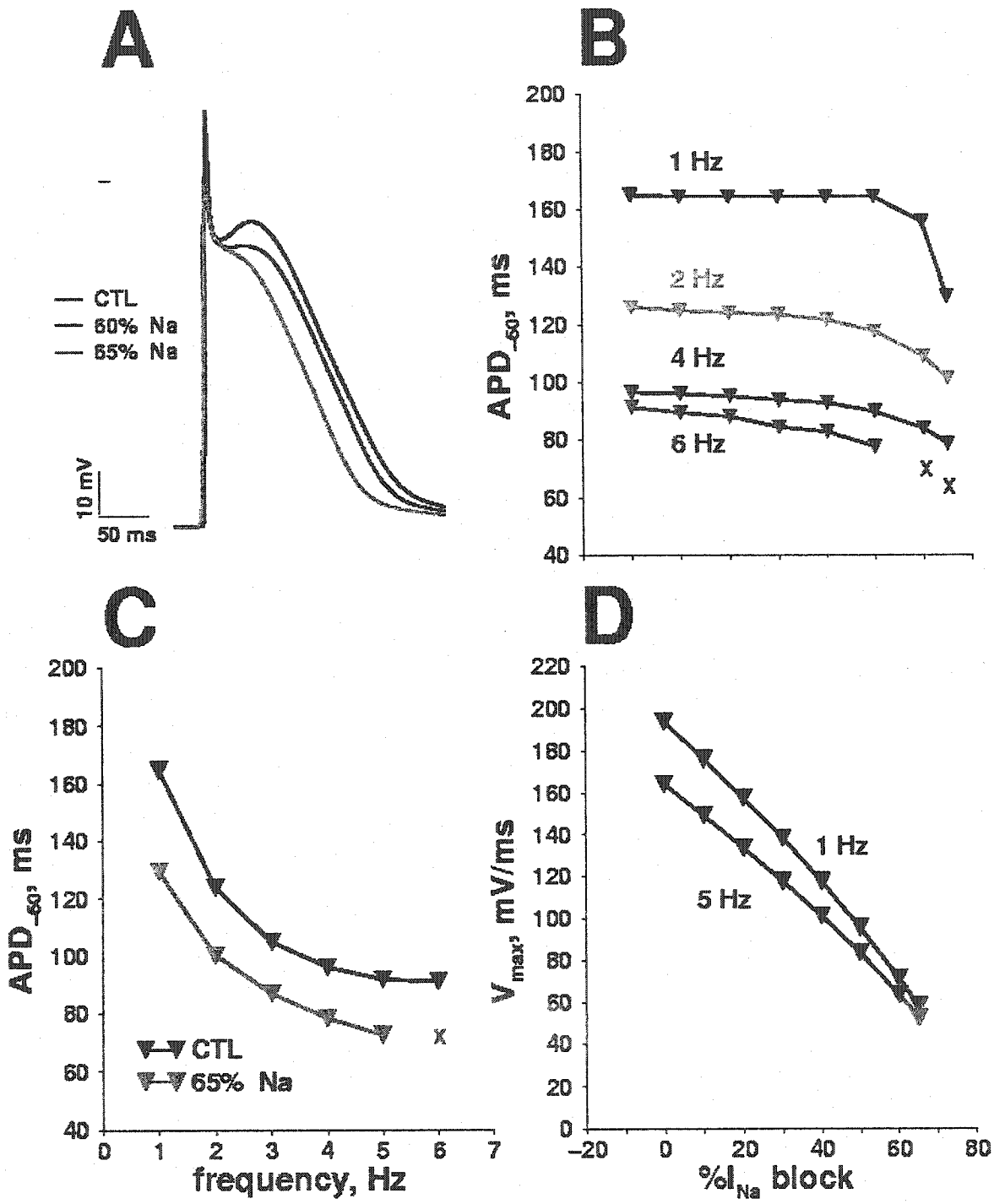
A
CTL
60% Na
65% Na
10 mV
50 ms
B
1 Hz
2 Hz
4 Hz
6 Hz
APD50, ms
C
CTL
65% Na
APD50, ms
frequency, Hz
D
1 Hz
5 Hz
Vmax, mV/ms
%INa block

FIGURE 4

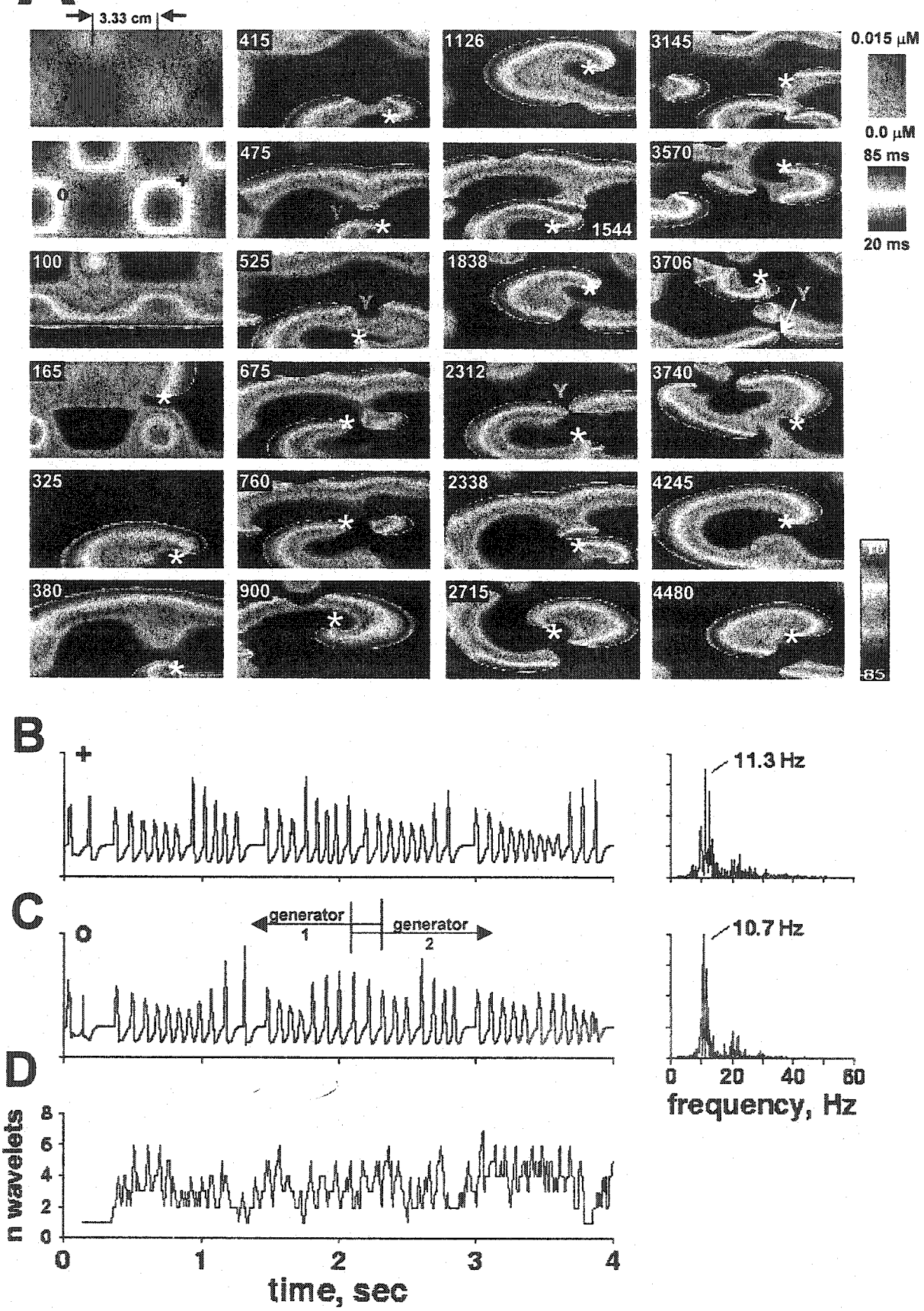
A
3.33 cm
0.015 μM
0.0 μM
85 ms
20 ms
415
1126
3145
475
1544
3570
100
525
1838
3706
165
675
2312
3740
325
760
2338
4245
380
900
2715
4480
B
+
11.3 Hz
C
o
generator 1
generator 2
10.7 Hz
0
20
40
60
frequency, Hz
D
n wavelets
8
6
4
2
0
0
1
2
3
4
time, sec

FIGURE 5

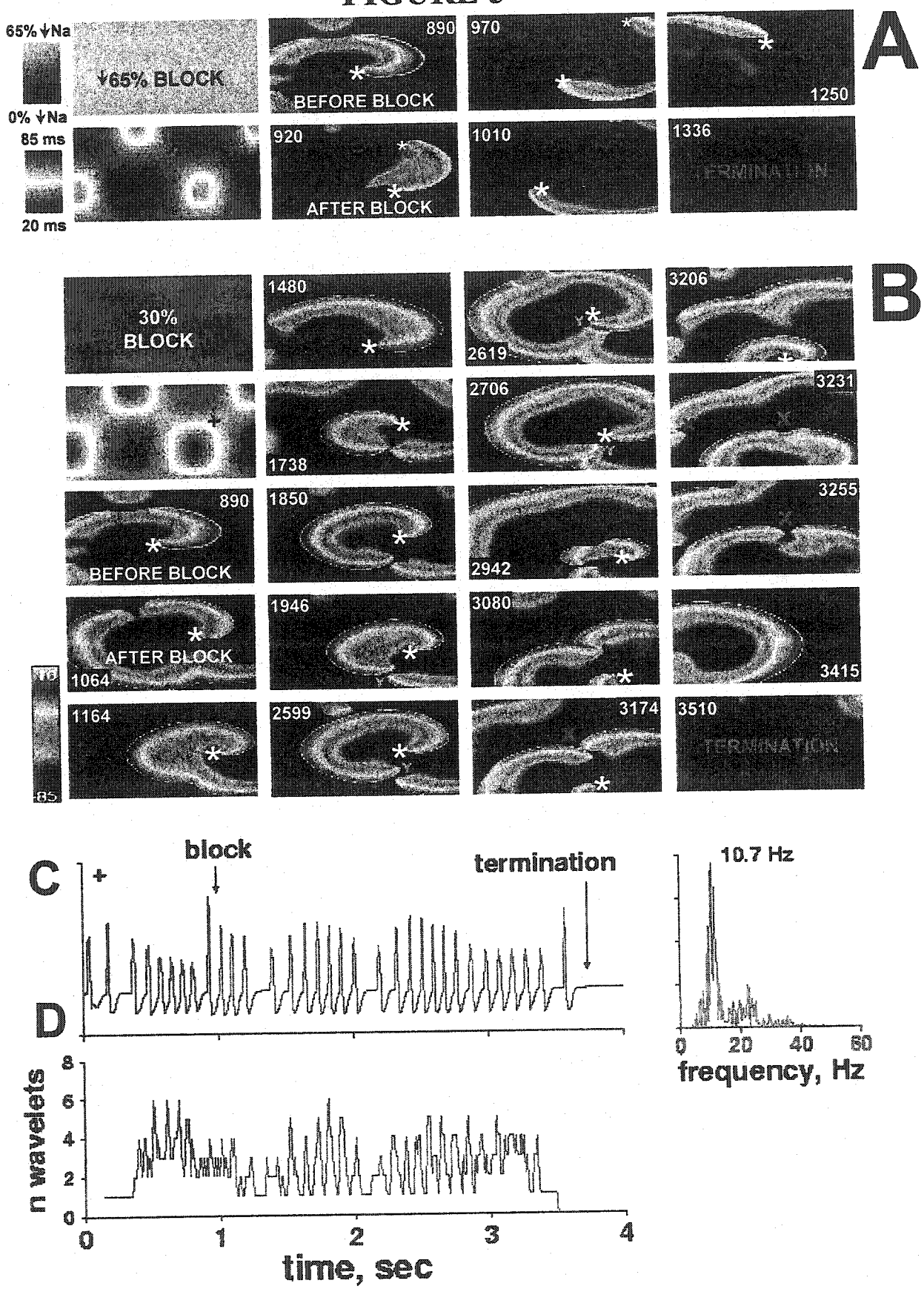
65% ↓Na
0% ↓Na
85 ms
20 ms
↓65% BLOCK
890
BEFORE BLOCK
970
1250
A
920
AFTER BLOCK
1010
1336
30%
BLOCK
1480
2619
3206
B
1738
2706
3231
890
BEFORE BLOCK
1850
2942
3255
AFTER BLOCK
1064
1946
3080
3415
1164
2599
3174
3510
TERMINATION
C
D
block
termination
+
10.7 Hz
0
20
40
60
frequency, Hz
n wavelets
8
6
4
2
0
0
1
2
3
4
time, sec

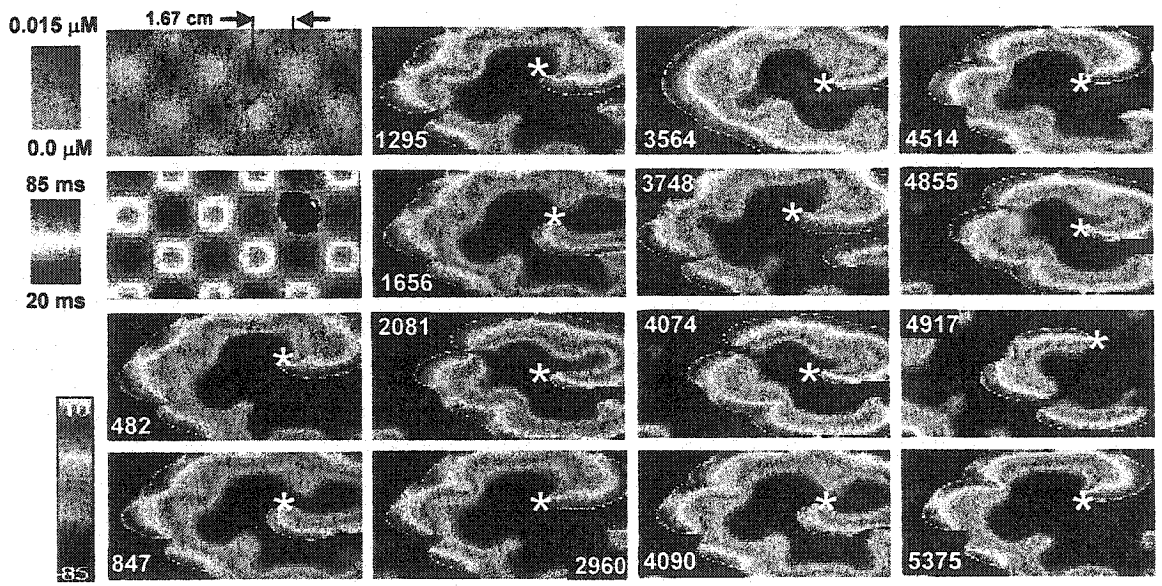
0.015 μM
0.0 μM
1.67 cm
85 ms
20 ms
1295
3564
4514
1656
3748
4855
482
2081
4074
4917
847
2960
4090
5375
A

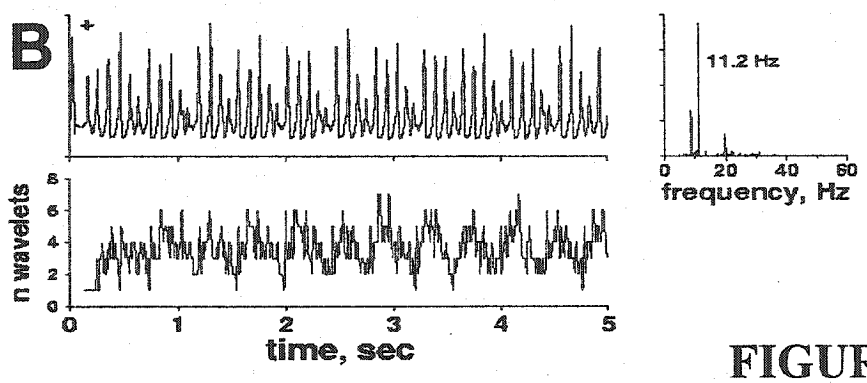
B
11.2 Hz
frequency, Hz
n wavelets
time, sec

FIGURE 6

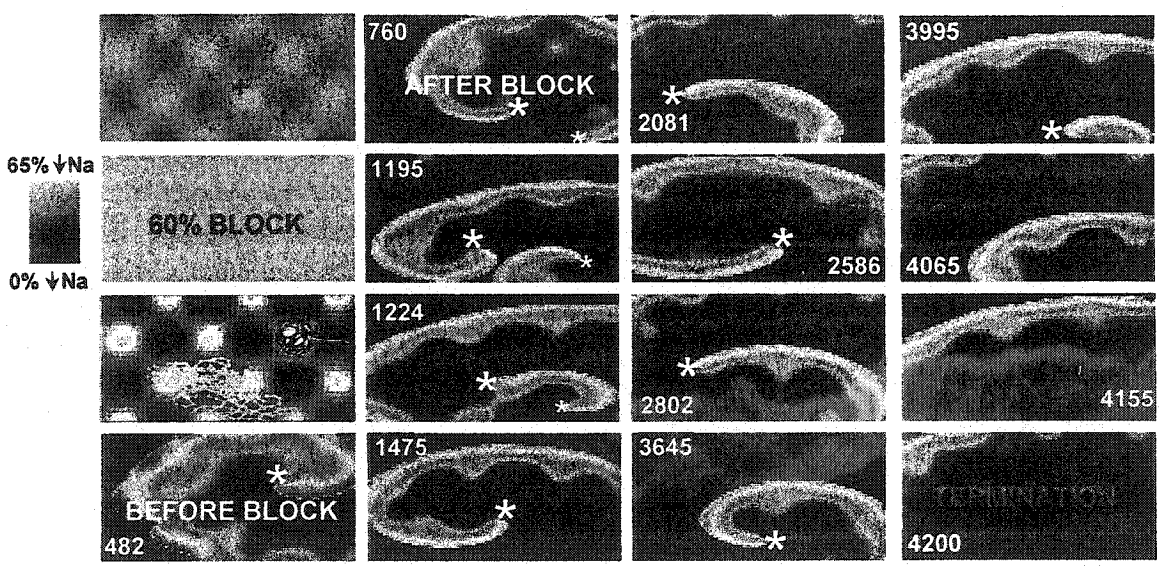
65% ↓Na
0% ↓Na
760
AFTER BLOCK
2081
3995
60% BLOCK
1195
2586
4065
1224
2802
4155
BEFORE BLOCK
482
1475
3645
4200
C

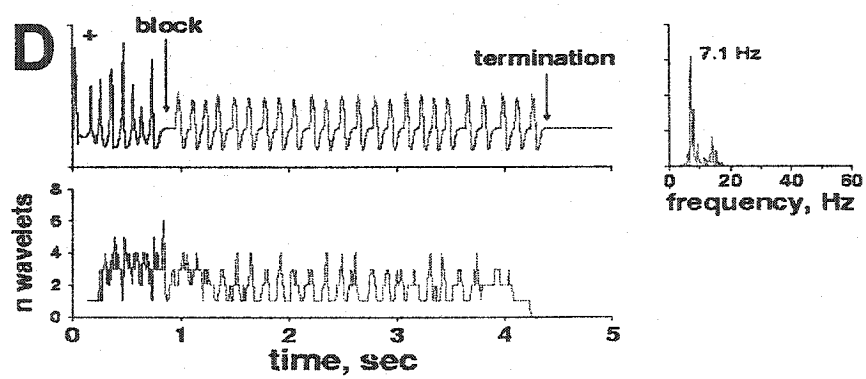
D
block
termination
7.1 Hz
frequency, Hz
n wavelets
time, sec

FIGURE 7

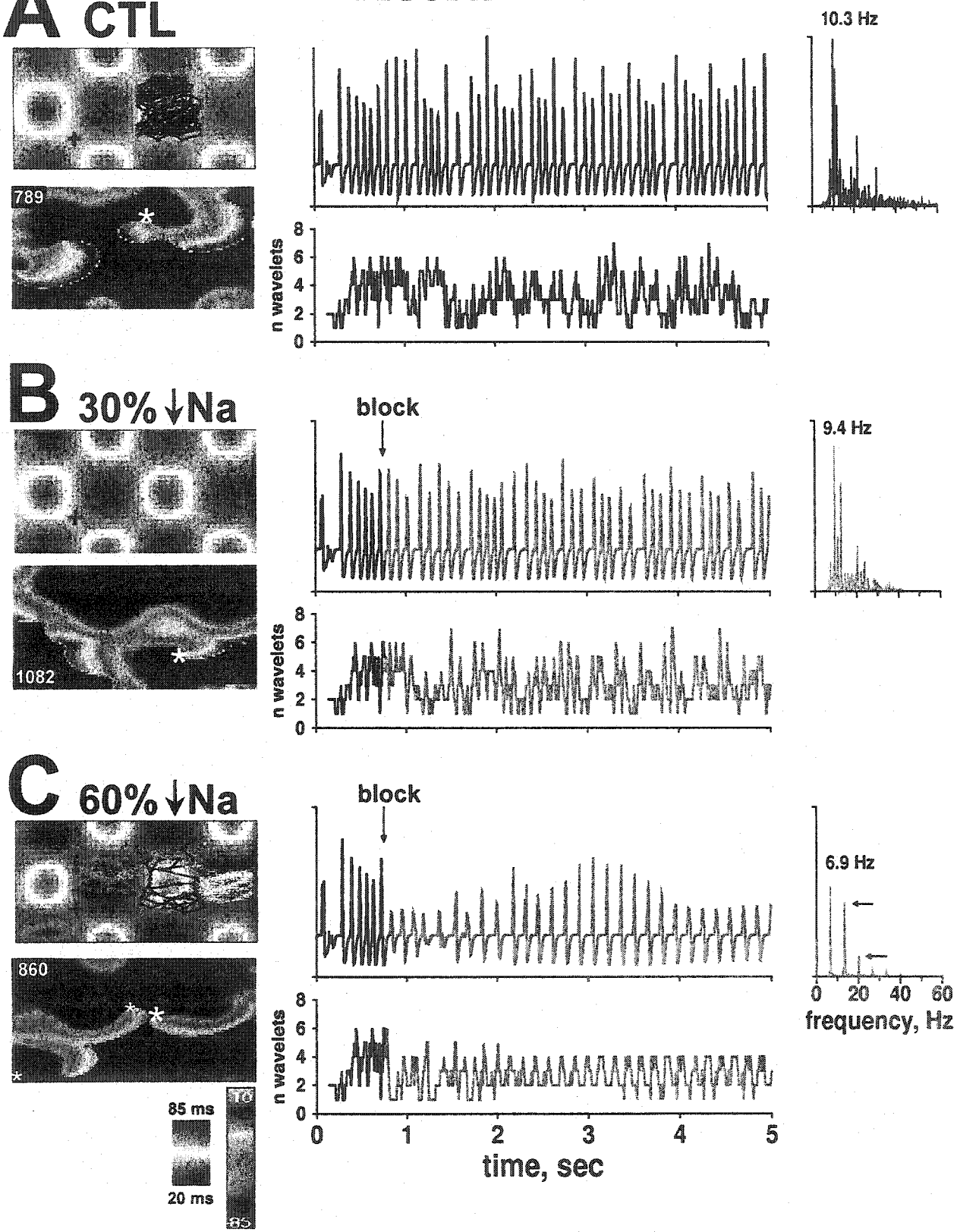
A CTL
789
10.3 Hz
n wavelets
8
6
4
2
0
B 30% ↓Na
block
1082
9.4 Hz
n wavelets
C 60% ↓Na
block
860
6.9 Hz
0 20 40 60
frequency, Hz
85 ms
20 ms
n wavelets
0 1 2 3 4 5
time, sec

FIGURE 8

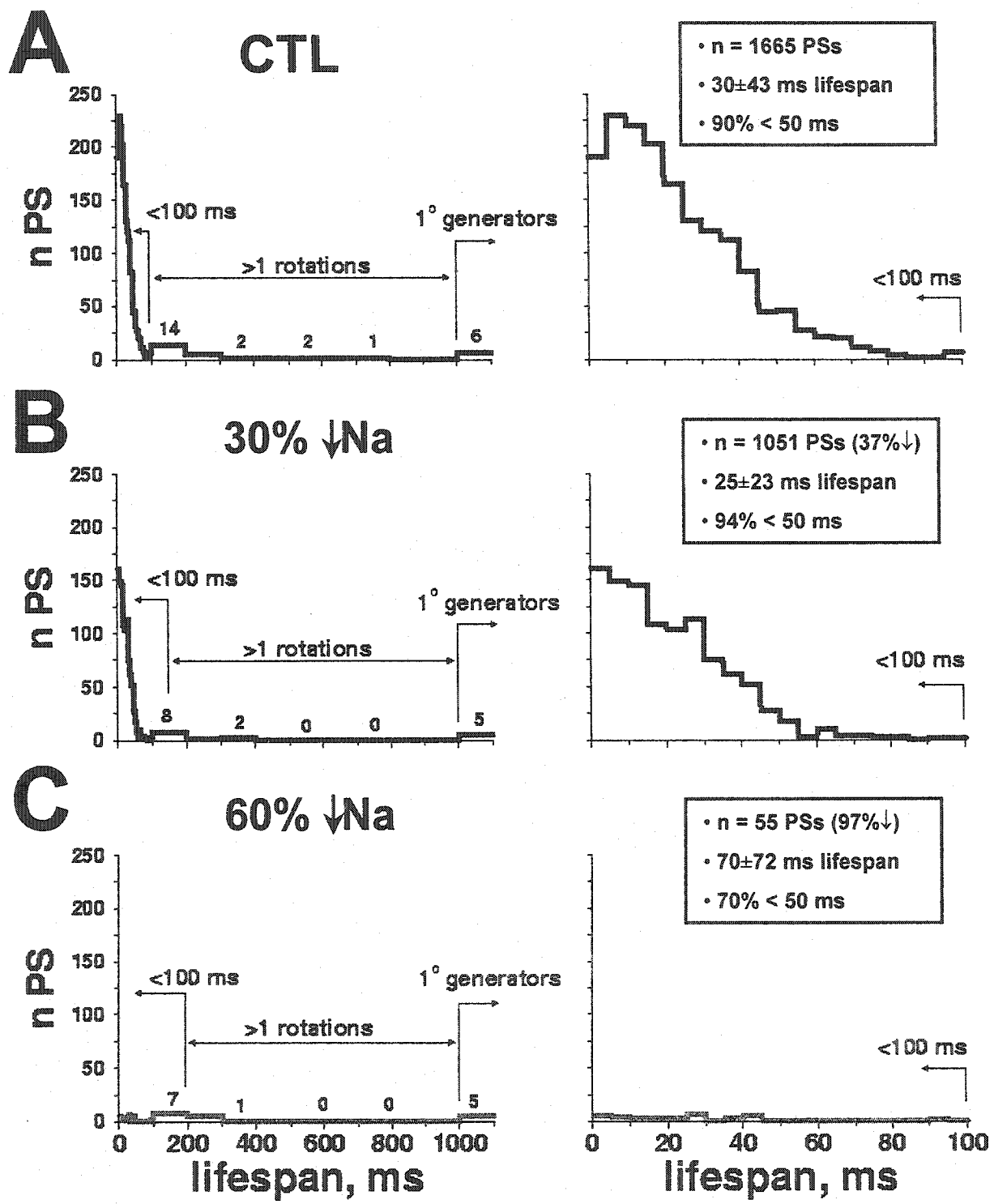
A
CTL
• n = 1665 PSs
• 30±43 ms lifespan
• 90% < 50 ms
nPS
<100 ms
1° generators
>1 rotations
14
2
2
1
6
<100 ms
B
30% ↓Na
• n = 1051 PSs (37%↓)
• 25±23 ms lifespan
• 94% < 50 ms
nPS
<100 ms
1° generators
>1 rotations
8
2
0
0
5
<100 ms
C
60% ↓Na
• n = 55 PSs (97%↓)
• 70±72 ms lifespan
• 70% < 50 ms
nPS
<100 ms
1° generators
>1 rotations
7
1
0
0
5
<100 ms
0 200 400 600 800 1000
lifespan, ms
0 20 40 60 80 100
lifespan, ms

CHAPTER 6 DISCUSSION

6.1 Contributions of Study 1 and Suggested Future Directions

The study entitled "Time-dependent transients in an ionically-based model of the canine atrial action potential" (Chapter 2) presents important theoretical results regarding dynamic cardiac AP models and provides potentially important insights into the mechanisms of pacing-induced functional transients in atrial tissue and the pathophysiology of chronic AF.

Theoretical contributions include the finding that tissue and model transients are comparable, and that any distortion arising from model equation instabilities (Section 1.7.1.3) is not likely to be significant. It was shown that dynamic models may reach absolute stability during sustained pacing, provided they contain complete homeostatic mechanisms for all ionic species. It was also found that assignment of the stimulus current, not normally done in model simulations, contributes importantly to long-term model stability. It was found that using K^+ as the stimulus charge-carrying species is likely the most appropriate assignment, as this assignment reproduced experimental observations of $[K^+]_i$ changes, best-preserved the intracellular ionic equilibrium, and because AP transients were most physiological for the K^+ stimulus current.

In a related study published shortly after that of Chapter 2, Hund et al. addressed ionic charge conservation and the phenomenon of drift in the Luo-Rudy dynamic mathematical model of the mammalian ventricular cell during prolonged pacing periods (264). It was pointed out that failure to assign the stimulus current to an ionic species (K^+, as in Chapter 2) momentarily violates conservation with each cycle, and that the existence of an infinite number of model steady states is only problematic when

conservation is violated. It was demonstrated that assignment of the stimulus current was sufficient to satisfy conservation, and therefore to eliminate drift caused by model stimulation. When conservation was satisfied, the calculation of membrane potential from ion concentrations ("algebraic" method) yielded identical results to calculation from transmembrane current ("differential" method, as was used in Chapter 2). The integration constant (C_o, as discussed in Chapter 2) of the conservation principle was calculated from initial values of dynamic model variables, while in Chapter 2, the significance of C_o was attributed to the presence of ionic species not accounted for by the models. As such species are also present in ventricle, calculated values of C_o would not be entirely accurate. It was generally assumed that model transients are non-physiologic, and no experiments were performed to compare model transients with those in ventricular tissue.

Physiological contributions of our work are related to functional ionic processes paralleling the onset of atrial tachycardia. As discussed in Section 1.5.2, tachycardia-induced remodeling shortens APD and abolishes AP rate adaptation, thereby enhancing atrial arrhythmogenicity (141). Underlying these changes, Yue et al. found that the densities of I_{Ca} and I_{to} were progressively decreased by 69 and 65% respectively, while no remodeling of I_{Kr}, I_{Ks}, $I_{Kur,d}$ or $I_{Cl,Ca}$ was found (148). The most extensive remodeling occurred early, and gradually attenuated toward the end of the pacing period. Studies in Chapter 2 indicate that initial AP shortening following the onset of pacing is related to intracellular Na^+ accumulation and outward I_{NaCa} augmentation. In this way, it was shown that normal functional adaptations, which precede molecular remodeling, contribute to early AF-promoting effects of atrial tachycardia.

Functional changes and transients in this study compared a model representing an isolated cell with a tissue syncytium. Future studies are needed to compare drift in coupled model cells with transients in a tissue model. Such work would contribute importantly to our understanding of how ionic redistribution during rapid activation influences AF. Preliminary cable simulations revealed that transients were augmented in coupled segments. The finding that reduced net stimulus current augmented the ionic transients is consistent with the exaggerated transients observed in the uncoupled cellular model when the stimulus current was not assigned. It was assumed that extracellular ionic concentrations were constant. Although this is a reasonable assumption for isolated cells, ion accumulation/depletion phenomena can occur in a multicellular preparation and contribute to rate-related changes. A more realistic modeling study would also include extracellular changes. Furthermore, although the model accounts for the concentrations of the ionic species predominantly responsible for the AP, other ionic species (e.g., HCO_3^-, SO_4^{-2}, PO_4^{-3}, and Mg^{+2}) are found within the cardiac myocyte as well as extracellularly. The presence of these additional ionic species in physiologic systems necessarily implies discrepancies with model results. Finally, AP morphology was the standard for assessing whether the model faithfully reproduced the changes in intracellular ion concentrations that occur during rapid pacing. A more robust test of the model would be to compare the changes in intracellular Na^+, K^+, and Ca^{2+} produced by the model with those determined experimentally using ion sensitive microelectrodes and Ca^{2+} indicators.

6.2 Contributions of Study 2 and Suggested Future Directions

The study entitled "Remodeling of Ca^{2+}-handling by atrial tachycardia: evidence for a role in loss of rate-adaptation" (Chapter 3) is the first to evaluate quantitatively the respective roles of ion channel remodeling and Ca^{2+}-handling abnormalities to the pathophysiologic features of the tachycardia-remodeled AP (Section 1.5.2). This study represents the first atrial AP model incorporating Ca^{2+}-handling formulations based on direct recordings of Ca^{2+}-transients. Results from this study point to the importance of subcellular Ca^{2+}-handling in governing the canine atrial AP and in understanding the electrophysiological basis of tachycardia-induced AP changes. These results are consistent with experimental AP studies in atrial tachycardia remodeling (148; 265), and give insights into underlying mechanisms. Because of the clinical importance of remodeling for AF (266; 267), these insights have potential clinical relevance.

Future directions indicated by these studies are at both the experimental and modeling levels. More experimental studies are necessary to understand the specific SR changes responsible for the observed intracellular Ca^{2+}-buffering dysfunction. This knowledge would permit the development of a more realistic SR model (similar to that of Winslow et al. (208)), enabling simulation studies to make mechanistic predictions with higher resolution and greater accuracy. Notwithstanding simplifications, our model predicts that slowing of intra-SR Ca^{2+} transfer processes (from NSR to JSR) was the major subcellular abnormality resulting from sustained tachycardia. As discussed in Chapter 3, the idea of 'uptake' and 'release' compartments is a hypothetical construct used to explain the delay between relaxation due to Ca^{2+} sequestration by the SR and

availability of Ca^{2+} for release (268). It was acknowledged that Ca^{2+} leak from the SR may arise from the ryanodine receptor itself, allowing more Ca^{2+} to flow during diastole. What was modeled as a change in JSR leakage may correspond to altered release processes. These may also be thought of as SR release channels recovering from inactivation (268). More extensive mechanistic and quantitative experimental studies including single Ca^{2+} channel analysis, are needed to determine the precise intra-SR changes corresponding to the conceptual predictions of the model. Still, model findings suggest that the development of new drugs countering such changes may significantly attenuate the remodeling process in patients suffering from frequent AF paroxysms, or drugs enhancing transfer may counter the effects of remodeling in those with longstanding AF. As presently available antiarrhythmic drugs target only sarcommal ion channels to terminate AF or control rate during AF, such subsarcolemmal agents would represent a new class of antiarrhythmic drugs (class V drugs). Putative class V agents may independently reduce AF recurrence and control rate, or act synergistically with drugs from other classes towards these ends.

6.3 Contributions of Study 3 and Suggested Future Directions

Moe's multiple wavelet hypothesis (71) and classical computer model (72) has shaped clinical and experimental conceptions of AF since the early 1960s (Section 1.4.4). As a result of early model predictions, AF is commonly thought to arise from multiple independent wavelets that propagate and multiply in a totally random fashion, and it is widely held that the ongoing multiplication of individual wavelets maintains AF. Recent

experimental work has raised questions about the multiple-wavelet mechanism, suggest a discrete "driver region" underlying AF (87; 91; 92), where wavelets generated by emanating wavefronts give rise to fibrillation but retain a significant degree of spatiotemporal periodicity and play a relatively passive role in maintaining AF. The study entitled "Cholinergic atrial fibrillation in a computer model of a two-dimensional sheet of canine atrial cells with realistic ionic properties" presents the first model of AF in a 2-dimensional system with realistic atrial ionic and propagation properties. The model agrees well with experimental observations and provides the first theoretical confirmation of this more recent experimentally-based mechanistic paradigm. This ends nearly 40 years of dominance by the Moe model of AF arguing that the multiple wavelet mechanism is the fundamental process underlying AF.

Mechanistically, the present model clarified the role of ACh-related acceleration of reentrant processes in potentiating the ongoing heterogeneity-induced wavebreak of AF. Reentry was faster in regions of high [ACh] with short ERP, causing wavefronts to impinge on zones of greater refractoriness in regions with low [ACh] where ERP was increased. Indeed, wavebreak would likely not occur without this acceleration. For sustained AF, the model predicts that AF may represent a ceaselessly-correcting balance between organization and disorganization of complex dynamics. While a perfect balance is never obtained, neither does a flutter-like rhythm or totally random activity ever gain lasting control. While recent experiments and the present model do not disprove the multiple wavelet mechanism, these results strongly indicate that AF should initially be considered to arise from relatively stable reentrant sources rather than from the wavelets themselves. Stable sources should be considered first, with the multiple wavelet

mechanism sometimes appearing at distal sites and possibly dominating activity for relatively brief periods.

This model representation of canine atrial tissue contains numerous simplifications. No area in the atria comprises a 2-dimensional 5×10-cm sheet. Rather, the normal atria have substantial areas of conduction discontinuity, in particular the septum (57) and the venae cavae. While many experimental studies of AF have been performed in isolated, unfolded atrial preparations (69; 89) and are therefore more comparable with the present model, even these possess atrial microstructure that may contribute importantly to the stability of AF, as reentry may occur within or be anchored by pectinate muscle bundles projecting from the plane of the tissue (58). In addition, the no-flux boundary conditions in the model may protect vortices from terminating, thereby influencing the balance between source-type spirals and resulting wavelets (269). Such simplifications were not considered limitations, as they facilitated the evaluation of basic mechanisms of fibrillation, and were a necessary first step before more complex representations of atrial tissue and AF were possible. While additional studies in this simplified substrate may be of great significance, the groundwork is thus laid for future studies to investigate other aspects of AF, such as the roles of tissue size, architecture, and anatomical obstacles.

In Chapter 3, ACh was distributed using a sinusoidal function, uniform in both the longitudinal and transverse directions. It would be interesting to adapt optical mapping techniques (73; 87; 92) to determine the distribution of vagal effects in vivo, towards developing a more realistic model substrate. Also in Chapter 3, the PS lifespan analysis was performed manually. We have since developed an automatic PS detection and

tracking algorithm based on both mathematical convolution and image analysis (252). The algorithm is presently being used to study mechanisms of AF in tissues of larger dimension, but with the same ACh levels and spatial distributions as in the Chapter 4. Preliminary results indicate that increased size facilitates sustained AF, as many "fibrillatory" ACh distributions (Chapter 4) supported sustained AF when the substrate was increased 4-fold from 5×10 cm (Chapter 4) to 10×20 cm (270). AF was sustained in 50% of cases on a 5×10-cm substrate, and in 100% of cases at 10×20 cm. Mechanistically, AF was maintained by single primary spiral wave generators in 80% of cases for sizes ≤5×10 cm, but by multiple spiral waves in 92% of cases for the 10×20 cm substrate, thus moving towards a multiple-wavelet mechanism of maintenance (Section 1.4.4) with increased size. This latter result is consistent with the original Moe model of AF (72), where the substrate exceeded normal physiologic size by ~2-fold. These results also indicate that atrial size is a determinant of sustained AF and that very large atria can support highly-stable multiple-circuit AF (270). It is generally held that decreasing ERP is equivalent to increasing substrate size with the same ERP. While this relation may hold under certain conditions, physiologic mechanisms of ERP reduction (increased vagal tone [Section 1.5.1], tachycardia-induced downregulation of I_{Ca} [Section 1.5.2]) often alter AP properties (e.g., loss of AP rate adaptation), which contribute importantly to the dynamics of AF. Hence, while periodic stimulation under steady-state conditions may support this principle, such a relation would be less likely to hold during AF. In addition to size, future studies may also evaluate the intrinsic arrhythmogenicity of anatomical obstacles and combinations of obstacles in a simple 2D substrate. Finally, the mechanisms and properties of AF reported in Chapter 4 should be compared to AF in an atrial model with

realistic geometry, as developed by Vigmond et al. (263), but with the same vagotonic properties as in Chapter 4.

Clinical AF occurs most commonly in the contexts of chronic AF and pathologies like congestive heart failure (CHF). Although the ionic mechanisms of action potential changes in tachycardia-remodeled atria are different from those in cholinergic AF (148), comparable changes in action potential properties (decreased APD and APD rate-adaptation, increased APD heterogeneity) suggest that basic mechanisms of AF maintenance may be similar. In contrast, CHF primarily alters the atrial substrate by promoting interstitial fibrosis: associated ionic remodeling, although substantial, minimally effects atrial ERP (160; 161). CHF-related AF appears to arise, at least in some instances, from a single macro-reentrant source (163). Further work is needed to evaluate quantitatively the potential mechanisms of AF based on substrates other than increased cholinergic tone, initially in 2D and subsequently with realistic geometry (263).

Towards these ends, a model of tachycardia-remodeled atrial tissue would employ the cellular model presented in Chapter 3, with Ca^{2+}-related heterogeneity distributed to reproduce appropriate levels of ERP heterogeneity as determined by Fareh et al (158). This would permit studies of AF mechanisms in chronic AF, and would aid in determining the clinical relevance of studies performed in vagotonic animal models. Also, the contribution of various remodeling processes (sarcolemmal versus subsarcolemmal changes) to the enhancement of atrial arrhythmogenicity by chronic AF could be assessed. Subsequently, effects of channel blockade could be evaluated (as was done in Chapter 5) in a broader clinical context than studies in Chapter 5. This work could then be extended to a morphologically realistic model of the atria (263) to account

for the potential role of the complex atrial geometry in AF mechanisms, and in antiarrhythmic drug action. A model of CHF-related AF would incorporate ion channel changes and match regional ERP differences (160; 161). The 2D substrate used in Chapter 4 is especially suited to reproducing the interstitial fibrosis and resulting conduction discontinuities (161) as transverse resistive elements may be selectively broken to mimic fiber dissociation (227).

6.4 Contributions of Study 4 and Suggested Future Directions

As discussed in Section 1.6.3, the sodium channel blockers constitute the most successful class of antiarrhythmic drugs in AF termination, yet their mechanisms of action are poorly understood. The study entitled "Mechanisms of AF termination by pure sodium channel blockade in an ionically-realistic mathematical model" (Chapter 5) used the model of AF developed in Chapter 4 to investigate the mechanisms of AF termination by pure sodium channel inhibition. It was found that I_{Na}-inhibition terminated AF in a fashion consistent with the ability of I_{Na}-blockers to terminate clinical AF. Mechanisms contributing to termination included: 1) enlargement of the primary spiral-wave generator so that it could no longer be accommodated by the substrate, 2) a decrease in the effectiveness of anchoring of the spiral-wave tip in zones of greater refractoriness, promoting hyper-meander and causing extinction at boundaries, and 3) a reduction in the number of daughter-waves (resulting from wavebreak) that could provide new primary spiral-waves to maintain AF should the initial generator-spiral be extinguished. These

results contribute greatly to the findings of previous model studies discussed in Section 1.7.2.2.2.

Mechanisms of AF termination, demonstrated simultaneously and unambiguously in the model, clarified a variety of related experimental observations which were previously enigmatic. The model reproduced the phenomenon of post-repolarization refractoriness, where block-induced reduction in APD abbreviation occurs with increased ERP, as is typical of class I drugs (80; 175). Strong I_{Na}-inhibition (>50%) also resulted in 2:1 capture in the model at rapid rates, as observed experimentally (80; 181). This result was consistent with the development of transient lines of block during intra-cardiac reentry (122; 173; 175; 181; 182), which may decrease the rate while increasing the variability of reentry by forcing circuits into larger trajectories for certain cycles, thereby promoting hyper-meander of sustained circuits. A mechanistic explanation for the findings of Wijffels et al. (170; 171) was thus provided. It was shown that the class I drugs cibenzoline and flecainide terminate sustained AF in an AF-remodeled substrate, while prolonging the AF cycle length (AFCL) with a concomitant decrease in the wavelength (170; 171). AFCL was consistently prolonged relative to the ERP during AF (RP_{AF}), and the only change correlating consistently with AF termination was an increased temporal excitable gap (AFCL-RP_{AF}) (171). It was suggested that the increased excitable gap might reduce the number of daughter wavelets due to decreased wavebreak, a phenomenon that was quite apparent in our model. The overall increase in AFCL values was accompanied by a ~2-fold (cibenzoline) (171) and 4-fold (flecainide) (170) increase in AFCL variability. The model demonstrated how such large increases in variability may arise from a hyper-meandering of the generator spiral, which was often the cause of AF

termination along tissue boundaries. In agreement with these experiments, model findings predicted that increased variability in AFCL may also be a strong predictor of AF termination by class I drugs. Finally, the model demonstrated how such destabilization of AF-generating mechanisms may manifest as slowing and increased organization of electrograms (82; 123; 172; 271), as determined by nonlinear analysis (255).

In studies by Wijffels et al. (170; 171), the maximum conduction slowing caused by these drugs was 42-44%, corresponding to inhibition of 64% and 69% of Na^+-channels (254), in the same range as I_{Na}-inhibition associated with complete efficacy in the present study. Sinus rhythm was restored in 80% of goats treated with cibenzoline, but only 40% of goats receiving flecainide, suggesting differences possibly related to the AF substrate (atrial remodeling in the Wijffels study, ACh in the present study). Future studies in a model of tachycardia-remodeled atrial tissue (as proposed in Section 6.3) may provide important insights into differences in the efficacy of I_{Na}-blockade in AF termination between substrate contexts. Alternately, the molecular mechanism of channel inhibition (decreased conduction versus altered gating kinetics (80)) may account for differences in efficacy. A cellular model incorporating a very detailed representation of I_{Na} current has been developed (272), and may potentially be adapted for atria to study very specific mechanisms of channel inhibition.

The model in Chapter 5 demonstrated how the effects of sodium channel inhibition in AF may be understood in terms of the biophysical principles discussed in Section 1.6.4. In contrast to classical notions of antiarrhythmic therapy, the model also demonstrated that AF termination mechanisms induced by pure I_{Na}-inhibition do not require wavelength changes (Section 1.6.1). These simulations showed, for the first time

to our knowledge, that pure Na^+-channel inhibition can terminate AF, and that Na^+-channel inhibition can account for many of the effects of class I drugs in AF. Our studies also provide potential insights into the mechanisms by which Na^+-channel blockers may terminate AF. One mechanism is an increase in the critical angle of curvature of spiral-wave activity, which may enlarge the spiral-wave generators beyond the available substrate. This mechanism parallels suggestions based on observations of the effects of flecainide on activation in a rabbit model of 2-dimensional ventricular reentry (181). The second potential contributor, decreased formation of multiple daughter wavelets, has been postulated based on increases in the temporal excitable gap during experimental AF (171). The final mechanism for AF termination, increased meander of the spiral-wave causing termination by movement to a boundary condition has not, to our knowledge, previously been suggested.

Boundary conditions exist at multiple atrial locations, including the atrio-ventricular valves, venae cavae, pulmonary veins and interatrial septum, which contains significant conduction discontinuities (261). Drift of the primary spiral-wave generator to a boundary, resulting in extinction as described by Gray et al. (258), could explain AF termination by class I antiarrhythmics at levels of I_{Na}-inhibition below those needed to enlarge the spiral beyond the capacity of the reentry substrate. As discussed, observations in Chapter 5 may, therefore, explain why class I antiarrhythmics terminate experimental and clinical AF, but not ventricular fibrillation. The effects of I_{Na}-inhibition on activation during ventricular fibrillation are qualitatively similar to those on AF, including increased organization with slowing and enlargement of reentrant rotors (123; 262). However, the ventricular mass is much greater than that of the atrium, potentially making it much more

difficult to enlarge rotors beyond the spatial capacity of ventricular tissue. In addition, boundary conditions are much more plentiful in the atria than the ventricles, making spiral-core drift to a boundary much more likely at the atrial level. Thus, Na^+-channel blockers slow, regularize and stabilize VF, while tending to terminate AF.

Given the prominent role of tissue boundaries in AF termination, future studies of I_{Na} blockade in a morphologically-realistic model of AF are needed. The use of optical mapping techniques (87; 92) to assess changes in AF dynamics by class I drugs could also be used to test model predictions. It would be of particular interest to correlate increased variability of AFCL with the promotion of hyper-meander of AF-generating circuits, and to document an associated reduction in wavelet production.

Preliminary studies by our group have been performed to evaluate the potential for K^+ channel blockade to terminate AF in the vagotonic model of AF presented in Chapter 4. As described in Section 1.3, numerous K^+ channels are present, providing multiple targets with potentially synergistic action (Section 1.6.2). Preliminary studies of the effects of I_{Kr} and I_{Kur}, or combined I_{Kr},I_{Kur} block were conducted. This class III action selectively prolonged APD_{-60} in regions with long APD (lowest [ACh] regions) from 65±24 ms to 89±27 ms (combined 50% I_{Kr},I_{Kur} block), causing a 41% increase in reentry wavelength, but had minimal effect on short-APD regions (eg, APD_{-60} from 28±1 ms to 30±1 ms) (unpublished data). Consequently, spatial variability in APD was greatly increased (e.g., maximal APD gradient from ~37 to ~59 ms), the primary spiral-wave generator was destabilized, activation became more heterogeneous and AF self-terminated. I_{Kr} block alone was relatively ineffective, consistent with its limited clinical value in AF termination, but 50% I_{Kur} block and combined I_{Kr},I_{Kur} blockade (50% each)

terminated over 80% of sustained AFs. These findings are consistent with studies discussed in Section 1.7.1.2, and indicate that class III actions may terminate AF, but by quite different mechanisms than the class I action observed in Chapter 5. Additional studies are needed to evaluate in detail the effects of class III actions in AF, and should later be extended to AF in other contexts and to models with realistic morphology (263).

6.5 Looking Ahead: The Future of Modeling in AF

In summary, mathematical models of AF allow us to evaluate all aspects of arrhythmias simultaneously, as both global and cellular activity may be accounted for, and simulations of the same AF may be rerun with various interventions applied at precise times and at precise levels. When models adequately reproduce a variety of experimental observations, the potential exists to fully characterize supporting mechanisms and intervening phenomena. Increased inter-disciplinary collaboration is needed to ensure that experiments are conducted with modeling approaches in mind, and modeling in a way that facilitates experimental confirmation. Together, the potential exists to rapidly advance both basic and clinical research.

Mathematical models of cardiac electrophysiology are rapidly converging on the establishment of ionically and morphologically realistic models of AF. The usefulness of these models is greatly potentiated by seemingly endless gains in computing power. Experimental techniques are also propelled forward by rapidly progressing technology, such that advances in theoretical and experimental initiatives may well continue, with increasing inter-disciplinary collaboration, along a hyperbolic course for many years to

come. Future developments in this area almost defy imagination. Not only will the need for animal experimentation be greatly reduced – I expect that computers will one day assimilate patient data, constructing in real time patient-specific models that are ionically, anatomically, and pathologically correct. This will enable physicians to rapidly and accurately design and test patient-specific therapies prior to treatment, thus optimizing clinical practice and greatly improving patient quality of life.

References

1. **Nattel S.** New ideas about atrial fibrillation 50 years on. *Nature* 415: 219-226, 2002.

2. **Nattel S., Courtemanche M. and Wang Z.** Functional and ionic mechanisms of antiarrhythmic drugs in atrial fibrillation. In: Atrial and ventricular fibrillation: mechanisms and device therapy., edited by Falk R.H. and Podrid P.J. Philadelphia: Lippincott-Raven, 1997, p. 75-108.

3. **Kannel W.B. and Wolf P.A.** Epidemiology of atrial fibrillation. In: Atrial Fibrillation: Mechanisms and Management, edited by Falk R.H. and Podrid P.J. New York: Raven Press Publishers, 1992, p. 81-92.

4. **Kannel WB, Abbott RD, Savage DD and McNamara PM.** Epidemiologic features of chronic atrial fibrillation: the Framingham study. *N Engl J Med* 306: 1018-1022, 1982.

5. **Onundarson PT, Thorgeirsson G, Jonmundsson E, Sigfusson N and Hardarson T.** Chronic atrial fibrillation--epidemiologic features and 14 year follow-up: a case control study. *Eur Heart J* 8: 521-527, 1987.

6. **Peterson P and Godtfredsen J.** Atrial fibrillation-a review course and prognosis. *Acta Med Scand* 216: 5-9, 1984.

7. **Ostrander LD, Jr.** Prevalence and stability of electrocardiographic abnormalities among members of a natural community. *Med Times* 95: 921-928, 1967.

8. **Brand FN, Abbott RD, Kannel WB and Wolf PA.** Characteristics and prognosis of lone atrial fibrillation. 30-year follow-up in the Framingham Study. *JAMA* 254: 3449-3453, 1985.

9. **Kannel WB, Abbott RD, Savage DD and McNamara PM.** Coronary heart disease and atrial fibrillation: the Framingham Study. *Am Heart J* 106: 389-396, 1983.

10. **Wolf PA, Kannel WB, McGee DL, Meeks SL, Bharucha NE and McNamara PM.** Duration of atrial fibrillation and imminence of stroke: the Framingham study. *Stroke* 14: 664-667, 1983.

11. **Wolf PA, Dawber TR, Thomas HE, Jr. and Kannel WB.** Epidemiologic assessment of chronic atrial fibrillation and risk of stroke: the Framingham study. *Neurology* 28: 973-977, 1978.

12. **Behar S, Tanne D, Zion M, Reicher-Reiss H, Kaplinsky E, Caspi A, Palant A and Goldbourt U.** Incidence and prognostic significance of chronic atrial fibrillation among 5,839 consecutive patients with acute myocardial infarction. The SPRINT Study Group. Secondary Prevention Reinfarction Israeli Nifedipine Trial. *Am J Cardiol* 70: 816-818, 1992.

13. **Behar S, Zahavi Z, Goldbourt U and Reicher-Reiss H.** Long-term prognosis of patients with paroxysmal atrial fibrillation complicating acute myocardial infarction. SPRINT Study Group. *Eur Heart J* 13: 45-50, 1992.

14. **Goldberg RJ, Seeley D, Becker RC, Brady P, Chen ZY, Osganian V, Gore JM, Alpert JS and Dalen JE.** Impact of atrial fibrillation on the in-hospital and long-term survival of patients with acute myocardial infarction: a community-wide perspective. *Am Heart J* 119: 996-1001, 1990.

15. **Fuller JA, Adams GG and Buxton B.** Atrial fibrillation after coronary artery bypass grafting. Is it a disorder of the elderly? *J Thorac Cardiovasc Surg* 97: 821-825, 1989.

16. **Hochberg MS, Levine FH, Daggett WM, Akins CW, Austen WG and Buckley MJ.** Isolated coronary artery bypass grafting in patients seventy years of age and older: early and late results. *J Thorac Cardiovasc Surg* 84: 219-223, 1982.

17. **Hirosawa K, Sekiguchi M, Kasanuki H, Kimata S, Kaneko N, Nakamura K, Aosaki M, Takahashi S and Kondo M.** Natural history of atrial fibrillation. *Heart Vessels Suppl* 2: 14-23, 1987.

18. **Shlofmitz RA, Hirsch BE and Meyer BR.** New-onset atrial fibrillation: is there need for emergent hospitalization? *J Gen Intern Med* 1: 139-142, 1986.

19. The urokinase pulmonary embolism trial. A national cooperative study. *Circulation* 47: II1-108, 1973.

20. **von Knorring J, Lepantalo M, Lindgren L and Lindfors O**. Cardiac arrhythmias and myocardial ischemia after thoracotomy for lung cancer. *Ann Thorac Surg* 53: 642-647, 1992.

21. **Hibbs RG, Ferrans VJ, Walsh JJ and Burch GE**. Electron microscopic observations on lysosomes and related cytoplasmic components of normal and pathological cardiac muscle. *Anat Rec* 153: 173-185, 1965.

22. **Gimeno AL, Gimeno MD and Webb JL**. Effects of ethanol on cellular membrane potentials and contractility of isolated atrium. *Am J Physiol* 203: 194-196, 1962.

23. **Engel TR and Luck JC**. Effect of whiskey on atrial vulnerability and "holiday heart". *J Am Coll Cardiol* 1: 816-818, 1983.

24. **Gould L, Reddy CV, Becker W, Oh KC and Kim SG**. Electrophysiologic properties of alcohol in man. *J Electrocardiol* 11: 219-226, 1978.

25. **Lamb LE and Pollard LW**. Atrial fibrillation in flying personnel. Report of 60 cases. *Circulation* 29: 694-710, 1964.

26. **Bartels EC**. Hyperthyroidism in patients over 65. *Geriatrics* 20: 459-462, 1965.

27. **Davies AB, Williams I, John R, Hall R and Scanlon MF**. Diagnostic value of thyrotrophin releasing hormone tests in elderly patients with atrial fibrillation. *Br Med J (Clin Res Ed)* 291: 773-776, 1985.

28. **Scott GR, Forfar JC and Toft AD**. Graves' disease and atrial fibrillation: the case for even higher doses of therapeutic iodine-131. *Br Med J (Clin Res Ed)* 289: 399-400, 1984.

29. **Forfar JC, Miller HC and Toft AD**. Occult thyrotoxicosis: a correctable cause of "idiopathic" atrial fibrillation. *Am J Cardiol* 44: 9-12, 1979.

30. **Forfar JC, Feek CM, Miller HC and Toft AD**. Atrial fibrillation and isolated suppression of the pituitary-thyroid axis: response to specific antithyroid therapy. *Int J Cardiol* 1: 43-48, 1981.

31. **Ridker PM, Gibson CM and Lopez R**. Atrial fibrillation induced by breath spray. *N Engl J Med* 320: 124, 1989.

32. **Breeden CC and Safirstein BH**. Spacer-induced atrial fibrillation. *N J Med* 87: 113-114, 1990.

33. **Bohnker BK, Feeks EF and McEwen G**. Catapult launch-associated cardioversion of atrial fibrillation. *Aviat Space Environ Med* 64: 939-940, 1993.

34. **Abbott WM, Maloney RD, McCabe CC, Lee CE and Wirthlin LS**. Arterial embolism: a 44 year perspective. *Am J Surg* 143: 460-464, 1982.

35. **Hinton RC, Kistler JP, Fallon JT, Friedlich AL and Fisher CM**. Influence of etiology of atrial fibrillation on incidence of systemic embolism. *Am J Cardiol* 40: 509-513, 1977.

36. **Aberg H**. Atrial fibrillation. I. A study of atrial thrombosis and systemic embolism in a necropsy material. *Acta Med Scand* 185: 373-379, 1969.

37. **Stafford WJ, Trohman RG, Bilsker M, Zaman L, Castellanos A and Myerburg RJ**. Cardiac arrest in an adolescent with atrial fibrillation and hypertrophic cardiomyopathy. *J Am Coll Cardiol* 7: 701-704, 1986.

38. **Peters KG and Kienzle MG**. Severe cardiomyopathy due to chronic rapidly conducted atrial fibrillation: complete recovery after restoration of sinus rhythm. *Am J Med* 85: 242-244, 1988.

39. **Grogan M, Smith HC, Gersh BJ and Wood DL**. Left ventricular dysfunction due to atrial fibrillation in patients initially believed to have idiopathic dilated cardiomyopathy. *Am J Cardiol* 69: 1570-1573, 1992.

40. **Zipes DP**. The seventh annual Gordon K. Moe Lecture. Atrial fibrillation: from cell t bedside. *J Cardiovasc Electrophysiol* 8: 927-938, 1997.

41. **Waktare JE and Camm AJ**. Atrial fibrillation begets trouble. *Heart* 77: 393-394, 1997.

42. **Ramirez RJ, Nattel S and Courtemanche M.** Mathematical analysis of canine atrial action potentials: rate, regional factors, and electrical remodeling. *Am J Physiol Heart Circ Physiol* 279: H1767-H1785, 2000.

43. **Lewis T.** Nature of flutter and fibrillation in the aurcle. Oliver-Sharpey lectures. *Lancet* i: 785-788, 1921.

44. **Lewis T.** Nature of flutter and fibrillation of the auricle. *Lancet* i: 845-848, 1921.

45. **Rothberger C.J. and Winterberg H.** Vorhofflimern und arrhythmia perpetua. *Wien Klin Wochenschr* 22: 839-844, 1909.

46. **Cushny A.R. and Edmunds C.W.** Paroxysmal irregularity of the heart and auricular fibrillation. *Am J Med Sci* 133: 66, 1907.

47. **Garrey WE.** Auricular Fibrillation. *Physiol Rev* 4: 215-250, 1924.

48. **McWilliam J.A.** Fibrillation contraction of the heart. *J Physiol (Lond)* 8: 296-310, 1887.

49. **Mayer AG.** Rhythmical pulsation in scyphomedusae: part II. *Papers Tortugas Lab Carnegie Institution of Washington* 115-131, 1908.

50. **Mines GR.** On dynamic equilibrium in the heart. *J Physiol (Lond)* 46: 349-383, 1913.

51. **Mines G.R.** On circulating excitations in heart muscles and their possible relation to tachycardia and fibrillation. *Proc Trans R Soc Can* 8: 43-53, 1914.

52. **Garrey WE.** Nature of fibrillary contraction of the heart: Its relation to tissue mass and form. *Am J Physiol* 33: 397-414, 1914.

53. **Lewis T.** *The Mechanism and Graphic Registration of the Heart Beat.* London: Shaw & Sons, 1925.

54. **Nattel S, Li D and Yue L.** Basic mechanisms of atrial fibrillation--very new insights into very old ideas. *Annu Rev Physiol* 62: 51-77, 2000.

55. **Haissaguerre M, Jais P, Shah DC, Takahashi A, Hocini M, Quiniou G, Garrigue S, Le Mouroux A, Le Metayer P and Clementy J.** Spontaneous initiation of atrial fibrillation by ectopic beats originating in the pulmonary veins. *N Engl J Med* 339: 659-666, 1998.

56. **Doshi RN, Wu TJ, Yashima M, Kim YH, Ong JJ, Cao JM, Hwang C, Yashar P, Fishbein MC, Karagueuzian HS and Chen PS.** Relation between ligament of Marshall and adrenergic atrial tachyarrhythmia. *Circulation* 100: 876-883, 1999.

57. **Tsai CF, Tai CT, Hsieh MH, Lin WS, Yu WC, Ueng KC, Ding YA, Chang MS and Chen SA.** Initiation of atrial fibrillation by ectopic beats originating from the superior vena cava: electrophysiological characteristics and results of radiofrequency ablation. *Circulation* 102: 67-74, 2000.

58. **Wu TJ, Yashima M, Xie F, Athill CA, Kim YH, Fishbein MC, Qu Z, Garfinkel A, Weiss JN, Karagueuzian HS and Chen PS.** Role of pectinate muscle bundles in the generation and maintenance of intra-atrial reentry: potential implications for the mechanism of conversion between atrial fibrillation and atrial flutter. *Circ Res* 83: 448-462, 1998.

59. **Allessie MA, Bonke FI and Schopman FJ.** Circus movement in rabbit atrial muscle as a mechanism of tachycardia. III. The "leading circle" concept: a new model of circus movement in cardiac tissue without the involvement of an anatomical obstacle. *Circ Res* 41: 9-18, 1977.

60. **Wiener N and Rosenblueth A.** The mathematical formulation of the problem of conduction of impulses in a network of connected excitable elements, specifically in cardiac muscle. *Arch Inst Cardiol Mex* 16: 205-265, 1946.

61. **Winfree AT.** Persistent tangled vortex rings in generic excitable media. *Nature* 371: 233-236, 1994.

62. **Davidenko JM, Pertsov AV, Salomonsz R, Baxter W and Jalife J.** Stationary and drifting spiral waves of excitation in isolated cardiac muscle. *Nature* 355: 349-351, 1992.

63. **Gray RA, Jalife J, Panfilov AV, Baxter WT, Cabo C, Davidenko JM and Pertsov AM.** Mechanisms of cardiac fibrillation. *Science* 270: 1222-1223, 1995.

64. **Ikeda T, Yashima M, Uchida T, Hough D, Fishbein MC, Mandel WJ, Chen PS and Karagueuzian HS.** Attachment of meandering reentrant wave fronts to anatomic obstacles in the atrium. Role of the obstacle size. *Circ Res* 81: 753-764, 1997.

65. **Ikeda T, Czer L, Trento A, Hwang C, Ong JJ, Hough D, Fishbein MC, Mandel WJ, Karagueuzian HS and Chen PS.** Induction of meandering functional reentrant wave front in isolated human atrial tissues. *Circulation* 96: 3013-3020, 1997.

66. **Ikeda T, Uchida T, Hough D, Lee JJ, Fishbein MC, Mandel WJ, Chen PS and Karagueuzian HS.** Mechanism of spontaneous termination of functional reentry in isolated canine right atrium. Evidence for the presence of an excitable but nonexcited core. *Circulation* 94: 1962-1973, 1996.

67. **Ikeda T, Wu TJ, Uchida T, Hough D, Fishbein MC, Mandel WJ, Chen PS and Karagueuzian HS.** Meandering and unstable reentrant wave fronts induced by acetylcholine in isolated canine right atrium. *Am J Physiol* 273: H356-H370, 1997.

68. **Pertsov AM, Davidenko JM, Salomonsz R, Baxter WT and Jalife J.** Spiral waves of excitation underlie reentrant activity in isolated cardiac muscle. *Circ Res* 72: 631-650, 1993.

69. **Athill CA, Ikeda T, Kim YH, Wu TJ, Fishbein MC, Karagueuzian HS and Chen PS.** Transmembrane potential properties at the core of functional reentrant wave fronts in isolated canine right atria. *Circulation* 98: 1556-1567, 1998.

70. **Moe G.K. and Abildskov J.A.** Atrial fibrillation as a self-perpetuating arrhythmia independent of focal discharge. *Am Heart J* 58: 59-70, 1959.

71. **Moe GK.** On the multiple wavelet hypothesis of atrial fibrillation. *Arch Int Pharmacodyn Ther* 140: 183-188, 1962.

72. **Moe GK, Rheinboldt WC and Abildskov JA.** A computer model of atrial fibrillation. *Am Heart J* 67: 200-220, 1964.

73. **Jalife J, Berenfeld O, Skanes A and Mandapati R.** Mechanisms of atrial fibrillation: mother rotors or multiple daughter wavelets, or both? *J Cardiovasc Electrophysiol* 9: S2-12, 1998.

74. **Tritton D.J.** Physical Fluid Dynamics. edited by Van Nostrand Reinhold. Berkshire, England: 1977, p. 21-27.

75. **Allessie MA, Lammers W.J.E.P., Bonke F.I.M. and Hollen J.** Experimental evaluation of Moe's multiple wavelet hypothesis of atrial fibrillation. In: Cardiac Arrhythmias, edited by Zipes DP and Jalife J. New York: Grune & Stratton, 1985, p. 265-276.

76. **Kirchhof C, Chorro F, Scheffer GJ, Brugada J, Konings K, Zetelaki Z and Allessie M.** Regional entrainment of atrial fibrillation studied by high-resolution mapping in open-chest dogs. *Circulation* 88: 736-749, 1993.

77. **Cox JL, Canavan TE, Schuessler RB, Cain ME, Lindsay BD, Stone C, Smith PK, Corr PB and Boineau JP.** The surgical treatment of atrial fibrillation. II. Intraoperative electrophysiologic mapping and description of the electrophysiologic basis of atrial flutter and atrial fibrillation. *J Thorac Cardiovasc Surg* 101: 406-426, 1991.

78. **Konings KT, Kirchhof CJ, Smeets JR, Wellens HJ, Penn OC and Allessie MA.** High-density mapping of electrically induced atrial fibrillation in humans. *Circulation* 89: 1665-1680, 1994.

79. **Shinagawa K, Mitamura H, Takeshita A, Sato T, Kanki H, Takatsuki S and Ogawa S.** Determination of refractory periods and conduction velocity during atrial fibrillation using atrial capture in dogs: direct assessment of the wavelength and its modulation by a sodium channel blocker, pilsicainide. *J Am Coll Cardiol* 35: 246-253, 2000.

80. **Kanki H, Mitamura H, Takatsuki S, Sueyoshi K, Shinagawa K, Sato T and Ogawa S.** Postrepolarization refractoriness as a potential anti-atrial fibrillation mechanism of pilsicainide, a pure sodium channel blocker with slow recovery kinetics. *Cardiovasc Drugs Ther* 12: 475-482, 1998.

81. **Esato M, Shimizu A, Chun YH, Tatsuno H, Yamagata T and Matsuzaki M.** Electrophysiologic effects of a class I antiarrhythmic agent, cibenzoline, on the refractoriness and conduction of the human atrium in vivo. *J Cardiovasc Pharmacol* 28: 321-327, 1996.

82. **Iwasa A, Okumura K, Tabuchi T, Tsuchiya T, Tsunoda R, Matsunaga T, Tayama S and Yasue H.** Effects of pilsicainide and propafenone on vagally

induced atrial fibrillation: role of suppressant effect in conductivity. *Eur J Pharmacol* 356: 31-40, 1998.

83. **Downar E, Harris L, Mickleborough LL, Shaikh N and Parson ID.** Endocardial mapping of ventricular tachycardia in the intact human ventricle: evidence for reentrant mechanisms. *J Am Coll Cardiol* 11: 783-791, 1988.

84. **Janse MJ, Wilms-Schopman FJ and Coronel R.** Ventricular fibrillation is not always due to multiple wavelet reentry. *J Cardiovasc Electrophysiol* 6: 512-521, 1995.

85. **Witkowski FX, Leon LJ, Penkoske PA, Giles WR, Spano ML, Ditto WL and Winfree AT.** Spatiotemporal evolution of ventricular fibrillation. *Nature* 392: 78-82, 1998.

86. **Epstein A.E. and Ideker R.E.** Ventricular fibrillation. In: Cardiac electrophysiology: from cell to bedside, edited by Zipes DP and Jalife J. Philadelphia: Saunders, 1995, p. 927-933.

87. **Chen J, Mandapati R, Berenfeld O, Skanes AC, Gray RA and Jalife J.** Dynamics of wavelets and their role in atrial fibrillation in the isolated sheep heart. *Cardiovasc Res* 48: 220-232, 2000.

88. **Winfree AT.** Sudden cardia death: a problem in topology. *Sci Am* 248: 144-7, 160, 1983.

89. **Schuessler RB, Grayson TM, Bromberg BI, Cox JL and Boineau JP.** Cholinergically mediated tachyarrhythmias induced by a single extrastimulus in the isolated canine right atrium. *Circ Res* 71: 1254-1267, 1992.

90. **Kumagai K, Khrestian C and Waldo AL.** Simultaneous multisite mapping studies during induced atrial fibrillation in the sterile pericarditis model. Insights into the mechanism of its maintenance. *Circulation* 95: 511-521, 1997.

91. **Skanes AC, Mandapati R, Berenfeld O, Davidenko JM and Jalife J.** Spatiotemporal periodicity during atrial fibrillation in the isolated sheep heart. *Circulation* 98: 1236-1248, 1998.

92. **Mandapati R, Skanes A, Chen J, Berenfeld O and Jalife J**. Stable microreentrant sources as a mechanism of atrial fibrillation in the isolated sheep heart. *Circulation* 101: 194-199, 2000.

93. **Berenfeld O, Mandapati R, Dixit S, Skanes AC, Chen J, Mansour M and Jalife J**. Spatially distributed dominant excitation frequencies reveal hidden organization in atrial fibrillation in the Langendorff-perfused sheep heart. *J Cardiovasc Electrophysiol* 11: 869-879, 2000.

94. **Karagueuzian HS, Khan SS, Peters W, Mandel WJ and Diamond GA**. Nonhomogeneous local atrial activity during acute atrial fibrillation: spectral and dynamic analysis. *Pacing Clin Electrophysiol* 13: 1937-1942, 1990.

95. **Pertsov AM, Panfilov AV and Medvedeva FU**. [Instabilities of autowaves in excitable media associated with critical curvature phenomena]. *Biofizika* 28: 100-102, 1983.

96. **Pertsov AM, Ermakova EA and Shnol EE**. On the diffraction of autowaves. *Physica D* 44: 178-190, 1990.

97. **Botteron GW and Smith JM**. Quantitative assessment of the spatial organization of atrial fibrillation in the intact human heart. *Circulation* 93: 513-518, 1996.

98. **Rosenbaum DS and Cohen RJ**. Frequency based measures of atrial fibrillation in man. *IEEE-EMBS* 12: 582-583, 1990.

99. **Gerstenfeld EP, Sahakian AV and Swiryn S**. Evidence for transient linking of atrial excitation during atrial fibrillation in humans. *Circulation* 86: 375-382, 1992.

100. **Lehmann MH, Denker S, Mahmud R, Addas A and Akhtar M**. Linking: a dynamic electrophysiologic phenomenon in macroreentry circuits. *Circulation* 71: 254-265, 1985.

101. **Mansour M, Mandapati R, Berenfeld O, Chen J, Samie FH and Jalife J**. Left-to-right gradient of atrial frequencies during acute atrial fibrillation in the isolated sheep heart. *Circulation* 103: 2631-2636, 2001.

102. **Li D, Zhang L, Kneller J and Nattel S**. Potential ionic mechanism for repolarization differences between canine right and left atrium. *Circ Res* 88: 1168-1175, 2001.

103. **Morillo CA, Klein GJ, Jones DL and Guiraudon CM**. Chronic rapid atrial pacing. Structural, functional, and electrophysiological characteristics of a new model of sustained atrial fibrillation. *Circulation* 91: 1588-1595, 1995.

104. **Sueda T, Nagata H, Shikata H, Orihashi K, Morita S, Sueshiro M, Okada K and Matsuura Y**. Simple left atrial procedure for chronic atrial fibrillation associated with mitral valve disease. *Ann Thorac Surg* 62: 1796-1800, 1996.

105. **Harada A, Sasaki K, Fukushima T, Ikeshita M, Asano T, Yamauchi S, Tanaka S and Shoji T**. Atrial activation during chronic atrial fibrillation in patients with isolated mitral valve disease. *Ann Thorac Surg* 61: 104-111, 1996.

106. **Harada A, Konishi T, Fukata M, Higuchi K, Sugimoto T and Sasaki K**. Intraoperative map guided operation for atrial fibrillation due to mitral valve disease. *Ann Thorac Surg* 69: 446-450, 2000.

107. **Jais P, Haissaguerre M, Shah DC, Chouairi S, Gencel L, Hocini M and Clementy J**. A focal source of atrial fibrillation treated by discrete radiofrequency ablation. *Circulation* 95: 572-576, 1997.

108. **Wu TJ, Ong JJ, Chang CM, Doshi RN, Yashima M, Huang HL, Fishbein MC, Ting CT, Karagueuzian HS and Chen PS**. Pulmonary veins and ligament of marshall as sources of rapid activations in a canine model of sustained atrial fibrillation. *Circulation* 103: 1157-1163, 2001.

109. **Schuessler RB**. Does size matter? *J Cardiovasc Electrophysiol* 12: 875-876, 2001.

110. **Schuessler RB, Boineau JP, Bromberg BI, Hand DE, Yamauchi S and Cox JL**. Normal and abnormal activation of the atrium. In: Cardiac Electrophysiology: From Cell to Bedside, edited by Zipes DP and Jalife J. Philadelphia: WB Saunders, 1995, p. 543-562.

111. **Cox JL, Schuessler RB, D'Agostino HJ, Jr., Stone CM, Chang BC, Cain ME, Corr PB and Boineau JP**. The surgical treatment of atrial fibrillation. III.

Development of a definitive surgical procedure. *J Thorac Cardiovasc Surg* 101: 569-583, 1991.

112. **Cox JL, Ad N, Palazzo T, Fitzpatrick S, Suyderhoud JP, DeGroot KW, Pirovic EA, Lou HC, Duvall WZ and Kim YD.** Current status of the Maze procedure for the treatment of atrial fibrillation. *Semin Thorac Cardiovasc Surg* 12: 15-19, 2000.

113. **McCarthy PM, Gillinov AM, Castle L, Chung M and Cosgrove D, III.** The Cox-Maze procedure: the Cleveland Clinic experience. *Semin Thorac Cardiovasc Surg* 12: 25-29, 2000.

114. **Schaff HV, Dearani JA, Daly RC, Orszulak TA and Danielson GK.** Cox-Maze procedure for atrial fibrillation: Mayo Clinic experience. *Semin Thorac Cardiovasc Surg* 12: 30-37, 2000.

115. **Arcidi JM, Jr., Doty DB and Millar RC.** The Maze procedure: the LDS Hospital experience. *Semin Thorac Cardiovasc Surg* 12: 38-43, 2000.

116. **Kosakai Y.** Treatment of atrial fibrillation using the Maze procedure: the Japanese experience. *Semin Thorac Cardiovasc Surg* 12: 44-52, 2000.

117. **Haissaguerre M, Jais P, Shah DC, Arentz T, Kalusche D, Takahashi A, Garrigue S, Hocini M, Peng JT and Clementy J.** Catheter ablation of chronic atrial fibrillation targeting the reinitiating triggers. *J Cardiovasc Electrophysiol* 11: 2-10, 2000.

118. **Tsai CF, Tai CT, Hsieh MH, Lin WS, Yu WC, Ueng KC, Ding YA, Chang MS and Chen SA.** Initiation of atrial fibrillation by ectopic beats originating from the superior vena cava: electrophysiological characteristics and results of radiofrequency ablation. *Circulation* 102: 67-74, 2000.

119. Nitta, T., Sakamoto, S. I., Saji, Y., Yosuke, I., Iwake, H., Ohkubo, N., Yajima, T., Ochi, M., and Tanaka, S. Focal activation underlying permanent atrial fibrillation in patients with mitral valve disease. Circulation 102. 2000.
Ref Type: Abstract

120. **Jalife J.** Ventricular fibrillation: mechanisms of initiation and maintenance. *Annu Rev Physiol* 62: 25-50, 2000.

121. **Leon LJ and Roberge FA.** Directional characteristics of action potential propagation in cardiac muscle. A model study. *Circ Res* 69: 378-395, 1991.

122. **Cabo C, Pertsov AM, Baxter WT, Davidenko JM, Gray RA and Jalife J.** Wave-front curvature as a cause of slow conduction and block in isolated cardiac muscle. *Circ Res* 75: 1014-1028, 1994.

123. **Mandapati R, Asano Y, Baxter WT, Gray R, Davidenko J and Jalife J.** Quantification of effects of global ischemia on dynamics of ventricular fibrillation in isolated rabbit heart. *Circulation* 98: 1688-1696, 1998.

124. **Frame LH, Page RL and Hoffman BF.** Atrial reentry around an anatomic barrier with a partially refractory excitable gap. A canine model of atrial flutter. *Circ Res* 58: 495-511, 1986.

125. **Spinelli W and Hoffman BF.** Mechanisms of termination of reentrant atrial arrhythmias by class I and class III antiarrhythmic agents. *Circ Res* 65: 1565-1579, 1989.

126. **Frame LH, Page RL, Boyden PA, Fenoglio JJ, Jr. and Hoffman BF.** Circus movement in the canine atrium around the tricuspid ring during experimental atrial flutter and during reentry in vitro. *Circulation* 76: 1155-1175, 1987.

127. **Rosenblueth A. and Gardia RJ.** Studies on flutter and fibrillation. II. The influence of artificial obstacles in experimental auricular flutter. *Am Heart J* 33: 677-684, 1947.

128. **Yamane T, Shah DC, Jais P and Haissaguerre M.** Pseudo sinus rhythm originating from the left superior pulmonary vein in a patient with paroxysmal atrial fibrillation. *J Cardiovasc Electrophysiol* 12: 1190-1191, 2001.

129. **Haissaguerre M, Jais P, Shah DC, Garrigue S, Takahashi A, Lavergne T, Hocini M, Peng JT, Roudaut R and Clementy J.** Electrophysiological end point for catheter ablation of atrial fibrillation initiated from multiple pulmonary venous foci. *Circulation* 101: 1409-1417, 2000.

130. **Gray RA, Pertsov AM and Jalife J.** Incomplete reentry and epicardial breakthrough patterns during atrial fibrillation in the sheep heart. *Circulation* 94: 2649-2661, 1996.

131. **Wang J, Liu L, Feng J and Nattel S.** Regional and functional factors determining induction and maintenance of atrial fibrillation in dogs. *Am J Physiol* 271: H148-H158, 1996.

132. **Nattel S, Bourne G and Talajic M.** Insights into mechanisms of antiarrhythmic drug action from experimental models of atrial fibrillation. *J Cardiovasc Electrophysiol* 8: 469-480, 1997.

133. **Rothberger C.J. and Winterberg H.** Uber Vorhofflimmern and Vorhofflattern. *Pflugers Arch* 160: 42-90, 1914.

134. **Kneller J, Zou R, Vigmond EJ, Wang Z, Leon LJ and Nattel S.** Cholinergic atrial fibrillation in a computer model of a two-dimensional sheet of canine atrial cells with realistic ionic properties. *Circ Res* 90: E73-E87, 2002.

135. **Ninomiya I.** Direct evidence of nonuniform distribution of vagal effects on dog atria. *Circ Res* 19: 576-583, 1966.

136. **Alessi R., Nusynowitz M., Abildskov J.A. and Moe G.K.** Nonuniform distribution of vagal effects on the atrial refractory period. *Am Heart J* 194: 406-410, 1958.

137. **Liu L and Nattel S.** Differing sympathetic and vagal effects on atrial fibrillation in dogs: role of refractoriness heterogeneity. *Am J Physiol* 273: H805-H816, 1997.

138. **Feng J, Yue L, Wang Z and Nattel S.** Ionic mechanisms of regional action potential heterogeneity in the canine right atrium. *Circ Res* 83: 541-551, 1998.

139. **Wang J, Feng J and Nattel S.** Class III antiarrhythmic drug action in experimental atrial fibrillation. Differences in reverse use dependence and effectiveness between d-sotalol and the new antiarrhythmic drug ambasilide. *Circulation* 90: 2032-2040, 1994.

140. **Wang J, Bourne GW, Wang Z, Villemaire C, Talajic M and Nattel S.** Comparative mechanisms of antiarrhythmic drug action in experimental atrial fibrillation. Importance of use-dependent effects on refractoriness. *Circulation* 88: 1030-1044, 1993.

141. **Wijffels MC, Kirchhof CJ, Dorland R and Allessie MA**. Atrial fibrillation begets atrial fibrillation. A study in awake chronically instrumented goats. *Circulation* 92: 1954-1968, 1995.

142. **Wijffels MC, Kirchhof CJ, Dorland R, Power J and Allessie MA**. Electrical remodeling due to atrial fibrillation in chronically instrumented conscious goats: roles of neurohumoral changes, ischemia, atrial stretch, and high rate of electrical activation. *Circulation* 96: 3710-3720, 1997.

143. **Sun H, Chartier D, Leblanc N and Nattel S**. Intracellular calcium changes and tachycardia-induced contractile dysfunction in canine atrial myocytes. *Cardiovasc Res* 49: 751-761, 2001.

144. **Courtemanche M, Ramirez RJ and Nattel S**. Ionic mechanisms underlying human atrial action potential properties: insights from a mathematical model. *Am J Physiol* 275: H301-H321, 1998.

145. **Yue L, Melnyk P, Gaspo R, Wang Z and Nattel S**. Molecular mechanisms underlying ionic remodeling in a dog model of atrial fibrillation. *Circ Res* 84: 776-784, 1999.

146. **Brundel BJ, van Gelder IC, Henning RH, Tuinenburg AE, Deelman LE, Tieleman RG, Grandjean JG, van Gilst WH and Crijns HJ**. Gene expression of proteins influencing the calcium homeostasis in patients with persistent and paroxysmal atrial fibrillation. *Cardiovasc Res* 42: 443-454, 1999.

147. **Lai LP, Su MJ, Lin JL, Lin FY, Tsai CH, Chen YS, Huang SK, Tseng YZ and Lien WP**. Down-regulation of L-type calcium channel and sarcoplasmic reticular Ca(2+)-ATPase mRNA in human atrial fibrillation without significant change in the mRNA of ryanodine receptor, calsequestrin and phospholamban: an insight into the mechanism of atrial electrical remodeling. *J Am Coll Cardiol* 33: 1231-1237, 1999.

148. **Yue L, Feng J, Gaspo R, Li GR, Wang Z and Nattel S**. Ionic remodeling underlying action potential changes in a canine model of atrial fibrillation. *Circ Res* 81: 512-525, 1997.

149. **Van Wagoner DR, Pond AL, Lamorgese M, Rossie SS, McCarthy PM and Nerbonne JM**. Atrial L-type Ca2+ currents and human atrial fibrillation. *Circ Res* 85: 428-436, 1999.

150. **Bosch RF, Zeng X, Grammer JB, Popovic K, Mewis C and Kuhlkamp V.** Ionic mechanisms of electrical remodeling in human atrial fibrillation. *Cardiovasc Res* 44: 121-131, 1999.

151. **Gaspo R, Bosch RF, Talajic M and Nattel S.** Functional mechanisms underlying tachycardia-induced sustained atrial fibrillation in a chronic dog model. *Circulation* 96: 4027-4035, 1997.

152. **Sun H, Gaspo R, Leblanc N and Nattel S.** Cellular mechanisms of atrial contractile dysfunction caused by sustained atrial tachycardia. *Circulation* 98: 719-727, 1998.

153. **Ohkusa T, Ueyama T, Yamada J, Yano M, Fujumura Y, Esato K and Matsuzaki M.** Alterations in cardiac sarcoplasmic reticulum Ca2+ regulatory proteins in the atrial tissue of patients with chronic atrial fibrillation. *J Am Coll Cardiol* 34: 255-263, 1999.

154. **Ausma J, Wijffels M, Thone F, Wouters L, Allessie M and Borgers M.** Structural changes of atrial myocardium due to sustained atrial fibrillation in the goat. *Circulation* 96: 3157-3163, 1997.

155. **Gaspo R, Bosch RF, Bou-Abboud E and Nattel S.** Tachycardia-induced changes in Na+ current in a chronic dog model of atrial fibrillation. *Circ Res* 81: 1045-1052, 1997.

156. **Van Wagoner DR, Pond AL, McCarthy PM, Trimmer JS and Nerbonne JM.** Outward K+ current densities and Kv1.5 expression are reduced in chronic human atrial fibrillation. *Circ Res* 80: 772-781, 1997.

157. **Elvan A, Wylie K and Zipes DP.** Pacing-induced chronic atrial fibrillation impairs sinus node function in dogs. Electrophysiological remodeling. *Circulation* 94: 2953-2960, 1996.

158. **Fareh S, Villemaire C and Nattel S.** Importance of refractoriness heterogeneity in the enhanced vulnerability to atrial fibrillation induction caused by tachycardia-induced atrial electrical remodeling. *Circulation* 98: 2202-2209, 1998.

159. **Vaziri SM, Larson MG, Benjamin EJ and Levy D.** Echocardiographic predictors of nonrheumatic atrial fibrillation. The Framingham Heart Study. *Circulation* 89: 724-730, 1994.

160. **Li D, Melnyk P, Feng J, Wang Z, Petrecca K, Shrier A and Nattel S.** Effects of experimental heart failure on atrial cellular and ionic electrophysiology. *Circulation* 101: 2631-2638, 2000.

161. **Li D, Fareh S, Leung TK and Nattel S.** Promotion of atrial fibrillation by heart failure in dogs: atrial remodeling of a different sort. *Circulation* 100: 87-95, 1999.

162. **Rossi L.** Histopathologic correlates of atrial arrhythmias. In: Atrial Arrhythmias. Current Concepts and Management, edited by Touboul P. and Waldo AL. St. Louis: Mosby Year Book, 1990, p. 27-41.

163. **Li D, Benardeau A and Nattel S.** Contrasting efficacy of dofetilide in differing experimental models of atrial fibrillation. *Circulation* 102: 104-112, 2000.

164. **Rensma PL, Allessie MA, Lammers WJ, Bonke FI and Schalij MJ.** Length of excitation wave and susceptibility to reentrant atrial arrhythmias in normal conscious dogs. *Circ Res* 62: 395-410, 1988.

165. **Smeets JL, Allessie MA, Lammers WJ, Bonke FI and Hollen J.** The wavelength of the cardiac impulse and reentrant arrhythmias in isolated rabbit atrium. The role of heart rate, autonomic transmitters, temperature, and potassium. *Circ Res* 58: 96-108, 1986.

166. **Guerra PG, Talajic M, Roy D, Dubuc M, Thibault B and Nattel S.** Is there a future for antiarrhythmic drug therapy? *Drugs* 56: 767-781, 1998.

167. **Spach MS, Barr RC, Serwer GA, Kootsey JM and Johnson EA.** Extracellular potentials related to intracellular action potentials in the dog Purkinje system. *Circ Res* 30: 505-519, 1972.

168. **Wang ZG, Pelletier LC, Talajic M and Nattel S.** Effects of flecainide and quinidine on human atrial action potentials. Role of rate-dependence and comparison with guinea pig, rabbit, and dog tissues. *Circulation* 82: 274-283, 1990.

169. **Wang J, Bourne GW, Wang Z, Villemaire C, Talajic M and Nattel S.** Comparative mechanisms of antiarrhythmic drug action in experimental atrial fibrillation. Importance of use-dependent effects on refractoriness. *Circulation* 88: 1030-1044, 1993.

170. **Wijffels MC, Dorland R and Allessie MA**. Pharmacologic cardioversion of chronic atrial fibrillation in the goat by class IA, IC, and III drugs: a comparison between hydroquinidine, cibenzoline, flecainide, and d-sotalol. *J Cardiovasc Electrophysiol* 10: 178-193, 1999.

171. **Wijffels MC, Dorland R, Mast F and Allessie MA**. Widening of the excitable gap during pharmacological cardioversion of atrial fibrillation in the goat: effects of cibenzoline, hydroquinidine, flecainide, and d-sotalol. *Circulation* 102: 260-267, 2000.

172. **Hayashi H, Fujiki A, Tani M, Usui M and Inoue H**. Different effects of class Ic and III antiarrhythmic drugs on vagotonic atrial fibrillation in the canine heart. *J Cardiovasc Pharmacol* 31: 101-107, 1998.

173. **Ortiz J, Nozaki A, Shimizu A, Khrestian C, Rudy Y and Waldo AL**. Mechanism of interruption of atrial flutter by moricizine. Electrophysiological and multiplexing studies in the canine sterile pericarditis model of atrial flutter. *Circulation* 89: 2860-2869, 1994.

174. **Namba T, Ashihara T, Nakazawa K and Ohe T**. Effect of pilsicainide, a pure sodium channel blocker, on spiral waves during atrial fibrillation: theoretical analysis by numerical simulation. *J Electrocardiol* 32: 321-334, 1999.

175. **Fei H, Yazmajian D, Hanna MS and Frame LH**. Termination of reentry by lidocaine in the tricuspid ring in vitro. Role of cycle-length oscillation, fast use-dependent kinetics, and fixed block. *Circ Res* 80: 242-252, 1997.

176. **Wang Z, Page P and Nattel S**. Mechanism of flecainide's antiarrhythmic action in experimental atrial fibrillation. *Circ Res* 71: 271-287, 1992.

177. **Krishnan SC and Antzelevitch C**. Flecainide-induced arrhythmia in canine ventricular epicardium. Phase 2 reentry? *Circulation* 87: 562-572, 1993.

178. **Stambler BS, Wood MA and Ellenbogen KA**. Antiarrhythmic actions of intravenous ibutilide compared with procainamide during human atrial flutter and fibrillation: electrophysiological determinants of enhanced conversion efficacy. *Circulation* 96: 4298-4306, 1997.

179. **Wang ZG, Pelletier LC, Talajic M and Nattel S**. Effects of flecainide and quinidine on human atrial action potentials. Role of rate-dependence and

comparison with guinea pig, rabbit, and dog tissues. *Circulation* 82: 274-283, 1990.

180. **Brugada J, Gursoy S, Brugada P, Atie J, Guiraudon G and Andries E.** Cibenzoline transforms random re-entry into ordered re-entry in the atria. *Eur Heart J* 14: 267-272, 1993.

181. **Danse PW, Garratt CJ, Mast F and Allessie MA.** Preferential depression of conduction around a pivot point in rabbit ventricular myocardium by potassium and flecainide. *J Cardiovasc Electrophysiol* 11: 262-273, 2000.

182. **Pinto JM, Graziano JN and Boyden PA.** Endocardial mapping of reentry around an anatomical barrier in the canine right atrium: observations during the action of the Class IC agent, flecainide. *J Cardiovasc Electrophysiol* 4: 672-685, 1993.

183. **Sakakibara Y, Wasserstrom JA, Furukawa T, Jia H, Arentzen CE, Hartz RS and Singer DH.** Characterization of the sodium current in single human atrial myocytes. *Circ Res* 71: 535-546, 1992.

184. **Rushton RAH.** Initiation of the propagated disturbance. *Proc R Soc Lond B Biol Sci* 124: 210-243, 1937.

185. **Fozzard HA and Schoenberg M.** Strength-duration curves in cardiac Purkinje fibres: effects of liminal length and charge distribution. *J Physiol* 226: 593-618, 1972.

186. **Noble D.** The relation of Rushton's 'liminal length' for excitation to the resting and active conductances of excitable cells. *J Physiol* 226: 573-591, 1972.

187. **Krinsky VI, Efimov IR and Jalife J.** Vortices with linear cores in excitable media. *Proc R Soc Lond* 437: 645-655, 1992.

188. **Spach MS, Miller WT, III, Miller-Jones E, Warren RB and Barr RC.** Extracellular potentials related to intracellular action potentials during impulse conduction in anisotropic canine cardiac muscle. *Circ Res* 45: 188-204, 1979.

189. **Spach MS, Miller WT, III, Geselowitz DB, Barr RC, Kootsey JM and Johnson EA.** The discontinuous nature of propagation in normal canine cardiac

muscle. Evidence for recurrent discontinuities of intracellular resistance that affect the membrane currents. *Circ Res* 48: 39-54, 1981.

190. **Spach MS**. The discontinuous nature of electrical propagation in cardiac muscle. Consideration of a quantitative model incorporating the membrane ionic properties and structural complexities. The ALZA distinguished lecture. *Ann Biomed Eng* 11: 209-261, 1983.

191. **Spach MS, Miller WT, III, Dolber PC, Kootsey JM, Sommer JR and Mosher CE, Jr.** The functional role of structural complexities in the propagation of depolarization in the atrium of the dog. Cardiac conduction disturbances due to discontinuities of effective axial resistivity. *Circ Res* 50: 175-191, 1982.

192. **Hodgkin A.L. and Huxley A.F.** A quantitative description of the membrane current and its application to conduction and excitation in nerve. *J Physiol* 117: 500-544, 1952.

193. **Guan S, Lu Q and Huang K**. A discussion about the DiFrancesco-Noble model. *J Theor Biol* 189: 27-32, 1997.

194. **Fitzhugh R**. Thresholds and plateaus in the Hodgkin-Huxley nerve equations. *J Gen Physiol* 43: 867-896, 1960.

195. **Noble D**. A modification of the Hodgkin-Huxley equations applicable to Purkinje fibre action and pacemaker potential. *J Physiol Lond* 160: 317-352, 1962.

196. **McAllister RE, Noble D and Tsien RW**. Reconstruction of the electrical activity of cardiac Purkinje fibres. *J Physiol* 251: 1-59, 1975.

197. **Beeler GW and Reuter H**. Reconstruction of the action potential of ventricular myocardial fibres. *J Physiol* 268: 177-210, 1977.

198. **DiFrancesco D and Noble D**. A model of cardiac electrical activity incorporating ionic pumps and concentration changes. *Philos Trans R Soc Lond B Biol Sci* 307: 353-398, 1985.

199. **Nygren A, Fiset C, Firek L, Clark JW, Lindblad DS, Clark RB and Giles WR**. Mathematical model of an adult human atrial cell: the role of K+ currents in repolarization. *Circ Res* 82: 63-81, 1998.

200. **Courtemanche M, Ramirez RJ and Nattel S.** Ionic mechanisms underlying human atrial action potential properties: insights from a mathematical model. *Am J Physiol* 275: H301-H321, 1998.

201. **Lindblad DS, Murphey CR, Clark JW and Giles WR.** A model of the action potential and underlying membrane currents in a rabbit atrial cell. *Am J Physiol* 271: H1666-H1696, 1996.

202. **Demir SS, Clark JW, Murphey CR and Giles WR.** A mathematical model of a rabbit sinoatrial node cell. *Am J Physiol* 266: C832-C852, 1994.

203. **Nordin C.** Computer model of membrane current and intracellular Ca2+ flux in the isolated guinea pig ventricular myocyte. *Am J Physiol* 265: H2117-H2136, 1993.

204. **Luo CH and Rudy Y.** A dynamic model of the cardiac ventricular action potential. II. Afterdepolarizations, triggered activity, and potentiation. *Circ Res* 74: 1097-1113, 1994.

205. **Rasmusson RL, Clark JW, Giles WR, Robinson K, Clark RB, Shibata EF and Campbell DL.** A mathematical model of electrophysiological activity in a bullfrog atrial cell. *Am J Physiol* 259: H370-H389, 1990.

206. **Rasmusson RL, Clark JW, Giles WR, Shibata EF and Campbell DL.** A mathematical model of a bullfrog cardiac pacemaker cell. *Am J Physiol* 259: H352-H369, 1990.

207. **Jafri MS, Rice JJ and Winslow RL.** Cardiac Ca2+ dynamics: the roles of ryanodine receptor adaptation and sarcoplasmic reticulum load. *Biophys J* 74: 1149-1168, 1998.

208. **Winslow RL, Rice J, Jafri S, Marban E and O'Rourke B.** Mechanisms of altered excitation-contraction coupling in canine tachycardia-induced heart failure, II: model studies. *Circ Res* 84: 571-586, 1999.

209. **Wang Z, Fermini B and Nattel S.** Delayed rectifier outward current and repolarization in human atrial myocytes. *Circ Res* 73: 276-285, 1993.

210. **Benardeau A, Hatem SN, Rucker-Martin C, Le Grand B, Mace L, Dervanian P, Mercadier JJ and Coraboeuf E.** Contribution of Na+/Ca2+ exchange to action potential of human atrial myocytes. *Am J Physiol* 271: H1151-H1161, 1996.

211. **Escande D, Loisance D, Planche C and Coraboeuf E.** Age-related changes of action potential plateau shape in isolated human atrial fibers. *Am J Physiol* 249: H843-H850, 1985.

212. **Gelband H, Bush HL, Rosen MR, Myerburg RJ and Hoffman BF.** Electrophysiologic properties of isolated preparations of human atrial myocardium. *Circ Res* 30: 293-300, 1972.

213. **Hille B, Woodhull AM and Shapiro BI.** Negative surface charge near sodium channels of nerve: divalent ions, monovalent ions, and pH. *Philos Trans R Soc Lond B Biol Sci* 270: 301-318, 1975.

214. **Trautwein W, Kassebaum D.G., Nelson R.M. and Hecht H.H.** Electrophysiological study of human heart muscle. *Circ Res* 10: 306-312, 1962.

215. **Van Dam R.T. and Durrer D.** Excitability and electrical activity of human myocardial strips from the left atrial appendage in cases of rheumatic mitral stenosis. *Circ Res* 9: 509-514, 1961.

216. **Li GR and Nattel S.** Properties of human atrial ICa at physiological temperatures and relevance to action potential. *Am J Physiol* 272: H227-H235, 1997.

217. **Courtemanche M, Ramirez RJ and Nattel S.** Ionic targets for drug therapy and atrial fibrillation-induced electrical remodeling: insights from a mathematical model. *Cardiovasc Res* 42: 477-489, 1999.

218. **Varghese A and Sell GR.** A conservation principle and its effect on the formulation of Na-Ca exchanger current in cardiac cells. *J Theor Biol* 189: 33-40, 1997.

219. **Dokos S, Celler BG and Lovell NH.** Modification of DiFrancesco-Noble equations to simulate the effects of vagal stimulation on in vivo mammalian sinoatrial node electrical activity. *Ann Biomed Eng* 21: 321-335, 1993.

220. **Starmer CF, Lastra AA, Nesterenko VV and Grant AO**. Proarrhythmic response to sodium channel blockade. Theoretical model and numerical experiments. *Circulation* 84: 1364-1377, 1991.

221. **Starmer CF, Romashko DN, Reddy RS, Zilberter YI, Starobin J, Grant AO and Krinsky VI**. Proarrhythmic response to potassium channel blockade. Numerical studies of polymorphic tachyarrhythmias. *Circulation* 92: 595-605, 1995.

222. **Beaumont J, Davidenko N, Davidenko JM and Jalife J**. Spiral waves in two-dimensional models of ventricular muscle: formation of a stationary core. *Biophys J* 75: 1-14, 1998.

223. **Qu Z, Weiss JN and Garfinkel A**. Cardiac electrical restitution properties and stability of reentrant spiral waves: a simulation study. *Am J Physiol* 276: H269-H283, 1999.

224. **Courtemanche M, Glass L and Keener JP**. Instabilities of a propagating pulse in a ring of excitable media. *PHYSICAL REVIEW LETTERS* 70: 2182-2185, 1993.

225. **Moe G.K.** Analysis of the initiation of fibrillation by electrocardiographic studies. *Am J Physiol* 134: 473-492, 1941.

226. **Saffitz JE, Kanter HL, Green KG, Tolley TK and Beyer EC**. Tissue-specific determinants of anisotropic conduction velocity in canine atrial and ventricular myocardium. *Circ Res* 74: 1065-1070, 1994.

227. **Leon LJ and Horacek BM**. Computer model of excitation and recovery in the anisotropic myocardium. I. Rectangular and cubic arrays of excitable elements. *J Electrocardiol* 24: 1-15, 1991.

228. **Vigmond EJ and Leon LJ**. Computationally efficient model for simulating electrical activity in cardiac tissue with fiber rotation. *Ann Biomed Eng* 27: 160-170, 1999.

229. **Courtemanche M. and Winfree A.T.** Re-entrant rotating waves in a Beeler-Reuter based model of two-dimensional cardiac activity. *Int J Bifurcation Chaos* 1: 431-444, 1991.

230. **Luo CH and Rudy Y.** A model of the ventricular cardiac action potential. Depolarization, repolarization, and their interaction. *Circ Res* 68: 1501-1526, 1991.

231. **Davidenko JM, Kent PF, Chialvo DR, Michaels DC and Jalife J.** Sustained vortex-like waves in normal isolated ventricular muscle. *Proc Natl Acad Sci U S A* 87: 8785-8789, 1990.

232. **Panfilov A and Hogeweg P.** Spiral breakup in a modified FitzHugh-Nagumo model. *Phys Rev A* 176: 295-299, 1993.

233. **Panfilov A.V. and Holden A.V.** Spatiotemporal chaos in a model of cardiac electrical activity. *Int J Bifurcation Chaos* 1: 219-225, 1991.

234. **Courtemanche M.** Complex spiral wave dynamics in a spatially distributed ionic model of cardiac electrical activity. *Chaos* 6: 579-600, 1996.

235. **Bar M and Eiswirth M.** Turbulence due to spiral breakup in a continuous excitable media. *Phys Rev E* 48: R1635, 1993.

236. **Leon LJ, Roberge FA and Vinet A.** Simulation of two-dimensional anisotropic cardiac reentry: effects of the wavelength on the reentry characteristics. *Ann Biomed Eng* 22: 592-609, 1994.

237. **Nygren A., Leon L.J. and Giles W.R.** Simulations of the human atrial action potential. *Phil Trans R Soc Lond A* 359: 1111-1125, 2001.

238. **Qu Z, Xie F, Garfinkel A and Weiss JN.** Origins of spiral wave meander and breakup in a two-dimensional cardiac tissue model. *Ann Biomed Eng* 28: 755-771, 2000.

239. **Weiss JN, Garfinkel A, Karagueuzian HS, Qu Z and Chen PS.** Chaos and the transition to ventricular fibrillation: a new approach to antiarrhythmic drug evaluation. *Circulation* 99: 2819-2826, 1999.

240. **Karma A.** Electrical alternans and spiral wave breakup in cardiac tissue. *Chaos* 4: 461-472, 1994.

241. **Karma A.** Spiral breakup in model equations of action potential propagation in cardiac tissue. *Phys Rev Lett* 71: 1103, 1993.

242. **Koller ML, Riccio ML and Gilmour RF, Jr.** Dynamic restitution of action potential duration during electrical alternans and ventricular fibrillation. *Am J Physiol* 275: H1635-H1642, 1998.

243. **Starobin JM and Starmer CF.** Boundary-layer analysis of waves propagating in an excitable medium: medium conditions for wave-front-obstacle separation. *Phys Rev E* 54: 430-437, 1996.

244. **Starobin JM, Zilberter YI, Rusnak EM and Starmer CF.** Wavelet formation in excitable cardiac tissue: the role of wavefront-obstacle interactions in initiating high-frequency fibrillatory-like arrhythmias. *Biophys J* 70: 581-594, 1996.

245. **Cabo C, Pertsov AM, Davidenko JM, Baxter WT, Gray RA and Jalife J.** Vortex shedding as a precursor of turbulent electrical activity in cardiac muscle. *Biophys J* 70: 1105-1111, 1996.

246. **Chay TR.** Proarrhythmic and antiarrhythmic actions of ion channel blockers on arrhythmias in the heart: model study. *Am J Physiol* 271: H329-H356, 1996.

247. **Chay TR.** Why are some antiarrhythmic drugs proarrhythmic? Cardiac arrhythmia study by bifurcation analysis. *J Electrocardiol* 28 Suppl: 191-197, 1995.

248. **Garfinkel A, Kim YH, Voroshilovsky O, Qu Z, Kil JR, Lee MH, Karagueuzian HS, Weiss JN and Chen PS.** Preventing ventricular fibrillation by flattening cardiac restitution. *Proc Natl Acad Sci U S A* 97: 6061-6066, 2000.

249. **Balser JR, Bennett PB, Hondeghem LM and Roden DM.** Suppression of time-dependent outward current in guinea pig ventricular myocytes. Actions of quinidine and amiodarone. *Circ Res* 69: 519-529, 1991.

250. **Wang DW, Kiyosue T, Sato T and Arita M.** Comparison of the effects of class I anti-arrhythmic drugs, cibenzoline, mexiletine and flecainide, on the delayed rectifier K+ current of guinea-pig ventricular myocytes. *J Mol Cell Cardiol* 28: 893-903, 1996.

251. **Duan D, Fermini B and Nattel S.** Potassium channel blocking properties of propafenone in rabbit atrial myocytes. *J Pharmacol Exp Ther* 264: 1113-1123, 1993.

252. **Zou R, Kneller J, Leon LJ and Nattel S.** Development of a computer algorithm for the detection of phase singularities and initial application to analyse simulations of atrial fibrillation. *Chaos* [in press]: 2002.

253. **Nygren A, Leon LJ and Giles WR.** Simulations of the human atrial action potential. *Phil Trans R Soc Lond A* 359: 1111-1125, 2001.

254. **Nattel S and Jing W.** Rate-dependent changes in intraventricular conduction produced by procainamide in anesthetized dogs. A quantitative analysis based on the relation between phase 0 inward current and conduction velocity. *Circ Res* 65: 1485-1498, 1989.

255. **Hoekstra BPT, Diks CGH, Allessie MA and DeGoede J.** Nonlinear analysis of the pharmacological conversion of sustained atrial fibrillation in conscious goats by the class Ic drug cibenzoline. *Chaos* 7: 430-446, 1997.

256. **David D, Lang RM, Neumann A, Borow KM, Akselrod S and Mor-Avi V.** Parasympathetically modulated antiarrhythmic action of lidocaine in atrial fibrillation. *Am Heart J* 119: 1061-1068, 1990.

257. **Biffi M, Boriani G, Bronzetti G, Capucci A, Branzi A and Magnani B.** Electrophysiological effects of flecainide and propafenone on atrial fibrillation cycle and relation with arrhythmia termination. *Heart* 82: 176-182, 1999.

258. **Gray RA, Pertsov AM and Jalife J.** Spatial and temporal organization during cardiac fibrillation. *Nature* 392: 75-78, 1998.

259. **Zykov VS.** *Simulation of Wave Processes in Excitable Media*. Manchester, England: Manchester University Press, 1987.

260. **Kirchhof C, Wijffels M, Brugada J, Planellas J and Allessie M.** Mode of action of a new class IC drug (ORG 7797) against atrial fibrillation in conscious dogs. *J Cardiovasc Pharmacol* 17: 116-124, 1991.

261. **Sun H, Velipasaoglu EO, Wu DE, Kopelen HA, Zoghbi WA, Spencer WH, III and Khoury DS**. Simultaneous multisite mapping of the right and the left atrial septum in the canine intact beating heart. *Circulation* 100: 312-319, 1999.

262. **Kim YH, Yashima M, Wu TJ, Doshi R, Chen PS and Karagueuzian HS**. Mechanism of procainamide-induced prevention of spontaneous wave break during ventricular fibrillation. Insight into the maintenance of fibrillation wave fronts. *Circulation* 100: 666-674, 1999.

263. **Vigmond EJ, Ruckdeschel R and Trayanova N**. Reentry in a morphologically realistic atrial model. *J Cardiovasc Electrophysiol* 12: 1046-1054, 2001.

264. **Hund TJ, Kucera JP, Otani NF and Rudy Y**. Ionic charge conservation and long-term steady state in the Luo-Rudy dynamic cell model. *Biophys J* 81: 3324-3331, 2001.

265. **Hara M, Shvilkin A, Rosen MR, Danilo P, Jr. and Boyden PA**. Steady-state and nonsteady-state action potentials in fibrillating canine atrium: abnormal rate adaptation and its possible mechanisms. *Cardiovasc Res* 42: 455-469, 1999.

266. **Zipes DP**. Atrial fibrillation. A tachycardia-induced atrial cardiomyopathy. *Circulation* 95: 562-564, 1997.

267. **Nattel S**. Atrial electrophysiological remodeling caused by rapid atrial activation: underlying mechanisms and clinical relevance to atrial fibrillation. *Cardiovasc Res* 42: 298-308, 1999.

268. **Yue DT, Burkhoff D, Franz MR, Hunter WC and Sagawa K**. Postextrasystolic potentiation of the isolated canine left ventricle. Relationship to mechanical restitution. *Circ Res* 56: 340-350, 1985.

269. **Samie FH, Berenfeld O, Anumonwo J, Mironov SF, Udassi S, Beaumont J, Taffet S, Pertsov AM and Jalife J**. Rectification of the background potassium current: a determinant of rotor dynamics in ventricular fibrillation. *Circ Res* 89: 1216-1223, 2001.

270. Zou, R., Kneller, J., Leon, L. J., and Nattel, S. Mechanisms of AF in substrates of varying size probed with a realistic mathematical model: Moe and Mines revisited. AHA [in press]. 2002.
Ref Type: Abstract

271. **Buxton AE, Josephson ME, Marchlinski FE and Miller JM**. Polymorphic ventricular tachycardia induced by programmed stimulation: Response to procainamide. *J Am Coll Cardiol* 21: 90-98, 1993.

272. **Clancy CE and Rudy Y**. Linking a genetic defect to its cellular phenotype in a cardiac arrhythmia. *Nature* 400: 566-569, 1999.